Dissertation

The late stages of human adenovirus infection
–
Characterising human adenovirus nuclear reorganisation and egress

This dissertation is submitted for the degree of Doctor rerum naturalium
at the Faculty of Mathematics, Informatics and Natural Sciences,
Department of Chemistry, University of Hamburg

by

Søren Pfitzner

Hamburg, 2021

Publications

Part of this work was published as:

PFITZNER S., HOFMANN-SIEBER H., BOSSE J. B., FRANKEN L. E., GRÜNEWALD K. and DOBNER T. (2020) Fluorescent protein tagging of adenoviral proteins pV and pIX reveals 'late virion accumulation compartment', *PLoS Pathogens* **16**(6), 1–25

Methodology developed as part of this work was published as:

FLOMM F. J., SOH T. K., SCHNEIDER C., BRITT H. M., THALASSINOS K., PFITZNER S., REIMER R., GRÜNEWALD K. and BOSSE J. B. (2021) Intermittent bulk release of human cytomegalovirus through multivesicular bodies, *bioRxiv* pp. 1–28

Contents

Abbreviations

A | B | C | D | E | F | G | H | I | K | L | M | N | O | P | R | S | T | U | V | W

A

ab   antibody

ADP   adenovirus death protein

AdV Pol adenoviral DNA polymerase

ANOVA   analysis of variance

APS   ammonium persulphate

ATCC   American Type Culture Collection

ATP   adenosine triphosphate

AVP   adenoviral protease

B

Bak   Bcl-2 homologous antagonist/killer protein

Bax   Bcl-2-associated protein x

Bcl-2   B-cell lymphoma 2

BFP   blue fluorescent protein

bp   base pairs

C

CAR   coxsackie adenovirus receptor

CLEM   correlative light and electron microscopy

CR1   conserved region 1

D

DBP   DNA-binding protein

DDR   DNA damage response

DDSA   (2-Dodecen-1-yl)succinic anhydride

DMEM   dulbecco's modified eagle medium

DMP-30   2,4,6-Tris(dimethylaminomethyl)-phenol

DNA   deoxyribonucleic acid

dpi   days post infection

dsDNA   double-stranded DNA

DTT   dithiotreithol

E

E2E   E2 early

E2L   E2 late

EM   electron microscopy

ER   endoplasmic reticulum

EtOH   ethanol

F

FACS   fluorescence-activated cell sorting

Fc   fragment crystallisable

FCS   fetal calf serum

ffu   fluorescence forming unit

FIB   focussed ion beam

FITC   fluorescein isothiocyanate

FM   fluorescence microscopy

FRAP   fluorescence recovery after photobleaching

G

GA   glutaraldehyde

GFP	green fluorescent protein
GHS	Globally Harmonized System of Classification and Labelling of Chemicals

H

HAdV	human adenovirus
HAdV5	human adenovirus type 5
hCMV	human cytomegalovirus
HEK	human embryonic kidney
HEPES	4-(2-hydroxyethyl)-1-piperazineethanesulfonic acid
HIV-1	human immunodeficiency virus 1
hpi	hours post infection
hpt	hours post transfection
HRP	horseradish peroxidase
HSV-1	herpes simplex virus 1
HVR	hypervariable region

I

IF	immunofluroescence
IP	immunoprecipitation
ITR	inverted terminal repeat

K

kbp	kilo base pairs

L

LB	lysogeny broth
LVAC	late virion accumulation compartment

M

MAC	mitochondrial apopotis-inducing channel

MCL-1 induced myeloid leukaemia cell differentiation protein

MLP major late promoter

MLTU major late transcription unit

MNA 1-Methyl-5-norbornene-2,3-dicarboxylic acid anhydride

MOI multiplicity of infection

MOPS 3-(N-morpholino) propanesulfonic acid

N

NA numerical aperture

NES nuclear export signal

NLS nuclear localisation signal

NPC nuclear pore complex

O

OD optical density

orf open reading frame

ori origin of replication

OTO osmium-thiocarbohydrazide-osmium

P

p protein

PAGE polyacrylamide gel electrophoresis

PBS phosphate buffered saline

PCR polymerase chain reaction

PEI polyethylenimine

PFA paraformaldehyde

PI3K phosphatidylinositol 3'-kinase

PLT progressive lowering of temperature

PML progressive multifocal leukoencephalopathy

PMSF phenylmethylsulfonyl fluoride

PP2A   protein phosphatase 2A

PTM   post-translational modification

R

RFP   red fluorescent protein

RID   receptor internalisation and degradation protein

RIPA   radio immunoprecipitation assay buffer

RNA   ribonucleic acid

ROI   region of interest

S

SDS   sodium dodecyl sulphate

SEM   scanning electron microscopy

sp100A speckled protein 100 kDa A

SUMO   small ubiquitin-like modifier

T

TEM   transmission electron microscopy

TEMED N, N, N', N'-tetramethylethylenediamine

TFB   transformation buffer

TNFα   tumour necrosis factor α

TP   terminal protein

TRAIL   TNFα-related apoptosis-inducing ligand

U

USP7   ubiquitin-specific-processing protease 7

UXP   U exon protein

V

VA-RNA viral associated RNA

ViPR   virus-induced post-replication

W

wt   wild type

List of Figures

Discussion   **130**

List of Tables

Zusammenfassung

Eine Infektion mit humanen Adenoviren des Typs 5 (HAdV5) führt zu einer Erkrankung der oberen und unteren Atemwege. Der Großteil der wissenschaftlichen Forschung hat sich bisher auf die frühen Abläufe des HAdV5 Lebenszyklus fokussiert. Diese beinhalten den HAdV5 Zelleintritt bis zur Genomreplikation im Zellkern der Wirtszellen. Späte Prozesse während der Infektion mit HAdV5 sind bisher nur spärlich beschrieben. Die Arbeit dieser Dissertation zielte darauf ab, zwei späte virale Prozesse, die virale Reorganisation des Zellkerns und den Austritt der Viruspartikel aus dem Zellkern, zu charakterisieren. Dazu wurden zuerst die beiden viralen Proteine pV und pIX innerhalb des viralen Genoms fluoreszent markiert. Das Kernprotein pV bindet an virale DNS und verbindet das virale Genom mit dem Kapsid. Das Kapsidprotein pIX gibt dem Viruspartikel Stabilität. Während der Produktion neuer Virionen wurde gezeigt, dass diese beiden Proteine zu einem membranlosen Kompartiment innerhalb des Zellkerns lokalisieren. Dieses Kompartiment wurde 'late virion accumulation compartment' (LVAC) benannt. Das LVAC wurde mittels verschiedener lichtmikroskopischer und elektronenmikroskopischer Techniken untersucht und wies eine hohe Undurchlässigkeit für Antikörper auf. Korrelative Licht- und Elektronenmikroskopie zeigte eine Anreicherung von parakristallinen Strukturen von neugebildeten Kapsiden auf. Diese lagen eng gepackt zwischen einer honigwabenartigen Struktur aus pV und viraler DNS. Lebenzell-Fluoreszenzmikroskopie und FRAP Messungen zeigten, dass das LVAC die Bewegung von viralen parakristallinen Strukturen behindert. Diese Beobachtung deutet an, dass die Virionen innerhalb des LVACs festgehalten werden. Die Entstehung von LVACs wurde mit der Verdichtung von viralen Replikationszentren in Verbindung gebracht.

Im zweiten Teil dieser Arbeit wurde der Austritt von neugebildeten Viruspartikeln aus dem Zellkern analysiert. Dabei lag ein spezieller Fokus auf dem kleinen Protein 'adenovirus death protein' (ADP). Obwohl ADP im Allgemeinen mit der Freisetzung von Virionen in Verbindung gebracht wird, ist der Mechanismus dahinter noch nicht bekannt. Es wurde

gezeigt, dass ADP zu einer Zunahme von Virionen im Zytoplasma und Mediumüberstand führt, allerdings hatte es keinen klaren Einfluss auf die Stabilität oder Durchlässigkeit der Kernmembran. Das Erscheinungsbild der Kernmembran wurde sowohl mittels Fluoreszenzmikroskopie als auch einer Vielzahl an verschiedenen elektronenmikroskopischen Techniken (klassischer Sektionierung, serieller Blockflächen-Rasterelektronenmikroskopie und Kryoelektronentomographie) untersucht. Es konnte gezeigt werden, dass die Infektion mit HAdV5 zu einer reduzierten Menge an Lamin A an der Kernhülle bei gleichzeitiger reduzierter Stabilität der Kernmembran führt. Zusätzlich wurden kleine Membranschäden entdeckt und eine allgemein erhöhte Durchlässigkeit der Kernmembran gemessen.

Abstract

Human adenovirus type 5 (HAdV5) infection causes disease of the upper and lower respiratory tract. Most research attention has been focussed on the early steps of the HAdV5 life cycle, including HAdV5 entry up until genome replication in the host cell nucleus. Late events during HAdV5 infection remain poorly characterised. The work of this dissertation aimed at further characterising two viral late events, nuclear reorganisation and nuclear egress. To this end, two viral proteins, pV and pIX, were fluorescently labelled within the HAdV5 genome. The core protein V binds to viral DNA and bridges between viral genome and capsid proteins. The capsid protein IX gives stability to the capsid. During virus progeny production both of these proteins were shown to localise to a membrane-less intranuclear compartment, which was termed 'late virion accumulation compartment' (LVAC). The LVAC was characterised by multiple light and electron microscopic techniques and showed high impermeability to antibodies. Correlative light and electron microscopy revealed the accumulation of paracrystalline arrays of newly formed capsids, which were tightly packed within a honeycomb-like structure consisting of pV and viral DNA. Live-cell fluorescence microscopy and FRAP measurements showed that the LVAC restricts the movement of viral paracrystalline arrays, an indication that virions are trapped within. The formation of LVACs was shown to be linked to the congregation of viral replication centres.

In the second part of this work, the nuclear egress of progeny virions was analysed with particular focus on the effect of the small adenovirus death protein (ADP). While ADP is generally implicated in the release of virions, its mechanism of action is not known. ADP expression was shown to increase virion levels in the cytoplasm and supernatant but did not have a clear effect on nuclear membrane stability or nuclear membrane permeability. The appearance of the nuclear membrane in infection was studied using fluorescence microscopy and a variety of electron microscopy techniques including classical sectioning, serial block-face scanning electron microscopy and electron cryo-tomography. HAdV5 infection was shown to reduce levels of lamin A at the nuclear envelope while destabilising the nuclear

membrane to form large-scale invaginations. Additionally, small nuclear membrane lesions were detected in infection and an overall increase in nuclear membrane permeability was measured.

Chapter 1

Introduction

1.1 Adenovirus discovery and classification

The first scientific encounter with human adenovirus (HAdV) was made by Rowe and colleagues in 1953 when they isolated a cytopathogenic agent from human adenoid tissue capable of causing degeneration in human tissue culture cells (ROWE *et al.*, 1953). The virus was initially titled 'adenoid degeneration agent', 'respiratory illness' agent or 'adenoid-pharyngeal conjunctival' agent by multiple groups who isolated different HAdV strains in the following years (HILLEMAN and WERNER, 1954; HUEBNER *et al.*, 1954; HILLEMAN *et al.*, 1955; JAWETZ *et al.*, 1955; KJELLEN, 1955). In 1956, the scientific field agreed upon a common nomenclature for these viruses now belonging to the 'adenovirus group' (ENDERS *et al.*, 1956).

Adenoviruses are not restricted to the human host but since their discovery in humans have been found in a variety of different host species. Accordingly, the International Committee on Taxonomy of Viruses agreed on classifying the family of *Adenoviridae* into five genera including *Atadenovirus*, *Aviadenovirus*, *Ichtadenoviruses*, *Siadenovirus* and *Mastadenovirus* (LEFKOWITZ *et al.*, 2018). Atadenoviruses were initially defined by their characteristic high AT nucleotide content (BENKÖ and HARRACH, 1998). Phylogenetic analysis placed multiple vertebrate hosts, including ruminants, marsupials, birds and reptiles within the genus, but evidence suggests atadenoviruses to be of reptilian origin (WELLEHAN *et al.*, 2004; MILLER *et al.*, 2017). Aviadenoviruses infect only birds including falcon, fowl and goose (GYOZO *et al.*, 2012). Ichtadenoviruses so far only contain one species infecting sturgeon (BENKÖ *et al.*, 2002; KOVÁCS *et al.*, 2003). Siadenoviruses were named after the presence of a sialidase homologue in their genome and contain three confirmed species

infecting frog, turkey and raptor (DAVISON *et al.*, 2000, 2003; KOVÁCS and BENKÖ, 2009). Mastadenoviruses infect mammalian species and comprise the human adenoviruses, which have been the major focus of adenovirus research (NORRBY *et al.*, 1976).

Human adenoviruses are further divided into 7 species (A - G), each containing multiple HAdV types. Initially, adenoviruses were classified by serotyping through serum neutralisation or hemagglutination assays, which led to the classification of 51 distinct adenovirus serotypes (HUEBNER *et al.*, 1954; ROSEN, 1960). A more recent classification is based predominantly on genotyping and phylogenetic analysis and led to the linguistical change of separating HAdVs into 'types' instead of 'serotypes' (JONES *et al.*, 2007; SETO *et al.*, 2011). Genotyping is generally complemented by accounting other virus characteristics such as nucleotide composition, transformation potential in rodents, host range and the ability to recombine (HARRACH *et al.*, 2012). To this day, 103 HAdV types have been described (HADV WORKING GROUP, 2019). This work focusses on HAdV5 of species C (Figure 1).
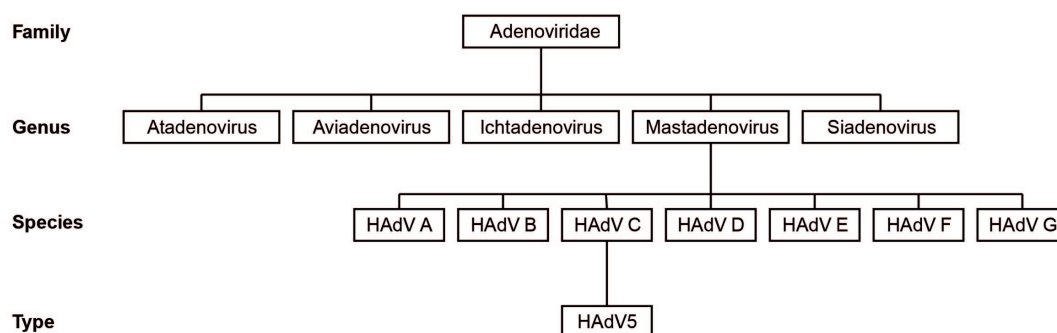
Figure 1: Taxonomy of human adenoviruses and classification of HAdV5. The family of *Adenoviridae* includes five genera including *Atadenovirus, Aviadenovirus, Ichtadenovirus, Mastadenovirus* and *Siadenovirus*. The genus of mastadenoviruses is subdivided into species A - G. HAdV5, the subject of this dissertation, belongs to species C of the HAdVs. The virus taxonomy has been defined by the International Committee on Taxonomy of Viruses (WALKER *et al.*, 2019).

1.2 Human adenovirus pathogenesis

Human adenoviruses readily circulate in the human population, in which especially young children are affected (HONG *et al.*, 2001). HAdVs display a broad tissue tropism causing a multitude of clinical symptoms. Infections with HAdVs have been shown to entail keratoconjunctivitis, often caused by adenovirus species D (JAWETZ *et al.*, 1955; KANEKO *et al.*, 2009; MARANHÃO *et al.*, 2009; LI *et al.*, 2019), gastroenteritis, caused by adenovirus

species F (FLEWETT *et al.*, 1975; UHNOO *et al.*, 1984; CHHABRA *et al.*, 2013; XIAO *et al.*, 2020), cystitis (NUMAZAKI *et al.*, 1973; SHINDO *et al.*, 1986; HO *et al.*, 2019) and a multitude of upper and lower respiratory tract infections (HILLEMAN, 1953; ROWE *et al.*, 1956; ZHANG *et al.*, 2009; LIN *et al.*, 2017; KAJON *et al.*, 2018; WU *et al.*, 2020). Mostly, such infections are mild and self-limiting in immunocompetent hosts and rarely lead to deaths (BERCIAUD *et al.*, 2012). However, particularly immunocompromised patients such as AIDS patients, cancer patients, organ transplant recipients or hematopoietic stem cell recipients are at risk for developing more severe symptoms (KAMPMANN *et al.*, 2005; NEBBIA *et al.*, 2005; ROCH *et al.*, 2008; ZAJĄC-SPYCHAŁA *et al.*, 2020). These symptoms include pneumonia (LEWIS *et al.*, 2009; KIM *et al.*, 2015; PARK *et al.*, 2017; HUANG *et al.*, 2019), meningoencephalitis (SOEUR *et al.*, 1991; STRAUSSBERG *et al.*, 2001; DE ORY *et al.*, 2013), myocarditis (BOWLES *et al.*, 2003; SAVÓN *et al.*, 2008; TREACY *et al.*, 2010) or hepatitis (RONAN *et al.*, 2014; DETRAIT *et al.*, 2015; SCHABERG *et al.*, 2017). In addition to these inflammatory diseases, human adenovirus species D type 36 has been implicated to be involved in obesity (RATHOD *et al.*, 2009; SHANG *et al.*, 2014; ZHOU *et al.*, 2018).

To this day, there is no antiviral drug for specific treatment of an adenovirus infection. The antivirals cidofovir or ribavirin were shown to be able to combat adenovirus infection at the risk of adverse effects, such as nephrotoxicity or neutropenia (GAVIN and KATZ, 2002; ABE *et al.*, 2003; LJUNGMAN *et al.*, 2003). These antivirals are usually administered in combination with lowering the dose of immunosuppressants to aid the patient's immune system in clearing the infection (FLORESCU and SCHAENMAN, 2019). So far, no anti-adenoviral vaccine has been made publicly available. An approved vaccine against HAdV4 and HAdV7 is only provided to recruits of the American military, since adenoviruses have been found to readily circulate in populations living in close quarters (POTTER *et al.*, 2012; KUSCHNER *et al.*, 2013).

HAdV has been shown to persist in the host after clearance of a lytic infection. Children are predominantly permissive for HAdV infection and were shown to undergo reactivation soon after beginning immunosuppressive treatment (VELTROP-DUITS *et al.*, 2011). The primary reservoir of HAdV latency is not definitively described. However, HAdV persistence has been detected in tonsil lymphocytes, intestinal T-lymphocytes and lung epithelial cells (GARNETT *et al.*, 2009; ZHENG *et al.*, 2016). In addition, the lower respiratory tract was speculated as a potential reservoir after HAdV11, 34 and 35 were detected in lower respiratory tract samples of patients without clinical respiratory disease (LEUNG *et al.*, 2005; KOSULIN *et al.*, 2016). Therefore, it is clinically relevant to monitor adenovirus reactivation

during immunosuppressive treatment of patients to be able to react with anti-adenoviral countermeasures before full onset of viremia.

1.3   Human adenovirus structure and capsid proteins

HAdVs are non-enveloped viruses which consisting of an icosahedral protein capsid of 90 - 110 nm diameter surrounding their genome. First images of isolated adenovirus particles were obtained by negative-stain transmission electron microscopy (TOUSIMIS and HILLEMAN, 1957; VALENTINE and HOPPER, 1957). Since then, the structure of the entire virion has been solved by transmission electron microscopy (TEM) as well as X-ray protein crystallography (STEWART *et al.*, 1991; LIU *et al.*, 2010; REDDY *et al.*, 2010; NATCHIAR *et al.*, 2018). The highest resolution of the entire capsid was recorded by TEM at 3.2 Å, which was facilitated by direct electron counting (DAI *et al.*, 2017).

The initial nomenclature of HAdV virion polypeptides was based on their separation on an SDS-PAGE gel, which identified 9 proteins of decreasing molecular weight, labelled protein (p) II - IX (MAIZEL *et al.*, 1968). Overall, a total of 13 proteins has been found in the HAdV capsid, which are separated into three groups: pII (hexon), pIII (penton) and pIV (fibre) belong to the major capsid proteins, pIIIa, pVI, pVIII and pIX belong to the minor capsid proteins and pIVa2, pV, pVII, pMu, adenoviral protease (AVP) and terminal protein (TP) belong to the core proteins (Figure 2). Each protein is introduced in the following sections in short.

A

B

Major capsid proteins	Minor capsid proteins	Core proteins
Penton	pIIIa	pV
Fibre	pVI	pVII
Hexon	pVIII	Mu
	pIX	TP
		pIVa2
		AVP
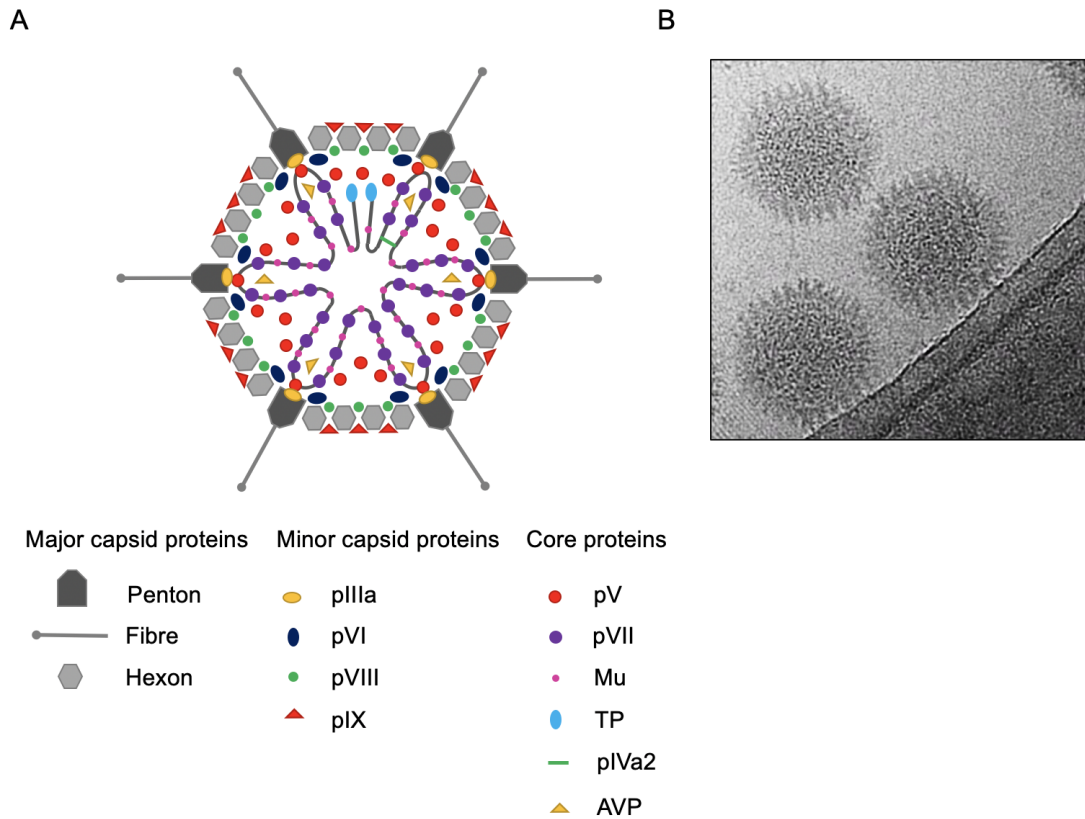
Figure 2: Overview of HAdV5 structure. A) Schematic structure of the HAdV particle. All HAdV5 proteins found in the mature capsid are represented as geometrical shapes. The location of the major and minor core proteins is derived from X-ray crystallographic and electron microscopic studies. The location of core proteins is approximated from their known interactions. The graphical representation has been adapted from (RUSSELL, 2009). **B)** Cryo-TEM image of purified HAdV5 particles. The icosahedral shape of HAdV5 virions and protruding hexon proteins are visible (image kindly provided by Dr. Linda E. Franken, Heinrich Pette Institute, Centre for Structural Systems Biology, Hamburg).

1.3.1 Major capsid proteins

pII is the most abundant major capsid protein, which, within the fully formed capsid, is found in a trimeric conformation. pII trimers have a hexameric base shape, which contributed to their nomenclature as 'hexon' proteins (RUX *et al.*, 2003). Overall, the HAdV capsid is made up of 240 hexon copies, which are equally distributed across the 20 faces of the adenovirus icosahedron (VAN OOSTRUM and BURNETT, 1985). Hexon proteins are classified according to their relative position in the capsid. In this way, four individual hexons (H1-H4) make up the asymmetric unit, which is the smallest repeatable unit within the entire HAdV capsid (REDDY *et al.*, 2010). In dissociation experiments, H1 dissociates separately, whereas H2-H4 of three neighbouring asymmetric units dissociate as a 'group of nine' (SMITH *et al.*, 1965). The hexon base is highly conserved and folds in a typical viral β-barrel fold, called 'jelly roll'. (ROBERTS *et al.*, 1986). Importantly, folding of pII trimers is

dependent on the action of the viral chaperone L4-100K protein (CEPKO and SHARP, 1982). The amino acid sequences of hexon regions presented to the capsid outside have been shown to vary strongly between HAdV types. Those hexon hypervariable regions (HVRs) contribute to immune system antibody recognition and neutralisation (CRAWFORD-MIKSZA and SCHNURR, 1996; MA et al., 2015).

pIII is found on the capsid vertices in a pentameric conformation which contributed to their nomenclature as 'penton' proteins. Like hexon protein, they possess a jelly roll fold in their base domain and are in contact with five hexons on each side of the pentamer (ZUBIETA et al., 2005). Each pIII monomer has an upper insertion domain consisting of two loops, the variable and hypervariable loop, which show sequence diversion between different HAdV species (MADISCH et al., 2007). The hypervariable loop is called 'RGD loop' after the conserved Arg-Gly-Asp sequence, which is important for interaction with cellular integrins and internalisation of the virus (SHAYAKHMETOV et al., 2005).

pIV is found on the capsid vertices in a trimeric conformation, forming HAdV fibres. Each fibre has three separate domains, the base attachment domain, shaft domain and knob domain (YU et al., 2017). The base attachment domain noncovalently binds to a penton base protein and positions fibres at the capsid vertices. The symmetry mismatch between pIII pentamer base and pIV trimer causes only three of the five possible binding sites on the penton base to be occupied (ZUBIETA et al., 2005). The shaft domain is responsible for the spatial protrusion of fibres from the capsid and its length is determined by the number of amino acid repeats in a β-sheet spiral conformation (GREEN et al., 1983; VAN RAAIJ et al., 1999). The globular knob domain is important in cellular receptor binding, most importantly the coxsackie adenovirus receptor (CAR) and has been co-crystallised with its receptor (BEWLEY et al., 1999; SEIRADAKE et al., 2006).

1.3.2   Minor capsid proteins

pIIIa is the largest protein in the group of capsid 'cement' proteins, named after their involvement in capsid assembly and stability. A mutation in the pIIIa gene generates a temperature-sensitive phenotype, which is not capable of producing fully matured virus particles at the restrictive temperature (D'HALLUIN et al., 1978; CHROHOCZEK et al., 1986). Additionally, the protein has been shown be involved in deoxyribonucleic acid (DNA) packaging, where it interacts with the adenoviral L1-52/55K protein and binds to the viral

DNA packaging domain (MA and HEARING, 2011). Initially, pIIIa was believed to be located on the outside of the capsid. However, the electron density it was assigned to was later attributed to pIX and pIIIa was instead found to be located on the capsid inside at the penton-hexon interfaces, cementing their interaction (MARTÍN *et al.*, 2008; REDDY *et al.*, 2010; DAI *et al.*, 2017).

pVI has been assigned on the inside of the capsid in close interaction with the inner hexon cavity, which is in agreement with previous observations of a strong binding interaction between both proteins (MATTHEWS and RUSSELL, 1994, 1995; DAI *et al.*, 2017). Only a section of the full-length pVI was assigned, leading to the hypothesis that the C- and N-termini of the protein are too flexible to be resolved. pVI has multiple roles in the HAdV infectious life cycle: i) regulation of hexon nuclear import, ii) causing membrane breakage in endocytic vesicles for virus particle escape, iii) inhibition of intrinsic immunity and iv) acting as a precursor for a cleavage peptide that is a cofactor for AVP (MANGEL *et al.*, 1993; WEBSTER *et al.*, 1993; WODRICH *et al.*, 2003; WIETHOFF *et al.*, 2005; SCHREINER *et al.*, 2012).

pVIII belongs to the capsid cement proteins and helps to stabilise interactions between hexons. The protein is cleaved into three sections by AVP, two of which were detected by cryo-TEM and X-ray protein crystallography (DAI *et al.*, 2017; NATCHIAR *et al.*, 2018). pVIII has two copies per asymmetric unit. The first copy together with pIIIa is stabilising peripentonal hexon interfaces. The second copy stabilises interactions between hexons of different 'groups of nines'. The role of pVIII was demonstrated by analysing mutations in HAdV5 pVIII as well as bovine adenovirus type 3 pVIII, which were shown to result in particles of reduced thermostability and infectivity (LIU *et al.*, 1985; GABA *et al.*, 2017).

pIX is the smallest of the capsid cement proteins and, unlike pIIIa and pVIII, is located on the outside of the HAdV capsid (FURCINITTI *et al.*, 1989). It is not essential for capsid formation, but deletion of the protein resulted in virus capsids with reduced thermostability (COLBY and SHENK, 1981; CARAVOKYRI and LEPPARD, 1995). Importantly, only the N-terminus is important for capsid stabilisation since a deletion of the C-terminal coiled-coil region was not detrimental to capsid stability (ROSA-CALATRAVA *et al.*, 2001; VELLINGA *et al.*, 2005). The N-terminus of three neighbouring pIX molecules forms a triskelion structure, whereas the α-helical C-terminus forms a four-helix coiled-coil structure with four neighbouring pIX molecules, all of which are part of a different triskelion (LIU *et al.*, 2010). In this way, an interlinked hexagonal network of pIX protein covers the capsid surface resembling a 'hairnet'. The electron density of the four-helix coiled-coil was initially assigned

to pIIIa in crystal structures but after conflicting assignment to pIX in the cryoEM structure, the crystal structure was later revised (REDDY and NEMEROW, 2014; NATCHIAR *et al.*, 2018). Next to its structural role, pIX has been functionally implicated in transcriptional regulation and nuclear reorganisation, even though deletion of the protein only resulted in a minor reduction in virus titres (ROSA-CALATRAVA *et al.*, 2001, 2003).

1.3.3 Core proteins

pIVa2 is a core protein involved in transcription of late adenoviral genes and capsid assembly. pIVa2 localises to the nucleus and was shown to be required for major late promoter (MLP) activity (LUTZ *et al.*, 1996; LUTZ and KEDINGER, 1996; PARDO-MATEOS and YOUNG, 2004). Therefore, the protein acts as part of the switch to the late transcriptional phase of the HAdV life cycle. Additionally, the protein was shown to bind the genome packaging sequence and interact with the packaging protein L1-52/55K (ZHANG *et al.*, 2001; ZHANG and IMPERIALE, 2003). Deletion of pIVa2 resulted in production of early and late proteins but did not yield HAdV particles.

pV is a core-capsid bridging protein since it interacts with the capsid protein pVI as well as forms a complex with the core proteins pVII and pMu (CHATTERJEE *et al.*, 1985; REDDY and NEMEROW, 2014). It was shown to bind to double-stranded DNA (dsDNA) in a non-sequence specific manner. So far, no functional domains were identified, but the protein is speculated to take a similar function as cellular histone H1 in further condensing DNA wrapped around core protein pVII (PEREZ-VARGAS *et al.*, 2014). Initially, the protein localises to nucleoli but later associates with replicated viral genomes in the peripheries of replication centres (UGAI *et al.*, 2012). As part of the infectious capsids, pV enters infected cells, but there are contrary results as to whether pV can enter the nucleus in a new round of virus infection (MATTHEWS and RUSSELL, 1998; HINDLEY *et al.*, 2007; PUNTENER *et al.*, 2011)

pVII is a core protein functioning as adenovirus histone-like protein (BURG *et al.*, 1983; VAYDA *et al.*, 1983). By means of its positive charges, it binds to viral DNA and causes its condensation to nucleosome-like structures. In this way, pVII is important for the protection of viral DNA from the cellular DNA damage response and only dissociates from the viral genome through active transcription (CHEN *et al.*, 2007; KAREN and HEARING, 2011). pVII has also been assumed to be important for genome injection into the nucleus via its interaction with cellular importins (WODRICH *et al.*, 2006; HINDLEY *et al.*, 2007). After

association with replicated viral genomes, pVII is required for genome packaging, which the protein mediates by interaction with packaging proteins L-52/55K protein and pIVa2 (ZHANG and ARCOS, 2005). pVII is synthesised as a precursor protein preVII. After packaging, preVII is cleaved to its mature form pVII and stays associated with the viral genome inside the mature capsid (WEBER, 1976).

pMu is derived from the precursor polypeptide X (preMu) by AVP cleavage and is the third core protein involved in forming HAdV nucleosome-like structures. The protein is positively charged and can bind and precipitate DNA (ANDERSON *et al.*, 1989). Additionally, it was shown to bind to core proteins pV and pVII (CHATTERJEE *et al.*, 1985). preMu, but not pMu, was shown to modulate the expression of E2 proteins (LEE *et al.*, 2004). Interestingly, pMu might share a functional role with pV, since deletion of pV was shown to be accommodated with increased accumulation of pMu in the capsids and distinct point mutations in pMu were able to rescue the thermal instability caused by pV deletion (UGAI *et al.*, 2007).

The adenovirus protease AVP is a cysteine protease expressed in an inactive form which is capable of binding DNA (WEBSTER *et al.*, 1989; MCGRATH *et al.*, 2001; GUPTA *et al.*, 2004). After binding, it becomes partially active to cleave pVI to yield a peptide which acts as a cofactor to fully activate AVP (WEBSTER *et al.*, 1994). AVP is then believed to move alongside the DNA to activate other precursors of pIIIa, pVI, pVII, pVIII and pMu. Cleavage of these viral proteins is required for maturation and full functionality of the virus. A thermosensitive protease mutant cannot mature at the non-permissive temperature and failure to cleave pVI has been demonstrated to block uncoating of the virus in infection, hindering the entry of particles (WEBER, 1976). Importantly, AVP might be involved in cellular lysis by destabilising the host cell structural integrity as it can cleave keratin and actin filaments. The cleaved C-terminus of actin is homologous to the pVI precursor and can also act as an AVP cofactor (CHEN *et al.*, 1993; ZHANG and SCHNEIDER, 1994; MANGEL *et al.*, 2003).

The terminal protein precursor pTP is covalently bound to either end of the HAdV genome (REKOSH *et al.*, 1977). pTP acts as a primer for HAdV genome replication and forms a complex with the adenoviral DNA polymerase (AdV Pol) (TAMANOI and STILLMAN, 1982; DE JONG *et al.*, 2003). Overexpression of pTP was shown to lead to higher virus titres likely through accelerated replication and packaging (WU *et al.*, 2014). Additionally, pTP localises to distinct sites within the nuclear matrix mediated through binding to the enzyme carbamyl phosphate synthetase. The interaction is thought to anchor viral replication sites in the nuclear matrix and ensure close proximity to cellular replication factors (ANGELETTI and

ENGLER, 1998). After packaging, pTP is cleaved by adenovirus protease to the mature TP. TP has been shown to lose DNA-binding and AdV Pol-binding properties (WEBSTER *et al.*, 1994).

1.4 HAdV genome organisation and transcripts

HAdVs are double-stranded DNA viruses with a linear genome of 26 – 45 kilo base pairs (kbp) depending on the HAdV type. HAdV5 possesses a genome of an intermediate length of 36 kbp (CHROBOCZEK *et al.*, 1992). The genome is flanked on either side by inverted terminal repeats (ITRs) of which 18 base pairs (bp) have been reported to be the minimal essential origin of replication (ori) (CHALLBERG and RAWLINS, 1984). The genome possesses a cis-acting packaging sequence that is essential for incorporating viral genomes into their capsid shell (HEARING *et al.*, 1987; GRÄBLE and HEARING, 1990). As opposed to other dsDNA viruses, such as herpes simplex virus 1 (HSV-1) or P22 bacteriophage, which show toroidal genome organisations, no defined structure could be assigned to the condensed viral genome inside the capsid (ZHANG *et al.*, 2000; PÉREZ-BERNÁ *et al.*, 2015; LIU *et al.*, 2019). However, a non-random organisation of condensed DNA-core protein spheres, titled 'adenosomes' was detected by electron cryo-tomography (PÉREZ-BERNÁ *et al.*, 2015).

The HAdV species C genome can be organised into 11 transcription units all of which possess their own promoter region. Their nomenclature is based on the temporal expression during HAdV infection. The early units are subdivided into the E1A, E1B, E2 early (E2E), E3 and E4 units and the intermediate units are subdivided into the IX, IVa2 and L4 units. Additionally, the genome contains the major late transcription unit (MLTU) and the two late units U exon protein (UXP) and E2 late (E2L) (MATHEWS, 1975; CHROBOCZEK *et al.*, 1992; TOLLEFSON *et al.*, 2007; MORRIS *et al.*, 2010; ZHAO *et al.*, 2014; DONOVAN-BANFIELD *et al.*, 2020) (Figure 3). The HAdV genes are transcribed by ribonucleic acid (RNA) polymerase II (WEINMANN *et al.*, 1974). Only two non-coding viral associated RNAs (VA-RNAs) are transcribed by RNA polymerase III from the E2E promoter (SÖDERLUND *et al.*, 1976; HUANG and FLINT, 2003). These VA-RNAs have a pro-viral effect by interfering with the cellular miRNA machinery and inhibiting the proapoptotic function of protein kinase R (MARAN and MATHEWS, 1988; LU and CULLEN, 2004). HAdVs show a complex system of alternative splicing and overlapping reading frames for efficient containment of all necessary genes within their genome (DONOVAN-BANFIELD *et al.*, 2020). The following sections give an overview of the HAdV species C transcripts and their functions.
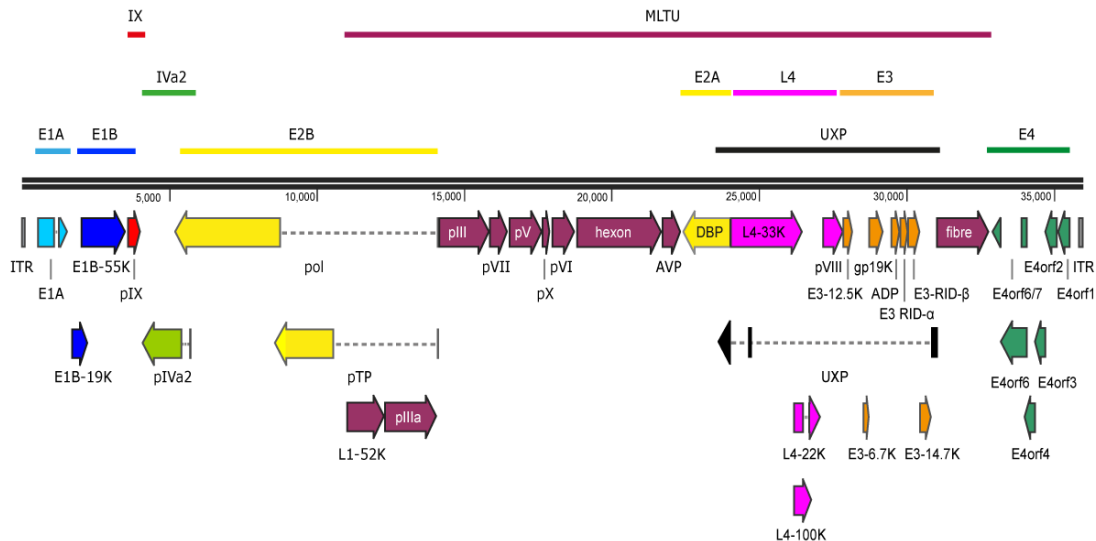
Figure 3: HAdV5 genome organisation. The transcription units are shown as coloured lines including E1A (light blue), E1B (blue), IX (red), IVa2 (light green), E2(A/B) (yellow), MLTU (plum), L4 (magenta), UXP (black), E3 (orange) and E4 (dark green). The respective proteins encoded by the transcription units are shown as arrows and are coloured accordingly. The direction of transcripts is indicated by the direction of arrow heads. Introns are represented as a dashed line. The MLTU includes the transcripts L1, L2, L3, L4 and L5. The genome is flanked on either side by ITRs. The genome sequence and annotation originates from (DAVISON *et al.*, 2003; CHROBOCZEK *et al.*, 1992) and is deposited at Refseq: AC_000008.

1.4.1 Early transcription units

The E1A unit codes for 5 differently spliced E1A protein variants, which all share a common 3' and 5' end (BERK and SHARP, 1976; SHENK and FLINT, 1991). In particular, the 12S and 13S variants of E1A are the most abundant transcripts early in infection (RADKO *et al.*, 2015). Overall, the E1A proteins act as transcriptional activators for the early viral transcription units E2-E4 as well as induce cell cycle progression into S-phase in which DNA is replicated (WINBERG and SHENK, 1984; FERGUSON *et al.*, 1985; GHOSH and HARTER, 2003; HORWITZ *et al.*, 2008). Transcriptional transactivation by E1A is facilitated through its interaction with several cellular transcription factors such as TATA-binding protein, ATFs, and p300/CREB-binding protein (LIU and GREEN, 1994; SONG *et al.*, 1997; O'CONNOR *et al.*, 1999; PELKA *et al.*, 2009). S-phase induction is based on E1A interaction with retinoblastoma protein, which in turn loses its inhibitory association with E2F transcription factors. Thus, E1A allows E2F transcription factors to drive cells from G0- or G1-phase into S-phase (WHYTE *et al.*, 1988; LIU and MARMORSTEIN, 2007). Without counterbalancing functions of other viral proteins, the growth stimulatory effect of E1A has been shown to lead to an upregulation of p53 and subsequent induction of apoptosis (QUERIDO *et al.*, 1997b).

The E1B unit codes for two E1B proteins, E1B-19K and E1B-55K (BERK and SHARP, 1976). Both proteins are required to counteract the pro-apoptotic effects of E1A to retain host cell viability. E1B-55K can bind directly to p53 and inhibit its function through multiple mechanisms. First, E1B-55K inhibits the N-terminal activation domain of p53 (QUERIDO *et al.*, 1997a; TEODORO and BRANTON, 1997). Second, by means of its nuclear export signal (NES) and small ubiquitin-like modifier (SUMO) consensus motif, E1B-55K can shuttle between the host cell nucleus and cytoplasm (KRÄTZER *et al.*, 2000; ENDTER *et al.*, 2001, 2005; KINDSMULLER *et al.*, 2007). In this way, E1B-55K re-localises p53 from the nucleus to perinuclear bodies in the cytoplasm. Third, E1B-55K together with E4 open reading frame (orf) 6 protein, a protein of the E4 transcription unit, can act as an E3 ubiquitin ligase to ubiquitinate p53 as well as other proteins involved in DNA damage response (Mre11, Rad50, Tip60, DNA ligase IV, Bloom helicase) and antiviral innate immunity (ATRX, integrin α-3, SPOC1) (QUERIDO *et al.*, 2001a,b; LIU *et al.*, 2005; BAKER *et al.*, 2007; DALLAIRE *et al.*, 2009; SCHREINER *et al.*, 2010, 2013; ORAZIO *et al.*, 2011; GUPTA *et al.*, 2013). Ubiquitinated proteins are subsequently targeted for proteolytic degradation by the 26S proteasome. Lastly, E1B-55K can act as a SUMO E3 ligase and SUMOylate p53 (MULLER and DOBNER, 2008). SUMOylation targets p53 to progressive multifocal leukoencephalopathy (PML)-nuclear bodies where its mobility and function is restricted before the protein is exported from the nucleus (PENNELLA *et al.*, 2010; WIMMER *et al.*, 2010).

E1B-19K has an anti-apoptotic function independent of p53. It can counteract the antiviral pro-apoptotic functions of tumour necrosis factor α (TNFα), Fas ligand, TNFα-related apoptosis-inducing ligand (TRAIL) and E1A (WHITE *et al.*, 1992; PEREZ and WHITE, 1998; SUNDARARAJAN and WHITE, 2001; TOLLEFSON *et al.*, 2001). E1B-19K acts downstream of death receptor signalling and functions as a B-cell lymphoma 2 (Bcl-2) homologue, which allows it to bind to Bcl-2-associated protein x (Bax) and Bcl-2 homologous antagonist/killer protein (Bak) (BOYD *et al.*, 1994). Upon death receptor activation and caspase 8 activity, Bax undergoes conformational changes and can interact with Bak (DESAGHER *et al.*, 1999). Additionally, Bak is released by E1A-dependent degradation of the anti-apoptotic induced myeloid leukaemia cell differentiation protein (MCL-1) from the MCL-1-Bak complex (CUCONATI *et al.*, 2003). E1B-19K-binding blocks Bak-Bax oligomerisation from forming the mitochondrial apopotis-inducing channel (MAC) (CUCONATI *et al.*, 2002; MARTINEZ-CABALLERO *et al.*, 2009). Formation of MACs induces pores in the mitochondrial membrane to release cytochrome c and SMAC, activating caspase 3 and 9 to cause apoptosis (ESKES *et al.*, 2000; SUNDARARAJAN *et al.*, 2001).

The E2 transcription unit can be split into two regions, E2A and E2B. E2A codes for the adenoviral DNA-binding protein (DBP) and E2B codes for AdV Pol and pTP (described in Section 1.3.3) (CARAVOKYRI and LEPPARD, 1996; SWAMINATHAN and THIMMAPAYA, 1995). All three proteins are essential for viral genome replication (RIJNDERS et al., 1983; PARKER et al., 1998). DBP molecules bind single-stranded DNA and form chains along the DNA, which stabilises and protects the individual adenovirus genome strands and aids in strand unwinding in an adenosine triphosphate (ATP)-independent mechanism (NAGATA et al., 1983; MONAGHAN et al., 1994; VAN BREUKELEN et al., 2000). In this way, DBP is required for initiation and elongation during adenovirus DNA replication. AdV Pol forms a complex with pTP and the cellular DNA-binding protein nuclear factor 1 and subsequently catalyses the covalent addition of deoxycytidine monophosphate to pTP after which the complex binds to the adenovirus DNA. (CHEN et al., 1990; MUL and VAN DER VLIET, 1992). AdV Pol then catalyses the adenoviral DNA replication. Interestingly, the first three nucleotides are added at nucleotide position 4-6 before the AdV Pol jumps back to position 1-3. This mechanism has been proposed to counteract single nucleotide deletions at the ends of the linear genome since the jumping-back mechanism has been demonstrated to allow the repair of a deletion of the first two nucleotides (KING and VAN DER VLIET, 1994). The E2A and E2B regions are both transcribed from the E2E promoter, but also the E2L promoter. The E2L promoter is transcribed later throughout infection and thereby meets the requirement for high E2 protein levels at late time-points in infection (BHAT et al., 1987).

The E3 transcription unit mainly encodes proteins involved in host cell immune evasion. In total, seven E3 transcripts code for the conserved region 1 (CR1)α, E3-12.5K, gp19K, CR1β (ADP), receptor internalisation and degradation protein (RID)-α, RID-β and E3-14.7K proteins. The glycoprotein gp19K blocks the transport of major histocompatibility complex class I molecules from the endoplasmic reticulum (ER) membrane to the plasma membrane and thus blocks the presentation of viral antigens on the surface of infected cells (BURGERT and KVIST, 1985; FEUERBACH et al., 1994). RID-α, RID-β, CR1α and E3-14.7K are all involved in blocking apoptosis by acting on different parts of the apoptosis signalling pathway. RID-α and RID-β form a RID complex and reduce the amounts of TNFα and Fas receptors on the cell surface (STEWART et al., 1995; SHISLER et al., 1997; HILGENDORF et al., 2003). The CR1α protein binds to the RID complex, a process through which it has been shown to reduce the amounts of TRAIL receptors 1 and 2 on the cell surface (BENEDICT et al., 2001). In contrast to CR1α and RID-α/β, E3-14.7K is a cytoplasmic protein and affects downstream signalling of the TNFα pathway by interaction with a GTPase signal mediator

(GOODING *et al.*, 1990; LI *et al.*, 1997). E3-12.5K protein is the only protein that so far has no known function. However, its conservation in HAdV2 and HAdV5 hints at a relevant function in infection (HAWKINS and WOLD, 1992). The only E3 protein that was implicated in a process different than host cell immune evasion is the CR1β adenovirus death protein ADP. ADP is required for the efficient lysis of infected cells and was shown to localise to the ER, Golgi and nuclear membrane in HAdV2 infection (SCARIA *et al.*, 1992; TOLLEFSON *et al.*, 1996a). Deletion of the protein leads to delayed detection of infectious particles in the supernatant, however, the exact mechanism of ADP function has not been determined (TOLLEFSON *et al.*, 1996b; DORONIN *et al.*, 2003).

The E4 transcription unit codes for six E4 proteins, including E4orf6/7, E4orf6, E4orf4, E4orf3, E4orf2 and E4orf1 (DIX and LEPPARD, 1993). E4orf1 has been shown to have different roles in different HAdV types. Cells infected with HAdV36 were shown to have an upregulated glucose uptake, whereas E4orf1 facilitates the transformation potential of HAdV9 in a rat embryo cell line (JAVIER, 1994; DHURANDHAR *et al.*, 2011). Additionally, E4orf1 has been shown to restrict the growth of E1B-55K deletion mutants of HAdV5 through means of affecting signalling of the phosphatidylinositol 3'-kinase (PI3K) pathway. However, a HAdV5 E4orf1 deletion mutant did not display reduced growth in cell culture (HALBERT *et al.*, 1985).

So far, no function could be assigned to E4orf2, even though it has been shown to be expressed in infection (DIX and LEPPARD, 1995). E4orf3 acts to reduce multiple antiviral responses of the host cell. It causes a redistribution of PML nuclear bodies to track-like structure in the nucleus, which was shown to reduce the host cell interferon-response (DOUCAS *et al.*, 1996; ULLMAN *et al.*, 2007). Similarly, E4orf3 sequesters proteins of the MRN complex (Mre11, Rad50, Nbs1) to these nuclear tracks and thus acts against the cellular DNA damage response (ARAUJO *et al.*, 2005; EVANS and HEARING, 2005). Additionally, it can destine the antiviral transcription factor transcriptional intermediary factor 1γ for proteolytic digestion and inhibit p53 activity independently of E1B-55K by repressing p53 promoter regions through induction of heterochromatin at these sites (SORIA *et al.*, 2010; FORRESTER *et al.*, 2012). Recently, E4orf3 has been shown to be involved in the control of adenoviral gene expression through interaction with E1A (SORIANO *et al.*, 2019).

E4orf4 acts in a negative feedback loop by affecting E1A transactivation of the E4 promoter region (MÜLLER *et al.*, 1992; BONDESSON *et al.*, 1996). The protein mainly acts via the protein phosphatase 2A (PP2A) (KLEINBERGER and SHENK, 1993). In this way, E4orf4 can also downregulate E2 promoter transcription by phosphorylation of transcription factors

through PP2A action (MANNERVIK *et al.*, 1999). Additionally, E4orf4 has been shown to induce apoptosis in a p53-independent manner by means of caspase activation (MARCELLUS *et al.*, 1998; LIVNE *et al.*, 2001). However, even though it is an early protein, it only contributes to cell death later in the virus life cycle (BRANTON and ROOPCHAND, 2001).

E4orf6 is partially functionally redundant with E4orf3 and is involved in multiple processes including mRNA splicing, DNA synthesis, host cell shut-off and inhibition of apoptosis. Thus, mutation of the protein strongly reduces viral yields. E4orf6 forms a complex with E1B-55K and affects transport of viral mRNAs and leads to proteolytic degradation of p53 as described for E4orf3 above (SARNOW *et al.*, 1984; CARVALHO *et al.*, 1995; QUERIDO *et al.*, 2001a). Furthermore, it interacts with DNA-dependent protein kinase and inhibits V(D)J-joining in lymphocytes (BOYER *et al.*, 1999). Additionally, E4orf6 acts on p53 independently of E1B-55K and reduces p53 transcriptional activation (DOBNER *et al.*, 1996). Interestingly, E4orf6 has recently been suggested to be the adenoviral portal protein required for DNA insertion into the capsid since it shows sequence homology with the clip region of other portal proteins, is present in assembled capsids and colocalises with other adenovirus packaging proteins (AHI *et al.*, 2017). E4orf6/7 promotes viral gene expression by acting as a transactivator as well as aiding E1A in facilitating viral E2 transcription and transcription of cellular E2F promoter regions (SCHALEY *et al.*, 2000). The protein has been shown to displace retinoblastoma protein and p107 from E2F promoters and induces E2F dimerisation and recruitment to the promoter regions (OBERT *et al.*, 1994; O'CONNOR and HEARING, 2000).

1.4.2 Intermediate and late transcription units

HAdV has three intermediate transcription units (IX, IVa2 and L4) and one MLTU, which is transcribed from the MLP. The MLTU transcripts can be subdivided into five families (L1 - L5) (SHAW and ZIFF, 1980). Each of the five transcript families has temporally different splice patterns (BINGER and FLINT, 1984; MORRIS *et al.*, 2010; ZHAO *et al.*, 2014).

The intermediate IX and IVa2 transcription units code for the minor capsid protein pIX and the packaging protein pIVa2 (described in Section1.3.2). The late L1 transcript codes for proteins L1-52/55K and pIIIa. pIIIa is a capsid cement protein (described in Section 1.3.2). L1-52/55K is a HAdV packaging protein (HASSON *et al.*, 1989; GUSTIN and IMPERIALE, 1998). Deletion of the protein only weakly affects adenoviral gene expression but yields empty

capsids. The protein initially interacts with the capsid vertices, dissociates after cleavage by AVP and cannot be detected in mature HAdV particles (PEREZ-BERNA *et al.*, 2014; CONDEZO *et al.*, 2015). The L2 transcript codes for the major capsid protein pIII (described in Section 1.3.1) and the core proteins pV, pVII and pX (described in Section 1.3.2). L3 codes for capsid proteins pII, pVI and AVP (described in Sections 1.3.1 & 1.3.3). The L4 transcript codes for proteins pVIII, L4-100K, L4-33K and L4-22K. As part of the MLTU, L4 was initially believed to be exclusively transcribed from the MLP. However, the detection of L4 transcripts at earlier time-points presented a paradox until an additional intermediate L4 promoter was found to initiate transcription of the L4 orfs L4-22K and L4-33K (MORRIS *et al.*, 2010). pVIII is a minor capsid protein (described in Section 1.3.2). L4-100K is involved in assembly, mRNA translation as well as in blocking the host immune response. It was shown to be required for hexon trimerisation by acting as a chaperone protein (CEPKO and SHARP, 1982; YAN *et al.*, 2016). L4-100K also is involved in translation by facilitating ribosome shunting, a process through which the ribosome skips parts of the mRNA and starts translation at alternative start codons (HAYES *et al.*, 1990; XI *et al.*, 2004, 2005). Additionally, L4-100K has been shown to play a role in immune evasion by inhibiting human lymphocyte granule serine protease B, an enzyme involved caspase cleavage to induce apoptosis (ANDRADE *et al.*, 2003). L4-33K has two functions as an RNA alternative splicing factor and capsid assembly facilitator (FARLEY *et al.*, 2004; PERSSON *et al.*, 2012; WU *et al.*, 2013). It has been shown to be required for altering the transcription pattern of the MLTU by causing selection of alternative splice sites. Interestingly, HAdV5 mutants with non-functional L4-33K produce empty capsids. However, the binding of other packaging proteins pIVa2, L1-52/55K and L4-22K to the packaging sequence was shown not be affected and L4-33K does not bind the packaging sequence itself. Similar to L4-33K, L4-22K controls the transcriptional switch of MLTU genes as well as is essential for genome packaging (WU *et al.*, 2012; GUIMET and HEARING, 2013; LAN *et al.*, 2017). Deletion of L4-22K leads to the formation of empty capsids, however, other than L4-33K, L4-22K binds to the HAdV packaging sequence. Lastly, the L5 transcript codes for the capsid protein pIV (described in Section 1.3.1).

The U exon transcription unit is expressed late in infection and codes for UXP (YING *et al.*, 2010). UXP shares part of its sequence with DBP but has a different reading frame. The protein is initially localised to the nucleoli and later associates with the periphery of replication centres. Hence, it has been implicated in genome replication or RNA transcription.

1.5 HAdV life cycle

HAdVs require a tightly controlled reorganisation and repurposing of the cellular host machinery. The incoming virus capsid contains and codes for viral proteins required for successful entry, evasion of the host immune system and transport to the nucleus to initiate progeny virion production. The host cell then acts as production machinery to amplify viral genomes and structural proteins for the assembly of new capsids. After assembly and maturation, the virions leave the host cell for a new round of infection. The HAdV life cycle has mainly been studied in the mastadenovirus types HAdV2 and HAdV5 (Figure 4). The individual steps of the HAdV life cycle are presented in the following sections.
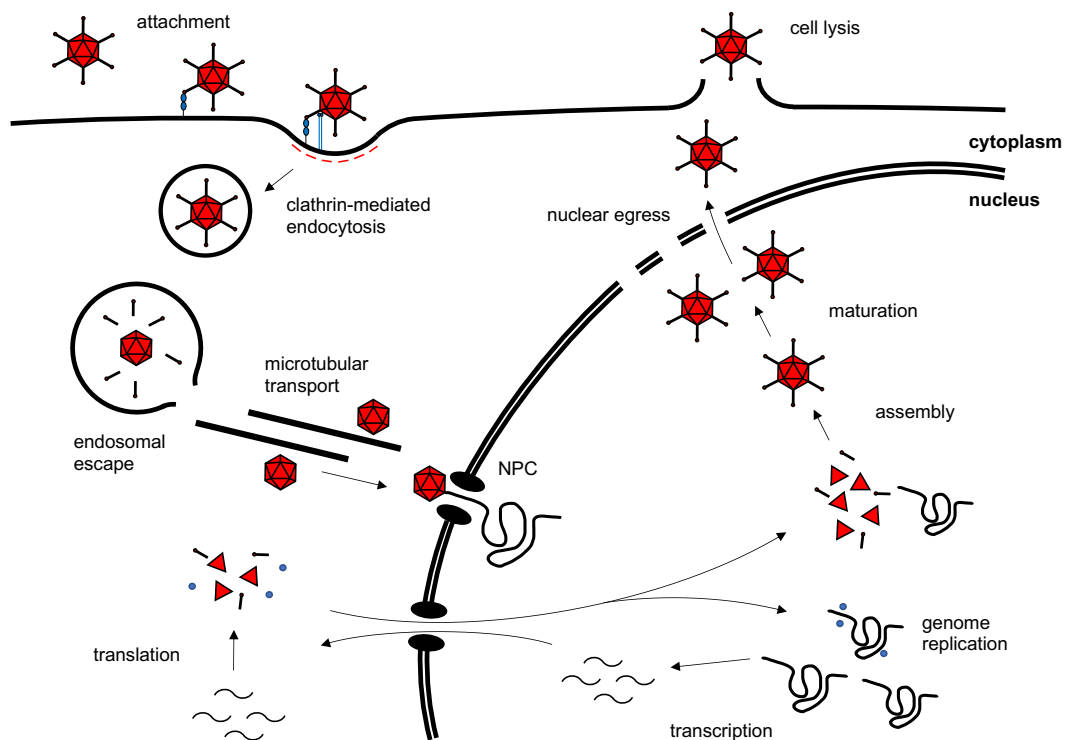
Figure 4: Overview of the major steps entailed in HAdV infection of a host cell. Initially, the virus attaches to the cell surface via interaction with primary receptors, such as CAR, and secondary receptors such as integrins. After attachment, the viral particle is internalised by the cell through clathrin-mediated endocytosis. Facilitated through the loss of fibres and capsid destabilisation, pVI is released from the capsid and aids in endosomal escape. The free capsid is transported along microtubules to the nuclear pore complex (NPC). At the NPC the viral genome is injected into the nucleus. First, early viral mRNAs are transcribed, which are transported into the cytoplasm to be translated there. Later, transcription of late viral mRNAs occurs, which mainly code for structural proteins to form progeny capsids. Virus genome replication occurs in replication centres. The newly replicated genomes together with capsid proteins assemble to form new virions. The progeny particles undergo maturation through multi-protein proteolytic cleavage of the adenoviral protease. Afterwards, virions cross the nuclear envelope and subsequently leave the cell by total cell lysis.

1.5.1 Virus adhesion and entry

The first step in the productive life cycle of HAdV is adhesion of a virus particle to a target cell by means of primary and secondary receptor interactions. The most-studied primary adhesion receptor is the coxsackie adenovirus receptor (CAR), which mediates both the internalisation of coxsackie B viruses and HAdVs (BERGELSON et al., 1997). Individual types of HAdV species A, C, D, E and F have been shown to require CAR for adhesion (ROELVINK et al., 1998). CAR interacts with a distinct site on the fibre knob domain (ROELVINK et al., 1999). Importantly, spatial restrictions require the HAdV fibres to be long and flexible to allow for secondary receptor binding (SHAYAKHMETOV and LIEBER, 2000; WU et al., 2004). HAdV species B has by comparison the shortest fibres and mainly relies on fibre binding to CD46 or non-classically on desmoglein 2 (FLEISCHLI et al., 2007; VASSAL-STERMANN et al., 2018). Other receptors have been shown to mediate HAdV internalisation in a variety of different cell lines for specific HAdV types including sialic acid-containing polysaccharides, GD1a glycan and SR-A6 receptor (ARNBERG et al., 2002; NILSSON et al., 2011; LENMAN et al., 2015; STICHLING et al., 2018; BAKER et al., 2019).

After attachment to the primary receptor, virus association with the secondary 'entry' receptor is necessary for successful virion uptake. HAdV species A-E require integrins αVβ3 and αVβ5 as secondary receptors, which bind to the RGD loop of the penton base (WICKHAM et al., 1993; SHAYAKHMETOV et al., 2005). HAdV species F lack the penton RGD loop and instead rely on laminin-binding integrins, in particular integrin α6β4 (RAJAN et al., 2018). Upon integrin binding, intracellular signalling via the PI3K pathway triggers remodelling of the actin cytoskeleton and formation of clathrin-coated pits (LI et al., 1998a,b). The virus particle subsequently enters the cell via the clathrin-mediated endocytosis pathway. This process was shown to be dependent on action of the modulatory GTPase protein dynamin (WANG et al., 1998). Virions lose their fibres during the process of internalisation, which is important for endosomal escape since mutant HAdV which is incapable of fibre-release was shown to remain in endosomes (GREBER et al., 1996; NAKANO et al., 2000; MARTIN-FERNANDEZ et al., 2004). Fibre release at the cell surface was proposed to result from physical stress due to CAR receptor drifting relative to stationary integrin receptors, which may pull fibres off their penton base (BURCKHARDT et al., 2011).

1.5.2 Endosomal escape and genome release

After the virus particle has been endocytosed it is targeted to early endosomes (GASTALDELLI *et al.*, 2008). It must escape the endosome to be transported to the nucleus. Failure to escape endosomes will lead to targeting of the virion to late endosomes and lysosomes and subsequent degradation of the particle (GASTALDELLI *et al.*, 2008). The penton-integrin interaction has not only been shown to be important for internalisation but also for virus uncoating for endosomal release. The penton base undergoes conformational changes upon integrin-binding, which might be important for releasing the capsid vertices during entry (LINDERT *et al.*, 2009). In agreement with this observation, integrin-binding induced structural softening of the vertex regions (SNIJDER *et al.*, 2013). Vertex dissociation is required for subsequent release of pVI, the membrane-lytic agent of HAdVs (WIETHOFF *et al.*, 2005; SMITH *et al.*, 2010). Protein VI causes a change in membrane curvature to the point of membrane rupture (MAIER *et al.*, 2010). Interestingly, there is a temporal gap between membrane rupture and particle release from the endosome (MAIER *et al.*, 2012).

The role of endosomal acidification in particle escape is not totally understood. Inhibition of endosomal acidification hindered general adenovirus escape but was shown to act on a process upstream of full virus uncoating (SETH *et al.*, 1984; GREBER *et al.*, 1993; RODRÍGUEZ and EVERITT, 1996). There is evidence that low pH facilitates disassembly of the metastable capsid vertices and allows the release of pVI into the endosomal space, which then acts on the endosomal membrane in a pH-independent mechanism (WIETHOFF *et al.*, 2005). However, other light microscopy evidence showed endosomal escape to be pH-independent (SUOMALAINEN *et al.*, 2013).

After the partially disassembled capsid has escaped the endosome it is transported to the nuclear pores along the cellular microtubular network. The transport depends on hexon protein, which interacts with the microtubule motor protein dynein via its HVR1 (BREMNER *et al.*, 2009). Importantly, the hexon-dynein interaction requires both a pH-dependent conformational change in the hexon protein and dynein phosphorylation (SCHERER *et al.*, 2014; SCHERER and VALLEE, 2015). At the nuclear membrane, the virus particle interacts with the NPC via the nucleoporin Nup214 (CASSANY *et al.*, 2015). Since virions are too large to pass the nuclear membrane, full disassembly of the particle is required to release the viral genome into the nucleoplasm. Physical stress induced by Nup214 binding and the action of microtubular motor protein kinesin-1 has been shown to cause capsid disruption (STRUNZE

et al., 2011). Import of the adenoviral genome requires cellular histone H1.2, heat-shock cognate protein Hsc70, transportin-1 and the classical proteins involved in NPC transport (importin-α, importin-β, nuclear transport factor 2 and Ras-related nuclear protein Ran (SAPHIRE *et al.*, 2000; TROTMAN *et al.*, 2001; HINDLEY *et al.*, 2007). The cellular nuclear import machinery does not interact with the viral genome directly but by means of interaction with core protein pVII. pVII possesses several nuclear localisation signals (NLSs), is bound to the viral genome, and was shown to efficiently be imported into the nucleus through interaction with importins and transportins (WODRICH *et al.*, 2006). The fate of other core proteins pMu and pV is not clear. There is both evidence for and against pV entering the nucleus with the viral genome (HINDLEY *et al.*, 2007; PUNTENER *et al.*, 2011).

1.5.3 Replication, nuclear morphogenesis and assembly

Individual incoming adenoviral genomes associate with cellular chromatin and bind the nuclear matrix via both terminal proteins (SCHAACK *et al.*, 1990; KOMATSU *et al.*, 2018). HAdV genomes were shown to be chromatinised with cellular histones upon nuclear entry (DANIELL *et al.*, 1981; KOMATSU *et al.*, 2018). Initial transcription is facilitated by the presence of core protein pVII and cellular template activating factor-I, which forms a complex with the HAdV genome and pVII and alters the DNA conformation to improve access for transcription factors (KOMATSU *et al.*, 2011). pVII is also important for protecting the genome from deactivation by the cellular DNA damage response (DDR) machinery after nuclear entry. During transcription, pVII is removed from the genome in an E1A-dependent mechanism, which coincides with increased DDR activation (CHEN *et al.*, 2007; KAREN and HEARING, 2011). The first genes to be transcribed are the immediate early proteins E1A and E1B (see Section 1.4.1).

HAdV transcription and replication is linked with PML nuclear bodies. Usually, PML nuclear bodies are involved in silencing of viral genomes including HSV-1, HSMV and EBV and localise to genomes shortly after infection (BELL *et al.*, 2000; SOURVINOS *et al.*, 2007). In HAdVs, the genome is initially protected by pVII, but also localises adjacently to PML nuclear bodies a few hours after nuclear entry (ISHOV and MAUL, 1996). The recruitment of PML is not DNA-dependent but relies on the viral DBP, which facilitates recruitment of individual PML constituents, such as speckled protein 100 kDa A (sp100A) and ubiquitin-specific-processing protease 7 (USP7), which improve viral transcription and replication (CHING *et al.*, 2013; BERSCHEMINSKI *et al.*, 2014; KOMATSU *et al.*, 2016a; STUBBE

et al., 2020). DPB is an indicator of adenovirus replication compartments, which are spatially distinct from sites of transcription (POMBO *et al.*, 1994). Early replication centres appear as dots which subsequently develop into ring-like replication centres. These replication rings were shown to contain DBP, E1B-55K, sp100A, USP7 and E4orf6 (ORNELLES and SHENK, 1991; DOUCAS *et al.*, 1996; KOMATSU *et al.*, 2016b). Replicated genomes accumulate on the outside of replication centres, acquire histones and act as sites for late viral transcription. After an unknown switch mechanism, replicated genomes accumulate in neighbouring compartments, termed virus-induced post-replication (ViPR) bodies, which has been shown to coincide with a rapid increase in HAdV genome replication (KOMATSU *et al.*, 2018). ViPR bodies were shown to contain nucleolar proteins such as myb-binding protein 1a or nucleophosmin 1 but also viral packaging protein IVa2 (KOMATSU *et al.*, 2016b; GENOVESO *et al.*, 2019). Since only pVII, but no cellular histones are found in ViPR bodies, they are the proposed sites for HAdV genome condensation with pVII.

HAdV genomes are packaged through means of their packaging sequence, which is positioned between the ITR and E1A orf and consists of functionally redundant AT-repeats (KOSTURKO *et al.*, 1982; GRÄBLE and HEARING, 1990). Incompletely assembled particles mostly include this side of the adenoviral genome, which is an indicator that packaging begins at the packaging sequence (DANIELL, 1976). Important packaging proteins that have been identified are IVa2, L4-22K, L4-33K, L1-52/55K and pIIIa (GUSTIN and IMPERIALE, 1998; ZHANG and IMPERIALE, 2003; EWING *et al.*, 2007; MA and HEARING, 2011; WU *et al.*, 2013).

So far, the exact mechanism of HAdV assembly remained elusive. Two main models have been proposed based on evidence favouring either one or the other. In the sequential packaging model, empty HAdV capsids are formed first and the genome is subsequently inserted through a portal at a capsid vertex. In the concomitant packaging model, the capsid gradually assembles around the HAdV genome and encases it without the requirement of a portal protein. Packaging of dsDNA viruses such as herpesviridae or T4 or λ phage requires a portal protein, a terminase and an ATPase (ORTEGA and CATALANO, 2006; SELVARAJAN SIGAMANI *et al.*, 2013). Similar functional proteins have been found in HAdV which hint at a sequential mechanism. Protein IVa2 has been shown to bind ATP and possesses ATPase activity (OSTAPCHUK and HEARING, 2008; OSTAPCHUK *et al.*, 2011). Additionally, L4-33K may act as terminase, as it forms oligomeric ring-like structures and activates ATPase activity of pIVa2 (AHI *et al.*, 2015). E4or6 has been suggested as the portal protein since it shares some

secondary structure homology with phage portal proteins and has a comparable predicted tertiary structure to other portal proteins (AHI *et al.*, 2017).

However, it remains unclear, how the HAdV genome in its condensed form, while bound to pVII, is able to be translocated through a portal protein. Importantly, analysis of a thermosensitive HAdV mutant not capable of packaging DNA at the restrictive temperature showed that fully formed empty capsids could not be matured into full capsids at the permissive temperature (KHITTOO and WEBER, 1977). These arguments would be accommodated in the concomitant packaging model. In this model, HAdV genomes are suggested to pre-condense and then associate with partially assembled capsid intermediates, which accumulate further minor and major capsid protein to close up the HAdV capsid around the condensed genome. Electron microscopy (EM) of particles inside cells showed particles in a variety of different assembly intermediate stages. Furthermore, a packaging mutant showed an accumulation of condensed genomes and empty virus capsids as failed assembly products (CONDEZO and SAN MARTÍN, 2017). After assembly, the particles mature, which involves the action of AVP.

1.5.4 Virus egress

So far, the exact mechanism of how the mature virions are released from the cell is not known. There are likely two possibly interlinked mechanisms present, the first to allow mature virions to cross the nuclear envelope and the second to exit the cell across the plasma membrane. Generally, cell lysis was shown to be dependent on virus-induced host cell translational shut-off accompanied by destabilisation of the intermediate filament network (ZHANG and SCHNEIDER, 1994). Inhibiting this translational shut-off led to a reduced cytopathic effect and intermediate filaments such as cytokeratins remained stable.

Multiple kinds of cell death pathways have been suggested to be the cause for ultimate host cell lysis. Although the process was initially described as apoptosis, a lack of membrane blebbing and DNA fragmentation were suggested as hinting against apoptosis and another necrosis-like cell death was suggested (TOLLEFSON *et al.*, 1996a; ABOU EL HASSAN *et al.*, 2004). Other groups have described the HAdV-caused cell death as autophagy due to the upregulation of caspases and appearance of autophagic vacuoles (JIANG *et al.*, 2011; RODRIGUEZ-ROCHA *et al.*, 2011). However, a HAdV5 E1A mutant was shown to induce controlled necrosis-like cell death in a RIPK3-dependent manner and the process of autophagy was described as a cell-

survival mechanism rather than the cause of cell death, since inhibition of autophagy increased virus-induced cytotoxicity (BAIRD *et al.*, 2008; WEIGERT *et al.*, 2017).

Importantly, ADP was shown to be involved in the efficient lysis of host cells (TOLLEFSON *et al.*, 1996a,b). HAdV5 ADP is a small protein with a size of 10.5 kDa. HAdV2 ADP was shown to be post-translationally modified by N-glycosylation, O-glycosylation and palmitoylation (SCARIA *et al.*, 1992; HAUSMANN *et al.*, 1998). Initially, the protein was described to localise to the ER and Golgi but ultimately is transported to the nuclear membrane (SCARIA *et al.*, 1992). Deletion of ADP induced a phenotype of small plaques and extended survival of infected cells for multiple days. Overexpression of ADP was shown to increase virus spread and to induce an apoptotic phenotype including membrane blebbing and shrunk cytoplasm and cell death via both caspase-dependent and caspase-independent mechanisms (DORONIN *et al.*, 2003; ZOU *et al.*, 2004). Additionally, the level of ADP has been shown to be responsible for the progression of infection in lymphocytes (MURALI *et al.*, 2014). Lymphocyte cell types which naturally express ADP to high levels when infected with wt virus proceed with a lytic infection, whereas lymphocytes with naturally low expression levels of ADP were associated with a persistent infection. Interestingly, the levels of ADP expression in lytic cell types correlated with the rate of cell death, whereas cell types that express low levels of ADP in HAdV wt infection remained doing so even after infection with an ADP-overexpression mutant and remained persistently infected. In reverse, the abolishing ADP expression in a naturally lytically-infected lymphocytes resulted in a persistent infection.

Analysis of the spread of HAdV2 and HAdV5 in monolayer cell culture showed the virus to mainly spread by cell-free transmission (WIGAND and KÜMEL, 1977; YAKIMOVICH *et al.*, 2012). Yakimovich et al. showed the formation of plaques to be dependent on the lysis of infected cells and free diffusion of virus particles in the extracellular medium. Through this effect, comet-shaped plaques appear when the surface of monolayer cell culture is tilted. Although ADP is not the sole determinant of lytic infection, it can increase cell-free spread. To exploit this effect, ADP has been inserted into oncolytic adenoviral vector systems to increase the virus spread by a factor of 10 (TOTH *et al.*, 2004). Similarly, the spread of HAdV41, a virus that has been suggested to display cell-to-cell spread, has been increased 10-50 fold (LU *et al.*, 2013). Recently, machine learning approaches were applied to analyse the spread of the virus (ANDRIASYAN *et al.*, 2019). Algorithms can predict lytic and non-lytic cells based on the DAPI stain of their nuclei.

Chapter 2

Materials

2.1 Chemicals

Unless stated differently, chemicals, enzymes and reagents were obtained from Agilent, Biomol, Merck, New England Biolabs, Roche, Roth and Sigma Aldrich. All buffers were prepared in double distilled water unless specified in the text.

2.2 Cells

2.2.1 Bacterial strains

The listed bacterial strains were used for storage, amplification and recombination of plasmid DNA.

Table 1: Genotype of bacterial strains used in molecular cloning

Strain	Genotype
DH5α	F$^-$, ϕ80lacZΔM15, Δ(lacZYA-argF)U169, recA1, endA1, hsdR17(r$_K$$^-$, m$_K$$^+$), phoA, supE44, $\gamma^-$$thi$-1, gyrA96, relA1 (Hanahan and Meselson, 1983)
GB05 red	DH10B including HS996, ΔrecET, ΔybcC, araC-BAD-$\gamma\beta\alpha$A (Wang et al., 2006)
GBred-gyrA462	DH10B including HS996, ΔrecET, ΔybcC, araC-BAD-$\gamma\beta\alpha$A, gyrA462 (Wang et al., 2014)
NEB 10-beta	Δ(ara-leu)7697, araD139, fhuA, ΔlacX74, galK16, galE15, e14, /phi80$dlac$ZΔM15, recA1, relA1, endA1, nupG, rpsL(Str^R), rph, spoT1, Δ(mrr-hsdRMS-mcrBC) (New England Biolabs)

2.2.2 Mammalian cell lines

The listed mammalian cell lines were used for studying HAdV5 infection and for production of lentivirus stocks. Where applicable, the American Type Culture Collection (ATCC) number is provided.

Table 2: Characteristics of mammalian cell lines

Name	Characteristics	ATCC
A549	Human lung epithelial carcinoma cell line expressing p53 (GIARD *et al.*, 1973)	CCL-185
A549 lamin A mTagGFP	Monoclonal A549 cell line expressing mTagGFP-fused chromobody against lamin A/C (PFITZNER *et al.*, 2020)	–
A549 mTagBFP-NES	Polyclonal A549 cell line expressing mTagBFP fused to a nuclear export signal (PFITZNER *et al.*, 2020)	–
BJ	Human foreskin fibroblast immortalised cell line (BODNAR *et al.*, 1998)	CRL-2522
H1299	Human lung epithelial carcinoma cell line, p53 negative (MITSUDOMI *et al.*, 1992)	CRL-5803
MRC-5	Human foreskin fibroblast immortalised cell line (BODNAR *et al.*, 1998)	CCL-171
HEK 293	Human embryonic kidney cell line, HAdV5 transformed, expressing E1A and E1B (GRAHAM *et al.*, 1977)	CRL-1573
HEK 293T	HEK 293 cell line expressing the SV-40 large T antigen (DUBRIDGE *et al.*, 1987)	CRL-3216

2.3   Viruses

The listed virus strains were used for infection of mammalian cells.

Table 3: Characteristics of virus strains

Virus strain	Characteristics
HAdV5 ΔE3	HAdV5 containing a 1863 bp deletion (nucleotides 28602 – 30465) in the E3 region (KINDSMULLER *et al.*, 2007)
HAdV5 ΔE3 ADP+	HAdV5 ΔE3 with ADP coding sequence reinserted into E3 region
HAdV5 DBP-mCherry ADP–	HAdV5 ΔE3 derived strain with N-terminal fusion of mCherry to DBP
HAdV5 DBP-mCherry ADP+	HAdV5 ΔE3 ADP+ derived strain with N-terminal fusion of mCherry to DBP
HAdV5 pV-mCherry ADP–	HAdV5 ΔE3 derived strain with C-terminal fusion of mCherry to pV
HAdV5 pV-mCherry ADP+	HAdV5 ΔE3 ADP+ derived strain with C-terminal fusion of mCherry to pV
HAdV5 pIX-mCherry ADP–	HAdV5 ΔE3 derived strain with C-terminal fusion of mCherry to pIX
HAdV5 pIX-mCherry ADP+	HAdV5 ΔE3 ADP+ derived strain with C-terminal fusion of mCherry to pIX
HAdV5 pIX-PA-TagRFP	HAdV5 ΔE3 ADP+ derived strain with C-terminal fusion of PA-TagRFP to pIX
HAdV5 pIX-mEos4a	HAdV5 ΔE3 ADP+ derived strain with C-terminal fusion of mEos4a to pIX
HAdV5 ADP-HA	HAdV5 ΔE3 ADP+ derived strain with C-terminal fusion of an HA tag to ADP
HAdV5 pV-mCherry pIX-mNeonGreen	HAdV5 ΔE3 ADP+ derived strain with C-terminal fusion of mNeonGreen to pIX and N-terminal fusion of mCherry to pV
HAdV5 DBP-mCherry pIX-mNeonGreen	HAdV5 has ΔE3 ADP+ derived strain with C-terminal fusion of mNeonGreen to pIX and N-terminal fusion of mCherry to DBP

2.4 Nucleic acids

2.4.1 Oligonucleotides

The listed oligonucleotides were used for sequencing, colony PCR or PCR amplification for Red recombination. Oligonucleotide numbers correspond to their Filemaker Pro Advanced database entry.

Table 4: Sequence and use of oligonucleotides

#	Name	Sequence	Use
820	Abra. seq fw 28097	5'-GCTAGTTGAGCGGGACAGG-3'	Sequencing
1101	T7 Prom fw	5'-TAATACGACTCACTATAGGG-3'	Sequencing
2621	T7 Terminator	5'-GCTAGTTATTGCTCAGCG-3'	Sequencing
3611	mCherry seq fw	5'-CCAAGGCCTACGTGAAGCAC-3'	Sequencing
3612	mCherry seq rv	5'-CTTCAGCCTCTGCTTGATCTCG-3'	Sequencing Colony PCR
810	Abra. seq fw 16410	5'-CATTAGTGCTATGACTCAGGG-3'	Colony PCR
822	Abra. seq fw 23481	5'-CGTGGTACTTGTCCATCAGC-3'	Colony PCR
1219	L4 100K early rev	5'-GACTTGTTCCTCGTTTGCCTC-3'	Colony PCR
3388	ADP rescue fw	5'-GCTTAGAAAACCCTTAGGGTATTAGGCCAA AGGCGCAGCTACTGTGGGGTTTATGACCAAC ACAACCAACG-3'	Red recomb.
3389	ADP rescue rv	5'-GGACAGAAATTTGCTAACTGATTTTAAGTA AGTGATGCTTTATTATTTTTTTTTATCATACTG TAAGAGAAAAGAACATGTG-3'	Red recomb.
3605	pV ccdB amp fw	5'-TAGACTCGTACTGTTGTATGTATCCAGCGG CGGCGGCGCGCAACGAAGCTGCCAGTATACA CTCCGCTAG-3'	Red recomb.
3606	pV ccdB amp rv	5'-TCCGGCGCGATGACCTGGAGCATCTCTTCT TTGATTTTGCGCTTGGACATCAGCCCCATACG ATATAAGTTG-3'	Red recomb.
3616	pIX ccdB amp fw	5'-TGCGCCAGCAGGTTTCTGCCCTGAAGGCTT CCTCCCCTCCCAATGCGGTTGCCAGTATACACT CCGCTAG-3'	Red recomb.
3617	pIX ccdB amp rv	5'-ACTTGCTTGATCCAAATCCAAACAGAGTCTG GTTTTTTATTTATGTTTTACAGCCCCATACGATA TAAGTTG-3'	Red recomb.
3619	HexH1 ccdB amp fw	5'-GGGATGAAGCTGCTACTGCTCTTGAAATA AACCTAGAAGAAGAGGACGATGCCAGTATACA CTCCGCTAG-3'	Red recomb.

#	Name	Sequence	Use
3620	HexH1 ccdB amp rv	5'-ACGTGAGTTTTTTGCTGCTCAGCTTGCTC GTCTACTTCGTCTTCGTTGTCCAGCCCCATAC GATATAAGTTG-3'	Red recomb.
3621	HexH5 ccdB amp fw	5'-AAAGTCAAGTGGAAATGCAATTTTTCTCAA CTACTGAGGCAGCCGCAGGCGCCAGTATACACT CCGCTAG-3'	Red recomb.
3622	HexH5 ccdB amp rv	5'-TCTACATCTTCACTGTACAATACCACTTTAG GAGTCAAGTTATCACCATTCAGCCCCATACGA TATAAGTTG-3'	Red recomb.
3746	ADP mCherry fw	5'-CAAGCTAGCATGACCAACACAACC-3'	Red recomb.
3747	ADP mCherry rv	5'-CTGACCGGTTACTGTAAGAGAAAAGAAC-3'	Red recomb.
4037	ADP HA ccdB amp fw	5'-GAATCCATAGATTGGACGGACTGAAACAC ATGTTCTTTTCTCTTACAGTAGCCAGTAT ACACTCCGCTAG-3'	Red recomb.
4038	ADP HA ccdB amp rev	5'-ATTTGCTAACTGATTTTAAGTAAGTGATGC TTTATTATTTTTTTTTATCACAGCCCCATA CGATATAAGTTG-3'	Red recomb.
4039	ADP HA rescue	5'-GAATCCATAGATTGGACGGACTGAAACACA TGTTCTTTTCTCTTACAGTATACCCATACGA TGTTCCAGATTACGCTTGATAAAAAAAAATA ATAAAGCATCACTTACTTAAAATCAGTTAGC AAATTTCTG-3'	Red recomb.

2.4.2 Vector plasmids

The listed vector plasmids were used for sub-cloning of recombinant plasmids or as vector controls in transfection experiments. Plasmid numbers correspond to their Filemaker Pro Advanced database entry.

Table 5: Characteristics of vector plasmids

#	Name	Characteristics	Source
136	pcDNA3	For expression in mammalian cells, CMV promoter	Invitrogen
146	pEGFP C1	For expression of EGFP or insertion of EGFP fusion proteins	Clontech
285	pCherry C1	For expression of mCherry or insertion of mCherry fusion proteins on the C-terminus	Group database
3483	pCherry C2	Includes an inserted linker corresponding to method in (PUNTENER *et al.*, 2011)	Group database
3484	pCherry C3	For insertion of mCherry fusion proteins on the N-terminus	Group database

2.4.3 Recombinant plasmids

The listed recombinant plasmids were used for or generated in this work. Their purpose is described and plasmid numbers correspond to their Filemaker Pro Advanced database entry.

Table 6: Characteristics of recombinant plasmids

#	Name	Characteristics	Source
271	p15A ccdB amp AgeI	PCR template for first red recombination	Group database
2520	p15A HAdV5 ΔE3 ADP+	Bacterial plasmid for generation of HAdV5 ΔE3 ADP+	Group database
3482	pADP-mCherry	Mammalian expression plasmid for transfection in H1299 cells and ADP-mCherry expression	Group database
3500	pcDNA3-ADP	Mammalian expression plasmid for transfection in H1299 cells ADP wt expression	Group database
3649	pcDNA3-Hom1+2	Plasmid including two homologous sequences of the HAdV5 pIX gene. Used for insertion of fluorophores in between homologous sequences	Group database
3650	pcDNA3 pIX-mNeonGreen	Plasmid for amplification of mNeonGreen flanked by pIX homologous sites for the second red recombination	Group database
3651	pcDNA3 pIX-PA-TagRFP	Plasmid for amplification of PA-TagRFP flanked by pIX homologous sites for the second red recombination	Group database
3652	pcDNA3 pIX-mEos4a	Plasmid for amplification of mEos4a flanked by pIX homologous sites for the second red recombination	Group database
3653	pcDNA3 mTagBFP-NES	Mammalian expression plasmid for transfection in H1299 cells and mTagBFP-NES expression	Group database
3490	p15A HAdV5 pV-mCherry ADP–	Bacterial plasmid for generation of virus strain HAdV5 pV-mCherry ADP–	Group database
3491	p15A HAdV5 pV-mCherry ADP+	Bacterial plasmid for generation of virus strain HAdV5 pV-mCherry ADP+	Group database
3492	p15A HAdV5 pIX-mCherry ADP–	Bacterial plasmid for generation of virus strain HAdV5 pIX-mCherry ADP–	Group database
3493	p15A HAdV5 pIX-mCherry ADP+	Bacterial plasmid for generation of virus strain HAdV5 pIX-mCherry ADP+	Group database

#	Name	Characteristics	Source
3495	p15A HAdV5 HexH1-mCherry	Bacterial plasmid for generation of virus strain HAdV5 HexonH1-mCherry	Group database
3497	p15A HAdV5 HexH5-mCherry	Bacterial plasmid for generation of virus strain HAdV5 HexonH5-mCherry	Group database
3636	p15A HAdV5 DBP-mCherry pIX-mNeonGreen	Bacterial plasmid for generation of virus strain HAdV5 DBP-mCherry pIX-mNeonGreen	Group database
3647	p15A HAdV5 pV-mCherry pIX-mNeonGreen	Bacterial plasmid for generation of virus strain HAdV5 pV-mCherry pIX-mNeonGreen	Group database
3643	p15A HAdV5 pIX-PA-TagRFP ADP+	Bacterial plasmid for generation of virus strain HAdV5 pIX-PA-TagRFP	Group database
3644	p15A HAdV5 pIX-mEos4a ADP+	Bacterial plasmid for generation of virus strain HAdV5 pIX-mEos4a	Group database
3648	p15A HAdV5 ADP-HA	Bacterial plasmid for generation of virus strain HAdV5 ADP-HA	Group database
3654	pLeGO iVLN2 mTagBFP-NES	Lentiviral vector for generation of an mTagBFP-NES expressing cell line	Group database
1970	pGagPol	Transfection plasmid for lentivirus production	Group database
1969	pRev	Transfection plasmid for lentivirus production	Group database
1968	pCMV-VSV-G	Transfection plasmid for lentivirus production	Group database
3485	pEX mCherry pV	Gene synthesis carrier plasmid for amplification of mCherry with pV homologous sites for homologous recombineering	Eurofins
3486	pGH mCherry pIX	Gene synthesis carrier plasmid for amplification of mCherry with pIX homologous sites for homologous recombineeringg	Eurofins
3487	pEX mCherry HexH1	Gene synthesis carrier plasmid for amplification of mCherry with hexon HVR1 homologous sites for homologous recombineering	Eurofins
3489	pEX mCherry HexH5	Gene synthesis carrier plasmid for amplification of mCherry with hexon HVR5 homologous sites for homologous recombineering	Eurofins

2.5 Antibodies

2.5.1 Primary antibodies

The listed primary antibodies were used for detecting viral and cellular proteins in western blot and IF microscopy.

Table 7: Characteristics of primary antibodies used for IF or western blot (WB) stain.

Name	Characteristics	Dilution (v/v)	Source
B6-8	Mouse monoclonal antibody (ab) against HAdV5 E2A protein (REICH *et al.*, 1983)	WB 1:10 IF 1:10	Group database
AC-15	Mouse monoclonal ab against β-actin	WB 1:5000	Sigma Aldrich, A5441
3F10	Rat monoclonal ab against HA tag	IF 1:1000	Roche, 2013819
4C11	Mouse monoclonal ab against lamin A	IF 1:1000	Abcam
α-pV	Rabbit polyclonal ab against HAdV5 pV (MATTHEWS and RUSSELL, 1998)	WB 1:5000 IF 1:1000	Dr. Harald Wodrich (Bordeaux)
α-pIX	Rabbit polyclonal ab against pIX (LUTZ *et al.*, 1997)	WB 1:5000 IF 1:1000	Dr. Harald Wodrich (Bordeaux)
α-hexon	Mouse monoclonal ab against HAdV5 hexon trimer (RUSSELL *et al.*, 1981)	If 1:500	Group database
α-RFP	Mouse monoclonal ab against red fluorescent protein (RFP)	WB 1:1000	Abcam

2.5.2 Secondary antibodies

The listed secondary antibodies were used for detecting primary antibody binding in western blot and IF microscopy.

Table 8: Characteristics of secondary antibodies

Name	Characteristics	Dilution (v/v)	Source
HRP-α-mouse	Goat polyclonal ab against mouse IgG (H+L) conjugated to horseradish peroxidase (HRP)	WB 1:10,000 in PBS-T	Jackson, 115-035-003
HRP-α-rabbit	Goat polyclonal ab against rabbit IgG (H+L) conjugated to HRP	WB 1:10,000 in PBS-T	Jackson, 111-035-003
HRP-α-rat	Goat polyclonal ab against rat IgG (H+L) conjugated to HRP	WB 1:10,000 in PBS-T	Jackson, 112-035-003
Alexa Fluor 488 α-mouse	Goat polyclonal ab against mouse IgG (H+L) conjugated to Alexa Fluor 488	IF 1:1000 in PBS	Invitrogen, A-11001
Alexa Fluor 488 α-rabbit	Goat polyclonal ab against rabbit IgG (H+L) conjugated to Alexa Fluor 488	IF 1:1000 in PBS	Invitrogen, A-11008
Alexa Fluor 555 α-rabbit	Goat polyclonal ab against rabbit IgG (H+L) conjugated to Alexa Fluor 555	IF 1:1000 in PBS	Invitrogen, A-21428
Alexa Fluor 647 α-mouse	Goat polyclonal ab against mouse IgG (H+L) conjugated to Alexa Fluor 647	IF 1:1000 in PBS	Invitrogen, A-21235
Alexa Fluor 647 α-rabbit	Goat polyclonal ab against rabbit IgG (H+L) conjugated to Alexa Fluor 647	IF 1:1000 in PBS	Invitrogen, A-21244
Alexa Fluor 647 α-rat	Goat polyclonal ab against rat IgG (H+L) conjugated to Alexa Fluor 647	IF 1:1000 in PBS	Invitrogen, A-21247

2.6   Standards and markers

The listed standards and markers were used for protein and DNA size estimation in agarose gel and sodium dodecyl sulphate (SDS)-polyacrylamide gel electrophoresis (PAGE) separation.

Table 9: Standards and markers

Marker	Use	Source
1 kbp DNA ladder	Agarose gels	New England Biolabs, N3232
100 bp DNA ladder	Agarose gels	New England Biolabs, N3232
Page Ruler Prestained Protein Ladder	SDS-PAGE	Thermo Scientific, 26617

2.7   Commercial systems

The listed commercial kits were used for DNA cloning purposes or western blot protein detection.

Table 10: Commercial systems for DNA and protein preparation

Kit	Application	Source
Gateway BP Clonase II enzyme mix	BP Gateway cloning reaction	Thermo Scientific
Gateway LR Clonase II enzyme mix	LR Gateway cloning reaction	Thermo Scientific
Protein Assay	Bradford determination of solubilised protein concentration	Biorad
SuperSignal West Pico PLUS Chemiluminescent Substrate	HRP substrate for western blot signal detection	Thermo Scientific
QIAPrep Spin Miniprep/Maxiprep kit	Isolation of *E. coli* plasmid DNA	Quiagen
QIAquick Gel Extraction kit	Purification of DNA from agarose gels	Quiagen
QIAquick PCR Purification kit	Purification of PCR product	Quiagen

2.8 Software and databases

The listed software and databases were used to store, record, analyse and visually represent data of this work.

Table 11: Use and source of software and databases.

Software	Implementation	Source
Al2CO	Protein residue conservation analysis	(PEI and GRISHIN, 2001)
Acrobat Pro	PDF data processing	Adobe
Chimera 1.12	Molecular structure visualisation and analysis	UCSF
CLC Main Workbench 7.9.1	Sequence data processing	Quiagen
Clustal Omega	Multiple sequence alignment	EMBL
DigitalMicrograph	Electron microscope control and image analysis	Gatan
Epson Scan	Western blot raw data digitisation	Epson
Fiji	Image processing and analysis	(SCHINDELIN et al., 2012)
FileMaker Pro Advanced 17.0.2	Database management	Claris
Gene tools	Agarose gel documentation	Syngene
GPS-Lipid	Palmitoylation prediction	(XIE et al., 2016)
GraphPad Prism 5	Data visualisation and statistics	Statcon
HeliQuest	α-helix property prediction	(GAUTIER et al., 2008)
Illustrator CS6	Data visualisation and layout processing	Adobe
Imaris 8.2.1	Microscopy image analysis	Bitplane
IMOD 4.10	3D biological data processing and visualisation	(KREMER et al., 1996)
JPred 4	Protein secondary structure prediction	(DROZDETSKIY et al., 2015)
Leica Application Suite X 2.0	Fluorescence microscopy image acquisition	Leica
MAPS 10.3	Microscopy data processing, correlation and navigation	Thermo Scientific

Software	Implementation	Source
Mendeley Desktop 1.17.13	Reference management	Mendeley
MotionCor2 1.4	Beam-induced TEM motion correction	(ZHENG *et al.*, 2017)
NetOGlyc 4.0	O-glycosylation prediction	(STEENTOFT *et al.*, 2013)
NIS Elements Advanced Research 4.51	Fluorescence microscopy image acquisition and analysis	Nikon
Office 365 Word/Excel	Text and numerical data processing	Microsoft
Pubmed	Literature database	NCIB
RELION 3.0	Cryo-EM data processing	(SCHERES, 2012)
SerialEM	Cryo-ET acquisition	(MASTRONARDE, 2005)
SnapGene Viewer 5.0.7	Sequence data processing	SnapGene
SPRINT-Gly	N-glycosylation prediction	(TAHERZADEH *et al.*, 2019)
Tecnai imaging and analysis	Electron microscopy control and raw data acquisition	Thermo Scientific
Tomography 5.1	Cryo-ET acquisition	Thermo Scientific

Chapter 3

Methods

3.1 Bacterial cell techniques

3.1.1 Growth and storage conditions

For selection of single colonies, *E. coli* cells were grown on 1x lysogeny broth (LB) agar plates (15 g/L agar; see Table 12) mixed with an appropriate antibiotic solution (1:1000 (v/v) see Table 13) in an incubator (Heraeus B6) at 37 °C for 16-20 h. LB agar plates can be stored at 4 °C for several weeks.

Liquid cultures of *E. coli* cells were inoculated from single colonies and grown overnight in 1x LB medium in the presence of an appropriate antibiotic (1:1000 (v/v) see Table 13). The cells were grown at 37 °C (Innova 4000, New Brunswick Scientific) and shaken at 200 rpm for 16 h. For storage of freshly grown cultures, 600 μL of cell culture were mixed with 600 μL 50 % (v/v) glycerol and stored in cryogenic tubes (1.8 mL CryoPure, Sarstedt) at −80 °C.

Table 12: LB medium composition

LB medium	10 g/L	tryptone
	5 g/L	yeast extract
	5 g/L	NaCl

Table 13: Antibiotic concentrations used for LB medium preparation

Antibiotic stock solutions		
	100 mg/mL	ampicillin
	15 mg/mL	chloramphenicol (in EtOH)
	25 mg/mL	kanamycin
	100 mg/mL	streptomycin

3.1.2 Preparation of competent cells

3.1.2.1 Chemically competent cells

50 μL of the *E. coli* strain DH5α was spread on an agar plate and grown overnight without antibiotics. A single colony was used to inoculate 10 mL of 1x LB medium. The cultures were grown overnight at 37 °C (Innova 4000, New Brunswick Scientific) and shaken at 200 rpm. 2 mL of *E. coli* DH5α was used to inoculate 200 mL of LB medium. The cultures were grown to an OD$_{600}$ of 0.43 at 37 °C and shaken at 200 rpm. Absorbance measurements were taken on a spectrophotometer (SmartSpec Plus, BioRad). The cells were cooled on ice for 15 min before centrifugation at 3,800 g for 5 min at 4 °C. The supernatant was removed and the cells were resuspended in 60 mL ice-cold transformation buffer (TFB) 1 (see Table 14). The cells were centrifuged again at 3,800 g for 5 min at 4 °C. The cell pellet was resuspended in 4 mL of ice-cold TFB 2 (see Table 14) each. The cell suspension was then split into 100 μL aliquots, snap-frozen in liquid nitrogen and stored at −80 °C.

Table 14: Transformation buffers for generation of chemically competent cells

TFB 1 (pH 5.8)		
	15 % (v/v)	glycerol
	10 mM	$CaCl_2$
	30 mM	KOAc
	100 mM	$RbCl_2$
	50 mM	$MnCl_2$
TFB 2 (pH 7.0)	15 % (v/v)	glycerol
	75 mM	$CaCl_2$
	10 mM	$RbCl_2$
	10 mM	K-3-(N-morpholino) propanesulfonic acid (MOPS)

3.1.2.2 Electro-competent cells

Electro-competent cells were prepared fresh for each transformation. All tubes were kept on ice during the entire process. The cells were centrifuged at 7,800 g for 30 s at 2 °C. The supernatant was discarded and the pellet was resuspended in 1 mL ice-cold H_2O. For another wash round, the cells were centrifuged at 9,600 g for 30 s at 2 °C. The wash step was repeated with 1 mL ice-cold H_2O. The last centrifugation was performed at 11,600 g for 30 s at 2 °C. Subsequently, the supernatant was decanted and the cell pellet was resuspended in the remaining H_2O. The cells were used for electro-transformation immediately.

3.1.3 Transformation of competent cells

3.1.3.1 Heat-shock transformation

100 µL of chemically competent E. coli DH5α cells were thawed on ice. Appropriate amounts of plasmid DNA (1 pg - 50 ng) were added and incubated on ice for 30 min. Cells were subjected to a heat shock at 42 °C for 45 s and subsequently incubated on ice for 5 min. 750 µL of LB medium was added and cells were grown for 1 h at 37 °C and shaken at 350 rpm. The cells were pelleted by centrifugation for 3 min at 800 g. The medium was discarded and the pellet was resuspended in 50 µL LB medium. Varying volumes of the cell suspension were plated on LB agar plates containing an appropriate antibiotic and grown for 16 h at 37 °C.

3.1.3.2 Electro-transformation

50 µL of electro-competent cells were mixed with plasmid DNA destined for transformation. The cells were transferred to an electroporation cuvette (Gene Pulser Cuvette, 0.1 cm electrode gap). The cells were pulsed with a single pulse at 1.8 kV (MicroPulser Electroporator, BioRad) before adding 600 µL of ice-cold LB medium. The cells were left to recover on ice for 5 min before they were grown for 1 h at 37 °C and shaken at 350 rpm. The cells were centrifuged at 800 g for 3 min. 550 µL of supernatant were removed and the cell pellet was resuspended in the remaining 50 µL of LB medium. The cells solution was plated on LB-agar plates containing an appropriate antibiotic.

3.1.4 Red recombination

A pre-culture of the appropriate *E. coli* strain (GBred *gyr A462*; GB05 red) was grown overnight at 37 °C for 16 h and shaken at 200 rpm. 1.4 mL of fresh LB medium containing 100 µg/mL streptomycin was inoculated with 30 µL of cell culture and grown in a thermomixer (ThermoMixer comfort, Eppendorf) at 37 °C for 2 h at 850 rpm. The cells were induced with 0.35 % (w/v) L-arabinose for 50 min before following the steps for making them electro-competent (as described in Section 3.1.2.2). 500 ng of vector DNA and 500 ng of ccdB-amp cassette DNA with appropriate homologous regions for insertion into the region of interest within the vector DNA were added into the electro-competent cell suspension. The cells were then transformed by electroporation (as described in Section 3.1.3.2).

3.2 Mammalian cell techniques

3.2.1 Maintenance and cell line passage

Mammalian cell culture techniques were performed under sterile conditions within class II biological safety cabinets (Herasafe KS 12, Thermo Scientific). Cells were grown in adherent monolayers on polystyrene tissue culture dishes (Sarsted; Thermo Scientific) in dulbecco's modified eagle medium (DMEM) (Gibco DMEM, high glucose, pyruvate, Thermo Scientific) supplemented with 10 % (v/v) fetal calf serum (FCS) (FCS Superior, Merck) and 1 % (v/v) penicillin/streptomycin solution (final 1000 U/mL penicillin and 1 mg/mL streptomycin, Pan-Biotech). All cells were grown at 37 °C in CO_2 incubators (Heraeus BBD 6220, Thermo Scientific) at 5 % (v/v) CO_2.

The cells were passaged at at 80-90 % confluency. First, the growth medium was removed and the cell monolayer was washed once with phosphate buffered saline (PBS) (Table 15). Next, the cells were covered with trypsin/EDTA solution (0.05 %, 0.02 % (v/v) in PBS, Pan-Biotech) and incubated for 15 min at 37 °C until all cells were detached. The trypsin solution was inactivated by addition of 1:1 (v/v) growth medium. The cell number was determined using a counting chamber (Neubauer Improved, Marienfeld). To distinguish between living and dead cells the cell suspension was mixed with trypan blue solution (0.15 % (w/v) trypan blue, 0.85 % (w/v) NaCl). The mixture was added onto the cell chamber and the cell number was counted in 4 squares under a light microscope (Leica DMIL). The total number of cells per

mL was given by the following formula:

$$cells/mL = \frac{counted\ cells}{number\ of\ counted\ squares} \times dilution\ factor \times 10^4 \qquad (1)$$

The inactivated cell suspension was transferred to a 50 mL reaction tube (Sarstedt) and centrifuged at 670 g (Heraeus Multifuge 3S-R, Thermo Scientific) for 3 min.

Table 15: Phosphate buffered saline composition

PBS (pH 7.0)	140 mM	NaCl
	3 mM	KCl
	5 mM	Na_2HPO_4
	1.5 mM	KH_2PO_4

3.2.2 Cryopreservation and re-cultivation

To store cells for later use, the cells were detached by trypsinisation (Section 3.2.1). After centrifugation, the cells were resuspended in FCS + 10 % DMSO (v/v). The cell suspension was stored in 1 mL aliquots in cryogenic tubes (1.8 mL CryoPure, Sarstedt). To achieve a cooling rate of 1 °C/min the tubes were stored in a freezing container (Mr. Frosty, Thermo Scientific) and kept at −80 °C.

Re-cultivation of a cell strain was achieved by thawing the cells in a water bath (GFL Gesellschaft für Labortechnik) at 37 °C. 1 mL of thawed cell suspension was diluted by addition of 20 mL pre-warmed culture medium. The cells were plated on a 15-cm culture dish and incubated at standard conditions (as described in Section 3.2.1) overnight. The following day the culture medium was replaced and cells were passaged as soon as they reached 90 % confluency.

3.2.3   Transfection

3.2.3.1   Transfection of viral genomes

A 6-cm cell culture dish was seeded with 1.8×10^6 H1299 cells. 20 μg of p15A plasmid DNA (prepared as described in Section 3.4.1) containing the viral genome were digested with the restriction enzyme SwaI for 5 h at 25 °C. The linearised viral genomic DNA was precipitated by addition of isopropanol. After wash and resuspension, the DNA was digested with PacI at 37 °C overnight. The following day, 8 μg of digested genomic DNA were mixed with DMEM to a final volume of 500 μL in a 1.5 mL reaction tube (Sarstedt). A second reaction tube was filled with 20 μL Lipofectamine 2000 Transfection Reagent (Thermo Scientific) and adjusted to a total volume of 500 mL with DMEM. The content of both tubes was mixed and incubated for 20 min at room temperature. Meanwhile, the H1299 cells were washed with DMEM once, before adding 600 μL DMEM. The Lipofectamine 2000/DNA mixture was added drop-wise onto the cells. The cells were then incubated for 6 h at 37 °C and 5 % CO_2. Within the incubation period the cell medium was mixed by swirling it hourly. After 6 h the medium was preplaced by full culture medium.

3.2.3.2   Transfection of plasmid DNA

A 6-cm cell culture dish was seeded with 2.5×10^6 H1299 cells. A polyethylenimine (PEI) stock solution was prepared in H_2O (1 mg/mL, pH 7.2 adjusted with HCl) and filter sterilised (0.45 nm pore size, Millex-GP). 1 μg of plasmid DNA (prepared as described in Section 3.4.1) was added to 500 μL DMEM in a 1.5 mL reaction tube. The PEI stock solution was added to the tube to a final DNA:PEI ratio of 1:10 (w/w). The solution was vortexed once and centrifuged down briefly. After 15 min incubation at room temperature the DNA-PEI mix was added onto the H1299 cells, which were washed with DMEM once. The cells were incubated for 5 h at 37 °C and 5 % CO_2. After the incubation period, the cell medium was replaced by full culture medium.

3.2.4   Generation of stable expression cell lines

3.2.4.1   Generation of recombinant lentivirus particles

A 10-cm cell culture dish was seeded with 5×10^6 human embryonic kidney (HEK) 293T cells. The cells were co-transfected with plasmids encoding for the gene of interest as well as the envelope and packaging proteins (pCMV-VSV-G; pGagPol; pRev). All plasmid DNA together with $CaCl_2$ was prepared in water (see Table 16). The transfection solution is mixed dropwise to final ratio 1:1 (v/v) with 2x precipitation buffer (see Table 17) under constant aeration and incubated for 15 min at room temperature. The cell culture medium was removed and replaced by DMEM mixed with 25 µM (w/v) chloroquine. DNA solution was added to the medium and swirled gently. After 8-12 h the medium was replaced by fresh DMEM supplemented with 10 % (v/v) FCS, 1 % (v/v) penicillin/streptomycin and 20 mM (w/v) 4-(2-hydroxyethyl)-1-piperazineethanesulfonic acid (HEPES). The medium containing lentivirus particles was collected 24 hpi and 48 hpi and passed through a sterile filter (0.22 nm, Millex-GP). The filtered medium was either stored at 4 °C for prompt use or at −80 °C for later use.

Table 16: Transfection solution composition

Transfection solution	20 ng/µL	pGagPol
	1 ng/µL	pRev
	0.4 ng/µL	pCMV-VSV-G
	20 ng/µL	plasmid of interest
	25 mM	$CaCl_2$

Table 17: Precipitation buffer composition

2x Precipitation buffer	12 mM	dextrose
	50 mML	HEPES
	10 mM	KCl
	280 mM	NaCl
	1.5 mM	NA_2HPO_4

3.2.4.2 Transduction of mammalian cell lines with lentivirus vectors

A 6-well cell culture dish was seeded with 2×10^5 A549 cells per well. Per condition, cells were covered by 1:1 (v/v) DMEM supplemented with 10 % (v/v) FCS, 1 % (v/v) penicillin/streptomycin and 8 µg/mL polybrene and lentivirus stock solution. The cells were prompted for infection by centrifugation at 670 g (Heraeus Multifuge 3S-R, Thermo Scientific) for 1 h. Afterwards, cells were incubated for 5 h at 37 °C and 5 % (v/v) CO2 after which DMEM supplemented with 10 % (v/v) FCS and 1 % (v/v) penicillin/streptomycin at a ratio of 1:1 (v/v). The next day, the cells were transduced a second time according to the procedure described above. Selection of cells was either achieved by subsequent addition of hygromycin (500 µg/mL) or selection of fluorescence markers by fluorescence-activated cell sorting (FACS).

3.3 Adenovirus techniques

3.3.1 Infection of mammalian cells

HAdV5 infection of mammalian cells was performed at a multiplicity of infection (MOI) of 1 ffu/cell. The correct virus stock amount was calculated according to the formula:

$$virus\ stock\ solution\ (\mu L) = number\ of\ cells \times \frac{MOI\ (ffu/cell)}{virus\ stock\ titre\ (ffu/\mu L)} \tag{2}$$

After addition of the virus stock solution, cells were incubated in DMEM without FCS or antibiotics for 1 h at 37 °C and 5 % (v/v) CO2. Subsequently, DMEM supplemented with 10 % (v/v) FCS and 1 % (v/v) penicillin/streptomycin was added to a final ratio of 1:1 (v/v) leading to a final supplement concentration of 5 % (v/v) FCS and 0.5 % (v/v) penicillin/streptomycin.

3.3.2 Virus progeny production

New recombinant virus particles were produced in H1299 cells. A 10-cm culture dish of 90 % confluent cells was transfected as described in Section 3.2.3.1 Alternatively, an existing virus stock solution was used to infect H1299 cells. Upon visible cytopathic effects, the cells were harvested by detaching them with a cell scraper (Sarstedt). The medium containing detached

cells was collected in 15-mL or 50-mL reaction tubes (Sarstedt). For non-lytic recombinant virus strains, the cells were centrifuged (Heraeus Multifuge 3S-R, Thermo Scientific) at 670 g for 2 min and the cell pellet was resuspended in DMEM without FCS or penicillin/streptomycin to concentrate the final virus stock solution. Virus particles were released from harvested cells by three freeze-thaw cycles. The resulting cell debris was removed by centrifugation (Heraeus Multifuge 3S-R, Thermo Scientific) at 3,400 g for 15 min. The supernatant was used to infect a 15-cm cell culture dish of 90 % confluent A549 cells for another round of infection. After 5 passages the supernatant was stored as virus stock solution in 200-500 µL aliquots in cryogenic tubes (1.8 mL CryoPure, Sarstedt) at −80 °C. The virus particle titre in the virus stock solution was determined via flow cytometry (as described in Section 3.3.3).

3.3.3 Titration of infectious particles

A 12-well cell culture dish was seeded with 2×10^5 A549 cells. The cells were infected in triplicate with 20 µL of a serial dilution of virus stock solution at a range between 10^{-2} and 10^{-6}. After 24 h, the cells were washed once with PBS and detached by addition of trypsin/EDTA solution (0.05 %, 0.02 % v/v in PBS, Pan-Biotech) and incubated for 15 min at 37 °C. The detached cells were transferred to a 96-well plate (Greiner Cellstar, clear well V-bottom) and pelleted by centrifugation (Heraeus Multifuge 3S-R, Thermo Scientific) at 3,400 g for 15 min. The supernatant was removed and the cells were fixed and permeabilised in 100 % (v/v) methanol. The cells were washed and blocked with fluorescence-activated cell sorting (FACS) buffer (1 % (v/v) FCS in PBS) twice and centrifuged at 3,400 g for 15 min after each wash step to discard the supernatant. Infected cells were incubated in 1:10 (v/v) primary mouse B6-8 anti-DBP antibody (REICH *et al.*, 1983) in FACS buffer for 1 h. Afterwards the cells were washed with FACS buffer twice. The cells were incubated in 1:1000 (v/v) secondary anti-mouse Alexa Fluor 488 antibody (Invitrogen) in FACS buffer for 45 min. The cells were washed once, resuspended in FACS buffer and transferred to 5-mL round bottom tubes (Falcon, cell strainer cap). The percentage of live, individual fluorescent cells in the population was determined by flow cytometry on a LSRFortessa cell analyzer (BD Biosciences). The titre of the virus stock solution was calculated according to the formula:

$$virus\ titre\ (ffu/\mu L) = \frac{\frac{no.\ fluorescent\ cells}{no.\ total\ cells}(ffu) \times dilution\ factor}{volume\ of\ virus\ stock\ used\ for\ infection\ (\mu L)} \tag{3}$$

3.3.4 Virus release growth curves

A 12-well cell culture dish was seeded with 1.5×10^5 A549 cells. The cells were infected in triplicate with HAdV5 strains of interest at an MOI of 1 ffu/cell. The supernatant medium was carefully collected at 0, 24, 48, 72 and 96 hpi and stored at $-80\,°C$. The virus titre in the supernatant from all time points was determined (as described in Section 3.3.3).

3.3.5 Purification of virus particles

Virus particles were purified from virus stock solution (stock made as described in Section 3.3.2). A single $CsCl_2$ gradient (1.25 g/cm^3/4.4 g/cm^3) was established by filling a 13.5-mL ultracentifugation tube (open top, polypropylene, Beckman Coulter) with 4.4 mL of 2.15 M $CsCl_2$. The first $CsCl_2$ layer was under-filled with 3.6 mL of 3.68 M $CsCl_2$. The virus stock solution was pipetted onto the $CsCl_2$ gradient and separated by densities by ultracentrifugation at 104,000 g for 3 h at $18\,°C$ (Optima L-90K Ultracentrifuge, Beckman Coulter). The band corresponding to purified virus particles was extracted from the ultracentrifugation tube by puncturing the tube from the side and removing the solution with a 5 mL syringe (Sarstedt). The virus particles were split in 50 μL aliquots and stored at $-80\,°C$.

3.4 Nucleic acid techniques

3.4.1 Plasmid isolation

Liquid *E. coli* cell cultures were grown overnight (as described in Section 3.1.1). For small scale analytic purposes, 1 mL of cell culture were pelleted in a 1.5-mL reaction tube (Eppendorf) by centrifugation at 12,000 g for 30 sec at $4\,°C$ (centrifuge 5417R, Eppendorf). Alkaline lysis was performed using commercially available buffers P1, P2 and P3 (Qiagen). The pellet was resuspended in 350 μL P1, cells were lysed by addition of 300 μL P2 and the reaction was neutralised by addition of 300 μL P3. Cell debris was removed by centrifugation at 12,000 g for 15 min at $4\,°C$. The 750 μL of the supernatant was transferred to a new 1.5-mL reaction tube and mixed with 600 μL 100 % (v/v) isopropanol. NaOAc was added to a final concentration of 15 mM. The precipitated DNA was pelleted by centrifugation at 12,000 g for 15 min at room temperature. The DNA pellet was washed once with 75 % (v/v) ethanol (EtOH) and centrifuged at 20,000 g for 10 min at room temperature. Subsequently, the supernatant was

removed by aspiration and the DNA pellet was dried at 37 °C for 5 min. The DNA pellet was rehydrated in H$_2$O and the DNA concentration was determined (as described in Section 3.4.2).

For large scale plasmid DNA isolation 250 mL of cell culture were pelleted by centrifugation at 4,000 g for 15 min at 4 °C (Aventi J-E, Beckman Coulter). The supernatant was discarded and plasmid DNA was extracted from the cell pellet according to the manufacturer's instructions using a QIAPrep Spin Maxiprep kit (Qiagen). The DNA was rehydrated overnight in 200 µL 10 mM TRIS/HCL (pH 8.0) and the DNA concentration was determined (as described in Section 3.4.2).

3.4.2 Quantification of DNA concentration

DNA concentration and quality were assessed using a microvolume spectrophotometer (NanoDrop 1000, Thermo Scientific). The optical density (OD) at 280 nm was measured and used to determine the nucleic acid concentration. Quality control was performed by comparison between the OD at 260 nm and 280 nm, which should have a ratio of 1.8 for DNA.

3.4.3 Agarose gel electrophoresis

Agarose gels were prepared by dissolving 0.8 – 2 % (w/v) agarose (Seakem LE agarose, Biozym) in TBE buffer (see Table 18) and heating it to boiling temperature. The dissolved agarose solution was left to cool, mixed with 0.3 µg/mL ethidium bromide and poured into appropriate gel chambers (PerfectBlue gel system, Peqlab). The gel was covered by TBE buffer and DNA samples were mixed with 6x loading buffer (see Tables 19 & 20) to a 1x final loading buffer concentration. PCR product or molecular cloning products were separated at 80 V (constant voltage). For restriction pattern analysis of HAdV5 bacmid DNA, the gel was run at 15 V (constant voltage). For reference of DNA fragment length either 1 kbp DNA ladder or 100 bp DNA ladder (New England Biolabs) was co-loaded with DNA samples of interest. DNA bands were visualised by UV light irradiation (302 nm) on a UV table (GelVue GVM20, Syngene) or UV transilluminator (G:Box System, Syngene). Images were recorded using GeneTools Syngene software. For isolation of DNA bands of interest from agarose gels, the desired bands were first excised from the gel using a scalpel. The weight of the gel pieces was determined. DNA was extracted from gel pieces according to the manufacturer's instructions using a QIAquick Gel extraction kit (Qiagen).

Table 18: Tris-borate-EDTA buffer composition

1x TBE buffer (pH 7.8)	90 mM	Tris/HCl
	90 mM	$B(OH)_3$
	2mM	EDTA

Table 19: DNA-loading buffer composition

6x loading buffer	0.25 % (v/v)	bromophenol blue
	0.25 % (v/v)	xylene cyanol
	50 % (v/v)	glycerol
	2 % (v/v)	50x TAE buffer

Table 20: Tris-acetate-EDTA buffer composition

50x TAE buffer (pH 8.3)	2 M	Tris/HCl
	1 M	$B(OH)_3$
	50 mM	EDTA

3.4.4 Polymerase chain reaction

Polymerase chain reaction (PCR) was performed to amplify DNA fragments of interest from template DNA in vitro (SAIKI *et al.*, 1988). The incorporation of additional nucleotides in the amplification primer sequence allowed for introduction of single nucleic acid changes as well as addition of linker or restriction enzyme sites. Reaction were run in 50 µL total volume per PCR reaction tube (Biozym) including 15 ng template DNA, 1 unit Q5 High-Fidelity DNA polymerase (New England Biolabs), 1x Q5 reaction buffer (New England Biolabs), 200 µM dNTPs, 0.5 µM forward primer, 0.5 µM reverse primer and 3 % (v/v) DMSO. The amplification reaction was performed in a thermal cycler (FlexCycler, Analytik Jena). After initial denaturation at 98 °C for 30 sec, 40 cycles of denaturation, annealing and elongation were performed. The double stranded DNA was denatured for 30 s at 95 °C, annealing was performed for 30 sec at 56 °C and extension was performed at 72 °C for 1 min for each kbp

fragment length. After 40 cycles, a final extension was performed for 5 min at 72 °C and the reaction stopped by lowering the temperature to 4 °C. To test for positive PCR results, 1 µL of reaction volume was separated on a 1.2 % (w/v) agarose gel (as described in Section 3.4.3).

3.4.5 Colony polymerase chain reaction

Individual *E. coli* colonies resulting from transformation of Red recombination DNA (as described in Section 3.1.4) were probed for successful recombination product by colony PCR prior to plasmid DNA isolation. The PCR reaction was performed using DreamTaq PCR Master Mix (Thermo Scientific). Reactions were run in 30 µL total volume per PCR reaction tube (Biozym) including 1x DreamTaq PCR Master Mix, 0.33 µM forward primer, 0.33 µM reverse primer and *E. coli* cells (a pipette tip used to pick the colony was briefly submerged in the reaction volume to add appropriate amounts of cells). After initial denaturation and lysis of *E. coli* cells at 95 °C for 3 min, 40 cycles of denaturation, annealing and elongation were performed. The double stranded DNA was denatured by incubation for 10 s at 98 °C. The annealing temperature varied between 55 °C and 70 °C depending on the primer melting temperature. Primers were left to anneal for 45 s. Extension was performed at 72 °C for 1 min for each kbp fragment length. After 40 cycles, a final extension was performed for 10 min at 72 °C and the reaction stopped by lowering the temperature to 4 °C. PCR quality control was achieved by separating the product on a 2 % (w/v) agarose gel (as described in Section 3.4.3).

3.4.6 Restriction enzyme digestion

Target DNA was fragmented along palindromic nucleotide sequences using restriction endonucleases (New England Biolabs). The reaction times and temperatures were chosen as recommended in the enzyme-specific protocols by New England Biolabs. 0.5 - 10 µg of target DNA was incubated with 5 - 30 units of enzyme in appropriate NEBuffer (New England Biolabs) in a thermomixer (ThermoMixer comfort, Eppendorf). In case of digestion with multiple enzymes requiring the same reaction buffer, the reaction was performed simultaneously. In case enzymes required different reaction buffers, digestions were run sequentially, with isopropanol precipitation of DNA after the first digestion and resuspension of DNA in the second buffer for the second restriction digestion. To validate the success of the enzymatic digestion and/or to purify DNA fragments, the reaction volume was separated

by gel electrophoresis (as described in Section 3.4.3).

3.4.7 Ligation of DNA fragments

Purified DNA digestion fragments with matching restriction overhangs were ligated using the Rapid DNA Dephos & Ligation Kit (Roche). 50 ng destination vector was mixed with ligation insert at a molar ratio of 1:3. 5 units of T4 DNA ligase were added and the ligation reaction was performed in 1x rapid ligation buffer in a total reaction volume of 20 µL. All ligation reactions were at 30 min at room temperature. 2 – 5 µL of reaction volume were used to transform chemically competent *E. coli* DH5α cells (as described in Section 3.1.3.1).

3.4.8 Gateway cloning

Gateway cloning was performed to insert genetic material into vectors of interest based on site-specific recombination (HARTLEY *et al.*, 2000). As first step of the Gateway cloning process the BP reaction was performed. The gene of interest was amplified by PCR (as described in Section 3.4.4). The PCR primers contained *att*B sites to flank the gene of interest. The gene was inserted into a donor vector by homologous recombination between the *att*B sites of the PCR product and the *att*P sites of the donor vector. 10-75 ng PCR plasmid was mixed with 75 ng of donor vector and incubated in TE buffer (see Table 21). The reaction was catalysed by the BP Clonase II enzyme mix (Thermo Scientific) for 1 h at 25 °C. The reaction was terminated by addition of 1 µg proteinase K (Thermo Scientific) and incubation for 10 min at 37 °C. 1 µL of the final reaction volume was used to transform *E. coli* DH5α chemically competent cells (as described in Section 3.1.3.1). As second step of the Gateway cloning process the LR reaction was performed. The gene of interest was inserted into the destination vector by homologous recombination between the *att*L sites of the entry vector and the *att*R sites of the destination vector. 25-75 ng of entry vector was mixed with 75 ng of destination vector and incubated in TE buffer. The reaction was catalysed by the LR Clonase II enzyme mix (Thermo Scientific) for 1 h at 25 °C. The reaction was terminated by addition of 1 µg proteinase K (Thermo Scientific) and incubation for 10 min at 37 °C. 1 µL of the final reaction volume was used to transform *E. coli* DH5α chemically competent cells (as described in Section 3.1.3.1).

Table 21: Tris-EDTA buffer composition

TE buffer (pH 8.0)	2 M	Tris/HCl
	1 M	EDTA-Na$_2$

3.4.9 Sanger sequencing

Sequence quality control of purified plasmid DNA or PCR product was performed by Sanger sequencing (SANGER *et al.*, 1977). 500 – 1200 ng plasmid DNA or 400 ng PCR product were mixed with 30 pmol of appropriate sequencing primer in a total volume of 15 μL. The sequencing reaction was performed by Microsynth Seqlab (Göttingen). The obtained sequence data was analysed using CLC Main Workbench (Qiagen) or SnapGene Viewer software (SnapGene).

3.5 Protein techniques

3.5.1 Preparation of whole-cell lysate

Cells were harvested by detaching them from the cell culture dish using a cell scraper (Sarstedt) or trypsinisation (as described in Section 3.2.1). The cells were pelleted by centrifugation at 670 g (Heraeus Multifuge 3S-R, Thermo Scientific) for 3 min, the supernatant was discarded, the cells were washed with PBS once and centrifuged again. The supernatant was discarded and the pellet was either stored at $-20\,°C$ or directly used for lysis. The cell pellet was resuspended in a suitable volume of ice-cold radio immunoprecipitation assay buffer (RIPA) buffer (see Table 22) supplemented with 0.2 mM phenylmethylsulfonyl fluoride (PMSF) (Sigma), 5 mg/mL aprotinin (Sigma), 1 mg/mg pepstatin (Sigma) and 10 mg/mL leupeptin (Sigma) protease inhibitors and incubated for 30 min with intermittent vortexing steps every 10 min. Afterwards the cells were lysed by sonication (Branson Sonifier 450, Branson) for 37.5 s at 0.8 pulses/s at $4\,°C$. The protein concentration in the whole-cell lysate was determined and normalised (as described in Section 3.5.2). The lysate was either prepared for immunoprecipitation (IP) (as described in Section 3.5.3) or directly prepared for SDS-PAGE separation (as described in Section 3.5.5). In this case, the cell lysate was mixed with SDS loading buffer (see Table 23) to a final concentration of 1x and boiled in a thermomixer (ThermoMixer comfort, Eppendorf) for 2 min at $95\,°C$. The denatured protein lysate was stored at $-20\,°C$.

Table 22: RIPA buffer composition

RIPA buffer		
	50 mM	Tris/HCl (pH 8.0)
	150 mM	NaCl
	5 mM	EDTA
	1 % (v/v)	nonidet P-40
	0.1 % (w/v)	SDS
	0.5 % (v/v)	sodium desoxycholate

Table 23: 5x SDS loading buffer composition

5x SDS loading buffer		
	100 mM	Tris/HCl (pH 6.8)
	200 mM	dithiotreithol (DTT)
	10 % (w/v)	SDS
	0.2 % (w/v)	bromophenol blue
	200 mM	β-mercaptoethanol

3.5.2 Determination of protein concentration in whole-cell lysate

The protein concentration of whole-cell lysate preparations was determined via the Bradford protein assay (BRADFORD, 1976). Per condition, 800 µL of diluted protein solution were mixed with 200 µL of Bradford reagent (Protein assay dye reagent concentrate, BioRad) in a semi-micro cuvette (Sarstedt). The solution was incubated for 5 min at room temperature and the absorbance at 595 nm was measured using a spectrophotometer (SmartSpec Plus, BioRad). First, a protein standard curve was established using BSA (New England Biolabs) protein concentrations ranging from 1 µg/mL to 16 µg/mL and absorbance values were measured. Finally, 1 µL of protein lysate (prepared as described in Section 3.5.1) was diluted in 799 µL $H_2O_d d$ and mixed with 200 µL Bradford reagent. After absorbance measurements, the protein concentration per sample was interpolated from the absorbance values of the standard curve.

3.5.3   Immunoprecipitation of proteins of interest

Proteins of interest were enriched from whole-cell lysate in RIPA buffer (as described in Section 3.5.1) by immunoprecipitation. The samples were pre-cleared by incubation with 50 µL pansorbin cells (Calbiochem) for 1.5 h at 10 rpm at 4 °C in an overhead shaker (GFL, Gesellschaft für Labortechnik) to reduce non-specific protein binding. Pansorbin solution contains heat-killed, fixed Staphylococcus aureus cells displaying protein A on their surface. Protein A has a high affinity for the fragment crystallisable (Fc) region of immunoglobulin G. Prior to incubation in whole-cell lysate, the pansorbin suspension was washed three times with RIPA buffer. The RIPA buffer was removed each time by centrifugation at 3,800 g for 3 min at 4 °C (centrifuge 5417R, Eppendorf). In parallel, per condition, 3 mg lyophilised protein A-sepharose beads (Sigma Aldrich) were re-hydrated in RIPA buffer for 30 min at 10 rpm at 4 °C. Afterwards they were washed three times with RIPA buffer with intermittent centrifugation at 600 g for 3 min at 4 °C. Appropriate amounts (Section 2.5.1) of antibody were bound to the protein A-sepharose beads by incubation for 2 h at 10 rpm at 4 °C. All non-bound antibody was removed by three wash steps with RIPA buffer and the beads were resuspended in 100 µl RIPA buffer. Subsequently, the pansorbin cells were sedimented by centrifugation at 3,800 g for 3 min at 4 °C and the supernatant was transferred to the protein A-sepharose beads. Antibody binding to proteins of interest in the protein supernatant was performed for 2 h at 10 rpm at 4 °C. Subsequently, the beads were sedimented by centrifugation at 600 g for 3 min at 4 °C and the supernatant was discarded. Non-specific proteins still bound to the beads were removed by 3 wash steps in RIPA buffer with intermittent centrifugation at 600 g for 3 min at 4 °C. Finally, the beads were resuspended in 10 µL 2x SDS loading buffer (see Table 24) and boiled for 5 min at 95 °C in a thermomixer (ThermoMixer® comfort, Eppendorf) to elute all specifically bound protein. The denatured protein-bead solution was stored at −20 °C for later use.

Table 24: 2x SDS loading buffer composition

2x SDS loading buffer	40 mM	Tris/HCl (pH 6.8)
	80 mM	DTT
	4 % (w/v)	SDS
	0.08 % (w/v)	bromophenol blue
	80 mM	β-mercaptoethanol

3.5.4   Preparation of purified virus lysate

Virus particles were purified (as described in Section 3.3.5). Purified virus particles in $CsCl_2$ were fixed by addition of PFA to a final concentration of 4 % (v/v) and incubated for 20 min at room temperature. The protein concentration was determined using a microvolume spectrophotometer (NanoDrop 1000, Thermo Scientific) measuring the absorbance at 280 nm. Appropriate amounts of virus solution were mixed with 5x SDS loading buffer (see Table 23) to a final buffer concentration of 1x and heated in a thermomixer (ThermoMixer comfort, Eppendorf) at 95 °C for 3 min. The denatured virus lysate was stored at −20 °C.

3.5.5   Protein separation by sodium dodecyl sulphate polyacrylamide gel electrophoresis

Denatured proteins were separated according to their molecular weight by SDS PAGE (LAEMMLI, 1970). Negatively charged SDS molecules in the running buffer surround denatured proteins, giving them a comparable charge-to-mass ratio. The proteins were run on discontinuous gels comprised of a stacking gel (see Table 25) to condense proteins in a sharp band and a resolving gel to separate proteins based on their molecular weight. Depending on the size of the proteins of interest varying acrylamide concentrations were used (see Tables 26 & 27). Electrophoresis was performed at 20 mA (constant current) in TGS buffer (see Table 28) in vertical electrophoresis system (Multigel SDS-PAGE system, Biometra).

Table 25: Stacking gel composition

5 % stacking gel	17 % (v/v)	30 % acrylamide/bisacrylamide stock solution (Rotiphorese gel 30, Roth)
	120 mM	Tris/HCl (pH 6.8)
	0.1 % (w/v)	SDS
	0.1 % (w/v)	APS
	0.1 % (v/v)	TEMED
	0.01 % (w/v)	bromophenol blue

Table 26: SDS-PAGE 10 % resolving gel composition

10 % resolving gel	34 % (v/v)	30 % acrylamide/bisacrylamide stock solution (Rotiphorese gel 30, Roth)
	250 mM	Tris/HCl (pH 8.8)
	0.1 % (w/v)	SDS
	0.1 % (w/v)	APS
	0.04 % (v/v)	TEMED

Table 27: SDS-PAGE 15 % resolving gel composition

10 % resolving gel	50 % (v/v)	30 % acrylamide/bisacrylamide stock solution (Rotiphorese gel 30, Roth)
	250 mM	Tris/HCl (pH 8.8)
	0.1 % (w/v)	SDS
	0.1 % (w/v)	APS
	0.04 % (v/v)	TEMED

Table 28: Tris-glycine-SDS buffer composition

TGS buffer	25 mM	Tris
	200 mM	glycine
	0.1 % (w/v)	SDS

3.5.6 Coomassie stain detection

To detect all proteins separated on a polyacrylamide gel, it was stained using Coomassie Blue stain (see Table 29). The gel was submerged in stain and heated for 30 s in a microwave at maximum power. All non-protein-bound stain was removed by submerging the gel in destaining solution (see Table 30) and heating it for 30 s in a microwave at full power. Afterwards the gel was incubated in the heated destaining solution for 30 min. Finally, the gel was fully destained in H_2O overnight.

Table 29: Coomassie blue stain composition

Coomassie blue stain		
	40 % (v/v)	isopropanol
	10 % (v/v)	glacial acetic acid
	0.1 % (w/v)	Coomassie brilliant blue

Table 30: Coomassie destaining solution composition

Coomassie destaining solution		
	25 % (v/v)	isopropanol
	10 % (v/v)	glacial acetic acid

3.5.7 Western blot detection

To detected specific proteins of interest on a polyacrylamide gel, a western blot was performed. All separated proteins were transferred from the polyacrylamide gel to a nitrocellulose membranes (Amersham Protran 0.45 µm, GE healthcare) or PVDF membranes (Immobilon 0.2 µm, Merck) for immobilisation and subsequent immunodetection. Proteins were transferred by wet blotting in a blotting cassette (Trans-Blot electrophoretic transfer cell, Biorad) in Towbin buffer (see Table 31) at 400 mA (constant current) for 75 min. To prevent non-specific antibody-binding to the membrane, it was blocked in 5 % (v/w) non-fat milk (Frema) in PBS overnight on an orbital shaker (3011 Analogue Orbital Rocking Motion Shaker, GFL) at 4 °C. Subsequently, the membrane was washed three times with PBS-T (0.1 % (v/v) polysorbate (Tween) 20 in PBS) for 5 min on an orbital shaker. Primary antibodies were diluted in PBS-T to appropriate concentrations (see Section 2.5.1) and proteins of interest were bound to their respective antibody by incubation for 2 h on an orbital shaker at 4 °C. After primary antibody incubation, the membrane was washed three times with PBS-T for 5 min. Secondary /glsHRP-coupled antibodies (see Section 2.5.2) were diluted in PBS-T at a ratio of 1:10,000 (v/v) and supplemented with 3 % (w/v) non-fat milk. The membrane was incubated in secondary antibody suspension for 45 min on an orbital shaker at 4 °C. After three wash steps in PBS-T for 5 min the membrane was incubated in chemiluminescent substrate (SuperSignal West Pico PLUS, Thermo Scientific) mixed with H_2O_2 at a ratio of 1:1 (v/v) for 2 min at room temperature. HRP is catalysing the chemiluminescence reaction

based on luminol in the substrate. Chemiluminescence was detected on medical X-ray film (RP new, CEA) in a dark room by varying exposure (2 sec – 16 h) of the X-ray film to the membrane and subsequent development (GBX developer and replenisher, Kodak). Protein signal on X-ray film was digitalised using a scanner (Epson Perfection 4490 Photo, Epson) and visualised on Illustrator CS6 (Adobe) software.

Table 31: Towbin transfer buffer composition

Towbin buffer		
	25 mM	Tris/HCl (pH 8.3)
	100 mM	glycine
	0.5 % (w/v)	SDS
	20 % (v/v)	methanol

3.6 Imaging techniques

3.6.1 Live-cell fluorescence microscopy

Cell culture dishes (μ-Dish 35 mm, glass bottom, ibidi) were coated with 1 % (v/v) fibronectin (Sigma Aldrich) for 40 min. Cells were seeded at varying densities (0.5×10^5 - 2×10^5), infected with HAdV5 strains of interest (as described in Section 3.3.1) and imaged at appropriate time points (16 – 72 hpi). Images were recorded using two microscope systems. For fast imaging of a large region of interest (ROI) at low sample irradiation an inverted confocal spinning-disk microscope (Nikon Eclipse Ti-2 stand, Yokogawa CSU-W1 spinning disk, 2x Andor888 EM-CCD camera, Nikon 100x oil-immersion numerical aperture (NA) 1.49 objective) equipped with a heating chamber at 37 °C and 5 % (v/v) CO_2 was used. For higher resolution images of smaller ROIs an inverted confocal scanning laser microscope (Nikon A1R HD25, Nikon 60x oil-immersion NA 1.40 objective) equipped with a heating chamber at 37 °C and 5 % (v/v) CO_2 was used. Images on both microscopes were recorded using Nikon NIS-Elements software. Further image processing was performed in Fiji (SCHINDELIN *et al.*, 2012), Imaris (Bitplane) or NIS-Elements (Nikon). Colocalisation quantification of fluorescence signal was performed using the Fiji JaCoP colocalisation plugin (BOLTE and CORDELIERES, 2006). Statistical significance was calculated using the unpaired Student's t-test. Manual image segmentation was done in NIS Elements Advanced Research

(Nikon) using a touchscreen tablet (Cintiq 16, Wacom).

For live-cell imaging of cells destined for plunge freezing (as described in Section 10.6.8), an inverted widefield microscope (Leica DMi8; 20x air NA 0.4 objective, Lumencore Sola SE FISH 365 LED-lightsource, filter cubes including 480/50 nm excitation and 527/30 nm emission for green fluorescent protein (GFP) and 560/40 nm excitation and 630/75 nm emission for mCherry) equipped with a heating chamber at 37 °C and 5 % (v/v) CO_2 was used. Images on the Leica widefield microscope were recorded using Leica LASX software. Further image processing was performed in Fiji (SCHINDELIN *et al.*, 2012).

3.6.2   Immunofluorescence microscopy

Cell culture dishes (μ-Dish 35 mm, glass bottom, ibidi) were coated with 1 % (v/v) fibronectin (Sigma Aldrich) for 40 min. Cells were seeded at varying densities (0.5×10^5 - 2×10^5), infected with HAdV5 strains of interest (as described in Section 3.3.1) and prepared at appropriate time points (24 – 48 hpi) for analysis of the localisation of proteins of interest. First, the cells were washed in PBS and subsequently fixed. Fixation was achieved by incubation in 4 % (v/v) PFA in PBS for 20 min at room temperature or incubation in 100 % (v/v) methanol for 20 min at −20 °C. In case of PFA fixation, the cells were quenched with 25 mM NH_4Cl for 10 min, washed in PBS for 5 min and permeabilised with 0.5 % (v/v) Triton X-100 for 10 min. Since methanol fixation also permeabilises the cells these steps were not necessary. After two wash steps in PBS for 5 min, the cells were blocked with 1x TBS-BG buffer (see Table 32) for 10 min to reduce non-specific antibody binding and washed three times for 5 min with PBS again. Primary antibodies were prepared at appropriate concentrations (see Section 2.5.1) in PBS and the cells were incubated in primary antibody suspension on an orbital shaker (3011 Analogue Orbital Rocking Motion Shaker, GFL) for 1 h at room temperature. Secondary antibodies were prepared at appropriate concentrations (see Section 2.5.2) After three wash steps for 5 min in PBS the cells were incubated in secondary antibody suspension containing 0.05 % (v/v) Hoechst 33342 in the dark on an orbital shaker for 30 min at room temperature. Images were recorded on an inverted confocal scanning laser microscope (Nikon A1R HD25 equipped with a Nikon 60x oil-immersion NA 1.40 objective). Images on the Nikon laser scanning microscope were recorded using the Nikon NIS-Elements software. Further image processing was performed in Fiji (SCHINDELIN *et al.*, 2012). Colocalisation quantification of fluorescence signal was performed using the Fiji JaCoP colocalisation plugin (BOLTE and CORDELIERES, 2006).

Statistical significance was calculated using the unpaired Student's t-test. Manual image segmentation was done in NIS Elements Advanced Research (Nikon) using a touchscreen tablet (Cintiq 16, Wacom).

Table 32: IF TBS-BG buffer composition

TBS-BG buffer		
	100 mM	Tris/HCl (pH 7.6)
	685 mM	NaCl
	15 mM	KCl
	7.7 mM	$MgCl_2$
	0.25 % (v/v)	polysorbate (Tween) 20
	0.25 % (w/v)	NaN_3
	25 mg/mL	BSA fraction IV (Roche)
	333 mM	glycine

3.6.3 Fluorescence recovery after photobleaching

Cell culture dishes (μ-Dish 35 mm, glass bottom, ibidi) were coated with 1 % (v/v) fibronectin (Sigma Aldrich) for 40 min. 0.5×10^5 A549 cells were seeded and infected with HAdV5 pIX-mCherry and HAdV5 pV-mCherry (as described in Section 3.3.1) and selected for fluorescence recovery after photobleaching (FRAP) analysis at 48 hpi. FRAP imaging was performed on an inverted confocal scanning laser microscope (Nikon A1R HD25, Nikon 60x oil-immersion NA 1.40 objective) equipped with a heating chamber at 37 °C and 5 % (v/v) CO_2. Stimulated image acquisition was performed using the Nikon NIS-Elements software. Three different ROIs of 1 μm diameter were selected. The stimulation ROI (A) marked the area of laser stimulation containing protein signal, the reference ROI (R) marked a non-stimulated area containing protein signal and the background ROI (BG) marked a non-stimulated area not containing any protein signal. The experimental sequence consisted of acquisition for 10 s, a laser pulse at the stimulation ROI at 561 nm excitation and 120 sec of subsequent acquisition for 2 min. Relative fluorescence intensities (I) were calculated according to the following procedure: Background correction of stimulation and reference ROIs:

$$A_{corrected1}(t) = A(t) - B(t) \tag{4}$$

$$R_{corrected1}(t) = R(t) - B(t) \tag{5}$$

Reference correction of stimulation ROI:

$$A_{corrected2}(t) = \frac{A_{corrected1}(t)}{R_{corrected1}(t)} \tag{6}$$

Normalisation of stimulation ROI pre-bleach level:

$$A_{corrected3}(t) = \frac{A_{corrected2}(t)}{A_{corrected2}(pre\text{-}bleach)} \tag{7}$$

Mobile fractions were calculated by curve fitting the signal intensities after bleaching in Fiji. Assuming exponential recovery described by:

$$y = a \times (1 - e^{-b \times x}) + c \tag{8}$$

with a being a slowly recovering fraction c being a rapidly diffusion fraction b being the recovery rate The fraction of mobile protein is given by:

$$f_{mobile} = a + c \tag{9}$$

3.6.4   Classical transmission electron microscopy

3.6.4.1   TEM of purified virus particles

Virus particles were purified (as described in Section 3.3.5) and fixed by addition of paraformaldehyde (PFA) to a final concentration of 4 % (v/v) and incubation for 20 min at room temperature. Copper-coated grids (200 mesh, Plano) were glow-discharged (Q150R ES Plasma cleaner, Quorum Technologies) for 1 min. Virus particles were absorbed to the grids by covering the carbon grid surface with a drop of diluted (1:10 (v/v) in PBS) virus suspension for 5 min. Subsequently, the grid was washed 3 times by sequentially covering the carbon grid surface by a drop of H_2O. Excess liquid was removed by touching the side of the grid to filter paper (Grade 1 Qualitative Filter Paper, Whatman). Virus particles were negatively stained by covering the carbon grid surface with a drop of 2 % (w/v) uranyl

acetate for 3 s. Excess liquid was removed again by touching the side of the grid to filter paper after which the grids were air-dried for 5 min at room temperature. Particles were imaged with a transmission electron microscope (CM120, Philips) equipped with a LaB6 cathode operated at 80 kV and CDD camera (MultiScan 794, Gatan).

3.6.4.2   TEM of ultra-thin sections of resin-embedded cells

Cell culture dishes (µ-Dish 35 mm, high Grid-500, ibidi) were seeded with 0.5×10^5 A549 cells, infected with varying HAdV5 strains and prepared at 48 hpi for TEM imaging. For correlative analysis, the cells were imaged on an inverted confocal spinning-disk microscope (as described in Section 3.6.1) directly before TEM preparation. First, the cells were washed with PBS and fixed by incubation in 2.5 % (v/v) glutaraldehyde in PBS at 4 °C overnight. The cells were washed twice in PBS for 10 min and stained with 1 % (w/v) OsO_4 in PBS for 20 min. After two wash steps in PBS and one wash step in H_2O for 10 min each the cells were incubated in 1 % (w/v) uranyl acetate solution for 20 min. After two wash steps in H_2O for 10 min, the cells were sequentially dehydrated in 50 %, 70 %, 90 % and 100 % (v/v) EtOH solution for 10 min each. Final dehydration in 100 % (v/v) EtOH was repeated three times before cells were embedded in epoxy resin (see Table 35) (Luft, 1961) by incubation with 1:1 (v/v) EtOH/epoxy for 30 min on a rocking platform (MR-1, Biosan), followed by incubation in 3:7 (v/v) EtOH/epoxy overnight. Afterwards, cells were incubated in 100 % (v/v) epoxy resin for 6 h before polymerisation at 60 °C for 48 h. Polymerised cells of interest were removed from the cell culture dish by a 6 mm disk punch (hollow punches twinnable, Hoffmann) and mounted onto an epoxy resin stub using epoxy glue (UHU PLUS Endfest 300, UHU). Rough trimming was performed using a scalpel to generate a flat-top pyramid with 4 sides at approximately 30° angles. 170 µm of the ibidi polymer culture dish layer on the face of the flat-top pyramid was removed by serial sectioning on an ultramicrotome (Leica Ultracut EM UCT, Leica Microsystems, Austria). The area of the pyramid block-face was further reduced by removing the access material with a scalpel. The pyramid was transferred back to the ultramicrotome and ultra-thin (∼50nm) sections were cut. Carbon-coated copper grids (200 mesh, Plano) were washed in 100 % (v/v) EtOH and left to dry. The ultra-thin resin sections were collected on grids and post-contrasted with saturated uranyl acetate solution in 70 % (v/v) EtOH for 7 min, thoroughly washed in a running stream of H_2O, dried on filter paper (Grade 1 Qualitative Filter Paper, Whatman) and finally imaged on a transmission electron microscope (CM120, Philips) equipped with a LaB6 cathode operated

at 80 kV and CDD camera (MultiScan 794, Gatan).

Table 33: Epon I resin composition

Epon I	44 % (w/w)	glycid ether 100 (Epon 812)
	56 % (w/w)	(2-Dodecen-1-yl)succinic anhydride (DDSA)

Table 34: Epon II resin composition

Epon II	53.6 % (w/w)	glycid ether 100 (Epon 812)
	46.4 % (w/w)	1-Methyl-5-norbornene-2,3-dicarboxylic acid anhydride (MNA)

Table 35: Epoxy resin composition for embedding of cells

Epoxy resin	27.4 % (w/w)	Epon I (see Table 33)
	71.3 % (w/w)	Epon II (see Table 34)
	1.3 % (w/w)	2,4,6-Tris(dimethylaminomethyl)-phenol (DMP-30)

3.6.5   3view block-face scanning electron microscopy

3.6.5.1   OTO contrasting and PLT dehydration

A culture dish (μ-Dish 35 mm, high Grid-500, ibidi) was seeded with 1×10^5 A549 cells and infected with varying HAdV5 strains (as described in Section 3.3.1). The cells were fixed at varying time-points by addition of 2 % (v/v) PFA and 2.5 % (v/v) glutaraldehyde (GA) in PBS for 5 min at room temperature. The cells were further fixed by addition of 2 % (v/v) PFA and 2.5 % (v/v) GA in PBS for 55 min 4 °C and washed with PBS for 1 min at room temperature once. For correlation between light microscopy and electron microscopy, z-stacks of fixed cells were recorded by confocal fluorescence microscopy (as described in Section 3.6.1). Afterwards the cells were post-fixed in ice-cold 2 % (w/v) OsO_4 and 2.5 % (v/v) GA in PBS for 30 min at 4 °C. After 5 wash steps in ice-cold PBS, cells were stained based on the osmium-thiocarbohydrazide-osmium (OTO) contrasting method (SELIGMAN

et al., 1966). Each contrasting step was followed by 10 wash steps in H_2O for 1 min at room temperature. First, cells were contrasted with 2 % (w/v) OsO_4, 1.5 % (w/v) potassium ferrocyanide and 2 mM $CaCl_2$ in H_2O for 1 h at room temperature. Then cells were incubated in 0.5 % (w/v) thiocarbohydrazide for 10 min at room temperature. Afterwards cells were contrasted again in 2 % (w/v) OsO_4 for 20 min at room temperature. Further staining was achieved by incubation in 1 % (w/v) gallic acid for 10 min at room temperature, 2 % (w/v) uranyl acetate overnight at 4 °C and Walton's lead aspartate solution (see Table 36) (WALTON, 1979) for 10 min at 60 °C. The cells were dehydrated according to the progressive lowering of temperature (PLT) principle (CARLEMALM *et al.*, 1982). First, cells were incubated in 30 % (v/v) EtOH for 30 min at 0 °C. Then, the EtOH concentration was increased to 50 % (v/v) while lowering the temperature to −20 °C for 30 min. Afterwards the cells were incubated in 70 % (v/v) EtOH for 30 min at 20 °C. The temperature was further lowered to −35 °C and cells were incubated in 100 % (v/v) EtOH for 20 min. This step was repeated with fresh 100 % (v/v) EtOH for 20 min at −35 °C. Finally, the cells were gradually embedded in epoxy resin (see Table 35). Cells were rocked in 1:1 (v/v) EtOH/epoxy resin for 30 min at 4 °C, followed by incubation in 1:1 (v/v) EtOH/epoxy resin for 1 h at room temperature and 100 % (v/v) epoxy resin overnight at room temperature. The next day, cells were incubated in polymerisation medium (see Table 37) for 6 h at room temperature. The medium was removed to a level that only a thin layer was covering the cells and polymerisation was carried out for 48 h at 60 °C.

Table 36: Walton's lead aspartate solution composition

Walton's solution (pH 5.5 with KOH)	30 mM	aspartic acid (pH 3.8 with KOH)
	20 mM	$PbNO_3$

Table 37: SEM charge-reducing epoxy resin composition for embedding of cells

polymerisation medium	3 % (w/v)	silver particles
	5 % (w/v)	Ketjenblack EC-600JD (Lion Specialty Chemicals)
	92 % (v/v)	epoxy resin (see Table 35)

3.6.5.2   Probe mounting and 3view imaging setup

Polymerised cells of interest were cut out of the culture dish with a heated scalpel and mounted onto an epoxy resin stub using epoxy glue (UHU PLUS Endfest 300, UHU). Rough trimming was performed using a high-speed milling system (Leica EM TRIM2, Leica) to generate a flat-top pyramid with 4 sides at 45° angles. 160 µm of the ibidi polymer culture dish layer on the face of the flat-top pyramid was removed by serial sectioning on an ultramicrotome (Leica Ultracut EM UCT, Leica Microsystems, Austria). The area of the pyramid block-face was further reduced to about 0.25 mm^2 by removing the access material with a scalpel. The top of the pyramid was then cut away at a depth of about 1 mm and transferred to an aluminium stub (3View SEM pin stub, Gatan). The sample block was attached to the stub by surrounding the sides and bottom of the block by conductive silver epoxy resin (CircuitWorks Conductive Silver Epoxy, Chemtronics). The silver epoxy was polymerised overnight at 60 °C and the sides of the pyramid were fine-trimmed to retain a thin silver epoxy layer covering the sample. As final step to increase conductivity of the sample surface, it was sputter-coated with a 8 nm layer of gold. The sample was then transferred to a serial block-face scanning electron microscope (Jeol) equipped with a 3view stage (Gatan) operating at 3 keV. A biasing-charge of 600 eV was applied to the stage to reduce charging effects of the sample during prolonged image acquisition. The sample block-face was sequentially trimmed by 50 nm followed by acquisition of scanning electron microscopy (SEM) images of the newly exposed surface using DigitalMicrograph software (Gatan). The same software was used to align SEM image stacks for generation of 3D volumes. Further image processing was performed in Fiji (SCHINDELIN *et al.*, 2012). Manual image segmentation was performed in IMOD software (KREMER *et al.*, 1996) using a touchscreen tablet (Cintiq 16, Wacom).

3.6.6   Electron cryo-tomography

3.6.6.1   Growing infected cells on electron microscopy grids

Before seeding, carbon-coated gold finder grids (Quantifoil, Au G200F1 finder R2/1) were glow-discharged (PDC-002-CE Plasma cleaner, Harrick Plasma) for 1.5 min. The grids were coated with 1 % (v/v) fibronectin and left to dry under UV-light for sterilisation for 1 h. The grids were re-moisturized with PBS and placed in a 2 x 9 chambered culture dishes (µ-Slide 2 Well Co-Culture, ibidi) and covered by 50 µl of DMEM (Gibco DMEM, high glucose,

pyruvate, Thermo Scientific) with 10 % (v/v) FCS (FCS Superior, Merck). A549 or A549 lamin A mTagGFP (PFITZNER *et al.*, 2020) cells were harvested from a 10-cm culture dish at 80 % confluency by addition of stable trypsin replacement enzyme (TrypLE Express enzyme, Gibco) for 15 minutes. The reaction was quenched through addition of DMEM to a final ratio of 2:3 (v/v), the cells were pelleted at 670 g (Centrifuge 5920 R, Thermo Scientific) for 3 min and the supernatant was replaced with DMEM at equal volume. The cell density was determined in a counting chamber (Neubauer Improved, Marienfeld) and the cells were mixed with HAdV-5 pIX-mCherry at an MOI of 1-2. Cells and virus were seeded on the gold grids by addition of 5 - 15 μL of cell suspension to each well. At 36-48 hpi, the grids were imaged by live-cell fluorescence microscopy (as described in Section 3.6.1) and subsequently plunge-frozen for focussed ion beam (FIB)-milling (as described in Section 3.6.6.3) and electron cryo tomography (as described in Section 3.6.6.4).

3.6.6.2 Plunge-freezing of infected cells

After live-cell fluorescence microscopy of infected cells (as described in Section 3.6.1) grown on carbon-coated gold Finder grids, the cells were cryo-fixed by plunge-freezing. Grids were removed from the growth chamber, wetted with 5 μL DMEM and transferred to a manual cryoplunger (Max Planck Institute of Biochemistry, Martinsried, Germany). Grids were blotted (Grade 1 Qualitative Filter Paper, Whatman) from the back for 8 s and plunged into a 37:63 (v/v) mixture of ethane/propane (Linde) cooled to liquid nitrogen temperature.

3.6.6.3 Focussed-ion beam milling

The cryo-fixed grids were clipped into Cryo-FIB Autogrids (Thermo Scientific) and loaded into an Aquilos Cryo-FIB microscope (Thermo Scientific). Correlation between live-cell fluorescence microscopy images was achieved by importing the images into MAPS software (Thermo Scientific) and overlaying them with an SEM tile-scan. Appropriate sites for milling were selected based on the HAdV5 pIX-mCherry fluorescence signal. After an initial SEM scan, grids were sputter-coated with platinum, followed by gas injection deposition of a platinum layer to protect the milling edge of the lamella and prevent curtaining (HAYLES *et al.*, 2007). The final lamella thickness was achieved by sequentially lowering the ion beam current and distance between milling areas. All lamellae on a grid were first pre-milled to 1,500 nm at a current of 1.0 nA. At this step, the overall stability of the lamella was improved

by addition of 'micro-expansion joints' adjacent to either side of the lamella (WOLFF *et al.*, 2019). Milling was continued to an intermediate lamella width of 800 nm at 0.1 nA, and further thinning to 300 nm at 0.05 nA. Final thinning to 180 - 280 nm was then performed at a current of 0.03 nA. A thin 2 nm layer of platinum was applied by sputter-coating to dissipate charge resulting from transmission electron microscopy imaging (see Section 3.6.6.4).

3.6.6.4 Cryo-tomography of thin lamella

Cryo-tomography of thin lamella was performed on a Titan Krios cryo electron microscope (Thermo Scientific) operating at 300 keV and equipped with a K3 direct electron detector (Gatan). Tomograms were acquired using a dose-symmetric tilt scheme (HAGEN *et al.*, 2017). The stage was tilted within the limits of the maximal allowed tilt range for each lamella at 3° tilt steps and a defocus of -4 or -5 μm. The total allowed electron dose per tomogram was 130 electrons. Data acquisition and microscope control was operated using Tomography 5.1 (Thermo Scientific) or SerialEM (MASTRONARDE, 2005) software.

Tomography raw data was corrected for sample motion using MotionCor2 as implemented in RELION 3.0 software (SCHERES, 2012; ZHENG *et al.*, 2017). Individual tilt images were aligned and reconstructed using IMOD software (KREMER *et al.*, 1996). Computational alignment was based on the IMOD patch tracking algorithm and tomography reconstruction was run using the IMOD SIRT-like reconstruction filter setting. Manual image segmentation was performed in IMOD using a touchscreen tablet (Cintiq 16, Wacom).

Chapter 4

Results

4.1 Late nuclear morphogenesis of adenovirus infection

4.1.1 Selection of HAdV5 target proteins for labelling with fluorescent fusion proteins

To generate fluorescently labelled adenovirus particles, three structural viral proteins, pII, pV and pIX, were selected as targets for fusion to fluorescent proteins. The target proteins exist in a high copy number in the mature capsid and are as such useful targets to result in a high fluorophore density per capsid and generate strong fluorescence signal. The core protein pV has a copy number of 150, the minor capsid protein pIX has a copy number of 240 and the major capsid protein pII exists as 720 copies forming 240 hexon trimers (LIU *et al.*, 2010; PÉREZ-BERNÁ *et al.*, 2015). pV was previously shown to accommodate fusion of proteins to the N-terminus (MATTHEWS, 2001; PUNTENER *et al.*, 2011). Similarly, pIX is known to allow for protein fusion to its C-terminus, which is forming a four-helix coiled-coil on the outside of the adenovirus capsid (Figure 5A) (DMITRIEV *et al.*, 2002; MEULENBROEK *et al.*, 2004; VELLINGA *et al.*, 2005). There are no examples of fluorescent protein fusions to pII. The HVRs, which are presented on the surface of pII trimers, were selected as potential fluorophore insertion sites. Such strategy was demonstrated as feasible for HIV-1 glycoprotein (NAKANE *et al.*, 2015). The fluorophore GFP was successfully inserted into the variable loops V4 and V5 for display and fluorescent imaging of HIV-1 particles. For the selection of appropriate hexon HVRs, a multiple sequence alignment was performed for pII sequences from HAdV species 1-51 to calculate the level of conservation present per residue of pII protein. This analysis allowed for the identification of pII loops with low conservation as indication for likely tolerance of amino

acid modifications (Figure 5B & 5C). The two most promising targets were HVR 1 and 5, which combine low sequence conservation, are positioned on the outside of the hexon trimer and suffer the least from sterical hindrance of neighbouring hexon trimers.
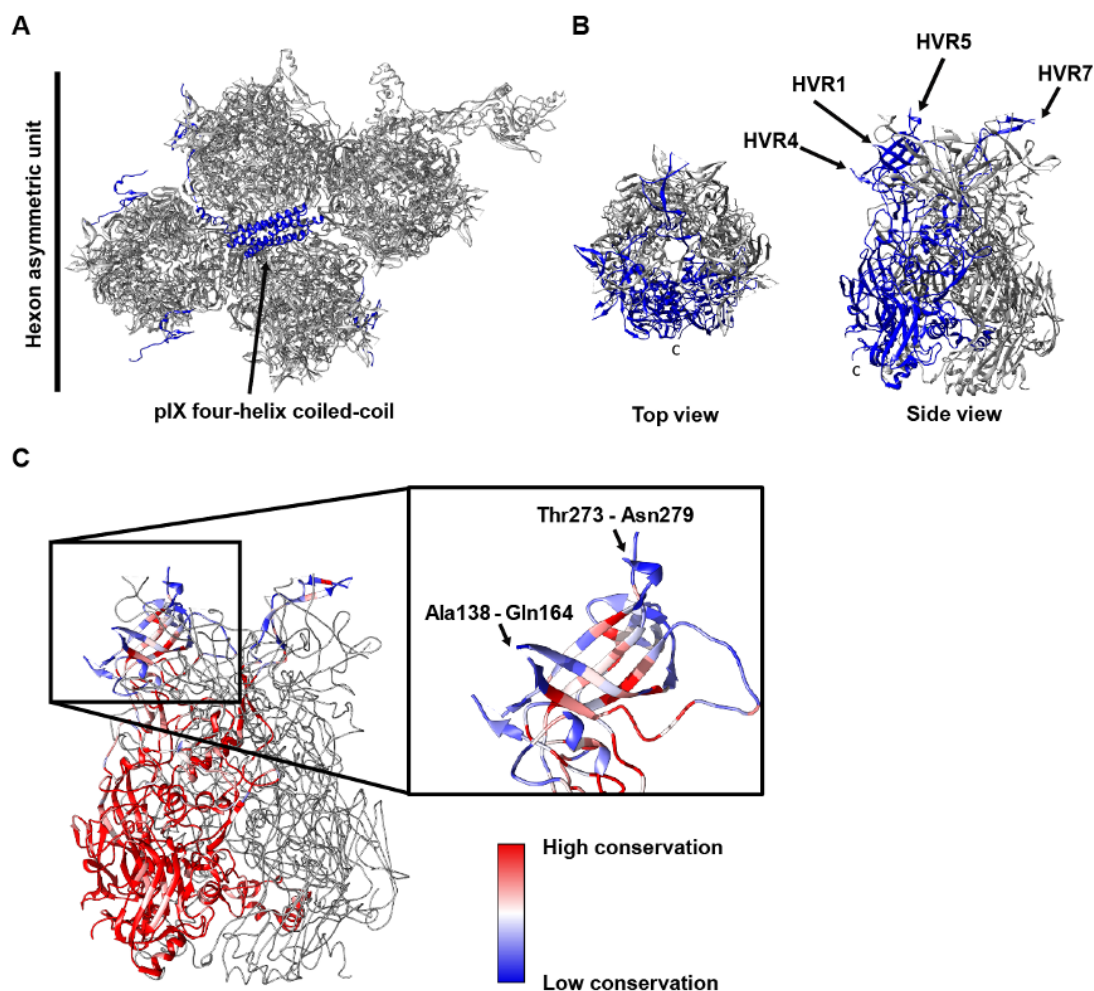
Figure 5: Structural and sequence homology analysis of pII identifies pII HVRs 1 and 5 as potential fluorophore fusion targets. A) Position of pIX four-helix coiled-coil bundle on the outside of hexon tetramer. The C-terminus of pIX is located on the capsid exterior and is accessible for fusion of fluorophores. **B)** Position of HVRs on pII protein as part of hexon trimer. HVR1, HVR4, HVR5 and HVR7 are facing the capsid exterior. **C)** Sequence conservation of pII monomer. pII sequences of HAdV types 1-51 were aligned and the conservation is presented as colour code on the tertiary structure of the protein. HVR1 (Ala138 – Gln164) and HVR5 (Thr273 – Asn279) were selected as targets for addition of mCherry fluorophore. The images were generated using Chimera software (PDB 6B1T & 1P30, structures solved by (Rux *et al.*, 2003; Dai *et al.*, 2017)). Multiple sequence alignment and sequence conservation analysis were performed using Clustal Omega and Al2CO software.

4.1.2 Fusion of mCherry fluorophore to hexon, pV and pIX by homologous recombination

The fluorophore mCherry was selected for fusion to all three HAdV5 target proteins (SHANER *et al.*, 2004). It combines fast folding with a strong monomeric stoichiometry, which differs from other brighter proteins that in turn dimerise and lead to aggregation artefacts upon expression of the tagged proteins (COSTANTINI *et al.*, 2012; CRANFILL *et al.*, 2016). pV, pIX and hexon were tagged within the HAdV5 genome which allows infection of target cells for visualisation of the proteins instead of transfection of the isolated proteins of interest. To allow for later analysis of the role of ADP in infection, fluorescent mutants were generated in both ADP- and ADP+ genomic backgrounds.

mCherry fusion mutants were generated by homologous recombineering in *E. coli* (WANG *et al.*, 2014). The integrity of the viral genome after homologous recombination was validated via restriction pattern analysis and Sanger sequencing of the modified genetic regions. Each restriction pattern resulting from HindIII, XmaI or EcoRV digest matched its *in-silico* prediction (Figure 6B). Virus particles were obtained by transfection of the linearised viral genome into H1299 cells. After transfection, the cells were analysed for mCherry fluorescence. All constructs were positive for fluorescence signal, which indicated a successful expression of pV-mCherry, pIX-mCherry, hexon-HVR1-mCherry and hexon-HVR5-mCherry but cannot be taken as proof for successful virion assembly (data not shown).

To test for the formation of infectious virus particles, the transfected cells were lysed by three freeze-thaw cycles to release virus particles from infected cells and the supernatant was used to infect fresh H1299 cells. After one week, mCherry fluorescence was analysed. Detection of fluorescence signal at this stage of the experiment indicates that the mutant virus particles are able to infect new cells. Only HAdV5 pV-mCherry ADP+/- and HAdV5 pIX-mCherry ADP+/- infection resulted in fluorescent cells. HAdV5 hexon-HVR1-mCherry ADP+/- and HAdV5 hexon-HVR5-mCherry ADP+/- showed no fluorescence. It is likely that due to the essential nature of hexon and its high copy number in the virion, either particle assembly was hindered, or the decoration of virus particles with mCherry fusion on the surface disturbed attachment of the virus to new cells. Nevertheless, pV-mCherry and pIX-mCherry fusion mutants were successfully generated and were the focus of the following analysis (Figure 6A/B).

4.1.3 Characterisation of HAdV5 pV-mCherry and HAdV5 pIX-mCherry mutants

The newly generated mutants were characterised regarding particle appearance, protein labelling success and virus growth kinetics. First, virus particles were purified by single $CsCl_2$ gradient ultracentrifugation. The virus particles were imaged in negative stain TEM (Figure 6C). Both HAdV5 pV-mCherry and pIX-mCherry mutants retained icosahedral shape and formed intact particles. Additionally, the virus release kinetics from infected cells were compared to wild type (wt) HAdV5 infection by flow cytometry (Figure 6D). The HAdV5 pV-mCherry and pIX-mCherry mutants show similar virus release at 24 and 48 hours post infection (hpi) compared to wt. Only from 72 hpi to 96 hpi, about tenfold more wt virus particles were released compared to the mutants. Additionally, the fluorescence of purified virus particles was tested by confocal laser-scanning fluorescence microscopy. Purified virus particles were adsorbed to a glass surface (Figure 6E). Both HAdV5 pV-mCherry and HAdV5 pIX-mCherry virus particles were visible as single fluorescent dots when imaged at 568 nm excitation.
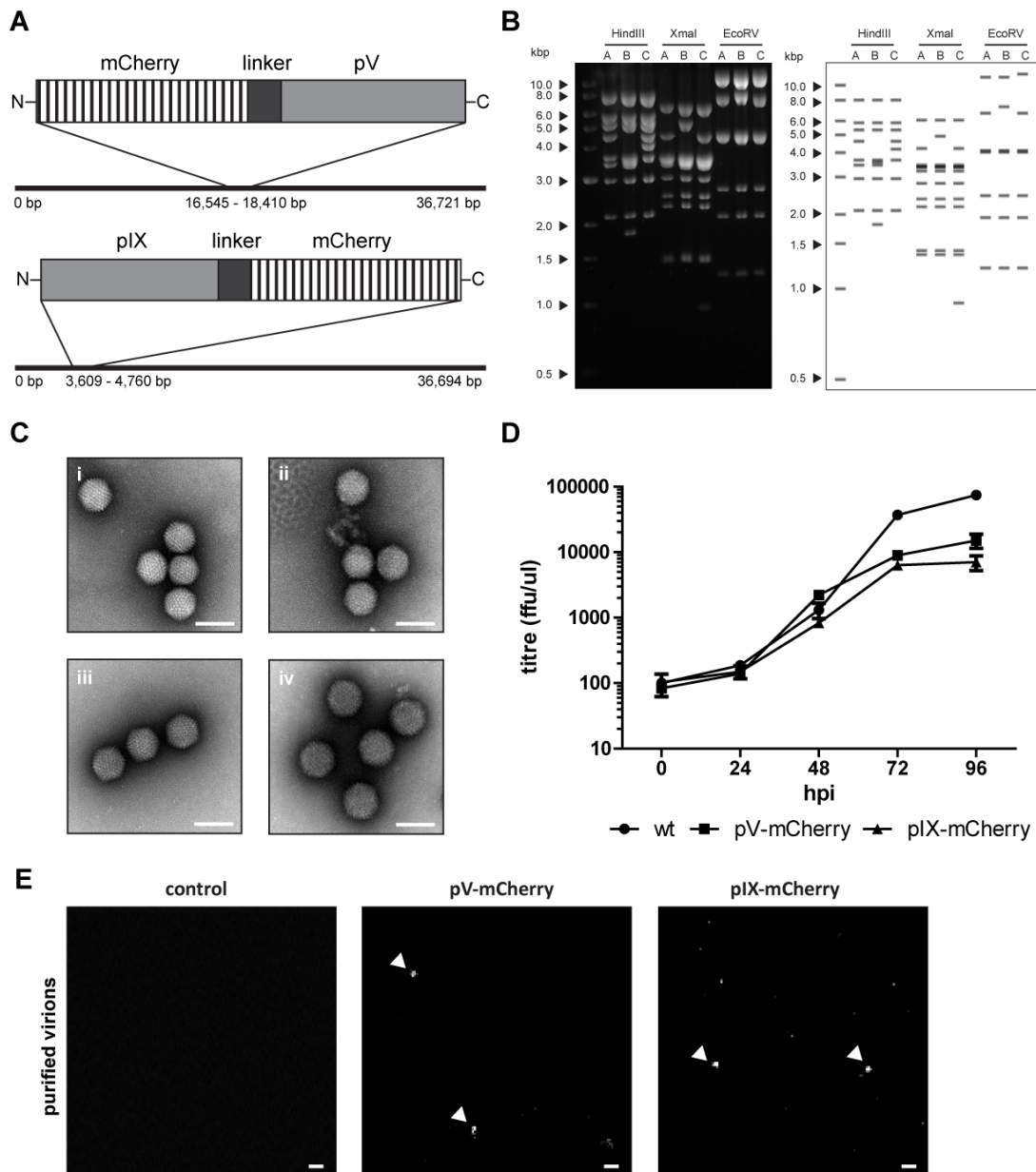
Figure 6: Characterisation of HAdV5 fusion mutants expressing pV and pIX fused to fluorophore mCherry shows successful labelling of particles. A) Schematic of pV and pIX mCherry-fusion constructs. Protein V and protein IX were fused to the mCherry fluorophore in combination with a varying flexible linker region. mCherry was fused N-terminally to pV and C-terminally to pIX. **B)** Restriction analysis of wt, pV-mCherry and pIX-mCherry bacmid DNA on the left (lanes labelled A, B, C) including *in-silico* prediction of restriction pattern on the right. The digested viral genomes show the expected restriction pattern. **C)** Negative stain TEM of purified virus particles. The virus particles of each mutant were purified, contrasted with uranyl acetate negative stain and imaged by TEM. Scalebars indicate 100 nm. HAdV5 pV-mCherry ADP– particles are shown in i), HAdV5 pV-mCherry ADP+ particles are shown in ii), HAdV5 pIX-mCherry ADP– particles are shown in iii), HAdV5 pIX-mCherry ADP+ particles are shown in iv). Virus particles show normal icosahedral shape. No difference between any of the mutants was observed **D)** Growth curve of virus particle release from infected A549 cells from 0 to 96 hpi. The supernatant of infected cells was collected at each time-point and their titre was measured as fluorescence forming unit (ffu)/μL by FACS analysis. Since ADP is important in the process of particle release, only ADP+ mutants were probed. Three replicates (n=3) were measured. **E)** Fluorescence microscopy of purified virions adsorbed to glass surface. Virions were purified by ultracentrifugation and analysed for fluorescence. Both HAdV5 pV-mCherry ADP+ and HAdV5 pIX-mCherry ADP+ were detected as fluorescent spots (white arrows). Scalebars indicate 1 μm.

For assessment of labelling success on the protein level, whole-cell lysate of infected cells was extracted, separated by SDS–PAGE and pV and pIX were probed by western blot in both ADP+/- backgrounds. As a control for having equal amount of protein in cell lysates, β-actin was stained. As a control for mCherry labelling, each fusion construct was additionally probed with an RFP antibody, which recognises the mCherry label. HAdV5 pV-mCherry and HAdV5 pIX-mCherry act as reciprocal controls such that infection with HAdV5 pV-mCherry expresses wt pIX and infection with HAdV5 pIX-mCherry expresses wt pV (Figure 7A).

Overall, no differences in protein expression between HAdV5 ADP– and HAdV5 ADP+ infected samples were detected when comparing lanes 1 & 2 and 3 & 4. The western blot probing pV wt (lanes 3 & 4) showed a pV band at the expected size of 41.6 kDa. pV-mCherry was expected to appear at a size of 70.2 kDa. Instead, multiple bands extending from about 70 kDa to 42 kDa were detected, indicating a variety of pV-mCherry protein lengths (lanes 1 & 2). The western blot probing pIX wt showed a pIX band at the expected size of 14.3 kDa (lanes 1 & 2). pIX-mCherry was expected to appear at a size of 43.1 kDa and did indeed show a band at the corresponding gel position (lanes 3 & 4). Additionally, a single band at about 24 kDa was detected. Interestingly the pIX-mCherry bands were stronger than pIX wt bands, which could indicate protein stabilisation by the tag. The anti-RFP stain showed a single band at the full-length pV-mCherry size as well as a single band at the full-length pIX-mCherry size. If degradation would have occurred in the pV or pIX part of the fusion proteins, then the RFP antibody would also show a band pattern. Since only single bands were detected, pV-mCherry and pIX-mCherry degradation most likely occurred within the mCherry locus of the fusion proteins. If the RFP epitope was lost in these degradation products, they would not show on the anti-RFP western blot.

Additionally, the labelling success of pV and pIX proteins that were incorporated into virions was probed by western blot. $CsCl_2$ gradient purified virions were denatured, separated by SDS–PAGE and pV and pIX were probed by western blot (Figure 7B) and Coomassie stain (Figure 7C). As in whole-cell lysate, pV and pIX wt protein showed a single band at their expected size. pV-mCherry appeared as a smear of multiple degradation intermediates (lane 1) and pIX-mCherry showed two bands at the sizes measured for whole-cell lysate before (lane 2). In the Coomassie-stained gel, the fragmented band pattern of pV-mCherry was visible as well. Additionally, other expected capsid proteins were detected, including, pII, pIII, pVI, pV and pVII.
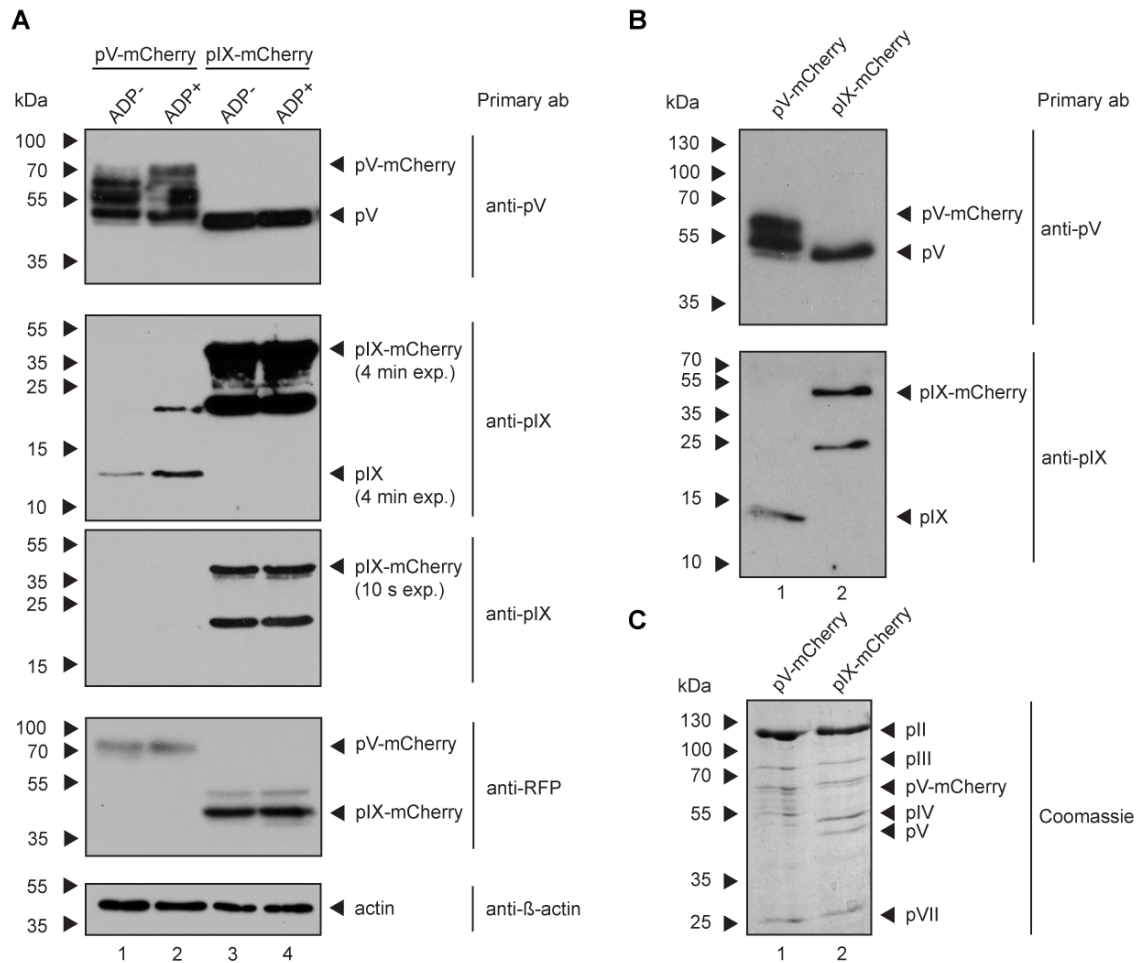
Figure 7: Fusion of mCherry to pV and pIX does not exclusively produce full length labelled protein but yields degradation products with shortened mCherry component. The protein labelling success of pV and pIX in whole-cell lysate of infected A549 cells and purified virus particles was probed. **A)** Whole-cell lysate analysis. A549 cells were infected with HAdV5 pV-mCherry ADP+/- and HAdV5 pIX-mCherry ADP+/- and cells were harvested at 48 hpi. The whole-cell lysate was analysed by western blot with primary antibodies against pV, pIX, RFP and β-actin. Each lane was numbered (1 - 4) for reference. Degradation products of pV-mCherry and pIX-mCherry were only detected when probing pV or pIX. The anti-RFP antibody only displayed full-length pV-mCherry and pIX-mCherry. **B/C)** Purified virus particle lysate analysis. A549 cells were infected with HAdV5 pV-mCherry ADP+ and HAdV5 pIX-mCherry ADP+ and the culture supernatant was harvested at 96 hpi. Virus particles were purified from the supernatant by single $CsCl_2$ gradient ultracentrifugation. Th virions were lysed and the proteins were separated by SDS-PAGE. Each lane was numbered (1 - 2) for reference. Labelling of pV and pIX with primary antibodies against pV and pIX in western blot (B) as well as labelling of all proteins by Coomassie stain (C) showed similar degradation product of pV-mCherry and pIX-mCherry being incorporated into progeny particles.

A549 cells were chosen as a suitable cell system to study HAdV5 infection. This cancer cell line originates from lung epithelial tissue and is a well-studied target cell line of HAdV5 (SMITH *et al.*, 1986). To allow an analysis of the localisation of pV-mCherry and pIX-mCherry signals in a more cellular context, the nuclear envelope was visualised through a mTagGFP-coupled nanobody recognising lamin A. This nanobody was stably expressed in a A549 monoclonal cell

line. The expression of free nanobody throughout the cells resulted in moderate background signal (Figure 8A). However, lamin A-specific signal of the nanobody was clearly visible over the background and colocalised with an anti-lamin A antibody. Similarly to purified virions, single virus particles could be detected when analysing infection at early time points in a cellular context (Figure 8B/C). Here, HAdV5 pV-mCherry and HAdV5 pIX-mCherry particles were located on the outside of the nuclear envelope, potentially in the process of virus genome release into the nucleoplasm.
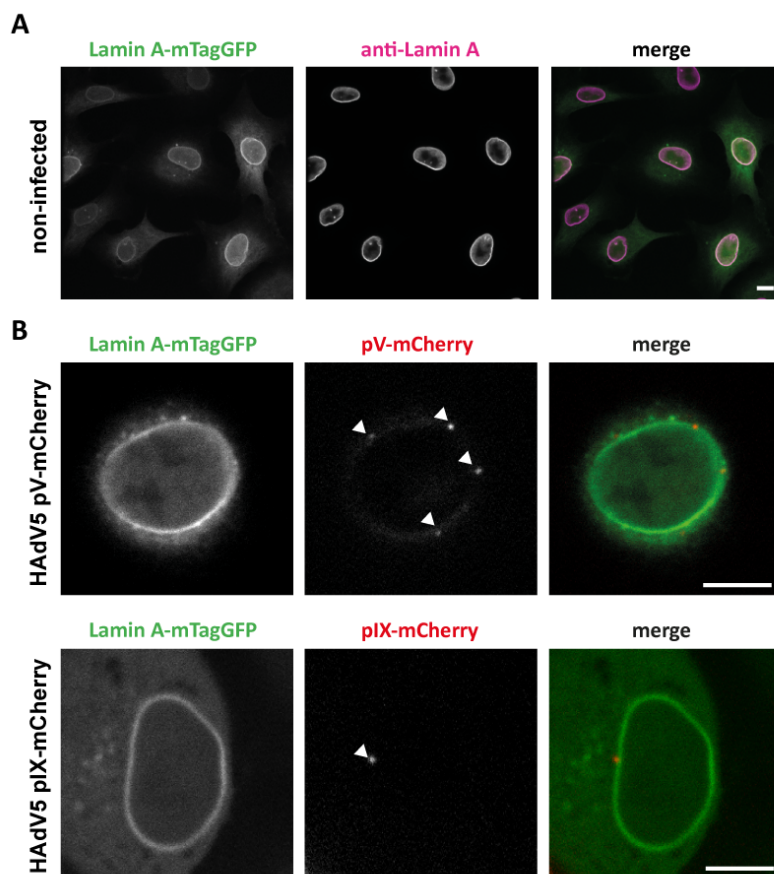
Figure 8: The cell line A549 lamin A mTagGFP allows to visualise the nuclear lamina and shows single virions early in infection. A) A549 lamin A mTagGFP cells were co-stained for lamin A as a control for the localisation of anti-lamin A mTagGFP-nanobodies. Both anti-lamin A nanobody-mTagGFP signal and anti-lamin A immunofluorescence antibody signal colocalised. B) Detection of HAdV5 pV-mCherry and HAdV5 pIX-mCherry particles at the nuclear lamina early in infection. The cells were imaged by live-cell confocal laser-scanning fluorescence microscopy. A representative cell is shown for each condition. The nuclear lamina is represented by an mTagGFP-nanobody recognising lamin A (Lamin A-mTagGFP) or by an anti-lamin A antibody (anti-Lamin A). pV and pIX localisation is detected through the viral pV-mCherry and pIX-mCherry fusion construct (pV-mCherry/pIX-mCherry). The signal overlap is represented in colour (merge). Scalebars indicate 10 μm.

As a first step, the phenotype of cells infected with HAdV5 pV-mCherry and HAdV5 pIX-mCherry was analysed at 24 hpi and 48 hpi. In addition to lamin A, dsDNA was stained by addition of Hoechst 33342, a dye which binds to the minor groove of dsDNA (Figure 9).

Non-infected cells displayed a clear lamin A-nanobody signal tracing the nuclear envelope. There was low background signal of unbound mTagGFP-nanobody throughout the cytoplasm. Hoechst 33342 stained the genomic DNA inside the entire nucleus. In infection, the localisation of lamin A and dsDNA changed considerably. At 24 hpi, the dsDNA lost its regular distribution throughout the nucleus and was partially condensed and marginalised to the nuclear envelope. At this time-point, the lamin A signal was still intact and comparable to non-infected conditions. At 48 hpi, Hoechst 33342 stained strongly marginalised dsDNA at the periphery of the nucleus as well as a dsDNA-filled compartment in the centre of the nucleus. The lamin A nanobody only showed residual staining at the nuclear envelope but instead was found to be weakly distributed throughout the infected cells with some signal enrichment in individual spots in the cytoplasm. Importantly, the phenotype of lamin A and dsDNA did not differ between HAdV5 pV-mCherry and HAdV pIX-mCherry-infected cells.

The fusion of mCherry to pV and pIX allowed for successful detection of soluble expressed protein in infected cells. At 24 hpi, the nucleus was filled by a faint pV-mCherry signal, which was locally enriched in subnuclear compartments previously identified as the nucleoli (MATTHEWS and RUSSELL, 1998). Noticeably, the weak pV-mCherry signal was excluded from ring- and dot-like subnuclear areas, which closely resemble the localisation that is known for adenoviral DBP replication centres at this time-point in infection (POMBO *et al.*, 1994). A549 cells infected with HAdV5 pIX-mCherry, showed the protein signal to be mainly localised to the cytoplasm at 24 hpi. Only a very weak signal was recorded in the nucleus, but, other than pV-mCherry, was not excluded from replication centre-resembling areas.

At 48 hpi, the pV-mCherry protein mainly localised to the same compartment within the nucleus that was also stained by Hoechst 33342. Importantly, pV-mCherry did not homogeneously fill out the compartment but instead appeared to be localised in a honeycomb-like distribution. pIX-mCherry protein was still strongly expressed in the cytoplasm at 48 hpi. Other than at 24 hpi, the protein was also found within the nucleus. The transition between cytoplasm nucleus was visible in the pIX-mCherry channel as the protein was devoid from the nuclear periphery. Besides homogeneously distributed signal within the nucleus, pIX-mCherry signal was detected as individual spots within the subnuclear compartment indicated by Hoechst 33342. A quantitative analysis of these pIX-mCherry spots at 48 hpi showed their occurrence in 77 % of infected cells imaged in a single confocal plane, making them a prevalent phenotype in infection. The subnuclear

compartment consisting of pV-mCherry, pIX-mCherry spots and dsDNA will be referred to as late virion accumulation compartment (LVAC) in the following.
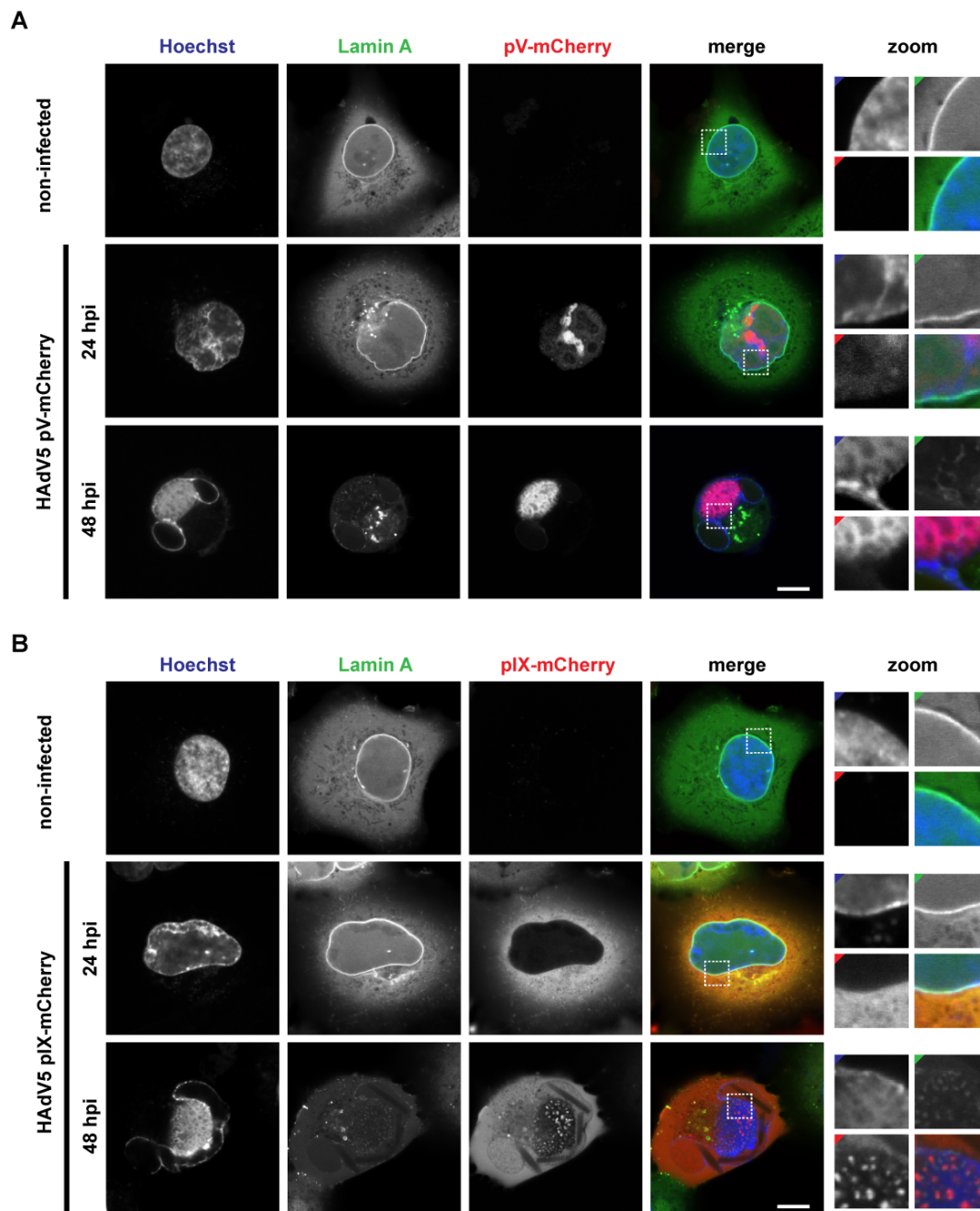
Figure 9: Infection with HAdV5 pV-mCherry and HAdV5 pIX-mCherry causes formation of a large intranuclear compartment late in infection. A) Infection of A549 cells with **A)** HAdV5 pV-mCherry and **B)** HAdV5 pIX-mCherry at 24 hpi and 48 hpi. The cells were imaged by live-cell confocal laser-scanning fluorescence microscopy. A representative cell is shown for each condition. The dsDNA signal is represented by Hoechst 33342 stain (Hoechst). The nuclear lamina is represented by an mTagGFP-nanobody recognising lamin A (Lamin A). pV and pIX localisation is detected through the viral pV-mCherry and pIX-mCherry fusion construct (pV-mCherry/pIX-mCherry). The signal overlap is represented in colour (merge). Nuclear regions of interest are enlarged (zoom) with coloured corners indicating the channel colour. Scalebars indicate 10 µm.

To exclude cell line-specific artefacts, the infection with HAdV5 pV-mCherry and HAdV5 pIX-mCherry was carried out in the lung epithelial cell line H1299 and the lung fibroblast cell line MRC-5 (Figures 10 & 11). All cell lines showed phenotypes similar to infection in A549 cells. At 24 hpi, pV-mCherry was enriched in nucleoli and excluded from DBP-replication centres. pIX-mCherry was mainly localised in the cytoplasm. At 48 hpi, the LVAC was formed in all cell lines. pV-mCherry and dsDNA localised in a honeycomb-like conformation and pIX-mCherry was detected as spots within the LVAC in addition to the dispersed signal throughout the cell.
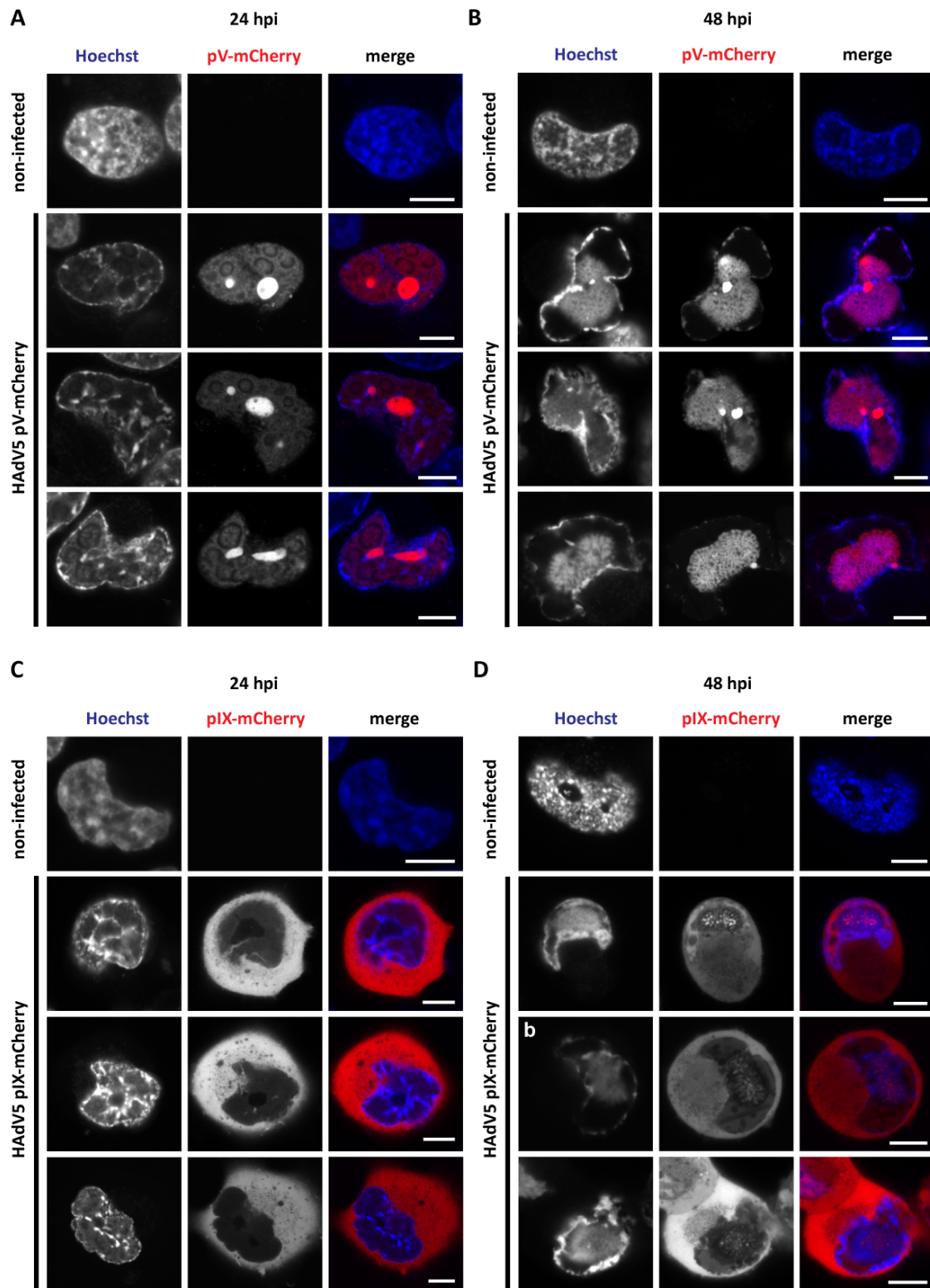
Figure 10: LVAC formation can be detected in H1299 cells. Infection of H1299 cells with **A/B)** HAdV5 pV-mCherry and **C/D)** HAdV5 pIX-mCherry at 24 hpi and 48 hpi. The cells were imaged by live-cell confocal laser-scanning fluorescence microscopy. Three representative cells are shown for each condition. The dsDNA signal is represented by Hoechst 33342 stain (Hoechst). The nuclear lamina is represented by an mTagGFP-nanobody recognising lamin A (Lamin A). pV and pIX localisation is detected through the viral pV-mCherry and pIX-mCherry fusion construct (pV-mCherry/pIX-mCherry). The signal overlap is represented in colour (merge). Scalebars indicate 10 μm.
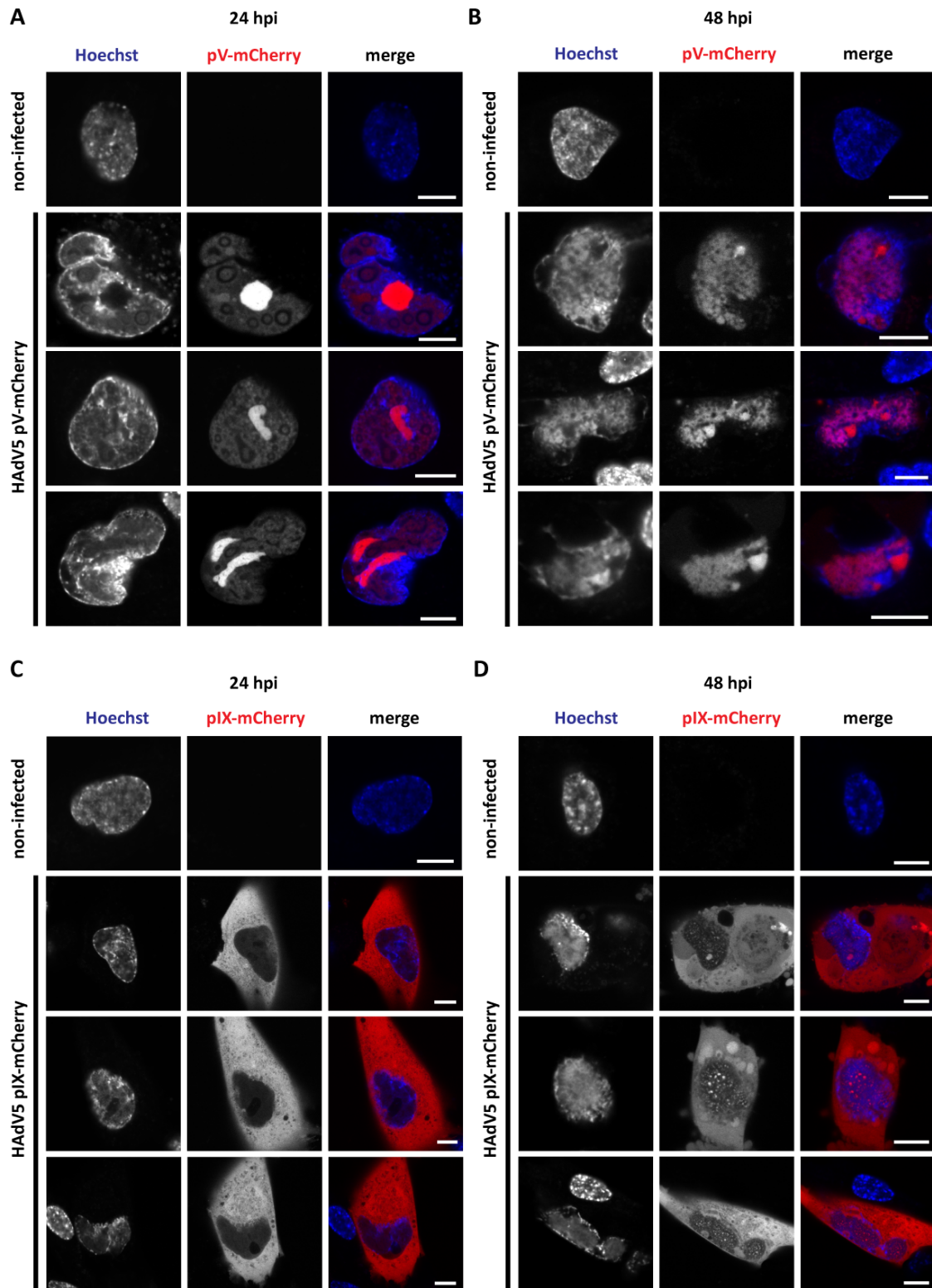
Figure 11: LVAC formation can be detected in MRC-5 cells. Infection of MRC-5 cells with **A/B)** HAdV5 pV-mCherry and **C/D)** HAdV5 pIX-mCherry at 24 hpi and 48 hpi. The cells were imaged by live-cell confocal laser-scanning fluorescence microscopy. Three representative cells are shown for each condition. The dsDNA signal is represented by Hoechst 33342 stain (Hoechst). The nuclear lamina is represented by an mTagGFP-nanobody recognizing lamin A (Lamin A). pV and pIX localization is detected through the viral pV-mCherry and pIX-mCherry fusion construct (pV-mCherry/pIX-mCherry). The signal overlap is represented in colour (merge). Scalebars indicate 10 μm.

So far, the involvement of DBP replication centres was only hypothesised from the appearance of pV-mCherry-devoid areas at 24 hpi. To confirm this observation, a co-immunofluorescence stain was performed to label wt pV and pIX as well as DBP in infection with HAdV5 wt virus. Infected cells were fixed with PFA at 24 hpi and stained with pV and DBP or pIX and DBP antibodies, respectively (Figures 12 & 13).
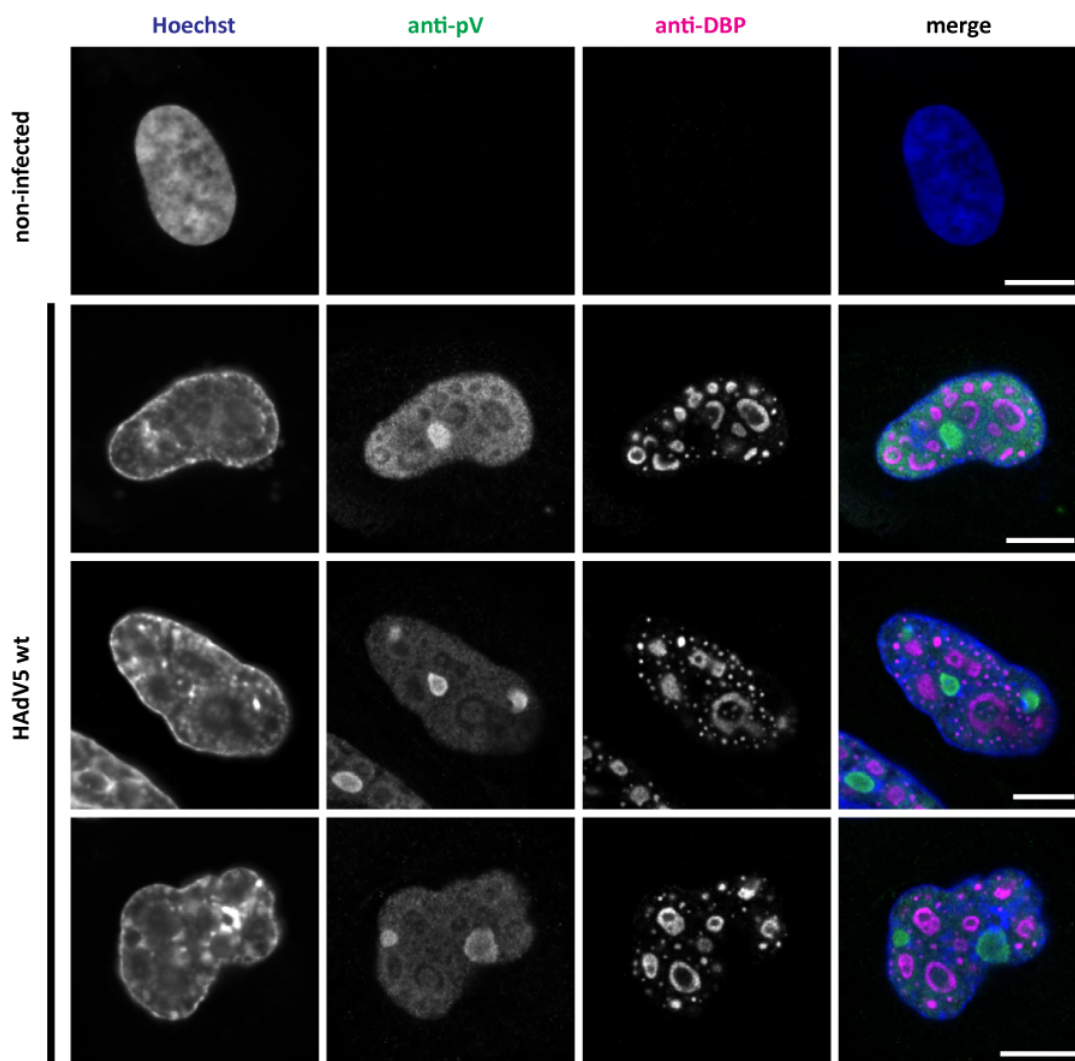
Figure 12: wt pV is devoid from replication centres and accumulates in nucleoli at 24 hpi. A549 cells were infected with HAdV5 wt, fixed at 24 hpi, stained with Hoechst 33342 (Hoechst), and immunostained against pV (anti-pV) and DBP (anti-DBP). The signal overlap is represented in colour (merge). Cells were imaged by confocal laser-scanning fluorescence microscopy. Three representative cells are shown. Scalebars indicate 10 μm.
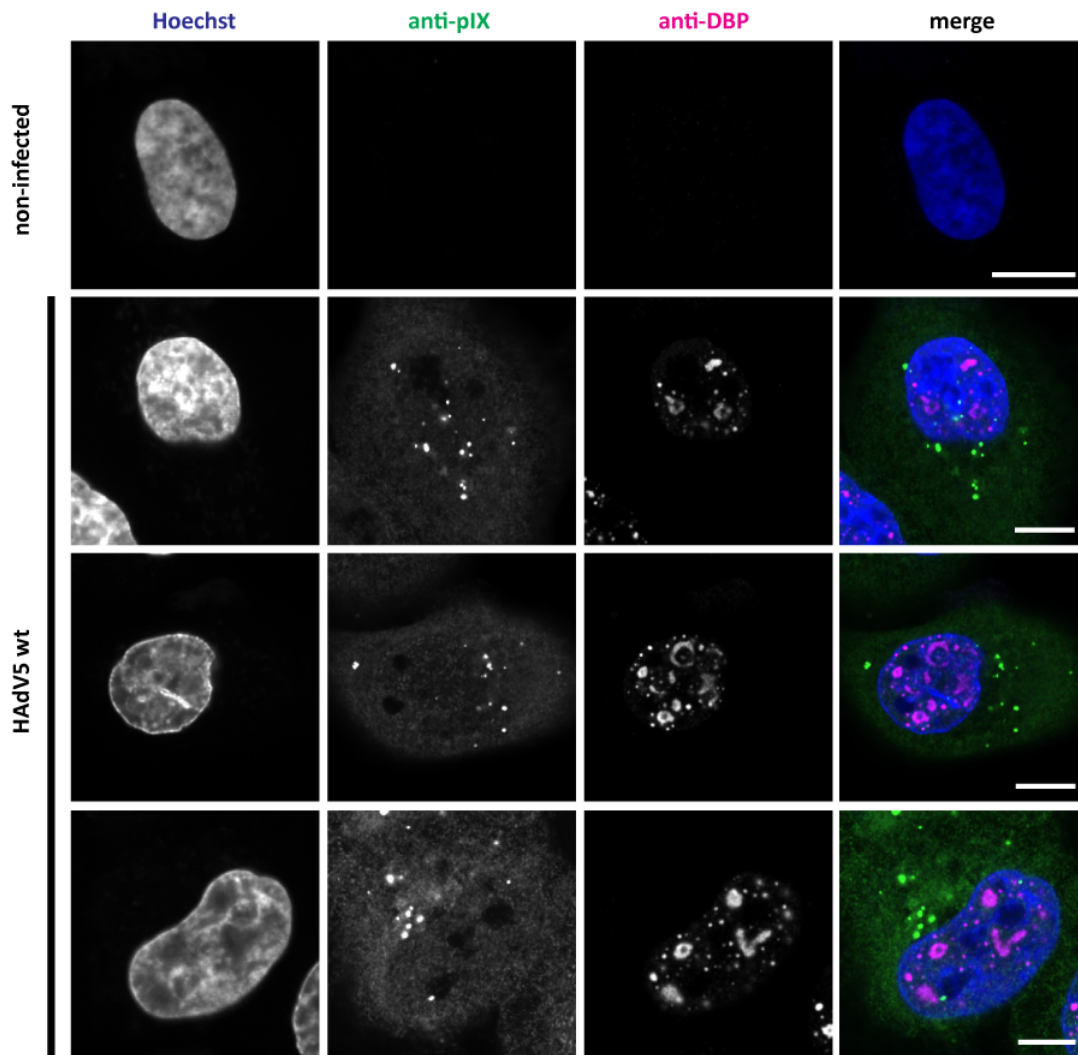
Figure 13: wt pIX forms aggregates throughout the cell at 24 hpi. A549 cells were infected with HAdV5 wt, fixed at 24 hpi, stained with Hoechst 33342 (Hoechst), and immunostained against pIX (anti-pIX) and DBP (anti-DBP). The signal overlap is represented in colour (merge). Cells were imaged by confocal laser-scanning fluorescence microscopy. Three representative cells are shown. Scalebars indicate 10 μm.

pV protein signal was weakly detected in the entire nucleus. Similar to the observation with pV-mCherry (Figure 9A), the protein was enriched in nucleoli and also was excluded from multiple foci and ring structures. The co-stain with DBP antibody confirmed these areas to be filled with DBP protein. pIX protein was found to be localised throughout the entire infected cells. Additionally, strongly fluorescent aggregates of pIX were detected both in the cytoplasm and nucleus. This phenotype differs from the observation of pIX-mCherry at 24 hpi, which did not show aggregates and had the majority of the protein expressed in the cytoplasm. As in the costain with pV, DPB localised as foci and rings in the nucleus. No apparent colocalisation or interaction between pIX and DBP was detected at 24 hpi.

4.1.4 IF microscopy characterisation of the 'late virion accumulation compartment'

Since the addition of fusion tags to proteins of interest may lead to the induction of functional and localisation artefacts, the localisation of pV and pIX was analysed at 48 hpi in HAdV5 wt infection to probe whether the LVAC is also formed in wt infection. pV and pIX were detected by their respective antibodies. The nuclear envelope was visualised through the anti-lamin A nanobody and dsDNA was stained by Hoechst 33342. Additionally, the adenoviral DBP was immunostained to reveal the connection of the LVAC with adenovirus replication centres (Figures 14 & 15).
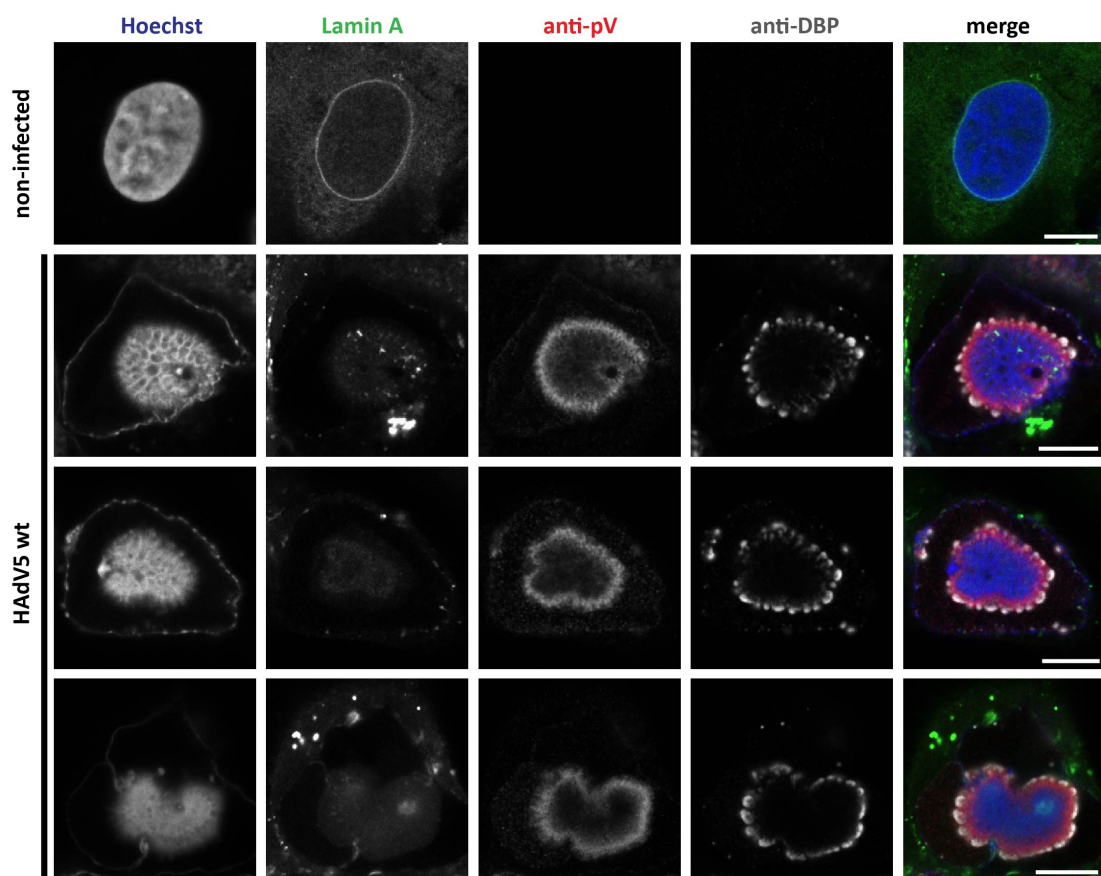
Figure 14: Antibody staining against wt pV and DBP in HAdV5 wt infection shows ring structure around LVAC at 48 hpi. A549 cells were infected with HAdV5 wt, fixed at 48 hpi, stained with Hoechst 33342 (Hoechst), and immunostained against pV (anti-pV) and DBP (anti-DBP). The nuclear lamina is represented by an mTagGFP-nanobody recognising lamin A (Lamin A). The signal overlap is represented in colour (merge). Cells were imaged by confocal laser-scanning fluorescence microscopy. Three representative cells are shown. Scalebars indicate 10 µm.
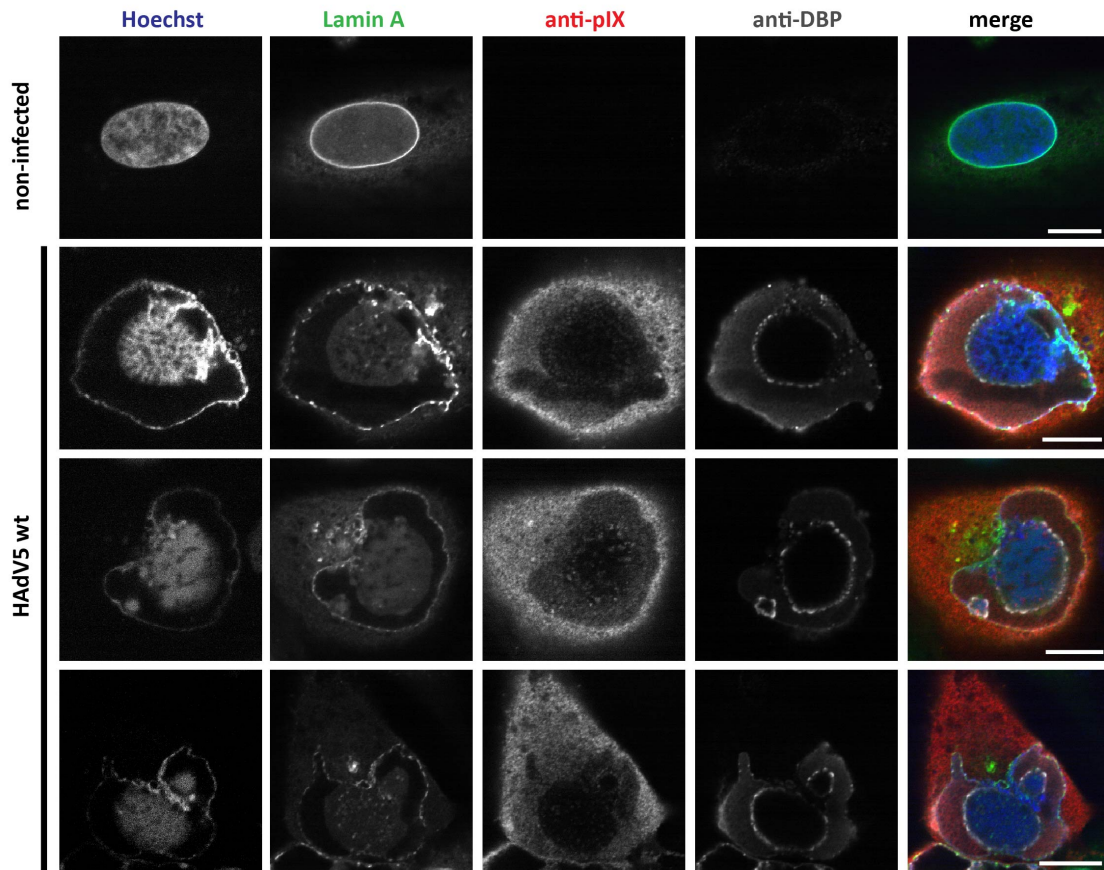
Figure 15: Antibody staining against wt pIX and DBP in HAdV5 wt infection does not show pIX spots within the LVAC. A549 cells were infected with HAdV5 wt, fixed at 48 hpi, stained with Hoechst 33342 (Hoechst), and immunostained against pIX (anti-pIX) and DBP (anti-DBP). The nuclear lamina is represented by an mTagGFP-nanobody recognising lamin A (Lamin A). The signal overlap is represented in colour (merge). Cells were imaged by confocal laser-scanning fluorescence microscopy. Three representative cells are shown. Scalebars indicate 10 μm.

The dsDNA localisation was identical to the phenotype observed in infection with HAdV5 pV-mCherry and HAdV5 pIX-mCherry. dsDNA localised to a large compartment within the nucleus, which was termed LVAC. Importantly, the phenotype of pV and pIX at 48 hpi did not fully resemble the observation that was made in infection with the fusion proteins. pV antibody signal was detected in a ring-like structure surrounding the LVAC. Intriguingly, the pV-ring signal intensity decreased towards the centre of the LVAC. As pV, the DBP antibody also stained a ring-like structure of closely spaced individual DBP foci. The DBP ring was located around the LVAC and, like for pV, the antibody signal decreased towards the centre. Similar to the pIX fusion protein, the pIX antibody signal was mainly detected in the cytoplasm of infected cells. However, the area of the LVAC was scarcely stained by the pIX antibody and no strong pIX spots were detected. Since the localisation of LVAC dsDNA is identical in wt and fusion mutant infection, LVAC formation does not seem to be an artefact of labelling pV

or pIX with mCherry. The ring of pV indicates that native pV is also localised to the LVAC in wt infection. Since none of the antibodies against pV, pIX and DBP showed signal within the centre of the nucleus, a limited antibody penetration into the LVAC was hypothesised.

The LVAC formation was further characterised by staining with anti-hexon antibody. For the purpose of this immunofluorescence stain, the protein is hypothesised to behave similarly to pIX since both are structural proteins that are incorporated into the progeny HAdV capsids. A549 cells were infected with HAdV5 wt and stained with antibodies against hexon and DBP. The nuclear envelope was visualised through the anti-lamin A nanobody and dsDNA was stained by Hoechst 33342 (Figure 16).
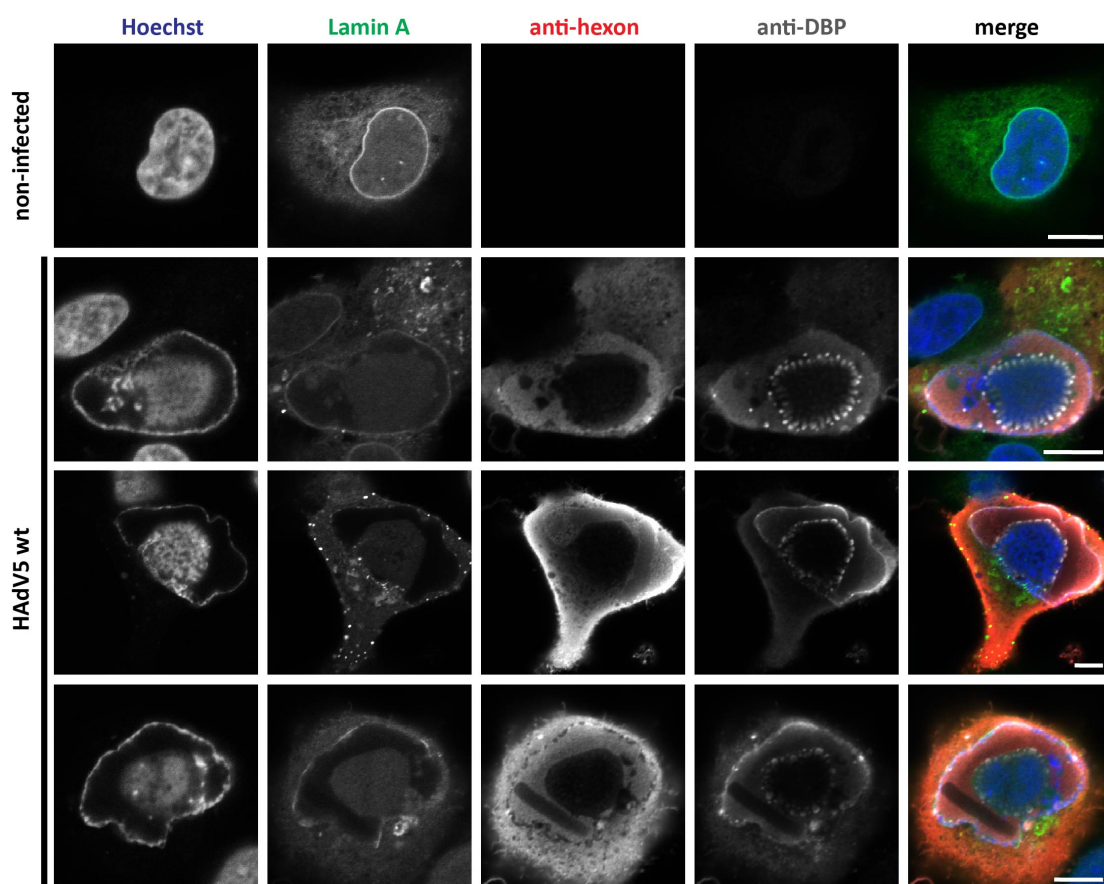
Figure 16: Antibodies against hexon in HAdV5 wt infection do not fully stain the LVAC. A549 cells were infected with HAdV5 wt, fixed at 48 hpi and imaged by confocal laser-scanning fluorescence microscopy. Cells were stained with Hoechst 33342 (Hoechst), and immunostained against hexon (anti-hexon) and DBP (anti-DBP). The nuclear lamina is represented by an mTagGFP-nanobody recognising lamin A (Lamin A). The signal overlap is represented in colour (merge). Three representative cells are shown. Scalebars indicate 10 μm.

The dsDNA, lamin A and DBP localisation was the same compared to the previous immunofluorescence stain with pV and pIX antibodies. Hexon protein localised throughout

the entire cell including cytoplasm and nucleoplasm. As pIX, hexon could not be detected in the centre of the nucleus, where most of the dsDNA signal was found. This observation again indicated a potential lack of epitope availability in this region of the cell.

As a first step to confirm the hypothesised antibody penetration limitations, the phenotype of anti-pV and anti-pIX antibody labelling was investigated in HAdV5 pV-mCherry and HAdV5 pIX-mCherry infection. Should the localisation of antibody signal be comparable to HAdV5 wt infection, it would indicate that the pV-mCherry honeycomb and pIX-mCherry spots within the LVAC are not labelling artefacts. To confirm this, an immunofluorescence stain of pV, pIX and DBP was repeated in cells infected with either of the two HAdV5 mutants. A549 cells expressing an mTagGFP-coupled nanobody recognising lamin A were infected and fixed with PFA at 48 hpi. pV, pIX and DBP were detected by immunofluorescence stains. dsDNA was visualised by Hoechst 33342 stain (Figures 17 & 18).
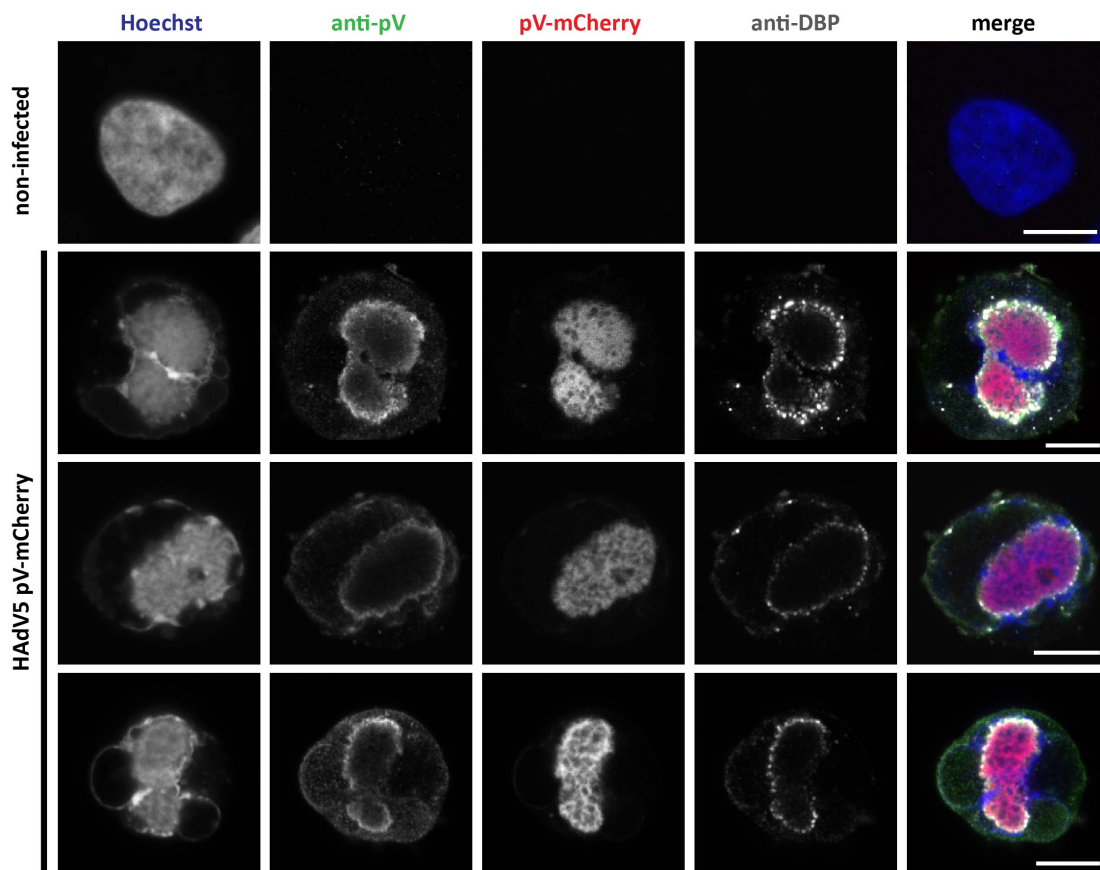
Figure 17: Antibody staining against pV and DBP in HAdV5 pV-mCherry infection does not the LVAC to be filled by a honeycomb-like structure of pV. A549 cells were infected with HAdV5 pV-mCherry, fixed at 48 hpi, stained with Hoechst 33342 (Hoechst), and immunostained against pV (anti-pV) and DBP (anti-DBP). pV localisation is detected through the viral pV-mCherry fusion construct (pV-mCherry). The signal overlap is represented in colour (merge). Cells were imaged by confocal laser-scanning fluorescence microscopy. Three representative cells are shown. Scalebars indicate 10 µm.
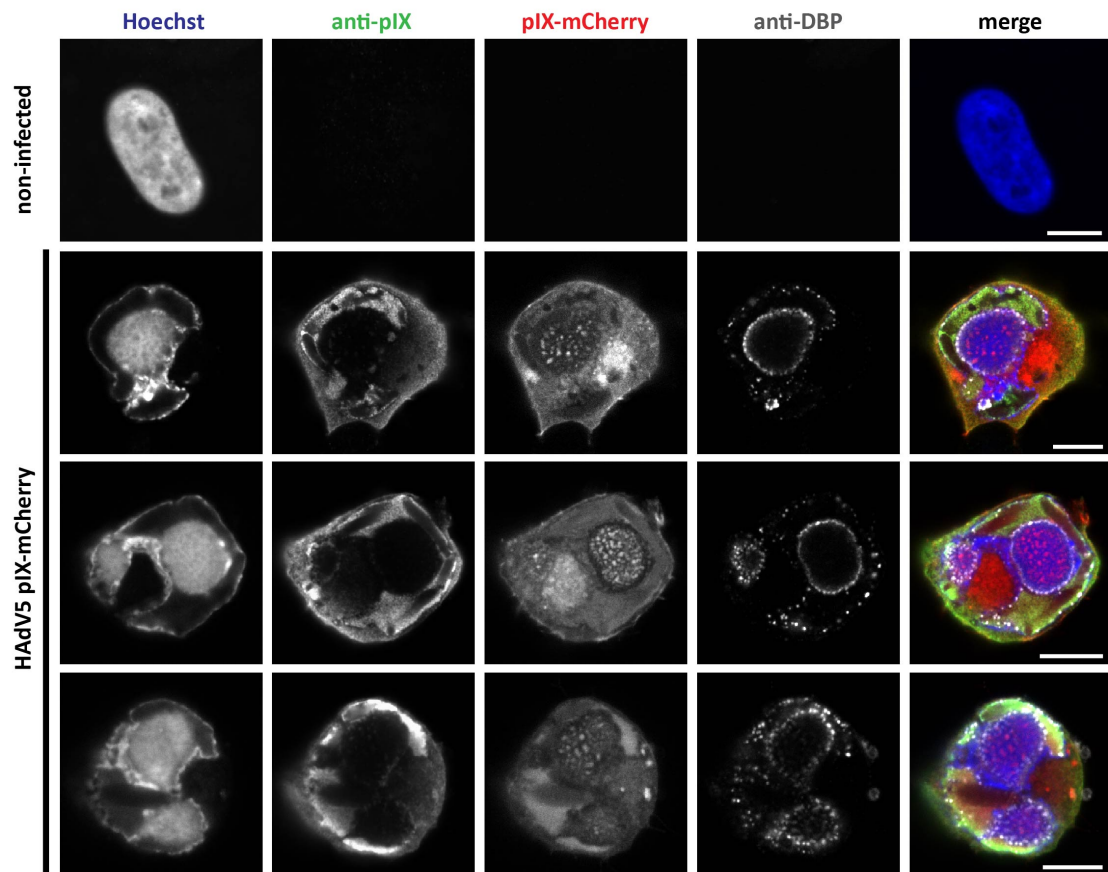
Figure 18: Antibody staining against pIX and DBP in HAdV5 pIX-mCherry infection does not show pIX spots within the LVAC. A549 cells were infected with HAdV5 pIX-mCherry, fixed at 48 hpi, stained with Hoechst 33342 (Hoechst), and immunostained against pIX (anti-pIX) and DBP (anti-DBP). pIX localisation is detected through the viral pIX-mCherry fusion construct (pIX-mCherry). The signal overlap is represented in colour (merge). Cells were imaged by confocal laser-scanning fluorescence microscopy. Three representative cells are shown. Scalebars indicate 10 μm.

Both DBP and Hoechst 33342 signals did not differ phenotypically from their previously observed localisation in wt infection (Figure 14 & 15), indicating that the infection phenotype observed in the HAdV5 mutants is comparable to HAdV5 wt. Additionally, the pV antibody stained a ring around the LVAC, similar to the pattern observed in HAdV5 wt infection. Also the pIX antibody localisation was comparable to HAdV5 wt infection as it only stained pIX protein in the cytoplasm and nucleoplasm excluding the dsDNA-filled LVAC.

4.1.5 Colocalisation analysis reveals limited antibody penetration into LVAC only late in infection

Since a divergence between mCherry-labelled pV and pIX protein signal and pV and pIX antibodies was detected, this phenomenon was further investigated by colocalisation

analyses between the respective fluorescent probes. A549 cells were infected with HAdV5 pV-mCherry or HAdV5 pIX-mCherry, fixed at 24 hpi or 48 hpi and probed with pV and pIX antibodies (Figure 19). The colocalisation of signal was quantified by calculating Pearson's correlation coefficient and Mander's coefficients. The Pearson's correlation coefficient is an indicator of the overall pixel intensity correlation. Mander's coefficients describe the overlap of antibody signal with mCherry signal (M1) and mCherry signal with antibody signal (M2).
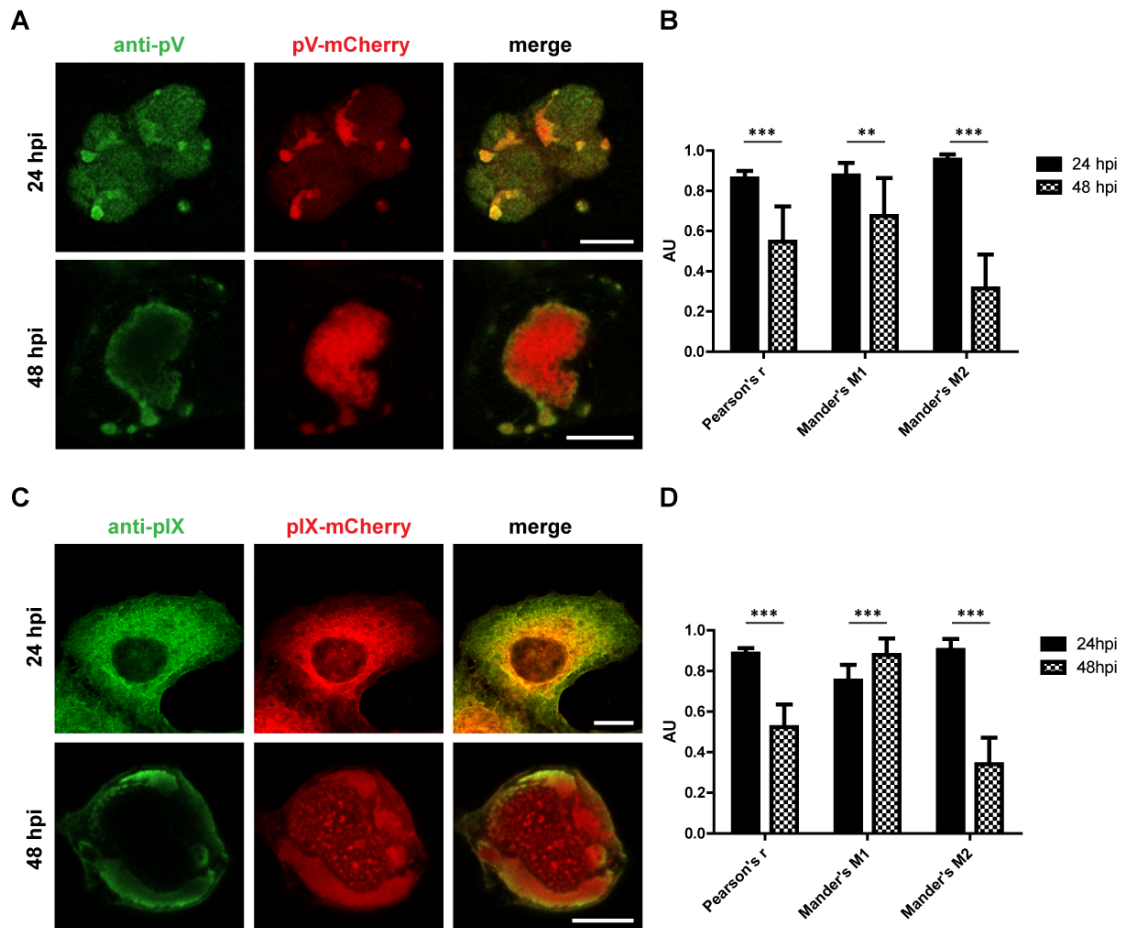
Figure 19: The signal of mCherry fusion constructs and pV and pIX antibody only diverges in late infection. A549 cells were infected with **A)** HAdV5 pV-mCherry and **B)** HAdV5 pIX-mCherry. The cells were fixed at 24 and 48 hpi, stained against pV-mCherry or pIX-mCherry using anti-pV and anti-pIX antibodies and imaged in confocal fluorescence microscopy. A representative cell for both time points of HAdV5 pV-mCherry and HAdV5 pIX-mCherry infection is shown. Scalebars indicate 10 µm. Quantification of mCherry-antibody signal colocalisation for **B)** pV and **D)** pIX as represented by the average Pearson's coefficient r and Mander's coefficients M1 and M2 (n = 12). Statistical significance was calculated using Student's t-test with preceding F-test and is indicated as stars above the bars.

At 24 hpi, the antibody stains showed high colocalisation with the respective fusion proteins. pV measured Mander's coefficients M1 and M2 of 0.88 and 0.95 as well as a Pearson's coefficient of 0.86. pIX measured Mander's coefficients M1 and M2 of 0.75 and 0.90 as well as a Pearson's coefficient of 0.89. These values indicate that areas of high

pV-mCherry signal are likewise populated by pV antibody signal. At 48 hpi, a discrepancy in localisation between pV and pIX antibodies and their respective fusion protein was detected. Interestingly, pV antibody signal still colocalised strongly with pV-mCherry signal, which was indicated by a Mander's coefficient M1 of 0.67. However, inversely, pV-mCherry signal only partially colocalised with pV antibody signal, as shown by a Mander's coefficient M2 of 0.31. Such phenomenon was also observed for pIX. pIX antibody signal still colocalised strongly with pIX-mCherry signal, measuring a Mander's coefficients M1 of 0.88, whereas the inverse relationship was reduced to an M2 of 0.34.

These results confirmed that the mCherry fusion tags successfully indicate the localisation of pV and pIX at early time points in a comparable fashion to pV and pIX antibodies. However, at late stages of infection, the staining capability of both fluorescent probes diverged. At 48 hpi, the antibodies only detected a subpopulation of pV and pIX. The ring stains that were observed indicate that the subpopulation is a spatially more readily accessible fraction of pV and pIX protein. Overall, the fusion tags provided more detail and allowed to uncover structures that were not detectable with the antibodies.

4.1.6 Live-cell imaging captures congregation of pV-mCherry rings to form the LVAC

As a next step, the phenotype progression of infection with both virus mutants was followed by time-lapse confocal spinning-disk fluorescence microscopy. Infected cells were selected at 24 hpi and recorded in 1 h intervals until 48 hpi. The suitability of mCherry fusion tags for live-cell microscopy allowed for recording cellular morphological changes that connected the phenotypes previously recorded at 24 and 48 hpi (Figure 20).

At the start of HAdV5 pV-mCherry imaging, pV mCherry was detected as weak, uniformly dispersed signal throughout the nucleoplasm, only devoid from ring- and dot-like intranuclear areas. Within the first hour of imaging, the pV signal changed localisation and congregated towards the previously devoid ring-structures, thus emulating ring-structures as well as foci in the centre of each ring. These pV-mCherry rings further congregated to a single LVAC, which could be observed at 48 hpi. Intriguingly, the pV intermediate rings resembled the ring structures observed for DBP replication centres in adenovirus infection (POMBO *et al.*, 1994).

At the beginning of the live-cell recording of HAdV5 pIX-mCherry signal, the protein was detected mainly in the cytoplasm. The signal remained in the cytoplasm throughout the entire

imaging period. Inside the nucleus, initially only a weak pIX-mCherry signal was observed. Throughout the progression of infection, the nuclear pIX-mCherry signal intensity increased. pIX-mCherry spots in the LVAC were first observed between 30 and 33 hpi.
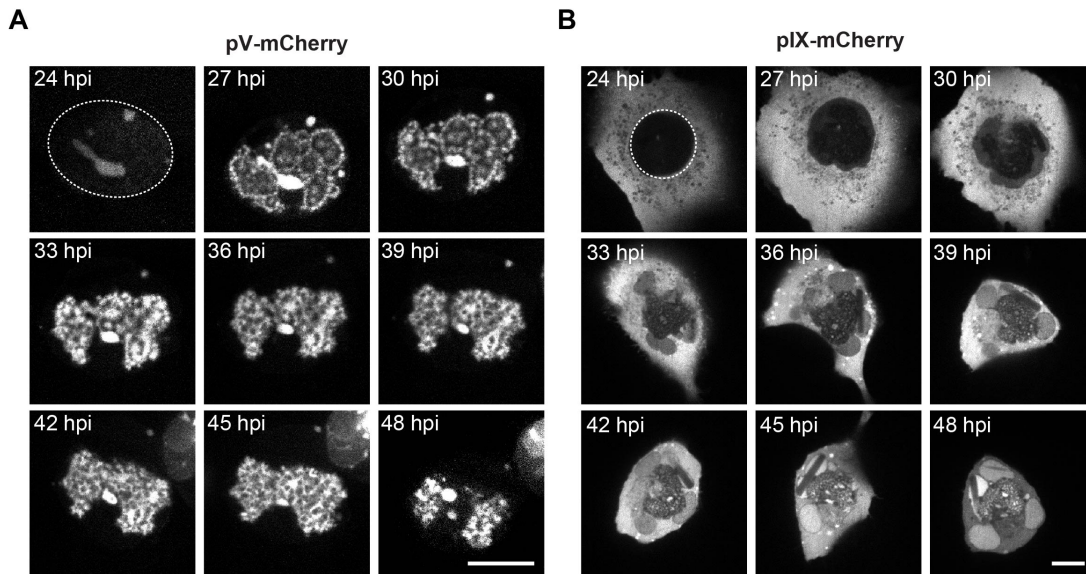
Figure 20: pV forms ring-like structures within the nucleus before congregating into the LVAC, while pIX-mCherry spots appear. Infection progression of a **A)** HAdV5 pV-mCherry and **B)** HAdV5 pIX-mCherry infected cell. The cells were selected for imaging in live-cell spinning-disk confocal fluorescence microscopy at 24 hpi. The initial nuclear boundaries for the HAdV5 pV-mCherry or pIX-mCherry infected cell are visualised as a dashed line. The cells were imaged as z-stack to be able to adjust for z-movement of infected cells. The image histograms along infection progression have been modified to adjust for changes in protein intensity. A representative cell for each condition is shown. Scalebars indicate 10 µm.

Since the formation of pV-mCherry ring-like structures was suspected to be connected to DBP replication centres, this intermediate pV-mCherry phenotype was further analysed with immunofluorescence confocal microscopy to allow for DBP staining. A549 cells were infected with HAdV5 wt and fixed with PFA at 30 hpi. The viral proteins pV and DBP were indirectly stained with antibodies and dsDNA was stained with Hoechst 33342. Cells of interest displaying the pV intermediate phenotype were analysed (Figure 21).

DBP was mainly localised as two phenotypes, including ring-like structures as well as smaller foci within the nucleus. Both Hoechst 33342 signal and pV protein were surrounding these DBP replication centres rings and foci. Thus, the co-immunofluorescence stain indicated that pV-mCherry ring formation is linked to the formation of DBP replication centres in the course of infection.
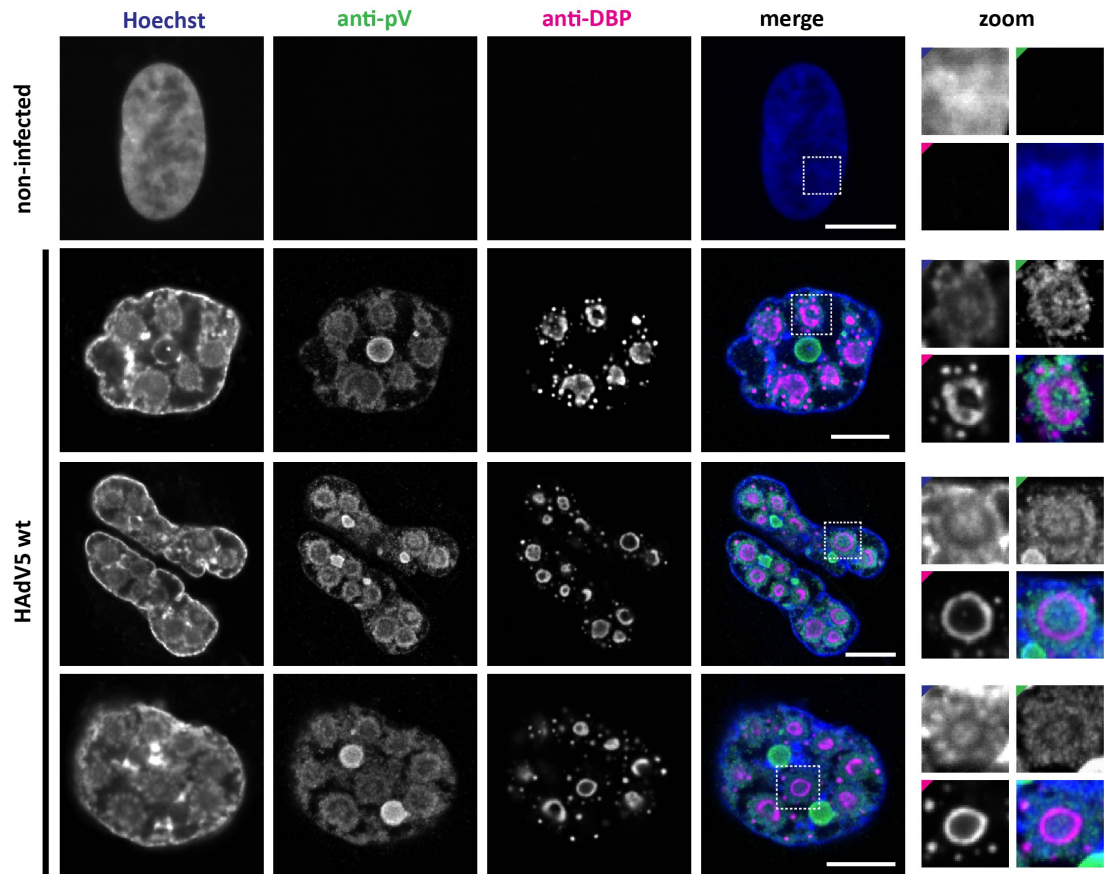
Figure 21: pV-ring formation is linked to DBP replication centres. A549 cells were infected with HAdV5 wt, fixed at 30 hpi, stained with Hoechst 33342 (Hoechst), and immunostained against pV (anti-pV) and DBP (anti-DBP). Selected DBP replication rings are enlarged (zoom) with coloured corners indicating the channel colour. Cells were imaged by confocal laser-scanning fluorescence microscopy. The signal overlap is represented in colour (merge). Three representative cells are shown. Scalebars indicate 10 μm.

4.1.7 The LVAC substructure resembles a honeycomb-like conformation of pV-mCherry and dsDNA surrounding pIX-mCherry spots

The relative localisation of pV-mCherry, pIX-mCherry and dsDNA within the LVAC was further investigated. Upon closer examination, pV-mCherry protein formed a connected protein network with pV-mCherry-free spaces in between. In this way, pV-mCherry resembled a honeycomb. Such honeycomb-like pattern was also populated by dsDNA as indicated by the Hoechst 33342 stain. In contrast, pIX-mCherry spots were detected at dsDNA-free spaces within the honeycomb-like network. To obtain a better picture of the pV-pIX-dsDNA spatial relationship within the LVAC, the colocalisation between pV-mCherry/pIX-mCherry and Hoechst 33342 signals was quantified (Figure 22).
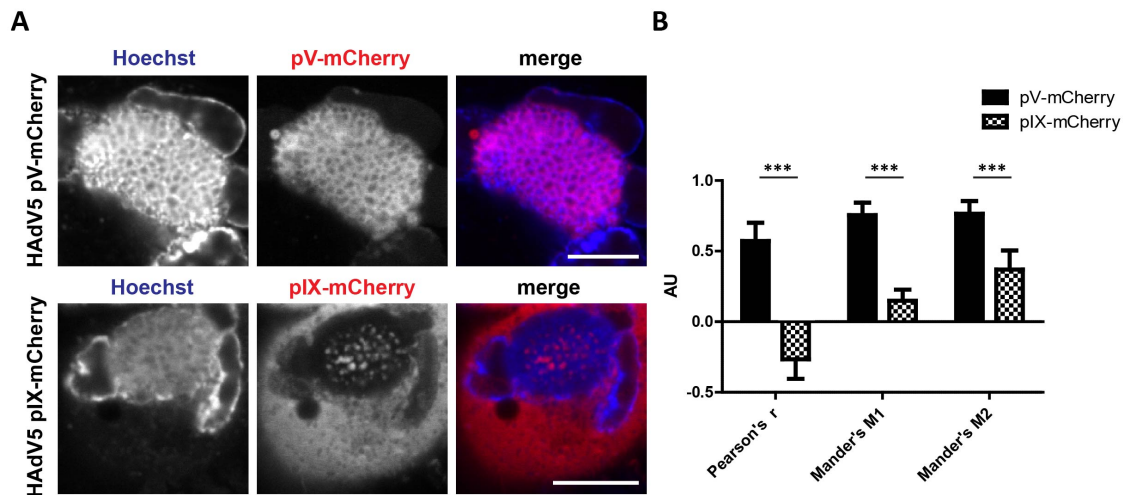
Figure 22: Inside the LVAC, pIX-spots are located within cavities of a dsDNA and pV honeycomb-like organization. A) Colocalisation of pV-mCherry or pIX-mCherry with dsDNA in the LVAC. A549 cells were infected with HAdV5 pV-mCherry or HAdV5 pIX-mCherry. At 48 hpi, the cells were stained with Hoechst 33342 and imaged in confocal laser-scanning live-cell fluorescence microscopy. A representative cell for each virus mutant is shown. Scalebars indicate 10 μm. **B)** Colocalisation quantification between Hoechst 33342 and pV-mCherry or pIX-mCherry signal in the LVAC. The overlap between both signals is represented by the average Pearson's coefficient r and Mander's coefficients M1 and M2 (n = 12). Statistical significance was calculated using Student's t-test with preceding F-test and is indicated as stars above the bars.

pV-mCherry and dsDNA significantly colocalised within the LVAC as shown by Mander's coefficients M1 and M2 of 0.75 and 0.76 as well as a positive Pearson's coefficient r of 0.57. On the contrary, pIX-mCherry and dsDNA significantly populated opposite spaces. Mander's coefficients M1 and M2 of 0.15 and 0.37 were measured, indicating a limited colocalisation of both signals. A Pearson's coefficient r of -0.27 showed a negative correlation between dsDNA and pIX-mCherry spots indicating pIX-mCherry signal to mainly populate the spaces devoid of dsDNA. The colocalisation analysis allowed to reveal indications of spatial interaction between dsDNA and pV-mCherry within the LVAC, as opposed to the spatial separation found between dsDNA and pIX-mCherry.

4.1.8 Correlative light and electron microscopy (CLEM) allows to identify pIX-mCherry spots as paracrystalline virus arrays

So far, the pV-mCherry and pIX-mCherry fluorescent tags allowed to probe the subcellular localisation of both proteins. However, fluorescence microscopy did not allow to ascertain whether the proteins exist as soluble protein, aggregate, or are incorporated into virions. With the aim of identifying the cause of pIX-mCherry spot formation within the LVAC, fluorescence

microscopy (FM) images were correlated with TEM images. For this purpose, A549 cells were infected with HAdV5 pV-mCherry and pIX-mCherry. At 48 hpi, selected cells were imaged as z-stacks by live-cell confocal spinning-disk fluorescence microscopy. The use of cell culture dishes with numbered grid squares allowed for exact identification of the individual cells of interest. After FM imaging, the cells were chemically fixed through addition of GA, embedded in Epon resin and cut into ultrathin 50 nm sections. The exact cells of interests were identified by their position on the cell culture dish grid squares and were selected for TEM imaging. Both TEM and FM images of cells of interest were correlated (Figure 23A & B).

The general cell shape showed slight deviations between FM and TEM imaging, as the cell retained plasticity in the time period between imaging and fixation. Nevertheless, important cellular features such as the position of large protein crystals could be found back in TEM images. These protein crystals appeared as large regular rectangular areas devoid of mCherry signal in FM images and as large regular rectangular areas consisting of a crystalline pattern in TEM images. As was the case for the overall cellular shape, the fine structure of the nuclear envelope showed some differences between both FM and TEM images. However, the overall kidney shape of the nuclear membrane was the same. In TEM, the LVAC could be identified by a difference in protein/DNA composition in the nucleoplasm which was made visible as a darker TEM stain.

In both HAdV5 pV-mCherry-infected and HAdV5 pIX-mCherry-infected cells, fully assembled virions could be detected within the LVAC (Figure 23Aiii & Biii). Interestingly, the majority of virions within the LVAC were grouped in a pattern of specific regular paracrystalline virus arrays of varying size and shape. Outside the LVAC, virions were detected as individual dispersed particles throughout the nucleus as well as in some cases as paracrystalline arrays positioned at the nuclear envelope (Figure 23Aiv). Comparison between the fluorescence microscopy images of HAdV5 pIX-mCherry suggested that the paracrystalline arrays are found in positions where pIX mCherry spots were detected. The spots of pIX-mCherry could therefore be caused by a local concentration of pIX-mCherry protein, incorporated within fully formed virus capsids. Other non-correlatively imaged cells in TEM also showed the same phenotype of paracrystalline arrays within the nucleus (Figure 23C).
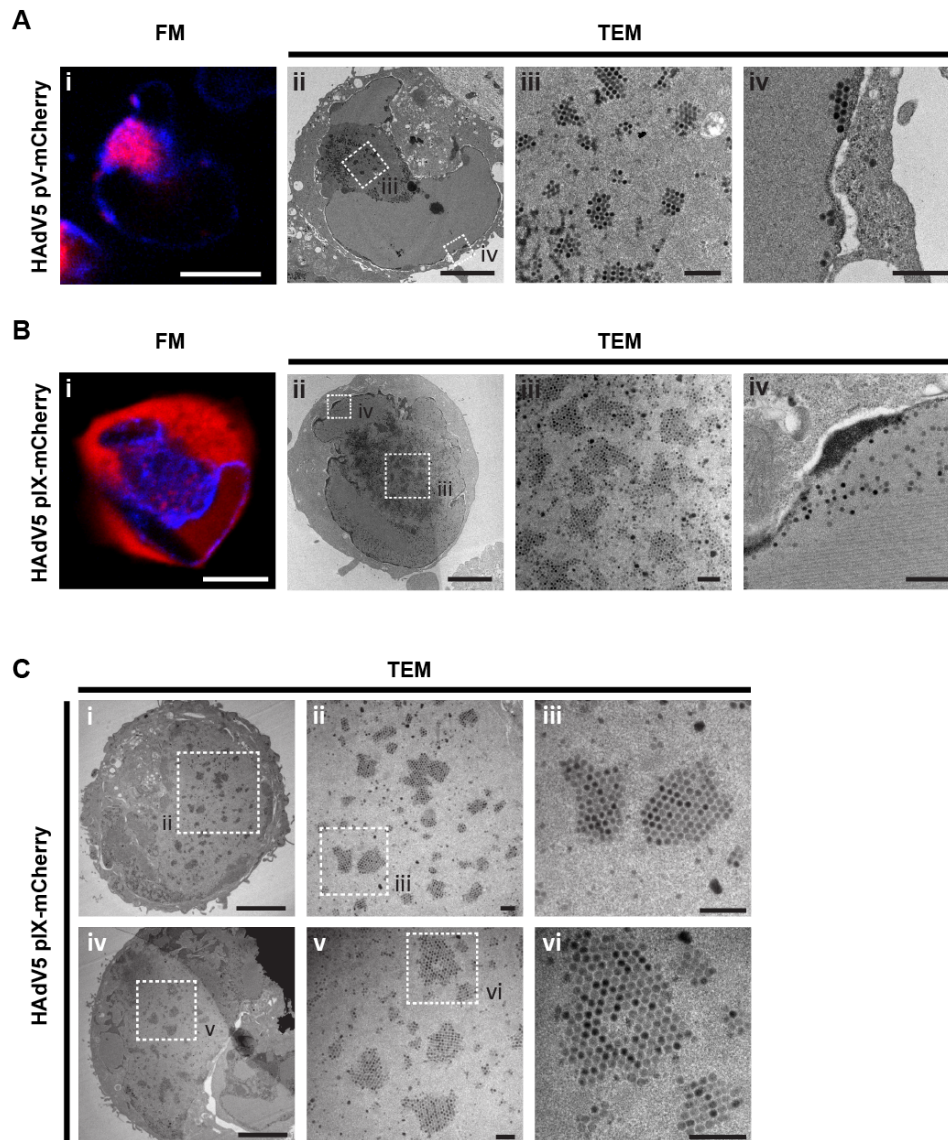
Figure 23: Paracrystalline virus arrays form within the LVAC and correspond to the pIX-mCherry spots found in the LVAC. Representative A549 cell infected with **A)** HAdV5 pV-mCherry and **B)** HAdV5 pIX-mCherry. Both cells show paracrystalline virus arrays within the LVAC. The cells were stained with Hoechst 33342 and imaged by live-cell spinning-disk confocal fluorescence microscopy at 48 hpi (FM). Immediately after imaging, the cells were fixed and prepared for TEM. 50 nm sections of the epon-embedded cells were imaged by TEM (TEM). FM cell overviews are shown in images i) with Hoechst 33342 in blue and pV-mCherry and pIX-mCherry in red. TEM cell overviews are shown in images ii) including scalebars indicating 5 µm. Higher magnification images of areas of interest are shown in images iii) and iv) for both sections A) and B) including scalebars indicating 0.5 µm. Scalebars for fluorescence images indicate 10 µm. **C)** Non-correlative TEM images of A549 cells infected with HAdV5 pIX-mCherry. These cells also show the phenotype of paracrystalline arrays forming within the nucleus. Scalebars of images i) and iv) indicate 5 µm, scalebars of images ii, iii, v and vi indicate 0.5 µm.

Since slight changes in cell morphology occurred between imaging and subsequent fixation in the first version of the correlative light and electron microscopy (CLEM) protocol, which only allowed a general comparison of an overlay of both images, a second modified correlation experiment was performed. Importantly, infected A549 cells were first fixed in

PFA and GA to prepare them for serial block-face SEM and only after initial fixation were imaged by spinning-disk confocal FM at 42 hpi. Subsequently, the cells were contrasted and imaged by serial block-face SEM. Individual sections of the SEM 3D data set were overlaid with the appropriate slice through the 3D light microscopy data set (Figure 24).
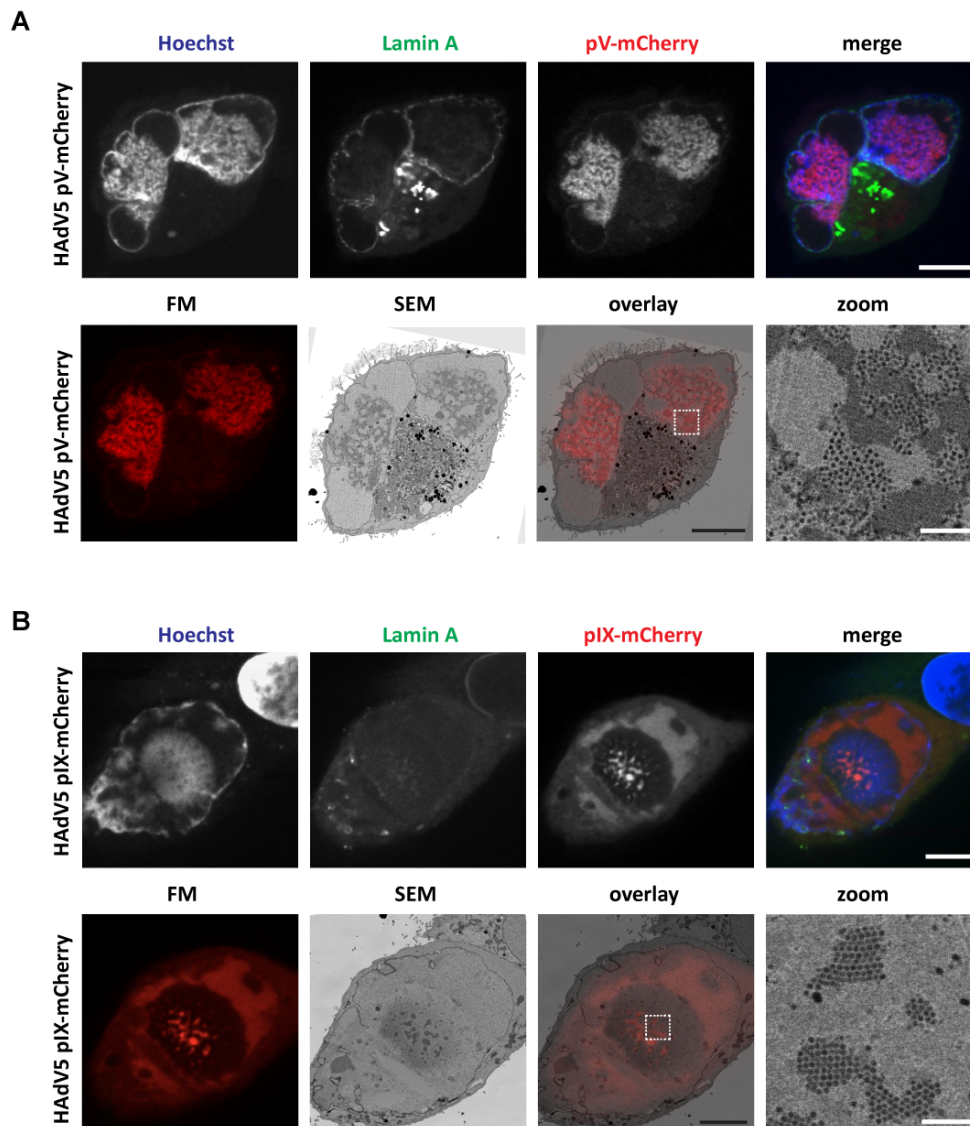
Figure 24: **Chemical fixation of cells before FM and TEM imaging allows CLEM and strong correlation between pIX-mCherry spots and paracrystalline arrays.** Representative A549 cell infected with **A)** HAdV5 pV-mCherry and **B)** HAdV5 pIX-mCherry. The cells were fixed with PFA and GA, stained with Hoechst 33342 and z-stacks were recorded by confocal spinning-disk fluorescence microscopy at 42 hpi. The dsDNA signals is represented by Hoechst 33342 stain (Hoechst). The nuclear lamina is represented by an mTagGFP-nanobody recognising lamin A (Lamin A). pV and pIX localisation is detected through the viral pV-mCherry and pIX-mCherry fusion construct (pV-mCherry/pIX-mCherry). The FM signal overlap is shown in colour (merge). After fluorescence microscopy imaging, the cells were prepared for serial block-face SEM and a 3D SEM image was recorded. A 2D slice of the fluorescence microscopy image of the mCherry channel (FM) is compared with a suitable z-slice of the electron microscopy image (SEM) by superimposing both images (overlay). An enlarged region is shown (zoom). Scalebars indicate 10 µm for overview images and 1 µm for zoom images.

The change in preparation and imaging sequence allowed for very fine correlation between light and electron microscopy images. In infection with HAdV5 pV-mCherry, the darker EM stain within the LVAC was correlated with the pV-mCherry red fluorescence signal of the FM image (Figure 24A). These areas appeared darker than in the previous TEM experiment, potentially due to the difference in contrasting protocol between TEM and SEM staining. In infection with HAdV5 pIX-mCherry, the identity of pIX-mCherry spots as paracrystalline arrays could be confirmed, since both signals in FM and SEM highly overlapped (Figure 24B).

4.1.9 Generation of a pIX fluorescent labelling toolset

Labelling pIX with fluorophores of different photoreactive characteristics is of interest to further analyse the mobility of pIX-spots and achieve co-labelling with other viral proteins such as pV or DBP. To allow for easier generation of these mutants, a cloning toolset was generated. The toolset required PCR amplification and ligation of the desired fluorophore orf into a recombination vector instead of requiring costly synthesis of the fluorescent protein flanked by long homologous repeats. First, both 400 bp homologous sites flanking the pIX gene were PCR-amplified. Primers were used to add the restriction sites EcoRV and BamHI to homologous site 1 (Hom1) and EcoRI and EcoRV to homologous site 2 (Hom2). These sites were ligated into a pcDNA3 vector to generate the pcDNA3 Hom1+2 vector. The desired fluorescent proteins of interest can then be PCR-amplified with primers adding the BamHI and EcoRI restriction sites to the N- and C-terminus of the protein which allowed for its ligation into the pcDNA Hom1+2 vector. The resulting protein includes the same linker region between pIX and the fluorophore as was used for the original pIX-mCherry construct with the exception of two amino acids that were introduced by the BamHI restriction site. The resulting final fluorescent protein construct is flanked by HAdV5 homologous sites on either end, can be excised by restriction digestion with EcoRV and can then be used for the second homologous recombineering step (Figure 25A).

This procedure was used to fluorescently label pIX with the fluorescent proteins mNeonGreen, mEos4a and PA-TagRFP. mNeonGreen was used to generate two double-labelled HAdV strains, HAdV5 pV-mCherry pIX-mNeonGreen and HAdV5 DBP-mCherry pIX-mNeonGreen. The fluorophores mEos4a and PA-TagRFP have photoactivation and photoswitching properties. PA-TagRFP is non-fluorescent in its naturally expressed form. Upon irradiation with light at 405 nm, the protein becomes activated and is

red-fluorescent (SUBACH *et al.*, 2011). mEos4a is green-fluorescent in its naturally expressed form. Irradiation with light at 405 nm causes the fluorophore to switch to a red-fluorescent state (SEGALA *et al.*, 2015). In this way, regions of interest of labelled pIX protein can selectively be activated and imaged in live-cell fluorescence microscopy. To test the photoswitching and photoactivation properties of PA-TagRFP and mEos4a, A549 cells were infected with either virus mutant, stained for dsDNA using DRAQ5 and imaged at 48 hpi. Cells which displayed an LVAC were irradiated at a wavelength of 405 nm (Figure 25B/C).
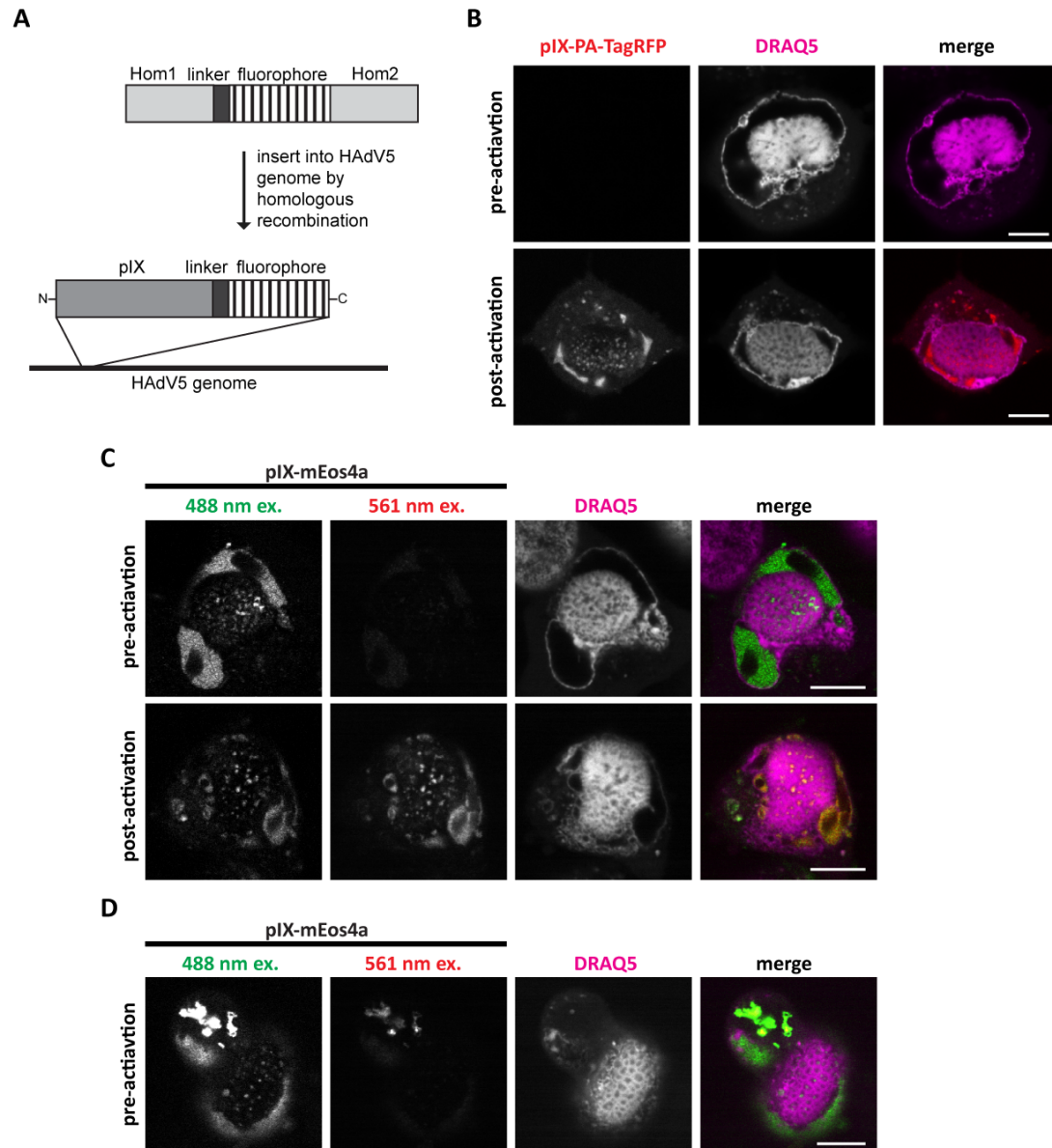
Figure 25: LVAC forms in infection with HAdV5 pIX-mEos4a and HAdV5 pIX-PA-TagRFP and both proteins display functional photoactivation. A) Photoactivation of pIX-PA-TagRFP via irradiation at 405 nm. The LVAC is visible via dsDNA localisation and pIX-PA-TagRFP spots appeared post-activation. **B)** Photoactivation of pIX-mEos4a via irradiation at 405 nm. The LVAC is visible via dsDNA localisation and pIX-mEos4a spots when imaged at 488 nm. The identical pIX-mEos4a spots appeared when imaged at 561 nm post-activation. **C)** Infection with HAdV5-mEos4a can lead to induction of bright fluorescent aggregates in a number of cells. The formation of aggregates did not appear to hinder LVAC formation. The dsDNA signal is represented by DRAQ5 stain (DRAQ5). pIX localisation is detected through the viral pIX-mEos4a or pIX-PA-TagRFP fusion construct (pV-mEos4a/pIX-PA-TagRFP). Acquisition of pIX-mEos4a was either performed by excitation at 488 nm or 561 nm (488 nm ex./ 561 nm ex.). The signal overlap is represented in colour (merge). Scalebars indicate 10 μm.

For HAdV5 pIX-mEos4a-infected cells, the LVAC was visible in the green channel, whereas for HAdV5 pIX-PA-TagRFP-infected cells the LVAC was detected only by the dsDNA stain. Prior to activation of pIX-PA-TagRFP, no pIX signal could be observed. After activation, clear pIX spots

could be detected within the LVAC. Apart from pIX spots, strong pIX signal was detected outside of the LVAC whereas pIX signal was only weak outside of the nucleus. Before photoswitching of pIX-mEos4a, the signal could be detected by excitation with the 488 nm laser. pIX spots as well as pIX signal outside of the LVAC were visible. Only weak pIX signal was observed outside the nucleus. After photoswitching, the LVAC could still be detected by excitation with the 488 nm laser, indicating that not all fluorophores were switched. Additionally, excitation at 561 nm allowed detecting the LVAC in a different imaging channel. Importantly, HAdV5 pIX-mEos4a infection resulted in a frequent occurrence of aggregates of labelled protein in the cytoplasm (Figure 25D). These aggregates were strongly fluorescent and were not detected in infection with pIX-mCherry or pIX-PA-TagRFP. The appearance of these aggregates did not affect LVAC formation.

4.1.10 Labelling pIX spots with photoswitchable fluorophores and FRAP analysis shows low mobility of HAdV5 paracrystalline arrays

pV-mCherry and pIX-mCherry within the LVAC of infected cells were probed by fluorescence recovery after photobleaching (FRAP) experiments to characterise the protein mobility within the compartment. FRAP is based on a short and focussed laser pulse that is aimed at a region of interest (ROI), which causes bleaching of fluorophores located within the ROI. After ROI irradiation, the temporal changes in fluorophore signal were recorded and compared to reference areas (Figure 26A). Individual pIX-mCherry spots, as well as pV-mCherry regions within the LVAC, were chosen for FRAP irradiation. The recovery of fluorescence signal was recorded for 2 min after bleaching and compared to fluorescence changes in a background ROI and non-bleached ROI to yield a relative fluorescence intensity change over time. Analysis of the fluorescence curve provides information about the mobile fraction in the population of protein of interest and the motility as given by the half-time of recovery (Figure 26B).

pIX-mCherry spots only slowly recovered after bleaching. Curve fitting showed the mobile fraction of pIX-mCherry to be 22 %, which indicated that a major fraction of the protein was immobilised within the LVAC spots and that there was only a limited exchange with the non-bleached surrounding pIX-mCherry population. Bleaching of pV-mCherry showed the protein to have different recovery properties than pIX-mCherry. The majority of the fluorescence signal recovered which corresponded to a mobile fraction of 80 %. Therefore, only a small fraction of pV-mCherry appeared to be immobilised within the honeycomb-like organisation and was not

capable of being replaced by the surrounding non-bleached pV-mCherry pool. Interestingly, despite the different mobile fractions, both proteins displayed similar half times of recovery, which were measured as 20 sec for pIX-mCherry and 18 sec for pV-mCherry. Accordingly, the exchange kinetics of both populations of fusion protein, appear to behave similarly within the LVAC.

Next, the mobility of entire paracrystalline virus arrays within the LVAC was analysed by live-cell confocal fluorescence microscopy. For this purpose, A549 cells were infected with HAdV5 pIX-mCherry, cells showing pIX-mCherry spots were selected and imaged over 54 min or 9 h, respectively. Over the shorter time period of 54 min, the position of pIX-mCherry spots remained stationary (Figure 26C). When imaged over multiple hours, the pIX-mCherry spots slightly shifted position within the LVAC, but did not show a high degree of mobility (Figure 26D).

To confirm the previous results that pIX spots display relatively low motility within the LVAC, live-cell confocal fluorescence microscopy was repeated in infection with HAdV5 pIX-mEos4a and HAdV5 pIX-PA-TagRFP (Figure 27). Selective photoactivation of individual pIX spots was shown to be possible by either direct selection and activation of pIX-mEos4a spots in the 488 nm channel or by targeting the empty spaces within dsDNA honeycomb of LVAC for pIX-PA-TagRFP. After a quick irradiation pulse at 405 nm, selected pIX spots were visible. (Figure 27A/B). To avoid the addition of the intercalating agent DRAQ5 prior to extended live-cell imaging, which was shown to cause cytotoxicity (Zhao *et al.*, 2009), HAdV5 pIX-mEos4a was selected over HAdV5 pIX-PA-TagRFP for imaging the movement of pIX spots over a period of 18 h (Figure 27C). During this time, the activated pIX spots did not escape the LVAC and showed very little movement relative to the position of the LVAC.
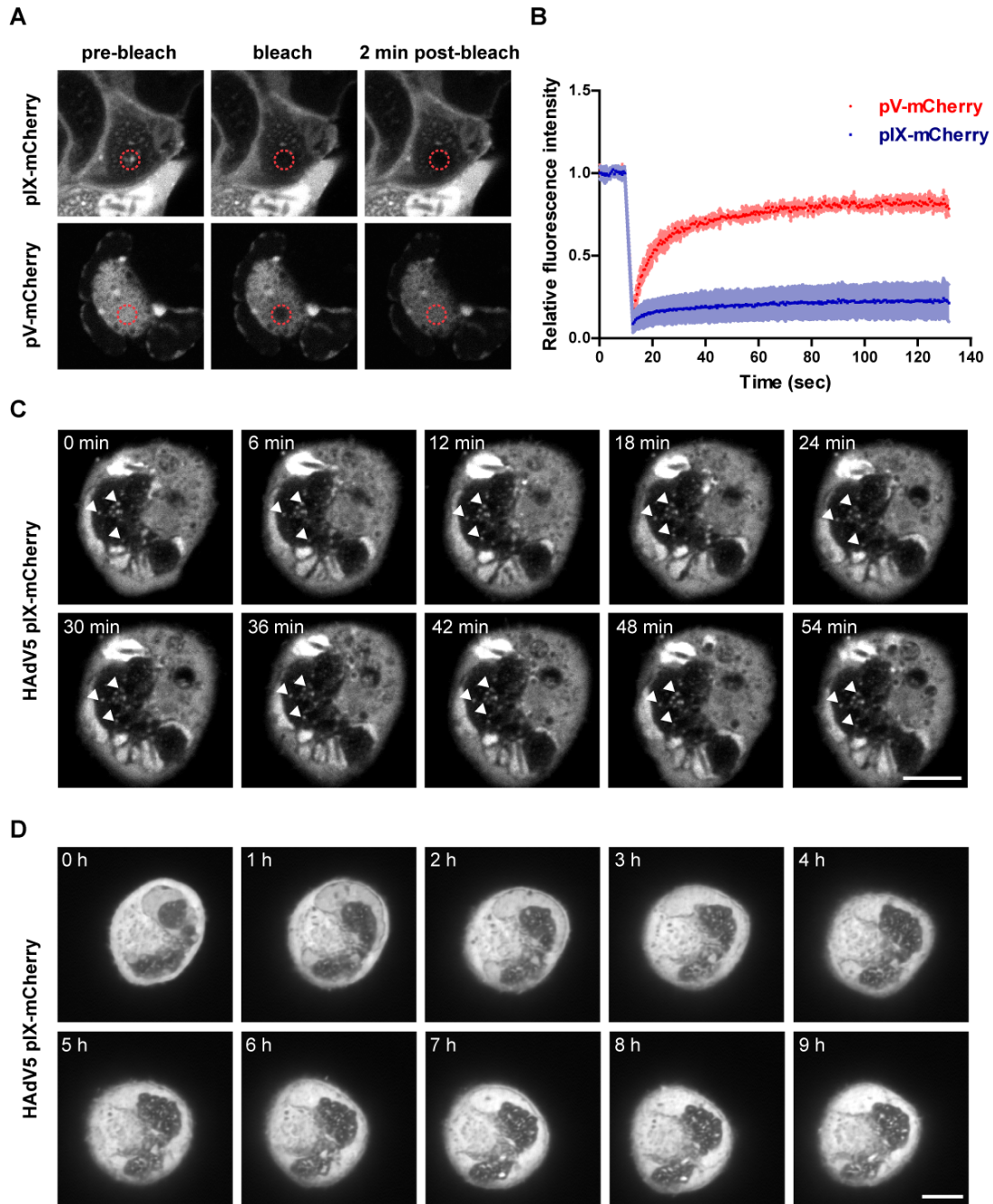
Figure 26: The paracrystalline virus arrays are highly immobile within LVAC and show little signal recovery after photobleaching. A) Overview of FRAP laser bleaching of pV-mCherry and pIX-mCherry signal within LVAC constituents in A549 cells infected with HAdV5 pV-mCherry and HAdV5 pIX-mCherry. A dashed red circle is indicating the laser target area for signal bleaching. A representative cell per virus strain is shown before bleaching (pre-bleach), at the time-point of bleaching (bleach) and after 2 min recovery (2 min post-bleach). **B)** Quantification of FRAP signal recovery. The relative fluorescence intensity is plotted against time. The average signal change is indicated (n = 6) with the standard deviation indicated as coloured underlying area. **C/D)** Time-lapse live-cell fluorescence microscopy analysis of A549 cells infected with pIX-mCherry. The position of paracrystalline virus arrays (pIX-mCherry spots) remained largely unchanged over 54 min (indicated by white arrows) and only slowly shifted in the course of multiple hours. Images in D) were denoised using the Noise2Void algorithm (KRULL *et al.*, 2018). Scalebars indicate 10 µm.
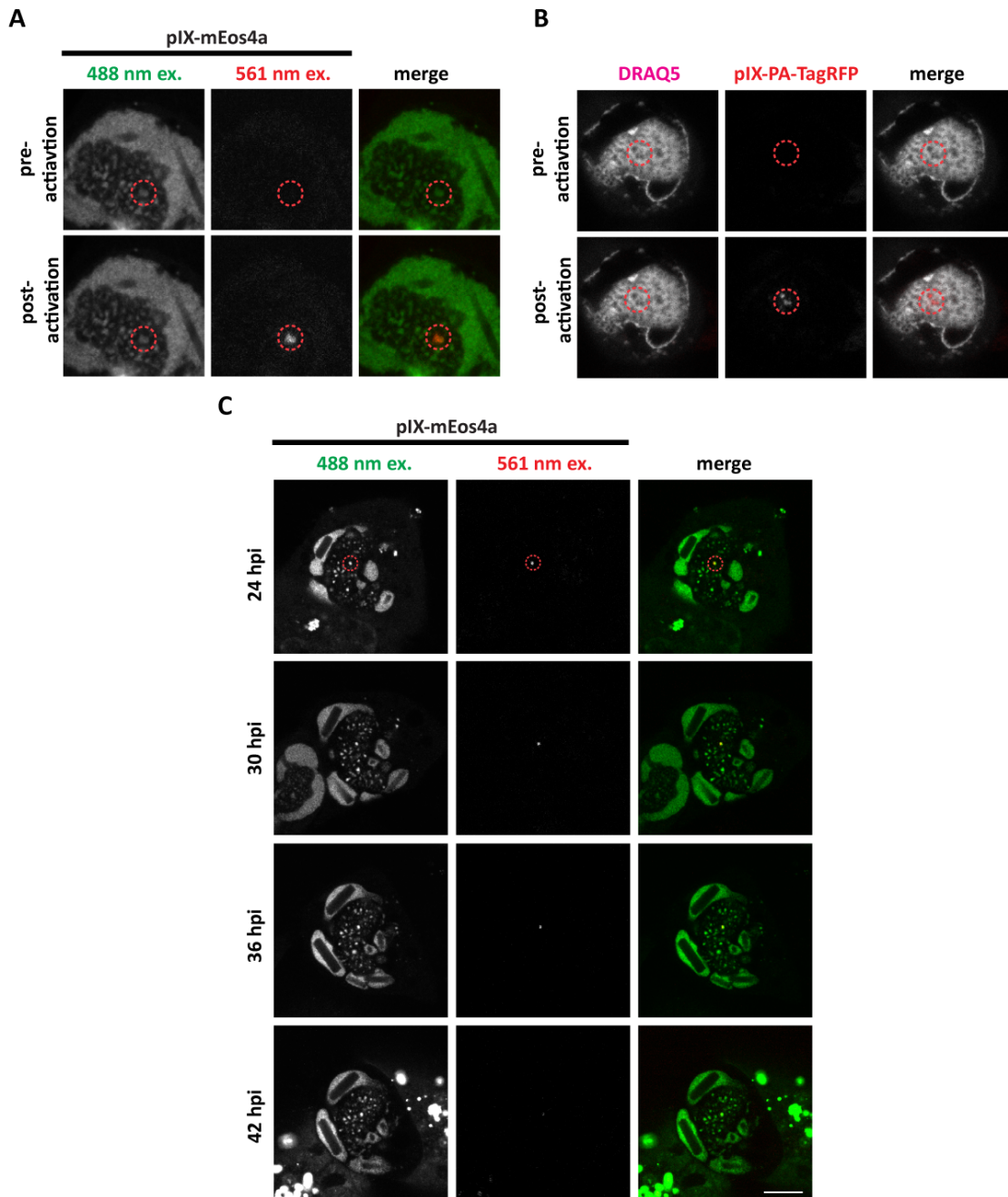
Figure 27: Selective photo-activation confirms pIX-mEos4a spots to display low mobility within LVAC. A) Selective activation of pIX-mEos4a spots within the LVAC. Prior to activation, the spots are visible at 488 nm excitation. After selective activation within a small ROI (red circle), a pIX-spot is visible through excitation at 561 nm. **B)** Selective activation of pIX-PA-TagRFP spots within the LVAC. Prior to activation, no pIX spots are visible and their position can only be estimated by the gaps within the dsDNA (DRAQ5). After selective activation within a small ROI (red circle), a pIX-spot is visible through excitation at 561 nm. **C)** Live-cell time-lapse imaging of a photoactivated pIx-mEos4a spot within the LVAC over 16 h starting at 24 hpi. The activated spot remains within the LVAC. Scalebars indicate 10 μm.

4.1.11   Double-labelled HAdV5 pV-mCherry pIX-mNeonGreen mutant confirms LVAC spatial organisation

The relative colocalisation of pV and pIX in comparison to the dsDNA honeycomb was previously analysed (see Section 4.1.7). However, a simultaneous co-stain of pV and pIX was neither achievable with the single fluorescently tagged virus mutants nor with antibody co-labelling due to the penetration restrictions of antibody labelling.   Thus, the new pIX-labelling toolset was used to generate the double mutant HAdV5 pV-mCherry pIX-mNeonGreen. The double-labelled mutant showed reduced growth and did not reach titres comparable to the single-labelled fusion mutants.   Nonetheless, A549 cells were infected and analysed by live-cell confocal fluorescence microscopy (Figure 28).
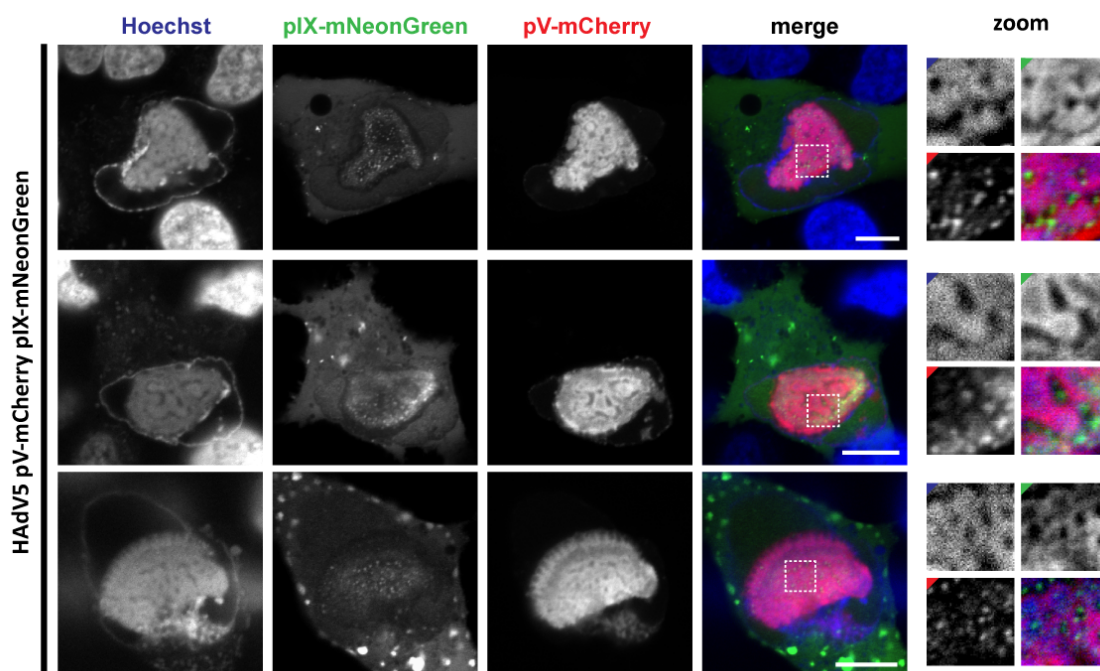
Figure 28: Double-labelled virus HAdV5 pV-mCherry pIX-mNeonGreen forms LVAC and confirms pIX-spots to sit within pV honeycomb-like structure. A549 cells were infected with the double mutant HAdV5 pV-mCherry pIX-mNeonGreen and imaged at 48 hpi. A region of the LVAC is enlarged (zoom) showing pIX-mNeonGreen spots to populate the cavities of the pV-mCherry honeycomb. Coloured corners indicate the channel colour. Three representative cells are shown. Scalebars indicate 10 μm.

At 48 hpi, the infection with HAdV5 pV-mCherry pIX-mNeonGreen resulted in the formation of an LVAC, as shown by the formation of a dsDNA honeycomb. As in wt infection, some dsDNA was found marginalised to the inner edge of the nuclear envelope. Similar to HAdV5 pIX-mCherry infection, pIX-mNeonGreen was expressed throughout the cytoplasm and the nucleus. Additionally, pIX-mNeonGreen spots were found within the empty cavities

of the dsDNA honeycomb, even though their size appeared to be reduced. Similar to the single labelled HAdV5 pV-mCherry mutant, pV-mCherry still localised to the LVAC in the double-labelled mutant. As dsDNA, pV-mCherry showed a honeycomb-like distribution and overlapped with the Hoechst 33342 signal. Enlargement of sections of the LVAC clearly showed the pIX-mNeonGreen spots to sit within the pV-mCherry. In this way, the double-labelled mutant confirmed the previous suggestion of the LVAC architecture.

4.1.12 Double-labelled HAdV5 DBP-mCherry pIX-mNeonGreen does not allow to reveal DBP localisation within LVAC

All previous immunofluorescence microscopy experiments at 48 hpi have shown DBP to localise as a ring of individual DBP spots around the LVAC. However, limited antibody penetration of pV and pIX antibodies gave rise to the hypothesis that DBP can also be found within the LVAC. To test this hypothesis, the pIX labelling toolset was used to generate a double-labelled HAdV5 DBP-mCherry pIX-mNeonGreen. Similar to the double-labelled HAdV pV-mCherry pIX-mNeonGreen (see Section 4.1.11), this double-labelled mutant showed reduced growth and did not reach titres comparable to the single-labelled fusion mutants. Nevertheless, A549 cells were infected with the single labelled HAdV5 DBP-mCherry and the double-labelled HAdV5 DBP-mCherry pIX-mNeonGreen and imaged by live-cell spinning-disk confocal fluorescence microscopy at 48 hpi (Figure 29).

At 24 hpi, cells infected with the single-labelled HAdV5 DBP-mCherry virus showed an intact nuclear lamina and partially marginalised dsDNA. DBP-mCherry was localised as small foci and large protein-filled regions. Interestingly, the DBP-mCherry signal occupied larger areas of nucleus than was previously observed for wt protein, which displayed a higher number of smaller rings and foci. At 48 hpi, the nuclear lamin A signal was strongly reduced. DBP-mCherry protein localised as a large non-structured area in the nucleus. Importantly, no honeycomb of dsDNA was visible. At this time-point, the double-labelled HAdV5 DBP-mCherry pIX-mNeonGreen showed a similar distribution of DBP-mCherry as was detected for the single labelled virus. DBP-mCherry occupied a large area of the nucleus but did not take up a particular structure. dsDNA was not detected in a honeycomb-like conformation. Instead, it mainly localised in areas devoid of DBP-mCherry. pIX-mNeonGreen signal was detected in the cytoplasm with some strongly fluorescent foci in the perinuclear region. However, generally, a lower fluorescence level of pIX-mNeonGreen protein was detected in the nucleus and no pIX-mNeonGreen spots were detected.

Overall, labelling with DBP-mCherry did not display the phenotype of the LVAC at 48 hpi since no dsDNA honeycomb, DBP foci surrounding an LVAC or pIX spots were detected within the nucleus. Therefore, it did not appear as a suitable system to study DBP localisation at late states of HAdV5 infection.
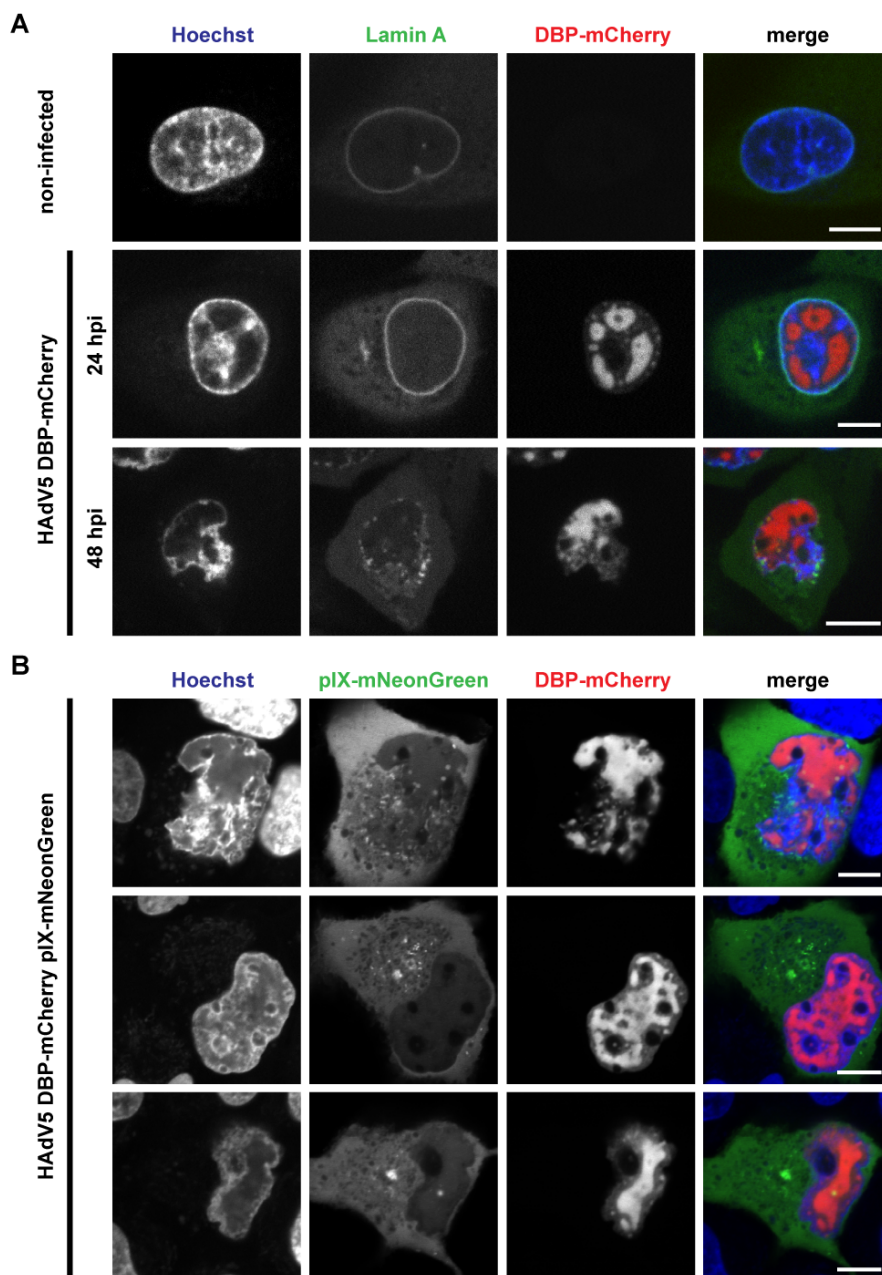
Figure 29: LVAC formation cannot be detected when infecting with DBP-mCherry labelled virus mutants. A) The infection of A549 cells with HAdV5 DBP-mCherry was analysed at 24 hpi and 48 hpi. A representative cell is shown for each condition. **B)** The formation of pIX-mNeonGreen spots was analysed in infection with the double mutant HAdV5 DBP-mCherry pIX-mNeonGreen. Three representative cells are shown. The cells were imaged by live-cell confocal spinning-disk fluorescence microscopy. The dsDNA signal is represented by Hoechst 33342 stain (Hoechst). The nuclear lamina is represented by an mTagGFP-nanobody recognizing lamin A (Lamin A). pIX localisation is detected through the viral pIX-mNeonGreen fusion construct (pIX-mNeonGreen). DBP localisation is detected through the viral DBP-mCherry fusion construct (DBP-mCherry). The signal overlap is represented in colour (merge). Scalebars indicate 10 μm.

4.1.13 DBP spots are likely populating space within pV honeycomb

A DBP-mCherry fluorescent fusion label was not successful to indicate the localisation of DBP within the LVAC since it caused DBP to localise differently than in HAdV5 wt infection and stopped the LVAC from forming. Instead, DBP protein was visualised by serial block-face SEM and compared to the DBP phenotype in immunofluorescence microscopy (Figure 30).

At 24 hpi, DBP can be found as replication rings, as shown by a single z-slice through a 3D fluorescence volume (Figure 30A). At 48 hpi, DBP was detected as a ring of individual foci, when imaging a z-slice in the centre of the LVAC. The periphery of the DBP ring can be visualised in a different z-slice. Here, multiple adjacent DBP foci covered a larger area in x and y (Figure 30B). These DBP replication centres can also be detected by serial block-face SEM. Here, DBP was detected as intranuclear rings of higher electron density than the surrounding nucleoplasm (Figure 30 C). At this stage of the infection, a few progeny virions were detected around the DBP replication ring. In cells containing an LVAC, protein spots of similar electron density were detected at the periphery of the LVAC (Figure 30D). Importantly, in a z-slice through the centre of the LVAC these spots were detected in multiple layers and not just as a single circle, as was indicated by fluorescence microscopy. In both slices, groups of progeny virions were found in close proximity to these protein spots. This experiment suggested the LVAC to be filled by DBP replication centres rather than being surrounded by a single ring of DBP replication spots as was previously shown by immunofluorescence microscopy.
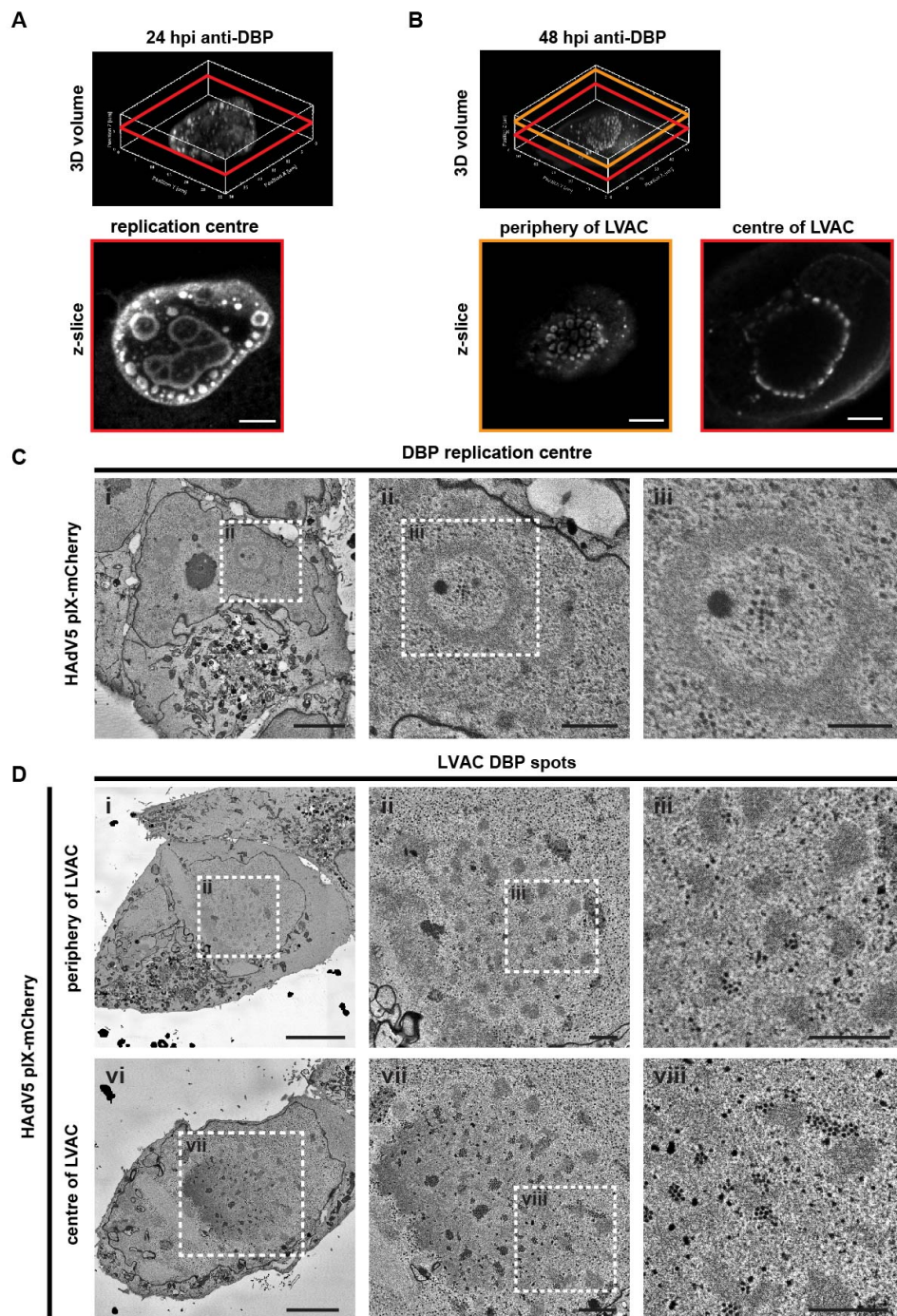
Figure 30: DBP replication foci intersperse LVAC and do not localise as a single ring of spots. DBP replication centres were analysed by IF microscopy and serial block-face SEM at 24 hpi and 48 hpi. **A)** DBP replication at 24 hpi. A 3D volume of an HAdV5-infected cell was recorded. A single z-slice of the 3D volume (red square) shows DBP to be localised as multiple rings. **B)** DBP replication foci at 48 hpi. A 3D volume of an HAdV5-infected cell including an LVAC was recorded. A single z-slice of the 3D volume at the periphery of the LVAC shows the DBP foci to be sitting adjacent to each other (orange square). A single z-slice of the 3D volume at the centre of the LVAC shows the DBP foci to be localised as a one-layered ring around the LVAC (red square). **C)** Serial block-face SEM z-slice of a cell displaying replication rings. The protein is visible as dark rings. **D)** Serial block-face SEM z-slices at the periphery and centre of an LVAC. At the periphery, dark protein foci are localised as adjacent spots. At the centre of the LVAC these spots do not localise a single-layered ring, but instead intersperse the LVAC. The fluorescence image scale bars indicate 5 μm, The SEM overview scale bars indicate 5 μm. Zoomed images are indicated by a white, dashed square and the scalebars indicate 2 μm.

4.2 Nuclear egress of adenovirus particles

4.2.1 Expression of adenovirus death protein facilitates release of infectious virus particles

The egress of HAdV5 particles has been described to be linked to the HAdV5 10.5 kDa protein ADP (DORONIN *et al.*, 2003; TOLLEFSON *et al.*, 1996a,b). However, the mechanism of ADP function is now known. Here, the protein was bioinformatically analysed for post-translational modifications (PTMs) and motifs that can give a hint towards its mechanism of function (Figure 31).

Figure 31: HAdV5 ADP protein is predicted to by glycosylated, palymitoylated and has a single transmembrane region. A) Overview of the ADP protein sequence including confirmed and putative PTMs and domains. ADP is a short protein of 93 amino acids consisting of a single-spanning transmembrane domain. A basic region in the cytoplasmic domain could act as nuclear localisation signal and the N-terminal region of ADP is predicted to possess intrinsically disordered properties. Single posttranslational modifications are predicted to consist of N-glycosylation at residue Asn3, O-glycosylation at residues Thr2, 4, 5, 11, 14, 16 and 17 and palmitoylation at residues Cys53 and Cys54. **B)** The ADP transmembrane helix has a hydrophobic surface and does not possess amphipathic properties. Small amino acids (Gly, Ala) are coloured in grey, hydrophobic amino acids are coloured in yellow and hydrophilic amino acids are coloured in red. Structural and PTM predictions were run using GPS-Lipid (XIE *et al.*, 2016), Heliquest (GAUTIER *et al.*, 2008), JPred (DROZDETSKIY *et al.*, 2015), NetOGlyc (STEENTOFT *et al.*, 2013), PrDOS (ISHIDA and KINOSHITA, 2007) and SPRINT-Gly (TAHERZADEH *et al.*, 2019).

ADP has a single transmembrane domain including two predicted palmitoylation sites at residues Cys53 and Cys54 for further anchoring in the membrane. The lumenal N-terminal side has predicted PTMs including N-glycosylation at residue Asn3 and O-glycosylation at residues Thr2, 4, 5, 11, 14, 16 and 17. The luminal N-terminus is predicted to be intrinsically disordered and a basic, proline-rich region in the cytoplasmic domain could act as a nuclear

localisation signal. The position and properties of the amino acid residues within the transmembrane domain were analysed but did not show properties of amphipathic helices. Amphipathic helices in viral proteins have been shown to lead to membrane pore formation aiding the release of viral particles (LEE *et al.*, 2008; RAGHAVA *et al.*, 2011; GIORDA *et al.*, 2013).

To test the effect of ADP expression on the release of virus particles, virus titre growth curves were measured. The usual laboratory HAdV5 strain has a deletion in the E3 region since most of the E3 proteins are required for host cell immune evasion and are not necessary for cell culture systems. This HAdV5 ΔE3 strain is labelled HAdV5 ADP– in this work. For expression of ADP, the protein was reinserted in the E3 region by homologous recombineering in *E. coli* (WANG *et al.*, 2014). Virus particles were generated by transfection of the linearised viral genome including ADP into H1299 cells. The virus strain was passaged three times by infection of A549 cells with infection supernatant of the previous infection cycle. The resulting strain was labelled HAdV5 ADP+. For virus release growth curves, A549 cells were infected and the supernatant medium was collected every 24 hpi from 0 hpi to 96 hpi. The titre of each supernatant was determined by FACS analysis of A549 cells infected with serial dilutions of the supernatant (Figure 32).
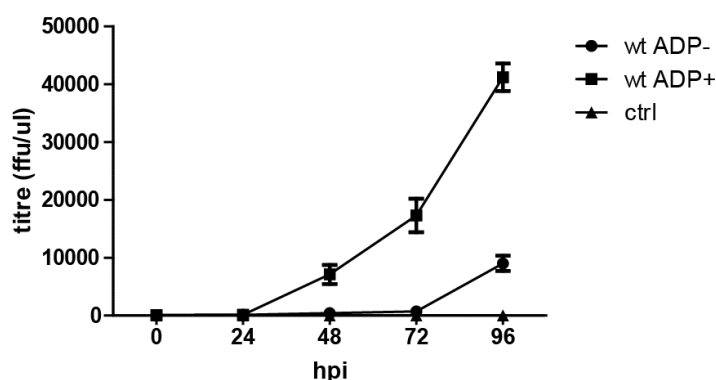
Figure 32: ADP expression accelerates HAdV5 particle release from infected cells. A growth curve of virus particle release from infected A549 cells from 0 to 96 hpi is displayed. The two virus strains HAdV5 ADP– and HAdV5 ADP+ were compared together with a ctrl in which no virus was used. The supernatant of infected cells was collected at each time-point and their titre was measured as ffu/μL by FACS analysis. Three replicates (n=3) were measured and the standard deviation is displayed.

At 24 hpi, no HAdV5 particles were detected in the supernatant for either virus strain. At 48 hpi, virus particles were detected to have been released from infected cells for HAdV5 ADP+. From 48 hpi to 96 hpi, increasing infectious particles were found in the supernatant for HAdV5 ADP+. HAdV5 ADP– particles were only detected at 96 hpi at a four-time lower level

compared to HAdV5 ADP+. This time-course experiment demonstrated the increased release of virus particles upon ADP expression in infection.

4.2.2 Fluorescent protein labelling of ADP with mCherry

ADP from HAdV type 2 was described to be localised in the nuclear envelope as well as Golgi and ER (SCARIA *et al.*, 1992; TOLLEFSON *et al.*, 2003). To analyse whether ADP from HAdV type 5 localises similarly, it was first tested in a transfection experiment. To this end, the HAdV5 *CR1β* gene coding for HAdV5 ADP was ligated into the mammalian expression plasmid pCherry-C2. In this way, ADP was fluorescently labelled by fusion to the fluorescent protein mCherry. Since HAdV2 was shown to retain lytic activity upon mutations within its C-terminus, C-terminal fusion of pCherry-C2 to HAdV5 ADP was performed (TOLLEFSON *et al.*, 2003). The ADP-mCherry expression plasmid was transfected into H1299 cells and the localisation of ADP-mCherry was analysed by live-cell fluorescence microscopy at 48 hours post transfection (hpt) (Figure 33).

The predominant ADP-mCherry phenotype showed localisation of the protein in vesicles in the perinuclear region. The second most common phenotype showed similar vesicles in the perinuclear region together with a dispersed mCherry signal throughout the entire cell. Only 3.7 % of transfected cells showed fluorescently labelled ADP to be localised in the nuclear envelope. In these cells, the protein could also be detected in the within the ER. The localisation of ADP-mCherry in these transfection experiments differed from the described localisation for HAdV2 ADP.
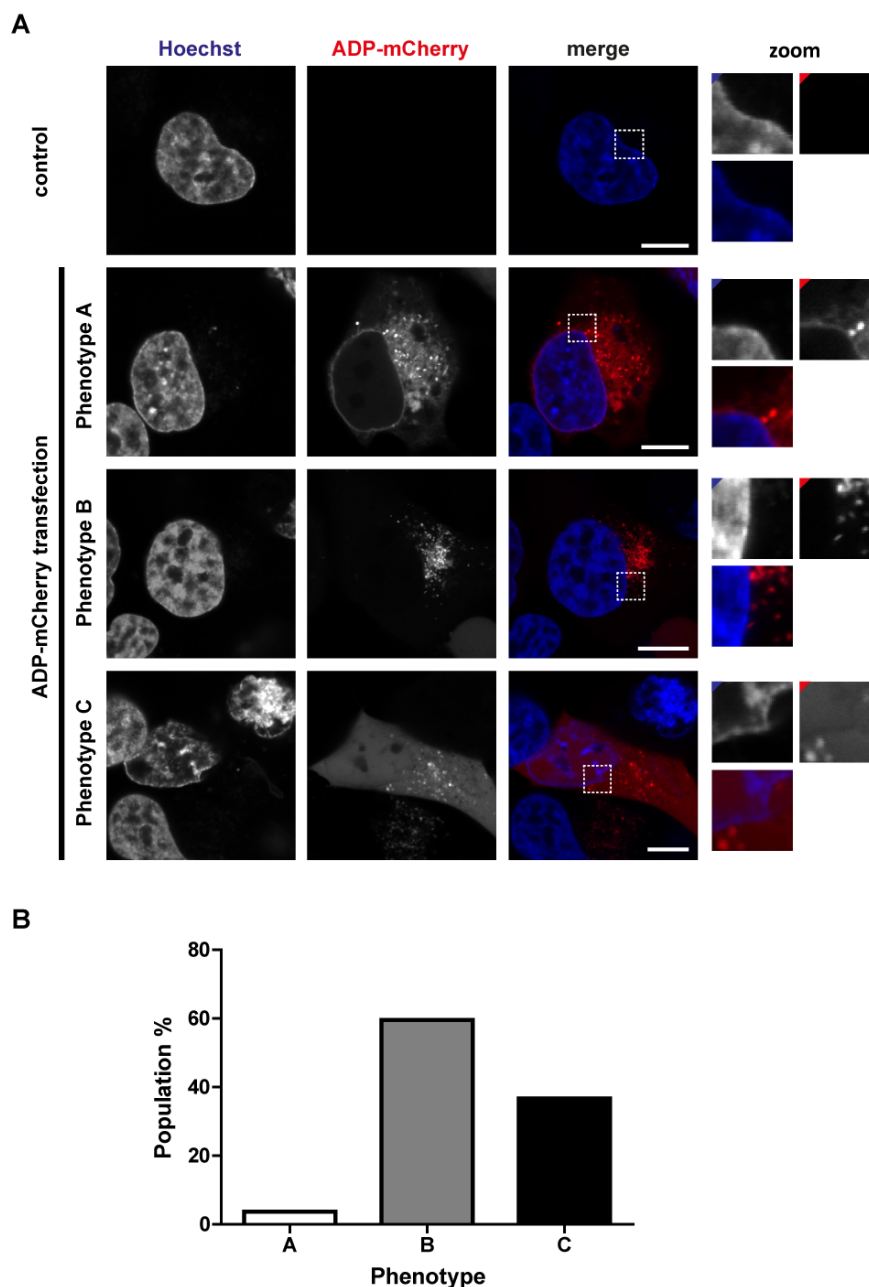
Figure 33: Only a minority of ADP-mCherry localises to the nuclear membrane. A) Transfection of H1299 cells with pcDNA3-mCherry and pcDNA3 plasmid DNA as a control. **B)** Quantification of protein localisation phenotypes (n=297). At 48 hpt, transfected H1299 cells were imaged by confocal laser-scanning fluorescence microscopy. The cells were stained with Hoechst 33342 (Hoechst) and the localisation of ADP-mCherry was probed (ADP-mCherry). The signal overlap is represented in colour (merge). Nuclear envelope regions of interest are enlarged (zoom) with coloured corners indicating the channel colour. A representative cell is shown for each observed transfection phenotype. Phenotype A showed ADP-mCherry in the nuclear membrane and perinuclear vesicles, phenotype B showed only perinuclear vesicles and phenotype C showed dispersed signal throughout the entire cell. Only 3.7 % of cells showed ADP-mCherry to be localised in the nuclear envelope and ER. Scalebars indicate 10 μm.

4.2.3 Addition of an HA tag to ADP by homologous recombination

Since the addition of an mCherry tag to HAdV5 ADP resulted in localisation differences of the protein compared to previous publications for HAdV2, two variables of the experiment were changed. First, a smaller protein tag, the HA tag was used instead of mCherry. This epitope tag is derived from the human influenza hemagglutinin (FIELD *et al.*, 1988). Second, in contrast to the mCherry fusion construct, ADP-HA fusions were generated in the context of the HAdV5 genome by homologous recombineering in *E. coli* (WANG *et al.*, 2014) to yield the virus strain HAdV5 ADP-HA which can be tested in infection instead of transfection experiments. Mutant virus particles were generated by transfection of the linearised viral genome into H1299 cells. After transfection, the cells were analysed for cytopathic effects. The culture supernatant was used to infect new A549 cells and progeny virions were produced by three rounds of infection. The localisation of ADP-HA in HAdV5 ADP-HA infection of A549 cells was analysed by immunofluorescence microscopy at 24 hpi and 48 hpi (Figure 34).
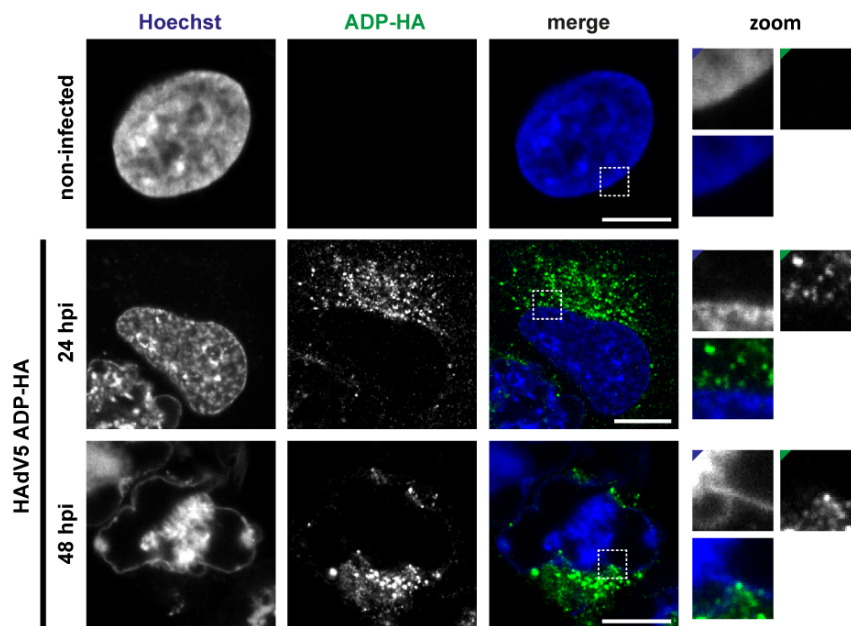
Figure 34: ADP-HA is localised to vesicles in the perinuclear region. A549 cells were infected with HAdV5 ADP-HA. At 24 and 48 hpi, the cells were fixed and imaged by confocal laser-scanning fluorescence microscopy. Cells were stained with Hoechst 33342 (Hoechst) and immunostained against the HA-tag (ADP-HA). The signal overlap is represented in colour (merge). Nuclear envelope regions of interest are enlarged (zoom) with coloured corners indicating the channel colour. A representative cell is shown for each time-point. Scalebars indicate 10 μm.

In contrast to some cells in ADP-mCherry transfection, ADP-HA was not detected in the nuclear envelope at all. The protein was found to be exclusively localised in cytoplasmic

spots, most likely vesicles. This phenotype was comparable to phenotype B described for ADP-mCherry. These vesicles appeared to be more strongly associated with the perinuclear regions at 48 hpi, compared to 24 hpi. Infection with HAdV5 ADP-HA showed marginalisation of cellular DNA and the formation of a central LVAC in the Hoechst 33342 fluorescence channel. Still, the localisation of HAdV5 ADP-HA in infection differed to the reported localisation of the HAdV2 ADP protein.

4.2.4 HAdV5 infection causes destabilisation of the nuclear envelope

Since fluorescent labelling of ADP did not point to specific regions of the nuclear envelope to be enriched of ADP protein, the overall nuclear envelope morphology of infected cells was compared in HAdV5 ADP– and HAdV5 ADP+ infection. For the selection of infected cells, the virus strains HAdV5 pIX-mCherry ADP– and HAdV5 pIX-mCherry ADP+ were used, which express mCherry labelled protein IX as a visible marker. The cell line A549 expressing a lamin A nanobody fused to mTagGFP was used to analyse the morphology of the nuclear envelope (Figure 35A).

Non-infected cells showed a clear nuclear envelope stain as was previously shown (Figure 8). Depending on the progression of infection, different lamin A phenotypes were detected. At an early stage, when no LVAC was detectable, the nuclear envelope was still visible. However, the mTagGFP-nanobody signal levels were already reduced. This observation was made for both virus strains. At a later stage when the LVAC was visible, very little mTagGFP-nanobody signal remained at the nuclear envelope. Again, this phenotype was visible for infection with both virus strains. Interestingly, a high proportion of cells showed a formation of strongly fluorescent lamin A-mTagGFP-nanobody spots in the cytoplasm. A reduction in anti-lamin A nanobody signal could originate from degradation of lamin A, redistribution of lamin A from the nuclear envelope to the ER and cytoplasm, a loss of nanobody affinity for lamin A in infection or infection-induced aggregation of the protein in the cytoplasm. To exclude a nanobody affinity loss for lamin A, A549 cells were infected with HAdV5 pIX-mCherry ADP+ and the nuclear lamina was immunostained for lamin A (Figure 35B). In non-infected cells, a strong lamin A signal was detected by the antibody. In comparison, the HAdV5 pIX-mCherry infected cells showed a reduced anti-lamin A antibody signal at the nuclear envelope. Thus, the anti-lamin A nanobody is a suitable system to analyse levels of lamin A at the nuclear envelope. Overall, judging from the nuclear lamin A morphology, no differences in infection with HAdV5 ADP– or ADP+ were detected.
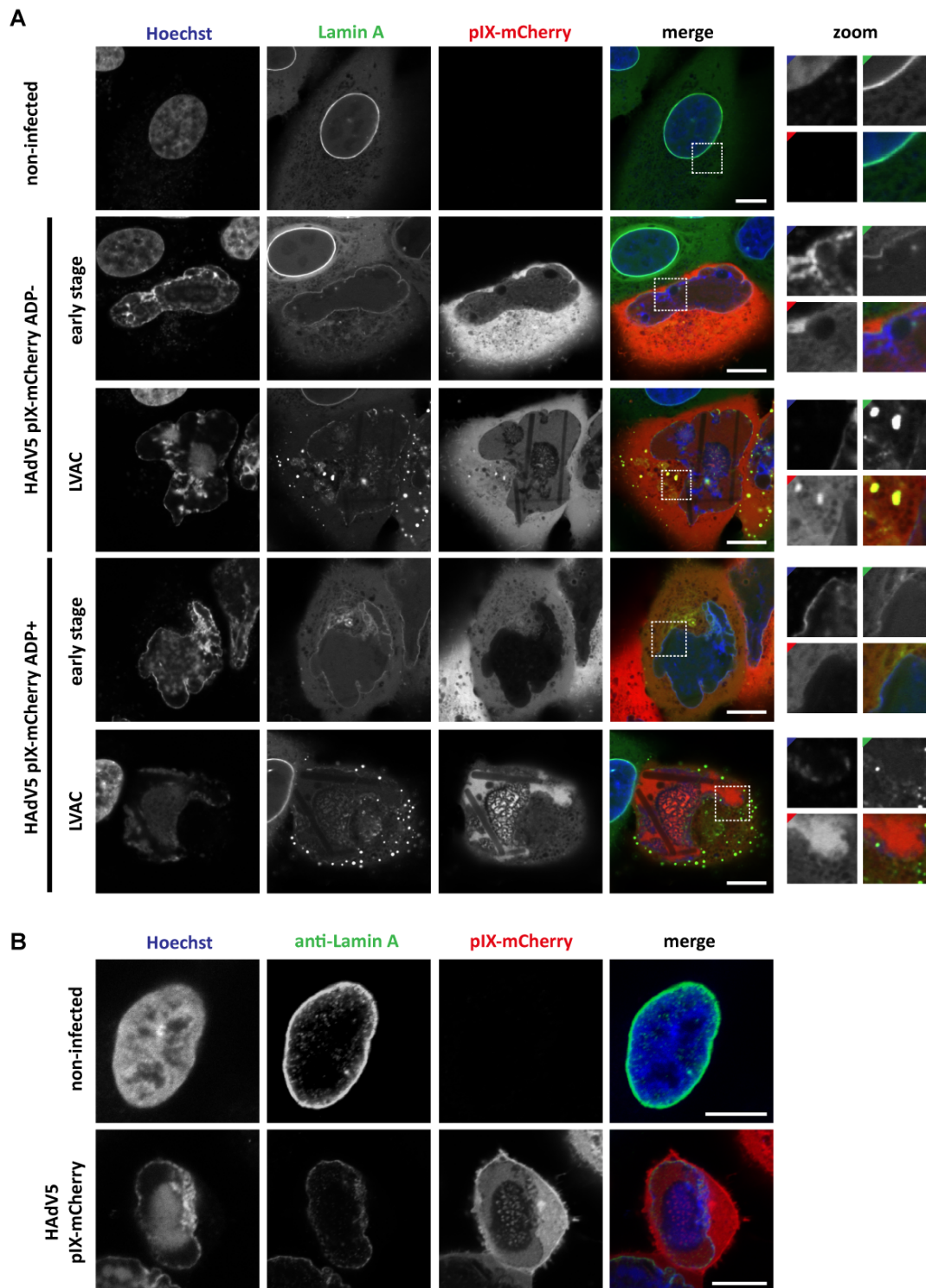
Figure 35: The nuclear membrane loses lamin A signal during infection. A) A549 cells were infected with HAdV5 pIX-mCherry ADP– and HAdV5 pIX-mCherry ADP+ and imaged by live-cell fluorescence microscopy at 48 hpi. **B)** A549 cells were infected with HAdV5 pIX-mCherry ADP+, fixed with PFA at 48 hpi and imaged by confocal fluorescence microscopy. The pIX-mCherry fluorescence was used to identify infected cells for analysis of their lamin A phenotype. A non-infected cell was analysed in comparison. A representative cell for each phenotype is shown. The dsDNA signal is represented by Hoechst 33342 stain (Hoechst). The nuclear lamina is represented by an mTagGFP-nanobody recognising lamin A (Lamin A) or an anti-lamin A antibody (anti-Lamin A). pIX localisation is detected through the viral pIX-mCherry fusion construct (pIX-mCherry). The signal overlap is represented in colour (merge). Nuclear membrane regions of interest are enlarged (zoom) with coloured corners indicating the channel colour. Scalebars indicating 10 μm.

To control for potential artefacts from pIX-mCherry labelling, the lamin A localisation was also tested in HAdV5 wt ADP– and HAdV5 wt ADP+ infection (Figure 36A). Additionally, the lamin A fluorescence levels at the nuclear envelope were quantified and compared between non-infected cells, and infected cells using HAdV5 pIX-mCherry ADP–/ADP+ and HAdV5 wt ADP–/ADP+ strains (Figure 36B).

No difference in lamin A phenotype was detected in infection with HAdV5 wt compared to HAdV5 pIX-mCherry. At the early infection stage, lamin A signals were reduced at the nuclear envelope. This effect was increased in cells showing the LVAC. Cells with LVAC were detected via their Hoechst 33342 dsDNA honeycomb-like conformation. To quantify the lamin A signal levels, the nuclear lamina was manually segmented and the average signal was measured across the entire nuclear envelope. No significant difference could be detected between any of the tested HAdV5 strains. All infected cells showed a significantly reduced lamin A signal compared to non-infected cells. These results indicated an infection-dependent reduction of lamin A, which is not modulated by ADP function.
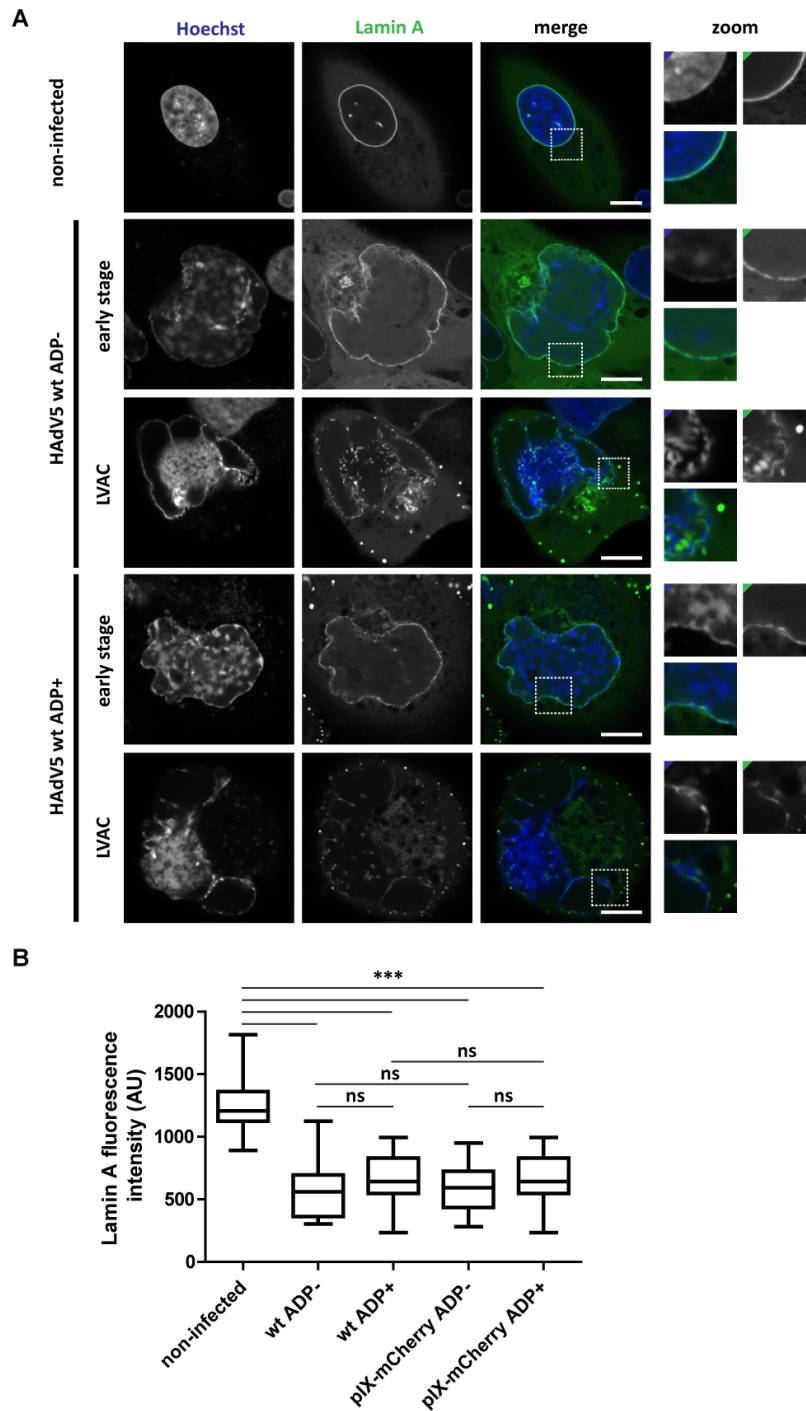
Figure 36: No difference in lamin A signal reduction at the nuclear envelope upon ADP expression of pIX labelling with mCherry. A) A549 cells were infected with HAdV5 wt ADP– or HAdV5 wt ADP and imaged by live-cell fluorescence microscopy at 48 hpi. The Hoechst 33342 fluorescence was used to identify infected cells for analysis of their lamin A phenotype. A non-infected cell was analysed in comparison. A representative cell for each phenotype is shown. The dsDNA signal is represented by Hoechst 33342 stain (Hoechst). The nuclear lamina is represented by an mTagGFP-nanobody recognising lamin A (Lamin A). pIX localisation is detected through the viral pIX-mCherry fusion construct (pIX-mCherry). The signal overlap is represented in colour (merge). Nuclear membrane regions of interest are enlarged (zoom) with coloured corners indicating the channel colour. Scalebars indicate 10 μm. **B)** Quantification of anti-lamin A mTagGFP-nanobody signal intensity at the nuclear envelope in infection with multiple virus strains. The fluorescence intensity of multiple cells is shown as a box plot including the median, upper quartile, lower quartile, maximum and minimum of the population (n = 20). Statistical significance was calculated using a one-way ANOVA with post-hoc Tukey test.

Apart from the reduction in lamin A fluorescence level, the nuclear envelope of infected cells showed a loss of structural integrity. In non-infected cells, the nuclear membrane had an oval shape, whereas the nuclear envelope of infected cells developed into a kidney shape and showed local membrane invaginations. To gain more information on the global membrane deformations caused by HAdV5 infection, these nuclear membrane invaginations were analysed using serial block-face SEM. A non-infected and HAdV5 pV-mCherry ADP+-infected cell each were recorded as sequential z-slices, allowing to reconstruct the 3D volume of the entire cells. By tracing and segmenting their nuclear envelopes, the nuclear global fold was analysed (Figure 37).

The non-infected cell had an oval-shaped nucleus. Interestingly, it had a small channel, which was spanning one side of the nucleus to the other (Figure 37 images i and iii). Overall, the nuclear envelope showed no major deformities (Figure 37 image v). In contrast, the infected cell showed a fragmentation of the nucleus into multiple parts including a small part of the nucleus that had separated into the cytoplasm (Figure 37 images ii and iv). Overall, the nucleus of the infected cell had a kidney-shape morphology. In particular, the part of the nuclear envelope which was facing the centre of the cell showed strong membrane invaginations and budding events of multiple small vesicles containing nucleoplasm (Figure 37 image vi).
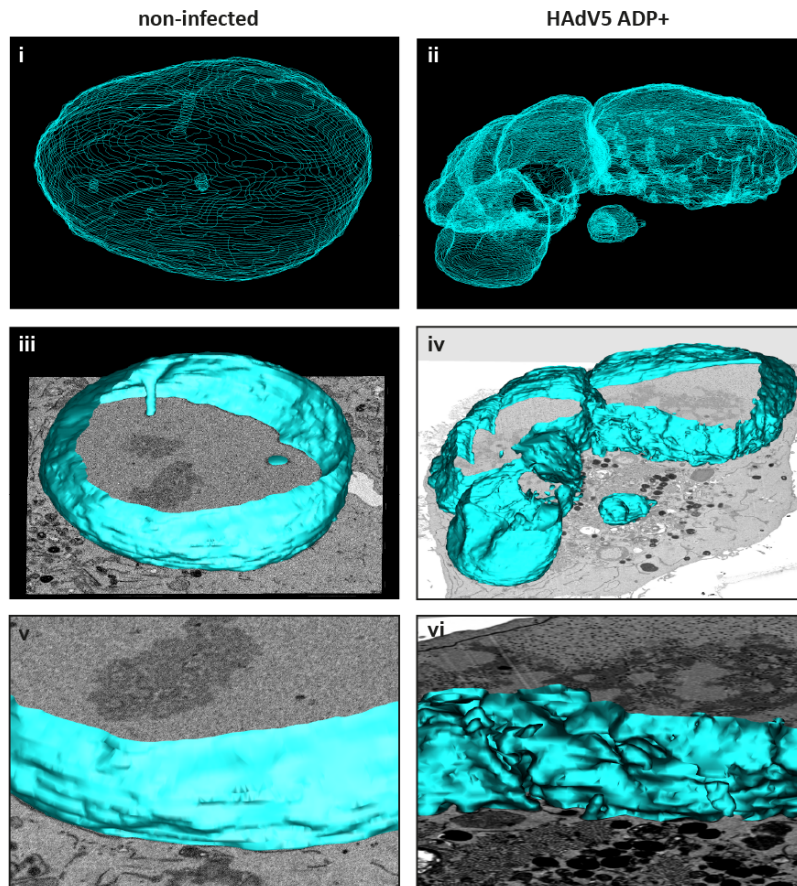
Figure 37: The nuclear membrane in HAdV5 infection loses global stability, fragments and forms invaginations. A549 cells were infected with HAdV5 pV-mCherry ADP+ and fixed at 42 hpi. The pV-mCherry fluorescence was used to identify infected cells for serial block-face SEM sample preparation. A non-infected cell was analysed in comparison. The 3D volume of cells of interest was recorded by serial block-face SEM. The nuclear envelope of a non-infected and infected cell was manually segmented using the IMOD segmentation tool (KREMER *et al.*, 1996). A mesh overview of both nuclei is shown in images i) and ii). An overlay of a surface render onto a SEM z-image is shown in images iii) and iv). An enlargement of a surface render of the nuclear envelope is shown in images v) and vi).

HAdV5 infection often induces the formation of large intranuclear protein crystals (Figure 38A). In TEM analysis, virus particles were found to localise around these crystal structures. The composition of these crystals was previously described as fibre and penton protein, which are imported into the nucleus to such a high extent that they pack in regular patterns (FRANQUEVILLE *et al.*, 2008). These large crystals were hypothesised to potentially lead to membrane rupture when they grow large enough to extend beyond the normal size of the nuclear envelope. Such examples were found by fluorescence microscopy in which the crystals can be detected as large rectangular structures devoid of pIX-mCherry (Figure 38B). The nuclear envelope appeared to be stretched around the spatial constraint that was given by the nuclear crystals. The shape of the nuclear envelope of these protein crystals was

analysed by TEM (Figure 38C). No evidence was found that the protein crystals caused membrane rupture of the infected cells that were analysed.
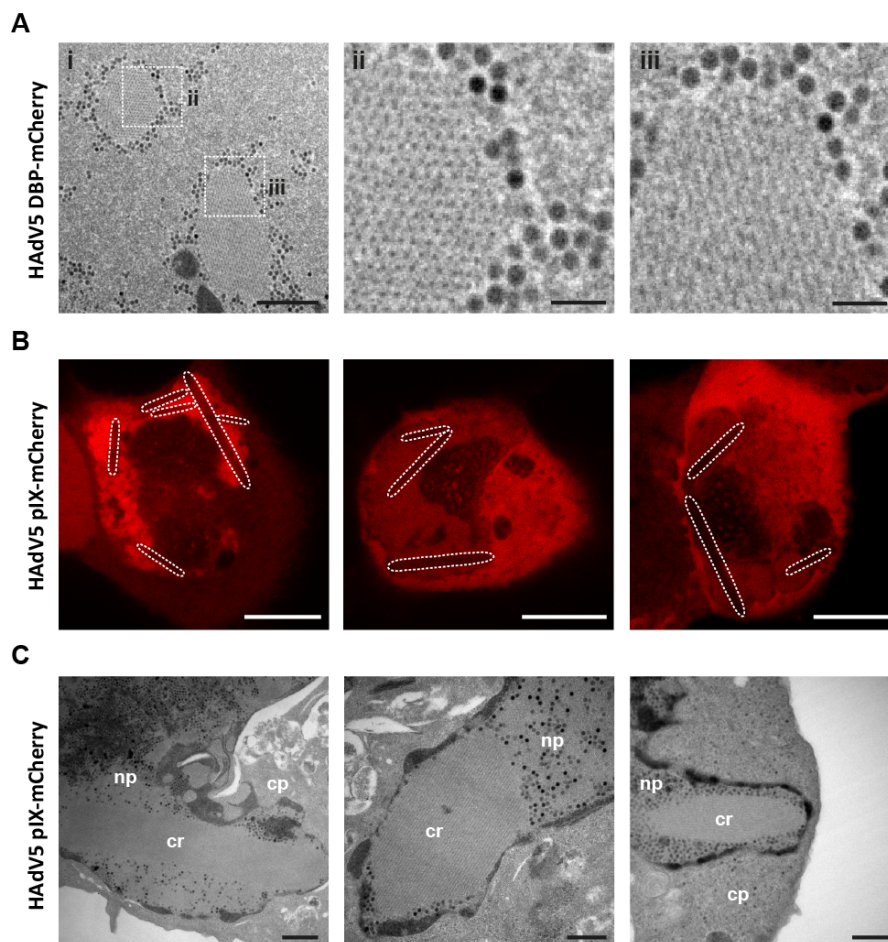
Figure 38: HAdV5 infection induces the formation of large intranuclear protein crystals that grow large enough to distort the nuclear membrane. **A)** Classical TEM image of intracellular protein crystals surrounded by HAdV5 particles in A549 infection with HAdV5 DBP-mCherry at 48 hpi. The crystal structure appeared as regular dots or slabs depending on the orientation of the crystal lattice. Scalebars indicate 1 μm in image i) and 200 nm in images ii) and iii). **B)** Appearance of large protein crystals in A549 cells infected with HAdV5 pIX-mCherry at 48 hpi. The proteins are visible as areas devoid of pIX-mCherry signal and are traced by white dotted lines. Crystals extend beyond the normal geometry of the nucleus and distort the nuclear envelope. Three representative cells are displayed. Scalebars indicate 10 μm. **C)** Protein crystals distorting the nuclear membrane. A549 cells were infected with HAdV5, fixed at 48 hpi and prepared for classical TEM. Three representative cells are shown. Areas of nucleoplasm (np), cytoplasm (cp) and protein crystals (cr) are labelled. Scale bars indicate 1 μm.

4.2.5   HAdV5 infection causes nuclear envelope damage

Due to the detection of large scale stability defects of the nuclear envelope of HAdV5-infected cells, the nuclear membrane was analysed in more detail. Initially, the presence of HAdV5 particles near the nuclear membrane was probed under the assumption

that the capsids themselves could be targeted to sites of egress or cause membrane damage by means of capsid-membrane interactions. Interestingly, there are only few a positions in infected cells in which particles localised close to the membrane. The nuclear envelope was often surrounded by a layer of marginalised chromatin that isolates virions from direct interaction with the inner nuclear membrane (Figure 38C). When comparing infection with HAdV5 expressing ADP and lacking ADP, there is a difference in HAdV5 particles found in the cytoplasm. Only HAdV5 ADP+ infection showed varying levels of particles outside of the nucleus at 48 hpi (Figure 39A/B). However, since only a small number of infected cells could be screened, no clear significance can be deduced from this observation. Instead of probing membrane damage on individual ultra-thin sections, serial block-face SEM was performed. This method allows recording the entire volume of the infected cell and thus increases the chances of finding regions of nuclear membrane damage. Cells were infected with HAdV5 pIX-mCherry ADP– and HAdV5 pIX-mCherry ADP+. Appropriately infected cells were detected via the pIX-mCherry fluorescence signal at 42 hpi. These cells were prepared for serial block-face SEM (Figure 39C).

The nuclear envelope of non-infected cells did not show any signs of membrane damage. In contrast, multiple sites of nuclear membrane disruptions could be detected in HAdV5 infection. While more of these sites were detected in infection with HAdV5 ADP+ than HAdV5 ADP-, the number of analysed cells does not allow for a meaningful quantification. However, since, no damage was detected in non-infected cells, it is unlikely that they arise from EM-preparation-induced artefacts.

In the process of analysing the nuclear membrane in infection, a few strongly infected cells were detected by TEM that showed strong nuclear membrane disruptions. (Figure 40). These cells did not only show small nuclear lesions, as were previously detected by serial block-face SEM, but had large membrane gaps through which nucleoplasm together with virus particles entered the cytoplasm. In one of these disrupted cells, a large protein crystals was detected in the cytoplasm. These cells were rarely detected, since strongly infected cells eventually lose contact to the cell culture support and are lost during the TEM preparation procedure.
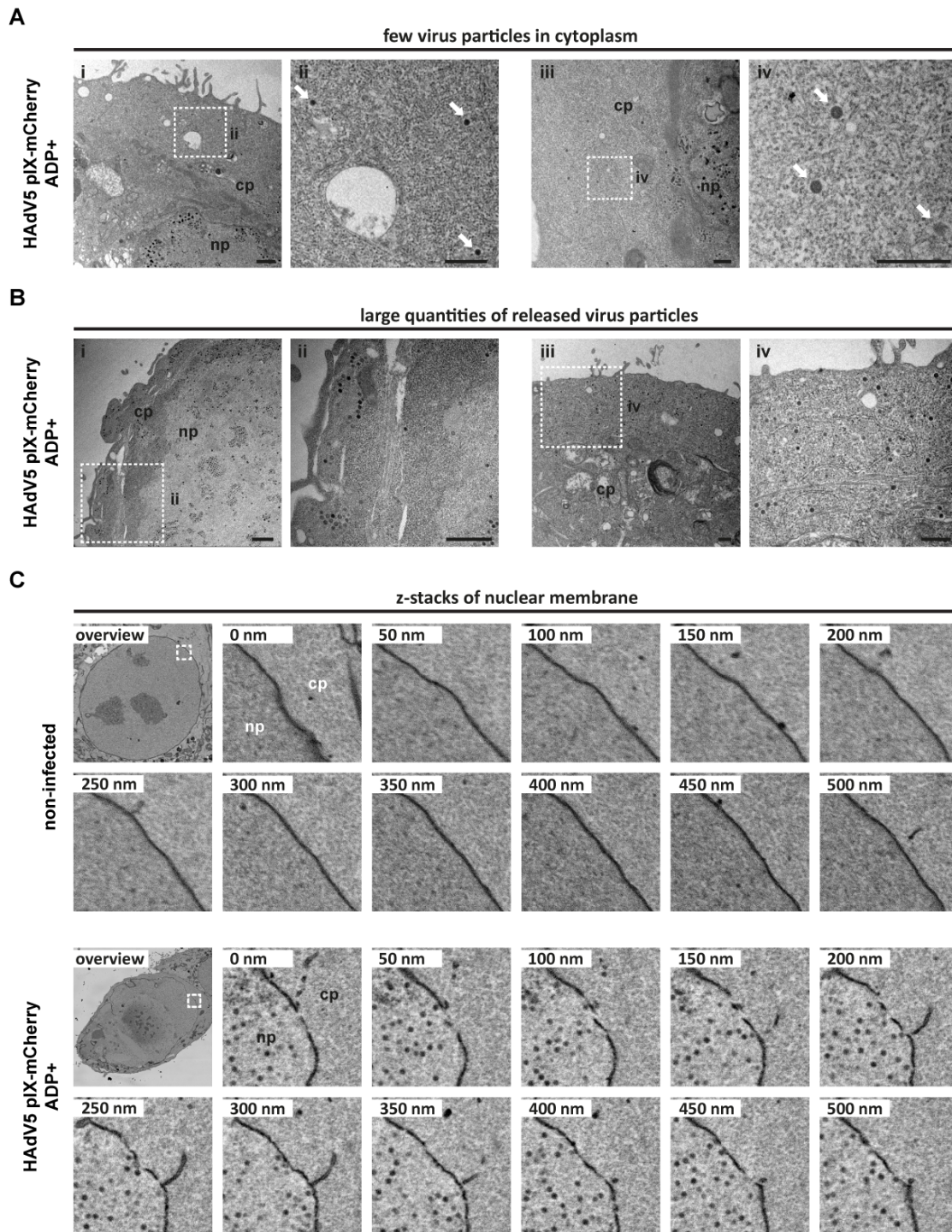
Figure 39: HAdV5 infection induces small membrane disruptions while initially only a few virus particles are found in the cytoplasm. A/B) Depending on the state of infection varying numbers of HAdV5 particles can be detected in the cytoplasm at 48 hpi. Cells were infected with HAdV5 pIX-mCherry ADP+ to allow for fluorescence-based targeting of cells of interest for ultra-thin sectioning of cells for TEM analysis. Two example cells are shown in images i) and iii) with scalebars indicating 1 μm. Higher magnification images selected areas of interest are shown in images ii) and iv) with scalebars indicating 500 nm. Areas of the nucleoplasm (np) and cytoplasm (cp) are indicated and virus particles are highlighted by white arrows. **C)** Nuclear membrane disruptions by HAdV5 pIX-mCherry ADP+ infection. A549 cells were infected with HAdV5 pIX-mCherry ADP+ and prepared for serial block-face SEM at 42 hpi. A non-infected cell was analysed as a comparison. An overview image is shown, with a white square indicating a selected ROI. Sequential z-sections of the ROIs are shown and the nucleoplasm (np) and cytoplasm (cp) are labelled.
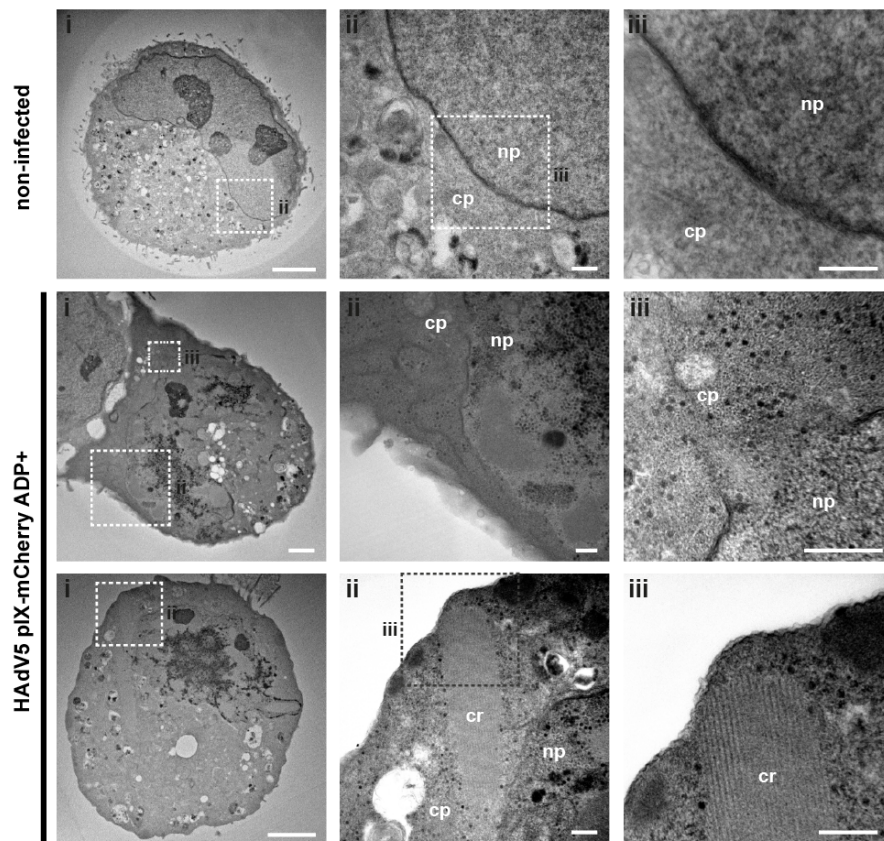
Figure 40: HAdV5 infection causes large membrane disruptions. A549 cells were infected with HAdV5 pIX-mCherry ADP+. A non-infected cell was analysed as a control. Before total cell lysis, large nuclear membrane disruptions were detected. Large quantities of HAdV5 particles were detected in the cytoplasm together with nuclear content and protein crystals. Two infected cells are shown with overview images in i) and higher magnification images ii) and iii) shown by white dotted squares. Areas of nucleoplasm (np), cytoplasm (cp) and protein crystals (cr) are labelled. Scalebars indicate 5 μm for images i) and 500 nm for images ii) and iii).

To confirm the apparent nuclear lesions of classically fixed EM probes, the nuclear membrane was analysed by electron cryo-tomography. For this method, instead of chemical fixation, the cells were preserved in their natural state by rapid freezing to liquid nitrogen temperature. While the edges of cells are thin enough to be penetrated by the electron beam, the thickness of nucleus would cause too much interaction of the beam with the sample and does not allow to simply target the nucleus without further preparation. Instead, cells were prepared by FIB-milling, which can clear away cellular material above and below a z-plane of interest (Figure 41). To allow for targeted milling of infected cells, A549 cells were infected with HAdV5 pIX-mCherry ADP+ and a fluorescent image was correlated with the SEM image in the FIB-SEM microscope (Figure 41A). After generation of ultra-thin (∼200 nm) lamellae, the nuclear envelope could be visualised by electron cryo-tomography (Figure 42).

The 3D reconstruction of tomograms allowed to detect a site of membrane damage, similar to the events previously detected by serial block-face SEM. The tomogram showed a cytoplasmic region flanked by two nucleoplasmic regions caused by nuclear envelope infolding. Within the volume of the tomogram, a high number of virions was detected in the nucleoplasm, but three particles were also detected in the cytoplasm. These particles sit close to an opening in the nuclear membrane, which is larger than the typical nuclear pore size and opens up further to the top of the tomogram. For better visualisation the nuclear membrane, four virions and a lipid droplet were segmented.
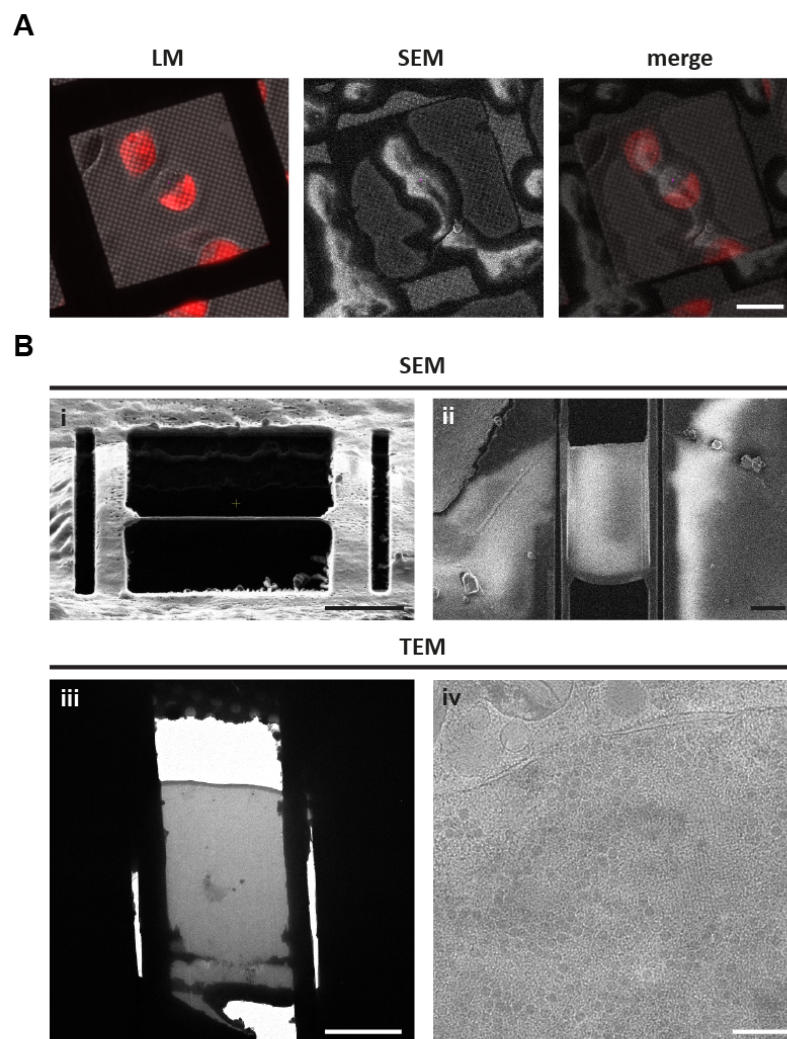
Figure 41: pIX-mCherry fluorescence correlation allows to target HAdV5 infected cells for FIB-milling. A) CLEM microscopy of A549 cells infected with HAdV5 pIX-mCherry ADP+. The cells were seeded on TEM gold grids and imaged by live-cell wide-field fluorescence microscopy (LM). Cells of interest to be targeted for FIB-milling in the scanning electron microscope (SEM) were identified by correlation with the light microscopy image. The scalebar indicates 10 μm. **B)** FIB-milling procedure to thin the cellular material to image HAdV5 particles in the nucleus in electron cryo-microscopy. The appearance of the thin lamella in SEM (SEM) is shown from the direction of milling and from the top in images i) and ii). The appearance of the entire lamella and a selected nuclear region in the cryo transmission electron microscope is shown in images iii) and iv). Scalebars indicate 5 μm for images i)-iii) and 500 nm for image iv).
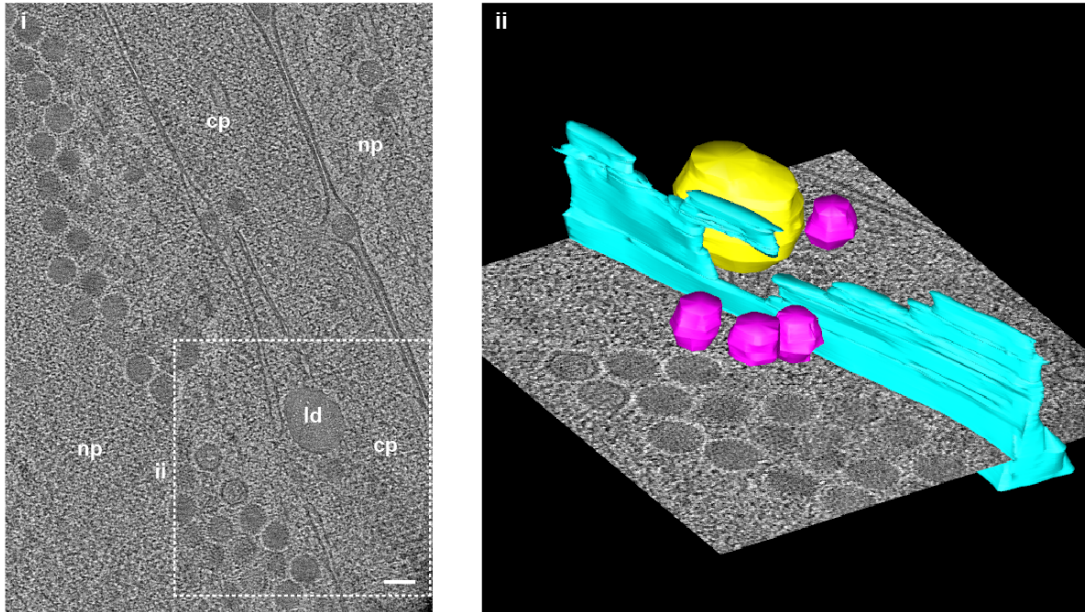
Figure 42: Cryo tomogram showing nuclear membrane disruptions together with virions outside of the nucleus A single z-slice of the reconstructed 3D volumen is shown in image i). Areas of nucleoplasm (np), cytoplasm (cp) and and a lipid droplet (ld) are labelled. The scalebar indicates 100 nm. A region of interest of the tomogram is shown in image ii). The nuclear membrane (cyan), selected HAdV5 particles (magenta) and a lipid droplet (yellow) were manually segmented using the IMOD segmentation tool (KREMER *et al.*, 1996). A virion outside the nucleus was found at a site of nuclear membrane damage.

4.2.6 HAdV5 infection causes nuclear membrane permeability late in infection independent of ADP

Since EM analysis detected nuclear lesions and virus particles in the cytoplasm of cells at 48 hpi, a mechanism leading to egress of particles independent of total nuclear rupture was hypothesised. To test the involvement of ADP in this process, the permeability of the nuclear envelope in infection was probed. The nuclear permeability assay was based on the influx of blue fluorescent protein (BFP) labelled with an NES. The BFP-NES fusion protein is efficiently transported out of the nucleus by CRM1 nuclear transport (FORNEROD *et al.*, 1997; FUKUDA *et al.*, 1997). The BFP-NES construct was constitutively expressed in a polyclonal A549 cell line. A population of similarly strong fluorescent cells was selected by FACS sorting. As part of the expression construct a GFP protein is expressed constitutively, which allowed tracing the cell boundaries. The rationale behind this assay is that, when nuclear pores or lesions appear in adenovirus infection, the influx of BFP-NES will increase and will not be efficiently counteracted by CRM1 export. The A549 BFP-NES cell line was infected with HAdV5 pIX-mCherry ADP– and HAdV5 pIX-mCherry ADP+ and analysed by spinning-disk confocal

fluorescence microscopy (Figure 43A).
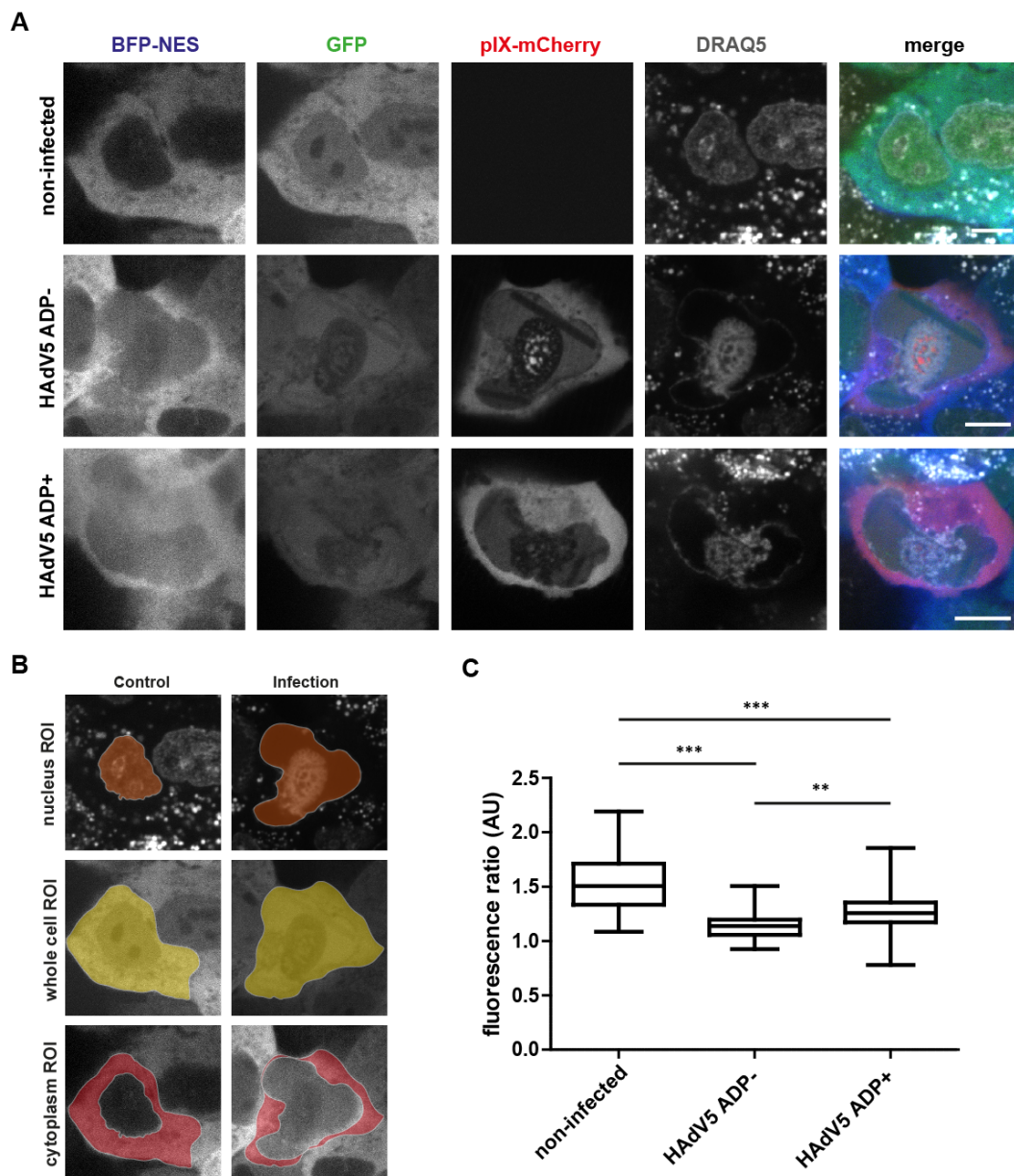
Figure 43: Infection by HAdV pIX-mCherry increases BFP-NES amounts in the nucleus. A549 cells were infected with HAdV5 pIX-mCherry ADP– or HAdV5 pIX-mCherry ADP+ and analysed at 48 hpi. A) Phenotype of A549 cells expressing BFP-NES construct. The cells were imaged by live-cell confocal spinning-disk fluorescence microscopy. A representative cell is shown for each condition. The permeability probe BFP-NES is detected via the BFP fluorescence (BFP-NES). The whole-cell area was detected via constitutively expressed GFP (GFP). Infected cells were detected by expression of pIX-mCherry (pIX-mCherry). The dsDNA signal is represented by DRAQ5 stain (DRAQ5). The signal overlap is represented in colour (merge). Scalebars indicate 10 μm. B) Representation of ROIs for BFP-NES signal analysis. The nuclear ROI was chosen based on the dsDNA signal, the whole-cell ROI was chosen based on GFP expression and the cytoplasmic ROI was selected as the whole-cell ROI excluding the nucleus ROI. C) Quantification of BFP-NES signal ratio between cytoplasm and nucleus of infected cells (n = 50). The ratio is shown as a box plot including the median, upper quartile, lower quartile, maximum and minimum of the population. Statistical significance was calculated using a one-way analysis of variance (ANOVA) with post-hoc Tukey test.

The non-infected cells showed BFP-NES fluorescence outside of the nucleus, while the NES caused the protein amounts in the nucleus to be minimal. DRAQ5 stained the nucleus but also accumulated in vesicles and led to background stain. GFP was expressed throughout the cell and in contrast to BFP-NES was not excluded from the nucleus. In infected cells, the exclusion of BFP-NES from the nucleus was not as clear anymore since more protein was detected in the nucleus. Phenotypically, no strong difference between cells infected with HAdV5 pIX-mCherry ADP– or ADP+ was observed. Originally, the separate fluorescent markers were intended to be used for automated cell segmentation of the nucleus, whole-cell area and cytoplasmic area to allow automated analysis of the BFP-NES fluorescent intensity inside the nucleus versus in the cytoplasm. However, the marginalisation of dsDNA and formation of the LVAC prevented automated detection. Alternatively, the nuclear area, whole-cell area and cytoplasmic area were traced as ROIs by hand (Figure 43B). Subsequent quantification of the BFP-NES ratio between cytoplasm and nucleus showed the average BFP-NES signal ratio to be 1.54 for non-infected cells, 1.14 for infection without ADP and 1.27 for infection with ADP (Figure 43C). Thus, infection by HAdV5 significantly increased BFP-NES levels inside the nucleus. While this assay indicates an increased nuclear permeability upon infection it does not control for changes in the CRM1-dependant export that might be induced by HAdV5 infection. It is unlikely that HAdV5 infection would block CRM1-mediated export since HAdV infection has been shown to rely on CRM1 function to catalyse nuclear export of mRNA transcripts (STRUNZE *et al.*, 2005; SCHMID *et al.*, 2012). Inhibitors of CRM1 have even been suggested as antivirals against influenza virus or human cytomegalovirus (hCMV) infection (WATANABE *et al.*, 2011; SANCHEZ *et al.*, 2007; SCHMID *et al.*, 2012).

Since ADP expression did not show an increase in nuclear permeability compared to infection lacking ADP, a second nuclear permeability assay was performed to control for possible inhibition of nuclear export during infection. The second assay was based on the nuclear influx of 70 kDa dextran molecules labelled with the fluorescent dye fluorescein isothiocyanate (FITC). Dextran-FITC molecules are not able to pass the NPC and can thus only reach the nucleoplasm through other, larger nuclear pores or lesions. The dye is not cell-permeable, which is why cells were pre-treated with digitonin to selectively permeabilise the cytoplasmic but not the nuclear membrane. To induce nuclear permeability in a positive control, cells were incubated in triton X-100. The A549 cells were infected with HAdV5 pIX-mCherry ΔE3 and HAdV ΔE3 ADP+, semi-permeabilised by digitonin, incubated in dextran-FITC and then analysed by spinning-disk confocal fluorescence microscopy (Figure 44A).

The non-infected cells showed dextran-FITC fluorescence in the space between cells as well as the cytoplasm. Dextran-FITC signal was weaker inside the cytoplasm compared to the extracellular space and the dye was excluded from intracellular vesicles. The dextran-FITC fluorescence inside the nucleus was very weak. Hoechst 33342 clearly stained cellular chromatin inside the nucleus. The positive control showed stronger dsDNA signal due to the increased permeation of the dye, which showed the nuclear area. The fluorescence of dextran-FITC appeared to be higher compared to the negative, non-infected control. In infection, Hoechst 33342 stained the marginalised dsDNA as well as viral DNA that has accumulated in the LVAC. Dextra-FITC signal was detected inside the nucleus, however, it did not show an even distribution. Instead, sub-nuclear areas outside of the LVAC showed high dextran-FITC fluorescence, while the probe was excluded from the LVAC. As for the BFP-NES assay, it was not possible to perform automated cell segmentation to quantify the ratio of dextran-FITC in the cytoplasm versus the nucleus. Instead, the nuclear area was hand-traced by means of the dsDNA signal and the whole-cell area was selected based on the cellular outline that was visible in the dextran-FITC channel (Figure 44B). Subsequent quantification of the dextran-FITC ratio between cytoplasm and nucleus showed the average signal ratio to be 1.25 for non-infected cells, 1.11 for the positive triton X-100 control, 1.03 for infection without ADP and 1.03 for infection with ADP (Figure 43C). As for the previous nuclear permeability assay, the nuclear permeation of the dye was significantly increased by infection. No statistically significant difference in nuclear permeability between infection with and without ADP was detected.
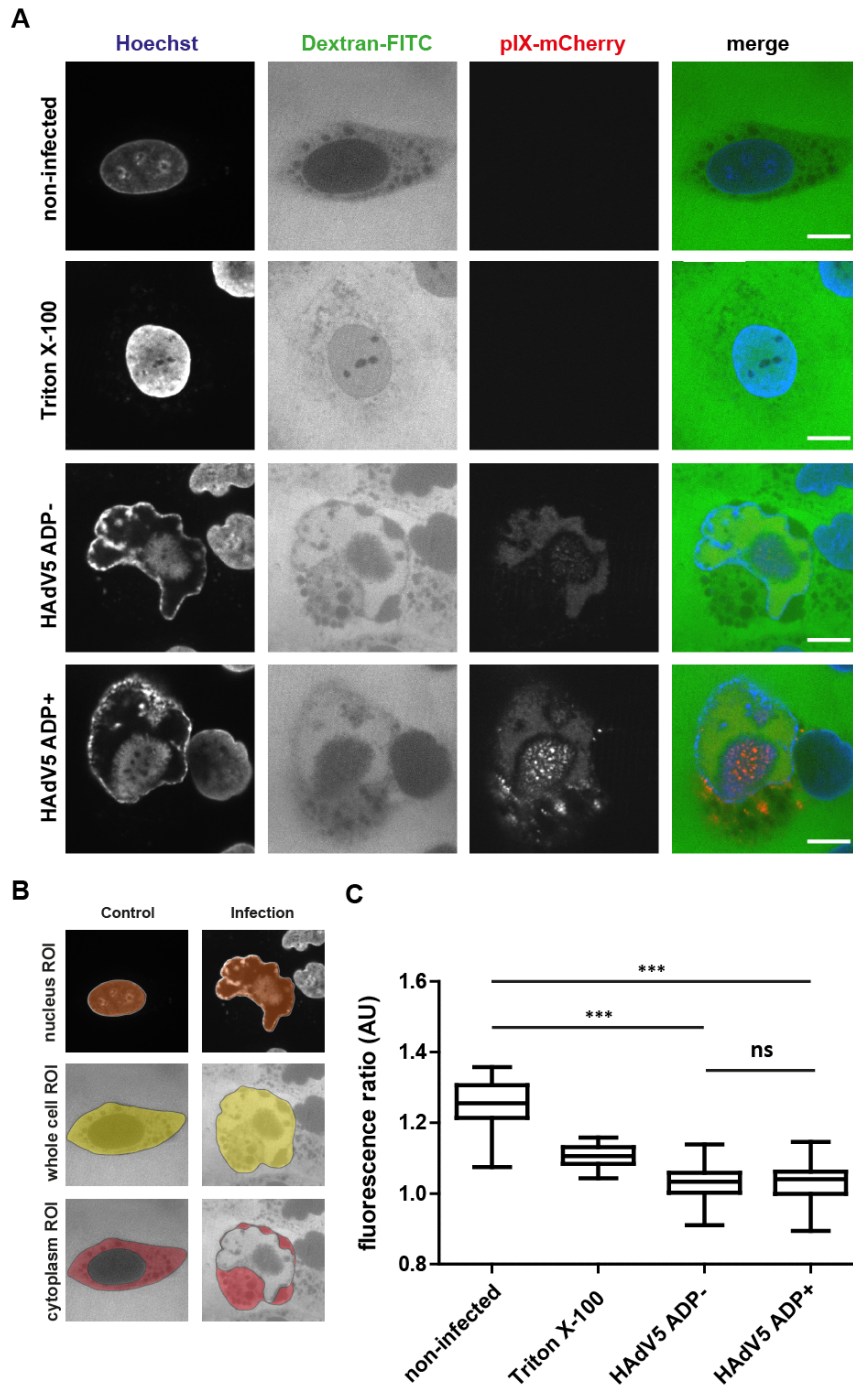
Figure 44: Infection by HAdV pIX-mCherry increases 70 kDa dextran-FITC permeability of the nuclear envelope. A549 cells were infected with HAdV5 pIX-mCherry ADP– or HAdV5 pIX-mCherry ADP+ and analysed at 48 hpi. A) Phenotype of A549 cells after incubation in dextran-FITC. The cells were imaged by live-cell confocal spinning-disk fluorescence microscopy. A representative cell is shown for each condition. The dsDNA signal is represented by Hoechst 33342 stain (Hoechst). The permeability probe dextran-FITC is detected via the FITC fluorescence (Dextran-FITC). Infected cells were detected by positive expression of pIX-mCherry (pIX-mCherry). The signal overlap is represented in colour (merge). Scalebars indicate 10 μm. B) Representation of ROIs for dextran-FITC signal analysis. The nuclear ROI was chosen based on the dsDNA signal, the whole-cell ROI was chosen based on dextran-FITC cell outline and the cytoplasmic ROI was selected as the whole-cell ROI excluding the nucleus ROI. C) Quantification of dextran-FITC signal ratio between cytoplasm and nucleus of infected cells (n = 50). The ratio is shown as a box plot including the median, upper quartile, lower quartile, maximum and minimum of the population. Statistical significance was calculated using a one-way ANOVA with post-hoc Tukey test.

4.2.7 pIX phenotype of lytic lymphocyte infection with HAdV5 pIX-mCherry is not dependent on the presence of ADP

It has been described that ADP expression is a modulator for lytic versus latent infection in lymphocytes (MURALI *et al.*, 2014). Infection with an ADP-deleted virus was shown to allow Jurkat survival for over a month. The effect of ADP on the formation of the LVAC in Jurkat cells was probed by immunofluorescence microscopy. This experiment could allow to show how latent infection might alter the phenotype of infected cells with respect to structural proteins required for productive infection of progeny particles.

To this end, Jurkat cells were infected with HAdV5 pIX-mCherry ADP– and HAdV5 pIX-mCherry ADP+ and fixed at 48 hpi (Figure 45A). The presence or absence of ADP did not have an effect on LVAC formation in the Jurkat cells. dsDNA was marginalised and accumulated as a honeycomb-like structure in the centre of the nucleus. Additionally, pIX-spots were detected within the LVAC. Additionally, the appearance of DBP was probed by immunofluorescence stain (Figure 45C). As for the cell line A549 (Figure 18), DBP was detected as a ring of individual foci surrounding the LVAC. To test the observation of Murali et al. that Jurkat cells can accommodate HAdV5 ADP– infection for long periods of time, a time-course experiment was performed to test the percentage of infected cells over the course of three weeks (Figure 45B). Indeed a clear difference between the presence or absence of ADP was measured. Over the first few days, the number of infected cells increased to about 25 % for both virus strains. After this, the percentage of infected cells for HAdV5 ADP– steadily decreased to about 5 % at 22 days post infection (dpi). In contrast, HAdV5 ADP+ reached an infection percentage of about 58 % at 6 dpi before that value decreased to a steady-state level of about 30 %. This experiment showed that the lytic LVAC phenotype of infection of Jurkat cells does not differ in the presence or absence of ADP. When analysing the population dynamics, ADP expression allows a faster infection of the cell population, whereas the absence of ADP leads to a slow loss of lytically infected cells over weeks.
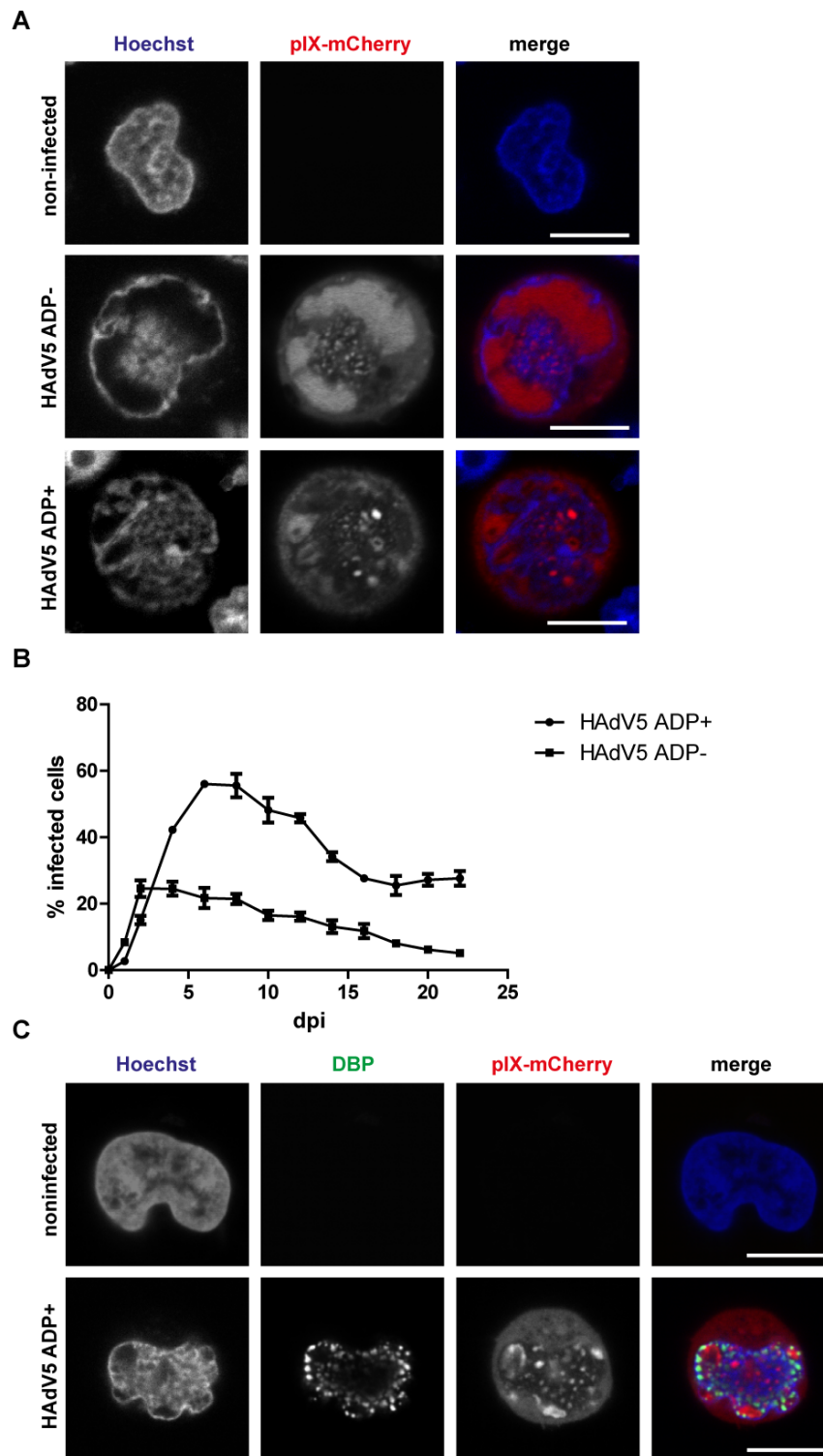
Figure 45: HAdV pIX-mCherry infection spreads faster in Jurkat cell population upon ADP expression, while and pIX-mCherry localisation is not altered by ADP expression. A) Comparison between pIX-mCherry localisation in infection with HAdV5 ADP– and HAdV5 ADP+ virus. B) FACS analysis of infection spread in Jurkat population. The average percentage of fluorescent cells indicating pIX-mCherry expression was measured over time (n = 3). C) DBP detection relative to LVAC in Jurkat infection with HAdV5 pIX-mCherry ADP+. The cells were imaged by confocal laser-scanning fluorescence microscopy. A representative cell is shown for each condition. The dsDNA signal is represented by Hoechst 33342 stain (Hoechst). pIX localisation is detected through the viral pIX-mCherry fusion construct (pIX-mCherry). DBP localisation is detected through an anti-DBP antibody (DBP). The signal overlap is represented in colour (merge). Scalebars indicate 10 μm.

Chapter 5

Discussion

5.1 Late nuclear morphogenesis of adenovirus infection

The majority of studies on the human adenovirus life-cycle characterise infection events within the first day of infection. These include virus adhesion within the first minutes, endosomal escape of virions within the first hour, viral genome import into the nucleus after about 3 hours, and the establishment of viral replication centres from 8 hours to up to 24 hours after infection (GREBER *et al.*, 1993; WICKHAM *et al.*, 1993; WODRICH *et al.*, 2006; KOMATSU *et al.*, 2016b, 2018). The first part of this work was aimed at even later infection events from 24 hpi to 48 hpi and mainly employed cellular imaging techniques including fluorescence and electron microscopy to study HAdV5-induced morphological changes. The analysis workflow was based on HAdV5 mutants expressing fluorescently tagged viral proteins V and IX. These mutants allowed to study the localisation of capsid components in live-cell conditions. The morphological changes that were observed included chromatin reorganisation as well as relocalisation of viral proteins DBP, pV and pIX to form a large intranuclear compartment. The compartment was characterised by an enrichment of pV-mCherry and dsDNA surrounding paracrystalline arrays of HAdV5 capsids. This large viral membrane-less compartment was termed 'late virion accumulation compartment'.

5.1.1 Fluorescent fusion protein labelling strategies allow to surmount antibody penetration limitations and can visualise the LVAC

In this project, the two adenoviral proteins V and IX were fused to fluorescent proteins as to study their intracellular localisation in light microscopy. One of the advantages of this

approach over immunofluorescence microscopy is that it allows to study morphological changes within single, live cells over time. Immunofluorescence microscopy can only achieve similar time-resolved results by analysing the phenotype of multiple chemically fixed cells within the entire population at different time-points. Another advantage of fluorescence fusion tagging is that the fluorescent tag is covalently bound to the protein of interest upon expression and enables direct imaging without the need for secondary probes. On the downside, fusion protein labelling should be carefully evaluated since the presence of a fusion partner can induce functional and structural alterations to the protein of interest.

Both pV and pIX were previously demonstrated to allow N-terminal or C-terminal modifications, respectively. In the case of pV, its N-terminus was fused to enhanced GFP and the resulting fusion protein was shown to localise identically to wt, non-tagged pV in transfection experiments (MATTHEWS and RUSSELL, 1998; MATTHEWS, 2001). In the case of pIX, the C-terminal coiled-coil domain was deleted without having an effect on incorporation of pIX into progeny capsids or their subsequent thermostability (VELLINGA *et al.*, 2005). Additionally, fusion of a FLAG tag and heparan sulfate binding motif to the C-terminus of pIX demonstrated the feasibility of this approach for ligand display on the HAdV capsid (DMITRIEV *et al.*, 2002).

A few further studies exist that use pV or pIX in combination with fluorophores to track virus particles in early HAdV infection. pV was fused to GFP in infection experiments, which allowed analysing the stability and disassembly of capsids at the NPC and showed that pV does not enter the nucleus (PUNTENER *et al.*, 2011). pIX was fused to enhanced GFP or mRFP1 to localise virions in the process of entry in single cells and even mouse tissue (LE *et al.*, 2004; MEULENBROEK *et al.*, 2004). Moreover, it was shown to be possible to generate a virus mutant that expresses both labelled pV and labelled pIX to allow for simultaneous detection via two fluorophores (UGAI *et al.*, 2010).

In this study, the nuclear morphology of HAdV5-infected cells was analysed by both fluorescently labelled fusion proteins and antibody probes. Comparison between the observable phenotype for each of these methods showed a lack of antibody penetration into the LVAC at late stages of the infection cycle. The antibody signal and tagged pV-mCherry and pIX-mCherry signals were only colocalising at 24 hpi, but not 48 hpi (Figure 19). Since no impairment to the antibody stain was observed at 24 hpi, a loss of antibody specificity for the tagged proteins can be ruled out as a cause for the divergence between phenotypes at 48 hpi.

Additionally, the pV-mCherry phenotype at 24 hpi was exactly the same as for wt pV when labelled with an antibody. Interestingly, wt pIX, when labelled at 24 hpi with an antibody, showed additional strongly fluorescent aggregates throughout the infected cell, a phenomenon not observed with the pIX-mCherry fusion protein. A similar phenomenon was described by Rosa-Calavatra et al. for pIX with the exception that the authors exclusively described nuclear inclusions of pIX (ROSA-CALATRAVA *et al.*, 2001, 2003). While in this work some of these inclusions were found in the nucleus, a large proportion was cytoplasmic. Only a few cells showed pIX aggregates exclusively in the nucleus. The authors proposed a model in which pIX sequesters in PML bodies which contributes to PML body neutralisation. However, judging from the aggregates in this work, it is entirely plausible that these inclusions simply originate from overexpression of the protein and thus would be found throughout the entire infected cell. Potentially, by tagging the small pIX with a large mCherry tag, its aggregation is reduced.

Importantly, the insertion of an mCherry fusion partner did not artificially induce LVAC formation since the LVAC was detectable in HAdV5 wt infection as well (Figures 14 & 15). In HAdV wt infection, the LVAC was observed as a honeycomb-like structure of dsDNA in the Hoechst channel, which was phenotypically identical to the honeycomb-like structure of dsDNA that was detected in HAdV5 pV-mCherry and HAdV5 pIX-mCherry infection. Assuming a lack of antibody penetration, it is conceivable how anti-pV would result in the observed ring structures at the edge of LVACs in HAdV5 wt infection. Presumably, the accumulation of viral proteins within the LVAC led to a phase, which in turn restricted the permeation of large antibodies. This explanation is also in line with the observation of the LVAC not being penetrated by dextran-FITC molecules, which was observed in the nuclear permeability assay (Figure 44).

Limitations in antibody penetration have already been suggested to be a result of high local amounts of protein (SCHNELL *et al.*, 2012). Schnell et al. pointed out that these issues most often could not be overcome by increasing the concentration of antibodies or permeabilisation agent. They demonstrated a lack of anti-GFP antibody penetration into the crowded protein environment of the nucleus to detect histone H2B-GFP protein and concluded that use of fixation and permeabilisation methods in immunofluorescence microscopy are often overlooked sources of artefacts in light microscopy. Similarly, antibodies targeting synaptic membrane proteins synapsin-1 and SNAP-25 were shown to not reach the perinuclear ER network, a limitation which was overcome by using significantly smaller cameloid nanobodies (MAIDORN *et al.*, 2019). Thus, a comparison with alternative

visualisation methods, such as genetically encoded fluorescent fusion proteins would enhance the biological conclusions that can be taken from immunofluorescence microscopy as well as control for staining artefacts. In the case of the LVAC, the penetration of Hoechst stain can also be explained by the significantly smaller size of the fluorophore. Therefore, these results strengthen the stance that ring-shaped structures in immunofluorescence microscopy should be cautiously interpreted.

The localisation of the anti-DBP antibody was comparable to the appearance of anti-pV, which formed a ring when staining the LVAC. The anti-DBP antibody stain also localised as a ring at 48 hpi, which consisted of individual DBP spots surrounding the LVAC (Figures 12 - 18). Similar separate DBP spots were reported by Genoveso et al. in late adenovirus replication compartments (GENOVESO *et al.*, 2019). The DBP ring phenotype can be explained by two hypotheses. Either DBP replication centres cluster on the edge of the LVAC, which could allow replicated viral genomes to be fed into the compartment. Alternatively, the LVAC is interspersed by DBP replication centres of which only the outer layer is stained by the antibody. The first hypothesis is aided by the observation that a similar ring stain appeared for hCMV DNA polymerase subunit UL44 (STRANG *et al.*, 2012). The authors reported the hCMV replication compartment to be surrounded by a ring of UL44, which led them to propose the model that newly replicated hCMV genomes are channelled towards to centre of the replication compartment. In contrast to this observation, a different UL44 antibody was shown to detect UL44 throughout the entire replication compartment and not just its periphery. This finding which reduces the likelihood of DBP just being localised on the edge of the LVAC as well (PENFOLD and MOCARSKI, 1997). The second hypothesis of the LVAC being interspersed by DBP would explain the formation of a dsDNA and pV honeycomb. In this scenario, DBP replication foci would sit within the empty holes of the pV honeycomb (Figure 46). A similar localisation was reported for the hCMV single-stranded DNA-binding protein UL57, which was found as multiple foci throughout the entire hCMV replication compartment (BENDER *et al.*, 2014). Evidence favouring the second hypothesis comes from 3view SEM analysis of the LVAC (Figure 30). Here, electron-dense spots were detected within the LVAC and not just as a single layer around the LVAC. Moreover, a gradual DBP antibody signal decrease towards the centre of the LVAC was visible, which is in accordance with the observation for pV and pIX antibodies.

Whereas pV and pIX localisation could be probed by using fluorescent fusion proteins, this approach was not successful for DBP. mCherry fusion to DBP led to phenotypical artefacts

compared to HAdV5 wt infection. The virus mutant HAdV5 DBP-mCherry was infectious and underwent successful replication in host cells, but no LVAC was formed and the dsDNA signal did not show a honeycomb-like conformation (Figure 29). Additionally, the double-labelled virus HAdV5 DBP-mCherry pIX-mNeonGreen did not form LVACs and also did not show any pIX spots late in infection. Accordingly, it can be concluded that even though the tool-set of fluorescent protein tags can be highly effective in studying the localisation of target proteins in live cells, potential artefacts arising from the fusion tag have to be carefully considered and ruled out by the right controls. Nevertheless, fusion of fluorescent proteins to pV and pIX has proven a powerful tool to study these proteins in live-cell conditions and to uncover nuclear reorganisation events in HAdV5 infection.

5.1.2 LVAC formation is associated with DBP replication centres and the LVAC retains assembled virions as paracrystalline virus arrays

The biological role of the LVAC is not entirely clear. It is reasonable to hypothesise the LVAC to be involved in HAdV5 assembly since the compartment contains necessary components of progeny virions. This study demonstrated the presence of replicated virus genomes and the virus core and capsid proteins pV and pIX. Furthermore, LVAC formation was shown to form in multiple cell lines including A549, H1299, MRC-5 and Jurkat cells (Figures 10, 11 & 45).

Early upon cellular expression, pV is known to be excluded from early DBP replication centres (MATTHEWS and RUSSELL, 1998). Wt pV, as well as pV-mCherry, showed this phenotype at 24 hpi. At this time-point, pV-devoid areas were observed to be filled with DBP (Figures 9 & 12). DBP was described as a marker of distinct nuclear viral replication centres (MONAGHAN et al., 1994; POMBO et al., 1994). After this early phenotype, pV undergoes nuclear redistribution, as was detected by live-cell fluorescence microscopy in this study. pV was found to organise into ring-like intermediate conformations before fully congregating to the honeycomb-like structure of the LVAC (Figure 20). Similarly, at 24 hpi dsDNA was detected as ring structures surrounding DBP replication centres. Since both pV and Hoechst 33342 bind double-stranded, but not single-stranded DNA, it is reasonable to hypothesise pV and Hoechst 33342 to interact with the replicated viral genomes which are accumulating around DBP replication centres. DBP, a binder of single-stranded DNA clearly occupied a different space to Hoechst 33342 and pV at time-points when pV rings were detected (Figure 21).

This organisation of early replication centres has also been described by Komatsu et al. The authors postulated single-stranded replicating genomes to be localised within the DBP replication centre and double-stranded replicated viral genomes spreading to the surroundings where they are histone-chromatinised for efficient transcription of late adenoviral genes (KOMATSU *et al.*, 2016b). These early replication centres were described to morph into late replication centres, also called ViPR bodies, after an unknown switch mechanism. These ViPR bodies consist of a site containing replicated, ready-to-assemble genomes, which is encircled by replicating genomes and DBP (KOMATSU *et al.*, 2018; GENOVESO *et al.*, 2019). In HAdV5 infection, multiple ViPR bodies can be detected, which were demonstrated to include chromatin remodelling proteins nucleophosmin-1 and Mybbp1a. In their study, Genoveso et al. hypothesised ViPR bodies to be relevant for adenoviral genome maintenance prior to packaging. Interestingly, the ViPR bodies were described to not contain capsid proteins such as pVI and pIX (GENOVESO *et al.*, 2019). In contrast, the LVAC was shown to include capsid proteins pV and pIX, which are required for the formation of progeny virus particles. The LVAC was detected at later time-points, which makes it likely that the LVAC develops after and out of viral ViPR bodies. In this timeline, early viral replication centres would first evolve into late replication centres, thus inducing ViPR body formation, and finally conclude in LVAC formation. This would be in accordance with the observation that infected nuclei contain multiple early replication compartments, late replication compartments and ViPR bodies, whereas mostly a single large LVAC compartment was detected.

Within the LVAC, pV-mCherry was forming a honeycomb-like structure (Figures 22). Quantification of the signal colocalisation between pV-mCherry and Hoechst 33342 showed that both probes occupy the same space within the LVAC. As they both bind replicated viral genomes, it can be assumed that they indicate the area of viral genomes to be assembled into progeny virions. The hypothesis of virus assembly within the LVAC is aided by the observation of pIX-mCherry spots to be localised contiguous to pV. Ugai et al. previously described the appearance of 'nuclear speckles' at a late time-point in infection when tagging pIX with mRFP1 and eGFP, but did not imply a biological function or speculate about the formation of these speckles (UGAI *et al.*, 2010). As part of this work, the pIX-mCherry spots within the LVAC could be described as paracrystalline arrays of fully assembled adenovirus particles. This was achieved by combining fluorescence microscopy images with transmission electron microscopy images of selected cells of interest (Figures 23 & 24). The formation of paracrystalline arrays is a known appearance for adenovirus as well as other viruses

including iridovirus, nodamura virus or zika virus (CHANDLER *et al.*, 1974; KIM *et al.*, 1997; LIU *et al.*, 2016; BALL *et al.*, 1992; LIU *et al.*, 2018). The biological role of these virus arrays is unknown and could be due to physical effects of the crowded environment of the cell. Molecular crowding was shown to affect the diffusion of larger particles and lead to abnormal motility in areas of high protein concentration (VILASECA *et al.*, 2011; PARRY *et al.*, 2014). It is imaginable that newly formed virus capsids accumulate due to a lack of motility within the LVAC leading to tight virion clustering. Such clusters could then be dispersed upon cell rupture in infection.   An effect that could contribute to the formation of these paracrystalline arrays could be the effect of Ostwald ripening (OSTWALD, 1900).   This physical effect has been suggested to be the driver for crystal formation as it reduces the total surface area of small solids within a liquid phase (ANDRIASYAN *et al.*, 2019).   A lack of mobility of these paracrystalline arrays within the LVAC was demonstrated by FRAP and live-cell analysis of the pIX spots (Figures 26 & 27). In FRAP, the pIX-mCherry spots were characterised as having very slow signal recovery when bleached. This conforms to the observation that pIX-mCherry spots were correlated with fully formed virions.   The population of pIX that is incorporated into virions would be immobilised by its capsid protein-protein interactions.   In the same FRAP experiment pV was only partially immobilised. Some pV protein is likely to be bound to dsDNA and corresponded to the measured 20 % immobile fraction. The remaining mobile 80 % of pV could contribute to a protein phase that might be hypothesised to be the cause of antibody penetration issues and could retain the progeny virions within.

5.1.3   Model of LVAC formation

The observations about pV-mCherry, pIX-mCherry and dsDNA localisation and motility can be joined in a model about the nuclear morphological changes that occur during late stages of human adenovirus infection (Figure 46). At 24 hpi, pV localises across the entire nuclear volume where it is interacting with newly synthesized double-stranded viral genomes. The viral genomes accumulate around viral DBP replication centres and cause pV to show an intermediate ring-like distribution. As soon as the DBP replication foci and rings congregate within the centre of the nucleus, pV migrates along subsequently forms the LVAC at 48 hpi. Since the DBP stain appeared not to penetrate the LVAC properly, the model includes the hypothesis that the LVAC is filled by DBP foci and does not only include a ring of DBP spots on its periphery. pV surrounding the DBP foci would appear to localise in the honeycomb

distribution that was detected by fluorescence microscopy. New progeny virions are likely to be formed adjacent to sites of replicated viral genomes and are assumed to accumulate within the LVAC. The motility of newly formed virions within the LVAC is restricted such that the formation of paracrystalline virus arrays is induced. As the minor capsid protein pIX is incorporated in progeny virions, it can be detected as fluorescent pIX-mCherry spots which show very limited signal recovery after photobleaching.
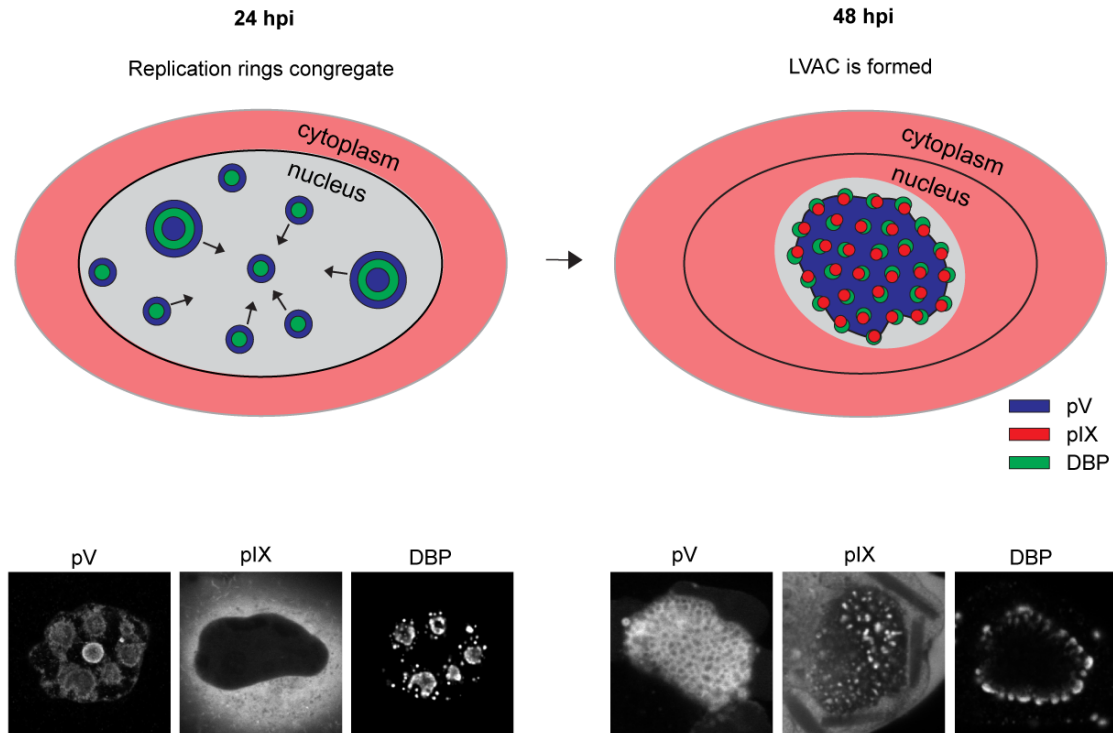
Figure 46: Model of LVAC formation. Starting from 24 hpi, pV accumulates around DBP replication centres driven by its interaction with replicated viral genomes. At this time-point, pIX is not found in the nucleus but is instead localised in the cytoplasm. During the transition between 24 and 48 hpi, the viral proteins pV and DBP congregate within the nucleus to form the LVAC at 48 hpi. At this time-point, pIX signal is found throughout the entire cell. Within the LVAC, pIX spots indicate the areas of accumulated assembled virus capsids. These pIX spots form in areas neighbouring viral genomes and pV. The model protein localisation of pV, pIX and DBP is accompanied by fluorescence microscopy images of the proteins observed in this work.

5.2 Nuclear egress of adenovirus particles

A crucial part of the HAdV life-cycle is the release of matured virions from the nucleus of infected cells into the cytoplasm and eventually into the surrounding of infected cells. This mechanism has been broadly described as lysis of the cell and release of most cellular content into the surrounding extracellular space (YAKIMOVICH *et al.*, 2012). However, an

exact mechanism is still elusive. An initial approach was to image and track HAdV5 particles crossing the nuclear envelope during egress. However, the strategy to label progeny virions by incorporating a fluorescent protein marker into capsid-incorporated proteins such as pV and pIX did not achieve the desired outcome. It was possible to detect individual pV or pIX labelled capsids upon entry into newly infected cells (Figure 8). However, the expression of soluble protein and the mere abundance of progeny virions led to a high signal background within infected cells which made it impossible to distinguish individual particles (Figure 24). Such an approach was demonstrated as feasible for the herpesviruses pseudorabies virus and HSV-1 (HOGUE *et al.*, 2014; BOSSE *et al.*, 2015). For these viruses, labelling capsid or tegument components with mRFP allowed to track individual capsid within the nucleus. To achieve single HAdV particle detection, the local concentration of fluorophores would have to be increased to give a signal over background, or a virus mutant capable of nuclear egress but incapable of producing such high virion progeny numbers would have to be used.

5.2.1   ADP localisation is altered upon addition of tags

ADP has been shown to be involved in the release of HAdV5 particles from infected epithelial cells and leads to higher infection spread within permissive lymphocyte populations (Figures 32 & 45). This effect has also been used in HAdV-based oncolytic vector systems, which overexpress ADP to increase the spread in cancer tissue and increase cell death (DORONIN *et al.*, 2003; GROS and GUEDAN, 2010). Since HAdV2 ADP was shown to localise in the nuclear membrane, it was speculated to facilitate nuclear egress of HAdV particles by causing nuclear pores or membrane breaks (SCARIA *et al.*, 1992).

To analyse the localisation of ADP in this work, it was tagged with fusion proteins mCherry and the small HA tag (Figures 33 & 34). No published work exists in which HAdV5 ADP was modified by the addition of tags. The only evidence as to which regions of ADP might accommodate changes comes from a mutagenesis study in which selected regions of the protein were deleted and the remaining lytic activity and localisation of ADP were analysed (TOLLEFSON *et al.*, 2003). The authors showed that ADP is permissive for changes at the C-terminus and can retain its lytic activity even when not localising to the nuclear membrane, which hints at an alternative mechanism of ADP function different from membrane pore formation. When tagging ADP with mCherry and an HA tag, a similar phenomenon was observed. The tagged ADP protein mainly localised in cytoplasmic vesicles, rather than in the nuclear envelope as was described for HAdV2 (SCARIA *et al.*, 1992;

TOLLEFSON *et al.*, 2003).

It is imaginable that ADP function is not dependent on its nuclear membrane localisation but rather on its post-translational modification in the Golgi apparatus. A mutation of HAdV2 ADP to abolish O-glycosylation has been described to also abolish the lytic function of ADP and its localisation to cytoplasmic vesicles associated with the Golgi apparatus (TOLLEFSON *et al.*, 2003). Moreover, the addition of Nelfinavir, an inhibitor against ADP, does not reduce ADP localisation to the nuclear membrane but abolishes its localisation within cytoplasmic vesicles (GEORGI *et al.*, 2020a). The HA-labelled ADP variant that was analysed in this work still retained lytic functionality but did not localise to the nuclear membrane (Figure 34). Georgi et al. speculate that ADP functionality could depend on its palmitoylation and that Nelfinavir could inhibit the palmitoyl acyltransferase or disperse its substrate palmitoyl-coenzyme A. Palmitoylation could be important for dimerisation of ADP and its membrane sorting. This is in accordance with the observation that palmitoylation is important for viral release by membrane permeabilisation in SARS-CoV-1 E protein and mouse hepatitis virus E protein orf3 which act as viroporins (LIAO *et al.*, 2006; DING *et al.*, 2017; GOUTTENOIRE *et al.*, 2018).

5.2.2 HAdV5 infection causes nuclear envelope destabilisation and nuclear membrane breaks independent of ADP expression

A prerequisite for nuclear rupture could be the global destabilisation of the nuclear membrane by HAdV5 infection. When analysing nuclear lamin A, a clear reduction of signal at the nuclear envelope could be detected (Figures 35 & 36). This effect was observed independently of ADP expression. Lamin A/C has been shown to be important for nuclear mechanics since lamin mutations cause nuclear deformation as well as nuclear membrane ruptures (LAMMERDING *et al.*, 2004; GUPTA *et al.*, 2010; CHEN *et al.*, 2018). HAdV5 potentially causes lamin A degradation as part of a cell death process that is induced by infection. Lamin A has been described to be cleaved by caspases during apoptosis (RUCHAUD *et al.*, 2002). Alternatively, lamin A cleavage could be caused by a viral candidate such as AVP, which has been shown to cleave cytokeratin 18 to disrupt the cytokeratin network of infected cells. This process has been hypothesised to lead to cellular destabilisation and more efficient virus release (CHEN *et al.*, 1993). Indeed, electron microscopy analysis of the nuclear membrane in HAdV5 infection showed frequent nuclear membrane invaginations, fragmentations, as well as breaks in the nuclear envelope (Figures 37 & 39).

HAdV infection can lead to the formation of intranuclear protein crystals, which were commonly described in HAdV2 and HAdV5 infection (WEBER and STICH, 1969; MORGAN *et al.*, 1960). These crystals were described to consist of penton and fibre protein (WILLS *et al.*, 1973; FRANQUEVILLE *et al.*, 2008). Franqueville et al. suggested the crystals to harbour a biological role as hubs for virus assembly rather than being overexpression byproducts, since virus mutants defective of assembly did not show an increased occurrence of penton-fibre protein crystals. It is also imaginable that these large protein crystals lead to rupture of the nuclear membrane when they physically grow larger that the confinement of the nuclear membrane. Some evidence of crystal growing larger than the regular nuclear boundary were detected for HAdV2 crystals (HENRY and ATCHISON, 1971). This phenomenon of crystals extending the nucleus could also be detected for HAdV5 (Figure 38). The nuclear membrane was shown to stretch around the edge of large protein crystals. However, no evidence for membrane breaks around these sites was observed. It is more likely that during the loss of cellular structural integrity, when infected cells lose contact to the support of the culture dish and become more round, the shape of the nucleus changes and clashes with the elongated shape of the protein crystals. In this way, crystal formation could aid the destabilisation of the nuclear membrane.

Many viruses express proteins that harbour membrane-modulating properties. In enveloped viruses, these proteins catalyse fusion between the virus and host cell membrane and include proteins such as influenza virus hemagglutinin, human immunodeficiency virus 1 (HIV-1) gp41, HSV-1 gB protein or SARS-CoV-2 spike glycoprotein (HAN *et al.*, 2001; MCCUNE *et al.*, 1988; VOLLMER *et al.*, 2020; BENTON *et al.*, 2020). In non-enveloped viruses, such proteins are involved in forming pores or disrupting the plasma or endosomal membrane. They include poliovirus VP1 and VP4, rotavirus VP4, reovirus penetration protein γ1, polyomavirus VP2 and VP3 or HAdV pVI (BRANDENBURG *et al.*, 2007; DORMITZER *et al.*, 2004; CHANDRAN *et al.*, 2002; WIETHOFF *et al.*, 2005; GIORDA *et al.*, 2013). These proteins are all required for overcoming the physical membrane barrier of the host cell during entry of the virus. However, much less is known about proteins modulating membranes during nuclear or cellular egress. While cell lysis as part of a cell death pathway is often suggested to be the main driver for virion release, viral proteins are likely to modulate the process to ensure strong progeny virion production before host cell death. In polyomaviruses, two proteins VP4 and agnoprotein have been reported to aid virus nuclear and cellular egress. Both proteins act as viroporins and can permeabilise membranes to allow for the passage of large molecules (DANIELS *et al.*, 2007; SUZUKI *et al.*, 2010; PANOU *et al.*,

2018). Agnoprotein has been shown to include an amphipathic helix which allows oligomerisation within the membrane leaflet to produce a hydrophilic core (CORIC *et al.*, 2014). It is imaginable that HAdVs possess a similar mechanism for membrane pore formation. However, analysis of the transmembrane helix of HAdV5 ADP showed that it does not form an amphipathic helix (Figure 31).

Nevertheless, the impact of ADP on nuclear membrane permeability was analysed. The effect of envelope breaks or pores can be quantified by fluorescence microscopy though nuclear permeability assays. Two strategies can be deployed here. Either a fluorescent dye is externally added to cells, or a fluorescent protein including an NES or NLS is intracellularly expressed. Previously, addition of external dyes of a specific size was used to analyse nuclear membrane permeability during apoptosis (ROEHRIG *et al.*, 2003; GROTE and FERRANDO-MAY, 2007). Fluorescent proteins with NLS tags were also previously used to quantify the effect of nuclear membrane breaks as a result of nuclear lamin deletion or cell migration during cancer metastasis (ROBIJNS *et al.*, 2016; DENAIS *et al.*, 2016; CHEN *et al.*, 2018). In this work, both assays were used to test the ADP-dependent nuclear membrane permeability in HAdV5 infection. Using BFP-NES expression, an increased signal of BFP-NES in the nuclei of infected cells compared to non-infected cells was detected (Figure 43). However, there was no statistically significant difference in BFP-NES levels with or without expression of ADP. This assay is dependent on the action of CRM1-dependent transport of the NES-tagged fluorophore. It is therefore also imaginable that the nuclear export machinery could be negatively affected by the viral infection rather than having an increased nuclear membrane permeability. An argument against this hypothesis is that HAdV infection relies on the action of CRM1 for virion trafficking at the nuclear envelope as well as for export of viral mRNA transcripts (STRUNZE *et al.*, 2005; SCHMID *et al.*, 2012; WANG *et al.*, 2017). CRM1 inhibitors have even been suggested as antiviral treatments against influenza A virus, hCMV and HAdV5 (SANCHEZ *et al.*, 2007; WATANABE *et al.*, 2011; SCHMID *et al.*, 2012). To avoid effects of the cellular machinery in the nuclear permeability assay, Dextran-FITC was used as a fluorescent substrate. Again, an increased nuclear permeability was detected in HAdV5 infection, but no ADP-dependence was measured (Figure 44). HAdV2 capsid disassembly at the NPC has been reported to increase nuclear pore permeability (STRUNZE *et al.*, 2011). Interestingly, the authors described a time-dependence of this effect in a way that Dextran-FITC only permeated upon immediate infection of cells, whereas the dye could not permeate the nucleus at 4 hpi. It is therefore unlikely, that the described effect is identical to the described nuclear permeability at 48 hpi.

The observed increased nuclear permeability in infection could be explained by the appearance of nuclear membrane lesions that were observed in this study through multiple electron microscopy-based techniques. Membrane breaks were detected by classical TEM and 3view serial block-face SEM (Figures 39 & 40) as well as cryo-tomography (Figure 42). By combining these techniques, potential artefacts that could occur during preparation for either method can be ruled out as a cause for membrane damage. Particularly, since no membrane damage was observed in non-infected cells the membrane damage can be ascribed to the effect of HAdV5 infection. Similar nuclear membrane lesions in adenovirus infection have been described for mouse adenovirus in infection of mouse adrenal glads (HOENIG *et al.*, 1974). TEM studies showed virions in the cytoplasm accompanied by large breaks in the nuclear membrane. Additionally, nuclear membrane breaks were reported for HAdV2 infection of A549 cells and HAdV5 infection of HeLa cells (MORGAN *et al.*, 1960; GEORGI *et al.*, 2020a). While no virions were observed to be sitting within a gap of the nuclear membrane, virus particles were observed in the cytoplasm close to nuclear membrane lesions (Figure 42), which hints at the particle release from the nucleus at these sites. This observation was only made for HAdV5 ADP+, whereas no virus particles were detected outside the nucleus for HAdV5 ADP– infection. A possible explanation for this observation could be that even though nuclear membrane breaks are not directly induced by ADP, their size or frequency may be increased to allow for more efficient release of virus particles from the nucleus.

5.2.3 The ADP functional mechanism remains elusive

With a size of 10.5 kDa, ADP is a small protein and does not include a known functional protein motif. Its transmembrane region and palmitoylation anchor the protein in membranes. It is imaginable that the protein acts as a membrane-anchored hub/scaffold to recruit further proteins that cause nuclear membrane breakdown and cell lysis. A potential cell death pathway that may be induced is necroptosis. During necroptosis, MLKL oligomerisation was shown to induce membrane disruption (WANG *et al.*, 2014). The effect of necroptosis inhibitors including inhibitors against caspase 8, RIPK1 and RIPK3 were tested, but none showed a clear effect on the survival of A549 cells during infection with and without ADP (data not shown). So far, contradictory results have been published as to which kind of cell death leads to cell lysis in HAdV infection, which has been described as autophagy, apoptosis, necroptosis or a combination of multiple pathways (JIANG *et al.*, 2011;

RODRIGUEZ-ROCHA *et al.*, 2011; ZOU *et al.*, 2004; BAIRD *et al.*, 2008; WEIGERT *et al.*, 2017).

To analyse potential binding partners of ADP, a co-immunoprecipitation analysis of ADP tagged with an HA was performed (data not shown). ADP binding to proposed interaction partners such as MAD2B, E4orf4 and E1B-19K was tested. MAD2B is, to date, the only confirmed interaction partner of ADP (YING and WOLD, 2003). E4orf4 is known to cause membrane blebbing by induction of apoptosis (MARCELLUS *et al.*, 1998; LIVNE *et al.*, 2001). E1B-19K was speculated to be involved in nuclear egress since it localises to the nuclear membrane and could thus potentially interact with ADP. In this context, ADP was hypothesised to inhibit E1B-19K which in turn could abrogate E1B-19Ks anti-apoptotic effect and cause the cell to undergo cell death to release virus particles. However, no evidence exists to confirm the interaction between ADP and E1B-19K. Both proteins did not interact in a Y2H approach (YING and WOLD, 2003) and also were not detected in Co-IP of ADP-HA with subsequent western blot analysis (data not shown).

Interestingly, the ADP equivalent of HAdV3 of species B, CR1β, does not have a known function yet. Knock-out of species B CR1β was shown to have no effect on virus progeny release, plaque size or general cell viability (FRIETZE *et al.*, 2012; NARAYAN and KAJON, 2020). Other than HAdV5 ADP, the HAdV3 CR1β localises to the cytoplasmic membrane and cytoplasmic vesicles when tagged with an HA tag. Additionally, the inhibitor Nelfinavir, which has recently been described to reduce lytic cell spread of HAdV2 in an ADP-dependent manner, also has an effect on cell spread independently of ADP (KALDOR *et al.*, 1997; GEORGI *et al.*, 2020a,b). This effect was demonstrated since HAdVs of species B also were Nelfinavir-sensitive despite their lack of ADP. In summary, there is still a lot to be discovered about the mode of action of ADP and the coexisting pathways that lead to virus egress independently of ADP.

5.2.4   Model of HAdV5 nuclear egress

The observations about lamin A localisation, TEM and SEM imaging of the nuclear membrane of HAdV5 infected cells and observations of virus particles outside of the membrane can be combined in a model about adenovirus nuclear egress. By means of infection, the lamin A stabilising network of the nucleus is degraded or redistributed such that the nuclear envelope loses stability. Consequently, the nuclear membrane develops invaginations. In addition to the global nuclear membrane instability, sites of nuclear damage occur, which are visible as lesions

in TEM and SEM imaging. Not in all cases virus particles are associated with these lesions, which is indicating that the lesions do not occur due to direct particle interactions. Single virus particles can escape via these lesions and are detected in the cytoplasm. Even later in infection, the nuclear membrane ruptures and releases larger amounts of nuclear material, including virus particles as well as virus protein crystals into the cytoplasm. The virus particles are released into the surrounding extracellular space when cells lyse due to cell death.
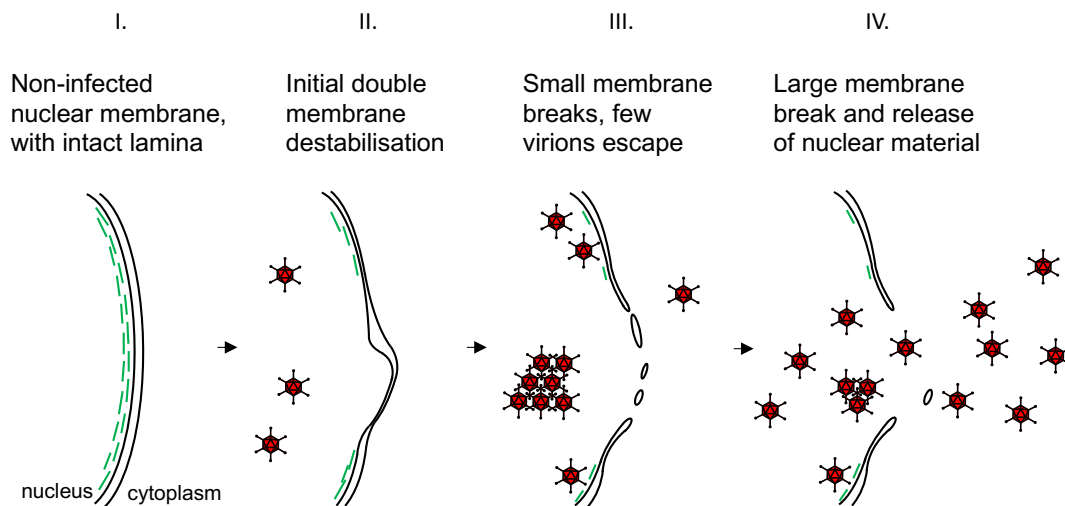
Figure 47: Model of nuclear membrane changes occurring in HAdV5 nuclear egress. The nuclear double membrane is represented as two separate black lines. I) The non-infected, intact nuclear envelope has a regular, evenly rounded appearance. Nuclear lamins (green lines) decorate the inner nuclear membrane in give it stability. II) During infection, the nuclear lamina is degraded and redistributed, likely resulting in a loss of nuclear membrane stability. The membrane loses its even structure and the distance between the two nuclear membrane layers varies. III) The nuclear membrane develops small lesions through which few virus particles can escape and can be found in the cytoplasm. Most of the virus particles stay retained within the nucleus. IV) The small lesions develop to large nuclear membrane breaks. Large quantities of virus and nucleoplasm can escape into the cytoplasm.

Chapter 6

Conclusion and Outlook

In summary, the work of this dissertation was aimed at characterising the late stages of human adenovirus infection. In the first part, a novel viral intranuclear compartment was identified in which virus capsid and core proteins accumulate. This compartment was termed LVAC and the formation of paracrystalline virus arrays was detected within. As part of characterising the LVAC with antibodies, a limited penetration capability of antibodies into the LVAC was detected and characterised. From these fluorescence and electron microscopy observations, a model of HAdV assembly within the LVAC was derived, which can be used as a basis to study virion assembly with higher resolution methods, such as PALM/STORM microscopy or electron cryo tomography after focussed ion beam milling. Higher spacial resolution imaging could elucidate the fine-organisation of ssDNA, dsDNA, packaging proteins, and structural proteins that accumulate around viral replication compartments. Higher temporal resolution imaging by lattice light-sheet microscopy could improve the understanding of virion mobility within the LVAC and could detect whether paracrystalline arrays at the edges of the LVAC dissociate to individual virions to be released into the nucleoplasm. The fluorescence protein labelling strategy that was employed in this study should be extended to other viral proteins involved in assembly such as packaging protein L1-52/55K or AVP.

In the second part of the work, the nuclear egress of progeny virions was analysed. While the exact mechanism still remains hidden, the global membrane destabilisation accompanied by the induction of nuclear membrane breaks was characterised by combining classical and electron cryo microscopy approaches. Nuclear membrane lesions were identified under cryo conditions, which can control for potential preparation induced artifacts of classical EM preparation approaches. The adenovirus death protein, the so-far only cell lysis modulating factor of HAdV5 egress, did not have a clear influence on the

nuclear membrane breaks that were observed. Further studies towards the exact localisation of ADP and its interactions partners could elucidate the mechanism by which ADP causes accelerated virion release from infected cells. In particular, proteomics approaches and screening for cell pathways involved in signalling for cell death would be suitable methods. A deeper understanding of pathways for virion release from cells could increase a targeted approach for inhibiting HAdV spread in infected tissue as well as improve the effectiveness of HAdV-based vector systems.

Chapter 7

Bibliography

ABE S., MIYAMURA K., OBA T., TERAKURA S., KASAI M., KITAORI K., SASAKI T. and KODERA Y. (2003) Oral ribavirin for severe adenovirus infection after allogeneic marrow transplantation, *Bone Marrow Transplantation* **32**, 1107–1108.

ABOU EL HASSAN M. A. I., VAN DER MEULEN-MUILEMAN I., ABBAS S. and KRUYT F. A. E. (2004) Conditionally Replicating Adenoviruses Kill Tumor Cells via a Basic Apoptotic Machinery-Independent Mechanism That Resembles Necrosis-Like Programmed Cell Death, *Journal of Virology* **78**(22), 12243–12251.

AHI Y. S., HASSAN A. O., VEMULA S. V., LI K., JIANG W., ZHANG G. J. and MITTAL S. K. (2017) Adenoviral E4 34K protein interacts with virus packaging components and may serve as the putative portal, *Scientific Reports* **7**(7582), 1–8.

AHI Y. S., VEMULA S. V., HASSAN A. O., COSTAKES G., STAUFFACHER C. and MITTAL S. K. (2015) Adenoviral L4 33K forms ring-like oligomers and stimulates ATPase activity of IVa2: Implications in viral genome packaging, *Frontiers in Microbiology* **6**(318), 1–11.

ANDERSON C. W., YOUNG M. E. and FLINT S. J. (1989) Characterization of the adenovirus 2 virion protein, Mu, *Virology* **172**(2), 506–512.

ANDRADE F., CASCIOLA-ROSEN L. A. and ROSEN A. (2003) A Novel Domain in Adenovirus L4-100K Is Required for Stable Binding and Efficient Inhibition of Human Granzyme B: Possible Interaction with a Species-Specific Exosite, *Molecular and Cellular Biology* **23**(17), 6315–6326.

ANDRIASYAN V., YAKIMOVICH A., GEORGI F., PETKIDIS A., WITTE R., PUNTENER D. and GREBER U. F. (2019) Deep learning of virus infections reveals mechanics of lytic cells, *bioRxiv* pp. 1–18.

ANGELETTI P. C. and ENGLER J. A. (1998) Adenovirus Preterminal Protein Binds to the CAD Enzyme at Active Sites of Viral DNA Replication on the Nuclear Matrix, *Journal of Virology* **72**(4), 2896–2904.

ARAUJO F. D., STRACKER T. H., CARSON C. T., LEE D. V. and WEITZMAN M. D. (2005) Adenovirus Type 5 E4orf3 Protein Targets the Mre11 Complex to Cytoplasmic Aggresomes, *Journal of Virology* **79**(17), 11382–11391.

ARNBERG N., PRING-AKERBLOM P. and WADELL G. (2002) Adenovirus Type 37 Uses Sialic Acid as a Cellular Receptor on Chang C Cells, *Journal of Virology* **76**(17), 8834–8841.

BAIRD S. K., AERTS J. L., EDDAOUDI A., LOCKLEY M., LEMOINE N. R. and MCNEISH I. A. (2008) Oncolytic adenoviral mutants induce a novel mode of programmed cell death in ovarian cancer, *Oncogene* **27**(22), 3081–3090.

BAKER A., ROHLEDER K. J., HANAKAHI L. A. and KETNER G. (2007) Adenovirus E4 34k and E1b 55k Oncoproteins Target Host DNA Ligase IV for Proteasomal Degradation, *Journal of Virology* **81**(13), 7034–7040.

BAKER A. T., MUNDY R. M., DAVIES J. A., RIZKALLAH P. J. and PARKER A. L. (2019) Human adenovirus type 26 uses sialic acid-bearing glycans as a primary cell entry receptor, *Science Advances* **5**(9), 2–11.

BALL L. A., AMANN J. M. and GARRETT B. K. (1992) Replication of nodamura virus after transfection of viral RNA into mammalian cells in culture, *Journal of Virology* **66**(4), 2326–2334.

BELL P., LIEBERMAN P. M. and MAUL G. G. (2000) Lytic but Not Latent Replication of Epstein-Barr Virus Is Associated with PML and Induces Sequential Release of Nuclear Domain 10 Proteins, *Journal of Virology* **74**(24), 11800–11810.

BENDER B. J., COEN D. M. and STRANG B. L. (2014) Dynamic and Nucleolin-Dependent Localization of Human Cytomegalovirus UL84 to the Periphery of Viral Replication Compartments and Nucleoli, *Journal of Virology* **88**(20), 11738–11747.

BENEDICT C. A., NORRIS P. S., PRIGOZY T. I., BODMER J.-L., MAHR J. A., GARNETT C. T., MARTINON F., GOODING L. R. and WARE C. F. (2001) Three Adenovirus E3 Proteins Cooperate to Evade Apoptosis by Tumor Necrosis Factor-related Apoptosis-inducing Ligand Receptor-1 and -2, *The Journal of Biological Chemistry* **276**(5), 3270–3278.

BENKÖ M., ELÖ P., URSU K., AHNE W., LAPATRA S. E., THOMSON D. and HARRACH B. (2002) First Molecular Evidence for the Existence of Distinct Fish and Snake Adenoviruses, *Journal of Virology* **76**(19), 10056–10059.

BENKÖ M. and HARRACH B. (1998) A proposal for a new (third) genus within the family Adenoviridae, *Archives of Virology* **143**(4), 829–837.

BENTON D. J., WROBEL A. G., XU P., ROUSTAN C., MARTIN S. R., ROSENTHAL P. B., SKEHEL J. J. and GAMBLIN S. J. (2020) Receptor binding and priming of the spike protein of SARS-CoV-2 for membrane fusion, *Nature* **588**(7837), 327–330.

BERCIAUD S., RAYNE F., KASSAB S., JUBERT C., FAURE-DELLA CORTE M., SALIN F., WODRICH H. and LAFON M. E. (2012) Adenovirus infections in Bordeaux University Hospital 2008–2010: Clinical and virological features, *Journal of Clinical Virology* **54**(4), 302–307.

BERGELSON J. M., CUNNINGHAM J. A., DROGUETT G., EVELYN A., KRITHIVAS A., HONG J. S., HORWITZ M. S., CROWELL R. L., FINBERG R. W., BERGELSON J. M., CUNNINGHAM J. A., DROGUETT G., KURT-JONES E. A., KRITHIVAS A., HONG J. S., HORWITZ M. S., CROWELL R. L. and FINBERG R. W. (1997) Isolation of a Common Receptor for Coxsackie B Viruses and Adenoviruses 2 and 5, *Science* **275**(5304), 1320–1323.

BERK A. J. and SHARP P. A. (1976) Structure of the Adenovirus 2 Early mRNAs, *Cell* **14**, 695–711.

BERSCHEMINSKI J., WIMMER P., BRUN J., IP W. H., GROITL P., HORLACHER T., JAFFRAY E., HAY R. T., DOBNER T. and SCHREINER S. (2014) Sp100 Isoform-Specific Regulation of Human Adenovirus 5 Gene Expression, *Journal of Virology* **88**(11), 6076–6092.

BEWLEY M. C., SPRINGER K., ZHANG Y.-B., FREIMUTH P. and FLANAGAN J. M. (1999) Structural Analysis of the Mechanism of Adenovirus Binding to Its Human Cellular Receptor, CAR, *Science* **286**(5444), 1579–1583.

BHAT G., SIVARAMAN L., MURTHY S., DOMER P. and THIMMAPPAYA B. (1987) In vivo identification of multiple promoter domains of adenovirus EIIA-late promoter, *The EMBO Journal* **6**(7), 2045–2052.

BINGER M. H. and FLINT S. J. (1984) Accumulation of early and intermediate mRNA species during subgroup C adenovirus productive infections, *Virology* **136**(2), 387–403.

BODNAR A. G., OUELLETTE M., FROLKIS M., HOLT S. E., CHIU C. P, MORIN G. B., HARLEY C. B., SHAY J. W., LICHTSTEINER S. and WRIGHT W. E. (1998) Extension of life-span by introduction of telomerase into normal human cells, *Science* **279**(5349), 349–352.

BOLTE S. and CORDELIERES F. P. (2006) A guided tour into subcellular colocalization analysis in light microscopy, *Journal of Microscopy* **224**(3), 213–232.

BONDESSON M., OHMAN K., MANERVIK M., FAN S. and AKUSJÄRVI G. (1996) Adenovirus E4 open reading frame 4 protein autoregulates E4 transcription by inhibiting E1A transactivation of the E4 promoter, *Journal of Virology* **70**(6), 3844–3851.

BOSSE J. B., HOGUE I. B., FERIC M., THIBERGE S. Y., SODEIK B., BRANGWYNNE C. P. and ENQUIST L. W. (2015) Remodeling nuclear architecture allows efficient transport of herpesvirus capsids by diffusion, *Proceedings of the National Academy of Sciences* **112**(42), E5725–E5733.

BOWLES N. E., NI J., KEARNEY D. L., PAUSCHINGER M., SCHULTHEISS H.-P, MCCARTHY R., HARE J., BRICKER J. T., BOWLES K. R. and TOWBIN J. A. (2003) Detection of viruses in myocardial tissues by polymerase chain reaction. evidence of adenovirus as a common cause of myocarditis in children and adults, *Journal of the American College of Cardiology* **42**(3), 466–472.

BOYD J. M., MALSTROM S., SUBRAMANIAN T., VENKATESH L. K., SCHAEPER U., ELANGOVAN B., D'SA-EIPPER C. and CHINNADURAI G. (1994) Adenovirus E1B 19 kDa and Bcl-2 proteins interact with a common set of cellular proteins, *Cell* **79**(2), 341–351.

BOYER J., ROHLEDER K. and KETNER G. (1999) Adenovirus E4 34k and E4 11k inhibit double strand break repair and are physically associated with the cellular DNA-dependent protein kinase, *Virology* **263**(2), 307–312.

BRADFORD M. M. (1976) A rapid and sensitive method for the quantitation of microgram quantities of protein utilizing the principle of protein-dye binding, *Analytical Biochemistry* **72**(1), 248–254.

BRANDENBURG B., LEE L. Y., LAKADAMYALI M., RUST M. J., ZHUANG X. and HOGLE J. M. (2007) Imaging poliovirus entry in live cells, *PLoS Biology* **5**(7), 1543–1555.

BRANTON P. E. and ROOPCHAND D. E. (2001) The role of adenovirus E4orf4 protein in viral replication and cell killing, *Oncogene* **20**, 7855–7865.

BREMNER K., SCHERER J., YI J., VERSHININ M., GROSS S. P. and VALLEE R. B. (2009) Adenovirus Transport through a Direct Cytoplasmic Dynein-Hexon Interaction, *Cell Host Microbe* **6**(6), 523–535.

BURCKHARDT C. J., SUOMALAINEN M., SCHOENENBERGER P., BOUCKE K., HEMMI S. and GREBER U. F. (2011) Drifting motions of the adenovirus receptor CAR and immobile integrins initiate virus uncoating and membrane lytic protein exposure, *Cell Host and Microbe* **10**(2), 105–117.

BURG J. L., SCHWEITZER J. and DANIELL E. (1983) Introduction of superhelical turns into DNA by adenoviral core proteins and chromatin assembly factors, *Journal of Virology* **46**(3), 749–755.

BURGERT H.-G. and KVIST S. (1985) An adenovirus type 2 glycoprotein blocks cell surface expression of human histocompatibility class I antigens, *Cell* **41**(3), 987–997.

CARAVOKYRI C. and LEPPARD K. N. (1995) Constitutive episomal expression of polypeptide IX (pIX) in a 293-based cell line complements the deficiency of pIX mutant adenovirus type 5, *Journal of Virology* **69**(11), 6627–33.

CARAVOKYRI C. and LEPPARD K. N. (1996) Human Adenovirus Type 5 Variants with Sequence Alterations Flanking the E2A Gene: Effects on E2 Expression and DNA Replication, *Virus Genes* **12**(1), 65–75.

CARLEMALM E., GARAVITO R. M. and VILLIGER W. (1982) Resin development for electron microscopy and an analysis of embedding at low temperature, *Journal of Microscopy* **126**(2), 123–143.

CARVALHO T., SEELER J. S., ÖHMAN K., JORDAN P., PETTERSSON U., AKUSJÄRVI G., CARMO-FONSECA M. and DEJEAN A. (1995) Targeting of adenovirus E1A and E4-ORF3 proteins to nuclear matrix-associated PML bodies, *Journal of Cell Biology* **131**(1), 45–56.

CASSANY A., RAGUES J., GUAN T., BÉGU D., WODRICH H., KANN M., NEMEROW G. R. and GERACE L. (2015) Nuclear Import of Adenovirus DNA Involves Direct Interaction of Hexon with an N-Terminal Domain of the Nucleoporin Nup214, *Journal of Virology* **89**(3), 1719–1730.

CEPKO L. and SHARP P. A. (1982) Assembly of Adenovirus Major Capsid Protein Is Mediated by a Nonvirion Protein, *Cell* **31**(2 Pt 1), 407–415.

CHALLBERG M. D. and RAWLINS D. R. (1984) Template requirements for the initiation of adenovirus DNA replication, *Proceedings of the National Academy of Sciences of the United States of America* **81**(1), 100–104.

CHANDLER F. W., CALLAWAY C. S. and ADAMS S. R. (1974) Pancreatitis Associated with an Adenovirus in a Rhesus Monkey, *Veterinary Pathology* **11**(2), 165–171.

CHANDRAN K., FARSETTA D. L. and NIBERT M. L. (2002) Strategy for Nonenveloped Virus Entry: a Hydrophobic Conformer of the Reovirus Membrane Penetration Protein μ1 Mediates Membrane Disruption, *Journal of Virology* **76**(19), 9920–9933.

CHATTERJEE P. K., VAYDA M. E. and FLINT S. J. (1985) Interactions among the three adenovirus core proteins, *Journal of Virology* **55**(2), 379–386.

CHEN J., MORRAL N. and ENGEL D. A. (2007) Transcription releases protein VII from adenovirus chromatin, *Virology* **369**(2), 411–422.

CHEN M., MERMOD N. and HORWITZ M. S. (1990) Protein-Protein Interactions between Adenovirus DNA Polymerase and Nuclear Factor I Mediate Formation of the DNA Replication Preinitiation Complex, *The Journal of Biological Chemistry* **265**(30), 18634–18642.

CHEN N. Y., KIM P., WESTON T. A., EDILLO L., TU Y., FONG L. G. and YOUNG S. G. (2018) Fibroblasts lacking nuclear lamins do not have nuclear blebs or protrusions but nevertheless have frequent nuclear membrane ruptures, *Proceedings of the National Academy of Sciences of the United States of America* **115**(40), 10100–10105.

CHEN P. H., ORNELLES D. A. and SHENK T. (1993) The adenovirus L3 23-kilodalton proteinase cleaves the amino-terminal head domain from cytokeratin 18 and disrupts the cytokeratin network of HeLa cells, *Journal of Virology* **67**(6), 3507–3514.

CHHABRA P., PAYNE D. C., SZILAGYI P. G., EDWARDS K. M., STAAT M. A., SHIRLEY S. H., WIKSWO M., NIX W. A., LU X., PARASHAR U. D. and VINJÉ J. (2013) Etiology of Viral Gastroenteritis in Children <5 Years of Age in the United States, 2008 – 2009, *Journal of Infectious Diseases* **208**(5), 790–800.

CHING W., KOYUNCU E., SINGH S., ARBELO-ROMAN C., HARTL B., KREMMER E., SPEISEDER T., MEIER C. and DOBNER T. (2013) A Ubiquitin-specific Protease Possesses a Decisive Role for Adenovirus Replication and Oncogene-mediated Transformation, *PLoS Pathogens* **9**(3), e1003273.

CHROBOCZEK J., BIEBER F. and JACROT B. (1992) The sequence of the genome of adenovirus type 5 and its comparison with the genome of adenovirus type 2, *Virology* **186**(1), 280–285.

CHROHOCZEK J., VIARD F. and D'HALLUIN J.-C. (1986) Human adenovirus 2 temperature-sensitive mutant 112 contains three mutations in the protein IIIa gene, *Gene* **49**, 157–160.

COLBY W. W. and SHENK T. (1981) Adenovirus type 5 virions can be assembled in vivo in the absence of detectable polypeptide IX, *Journal of Virology* **39**(3), 977–80.

CONDEZO G. N., MARABINI R., AYORA S., CARAZO J. M., ALBA R., CHILLÓN M. and SAN MARTÍN C. (2015) Structures of Adenovirus Incomplete Particles Clarify Capsid Architecture and Show Maturation Changes of Packaging Protein L1 52/55k, *Journal of Virology* **89**(18), 9653–9664.

CONDEZO G. N. and SAN MARTÍN C. (2017) Localization of adenovirus morphogenesis players, together with visualization of assembly intermediates and failed products, favor a model where assembly and packaging occur concurrently at the periphery of the replication center, *PLoS Pathogens* **13**(4), 1–26.

CORIC P., SARIBAS A. S., ABOU-GHARBIA M., CHILDERS W., WHITE M. K., BOUAZIZ S. and SAFAK M. (2014) Nuclear Magnetic Resonance Structure Revealed that the Human Polyomavirus JC Virus Agnoprotein Contains an -Helix Encompassing the Leu/Ile/Phe-Rich Domain, *Journal of Virology* **88**(12), 6556–6575.

COSTANTINI M. L., FOSSATI M., FRANCOLINI M. and SNAPP E. L. (2012) Assessing the Tendency of Fluorescent Proteins to Oligomerize under Physiologic Conditions, *Traffic* **13**(5), 643–649.

CRANFILL P. J., SELL B. R., BAIRD M. A., ALLEN J. R., LAVAGNINO Z., DE GRUITER H. M., KREMERS G. J., DAVIDSON M. W., USTIONE A. and PISTON D. W. (2016) Quantitative assessment of fluorescent proteins, *Nature Methods* **13**(7), 557–562.

CRAWFORD-MIKSZA L. and SCHNURR D. P. (1996) Analysis of 15 Adenovirus Hexon Proteins Reveals the Location and Structure of Seven Hypervariable Regions Containing Serotype-Specific Residues, *Journal of Virology* **70**(3), 1836–1844.

CUCONATI A., DEGENHARDT K., SUNDARARAJAN R., ANSCHEL A. and WHITE E. (2002) Bak and Bax Function To Limit Adenovirus Replication through Apoptosis Induction, *Journal of Virology* **76**(9), 4547–4558.

CUCONATI A., MUKHERJEE C., PEREZ D. and WHITE E. (2003) DNA damage response and MCL-1 destruction initiate apoptosis in adenovirus-infected cells, *Genes & Development* **17**, 2922–2932.

DAI X., WU L., SUN R. and ZHOU Z. H. (2017) Atomic Structures of Minor Proteins VI and VII in Human Adenovirus, *Journal of Virology* **91**(24), 1–15.

DALLAIRE F., BLANCHETTE P., GROITL P., DOBNER T. and BRANTON P. E. (2009) Identification of Integrin α3 as a New Substrate of the Adenovirus E4orf6/E1B 55-Kilodalton E3 Ubiquitin Ligase Complex, *Journal of Virology* **83**(11), 5329–5338.

DANIELL E. (1976) Genome structure of incomplete particles of adenovirus, *Journal of Virology* **19**(2), 685–708.

DANIELL E., GROFF D. E. and FEDOR M. J. (1981) Adenovirus chromatin structure at different stages of infection, *Molecular and Cellular Biology* **1**(12), 1094–1105.

DANIELS R., SADOWICZ D. and HEBERT D. N. (2007) A very late viral protein triggers the lytic release of SV40, *PLoS Pathogens* **3**(7), 928–938.

DAVISON A. J., BENKO M. and HARRACH B. (2003) Genetic content and evolution of adenoviruses, *Journal of General Virology* **84**(11), 2895–2908.

DAVISON A. J., WRIGHT K. M. and HARRACH B. (2000) DNA sequence of frog adenovirus, *Journal of General Virology* **81**, 2431–2439.

DE JONG R. N., MEIJER L. A. T. and VAN DER VLIET P. C. (2003) DNA binding properties of the adenovirus DNA replication priming protein pTP, *Nucleic Acids Research* **31**(12), 3274–3286.

DE ORY F., AVELLÓN A., ECHEVARRÍA J. E., SÁNCHEZ-SECO M. P., TRALLERO G., CABRERIZO M., CASAS I., POZO F., FEDELE G., VICENTE D., PENA M. J., MORENO A., NIUBO J., RABELLA N., RUBIO G., PÉREZ-RUIZ M., RODRÍGUEZ-IGLESIAS M., GIMENO C., EIROS J. M., MELÓN S., BLASCO M., LÓPEZ-MIRAGAYA I., VARELA E., MARTINEZ-SAPIÑA A., RODRÍGUEZ G., MARCOS M. Á., GEGÚNDEZ M. I., CILLA G., GABILONDO I., NAVARRO J. M., TORRES J., AZNAR C., CASTELLANOS A., GUISASOLA M. E., NEGREDO A. I., TENORIO A. and VÁZQUEZ-MORÓN S. (2013) Viral infections of the central nervous system in Spain: a prospective study, *Journal of Medical Virology* **85**(3), 554–562.

DENAIS C. M., GILBERT R. M., ISERMANN P., MCGREGOR A. L., LINDERT M., WEIGELIN B., DAVIDSON P. M., FRIEDL P. and LAMMERDING J. (2016) Nuclear envelope rupture and repair during cancer cell migration, *Science* **352**(6283), 353–358.

DESAGHER S., OSEN-SAND A., NICHOLS A., ESKES R., MONTESSUIT S., LAUPER S., MAUNDRELL K., ANTONSSON B. and MARTINOU J.-C. (1999) Bid-induced Conformational Change of Bax Is Responsible for Mitochondrial Cytochrome c Release during Apoptosis, *The Journal of Cell Biology* **144**(5), 891–902.

DETRAIT M., PROPHETIS S. D., DELVILLE J.-P. and KOMUTA M. (2015) Fulminant isolated adenovirus hepatitis 5 months after haplo-identical HSCT for AML, *Clinical Case Reports* **3**(10), 802–805.

D'HALLUIN J. C., MILLEVILLE M., BOULANGER P. A. and MARTIN G. R. (1978) Temperature-sensitive mutant of adenovirus type 2 blocked in virion assembly: accumulation of light intermediate particles, *Journal of Virology* **26**(2), 344–56.

DHURANDHAR E. J., DUBUISSON O., MASHTALIR N., KRISHNAPURAM R., HEGDE V. and DHURANDHAR N. V. (2011) E4orf1: A Novel Ligand That Improves Glucose Disposal in Cell Culture, *Plos One* **6**(8), 1–11.

DING Q., HELLER B., CAPUCCINO J. M. V., SONG B., NIMGAONKAR I., HREBIKOVA G., CONTRERAS J. E. and PLOSS A. (2017) Hepatitis E virus ORF3 is a functional ion channel required for release of infectious particles, *Proceedings of the National Academy of Sciences of the United States of America* **114**(5), 1147–1152.

DIX I. and LEPPARD K. N. (1993) Regulated Splicing of Adenovirus Type 5 E4 Transcripts and Regulated Cytoplasmic Accumulation of E4 mRNA, *Journal of Virology* **67**(6), 3226–3231.

DIX I. and LEPPARD K. N. (1995) Expression of adenovirus type 5 E4Orf2 protein during lytic infection, *Journal of General Virology* **76**(4), 1051–1055.

DMITRIEV I. P., KASHENTSEVA E. A. and CURIEL D. T. (2002) Engineering of Adenovirus Vectors Containing Heterologous Peptide Sequences in the C Terminus of Capsid Protein IX Engineering of Adenovirus Vectors Containing Heterologous Peptide Sequences in the C Terminus of Capsid Protein IX, *Journal of Virology* **76**(14), 6893–6899.

DOBNER T., HORIKOSHI N., RUBENWOLF S. and SHENK T. (1996) Blockage by Adenovirus E4orf6 of Transcriptional Activation by the p53 Tumor Suppressor, *Science* **272**(5267), 1470–1473.

DONOVAN-BANFIELD I., TURNELL A. S., HISCOX J. A., LEPPARD K. N. and MATTHEWS D. A. (2020) Deep splicing plasticity of the human adenovirus type 5 transcriptome drives virus evolution, *Communications Biology* **3**(1), 1–14.

DORMITZER P. R., NASON E. B., PRASA B. V. V. and HARRISON S. C. (2004) Structural rearrangements in the membrane penetration protein of a non-enveloped virus, *Nature* **26**(430), 1053–1058.

DORONIN K., TOTH K., KUPPUSWAMY M., KRAJCSI P., TOLLEFSON A. E. and WOLD W. S. M. (2003) Overexpression of the ADP (E3-11.6K) protein increases cell lysis and spread of Adenovirus, *Virology* **305**(2), 378–387.

DOUCAS V., ISHOV A. M., ROMO A., JUGUILON H., WEITZMAN M. D., EVANS R. M. and MAUL G. G. (1996) Adenovirus replication is coupled with the dynamic properties of the PML nuclear structure, *Genes and Development* **10**(2), 196–207.

DROZDETSKIY A., COLE C., PROCTER J. and BARTON G. J. (2015) JPred4: A protein secondary structure prediction server, *Nucleic Acids Research* **43**(W1), W389–W394.

DUBRIDGE R. B., TANG P., HSIA H. C., LEONG P. M., MILLER J. H. and CALOS M. P. (1987) Analysis of mutation in human cells by using an Epstein-Barr virus shuttle system., *Molecular and Cellular Biology* **7**(1), 379–387.

ENDERS J. F., BELL J. A., DINGLE J. H., FRANCIS T. J., HILLEMAN M. R., HUEBNER R. J. and PAYNE A. M. (1956) Adenoviruses: group name proposed for new respiratory-tract viruses., *Science* **124**(3212), 119–120.

ENDTER C., HA B., SPRUSS T., HAUBER J. and DOBNER T. (2005) Blockage of CRM1-dependent nuclear export of the adenovirus type 5 early region 1B 55-kDa protein augments oncogenic transformation of primary rat cells, *Oncogene* **24**, 55–64.

ENDTER C., KZHYSHKOWSKA J., STAUBER R. and DOBNER T. (2001) SUMO-1 modification required for transformation by adenovirus type 5 early region 1B 55-kDa oncoprotein, *Proceedings of the National Academy of Sciences* **98**(20), 11312–11317.

ESKES R., DESAGHER S., ANTONSSON B. and MARTINOU J.-C. (2000) Bid Induces the Oligomerization and Insertion of Bax into the Outer Mitochondrial Membrane, *Molecular and Cellular Biology* **20**(3), 929–935.

EVANS J. D. and HEARING P. (2005) Relocalization of the Mre11-Rad50-Nbs1 Complex by the Adenovirus E4 ORF3 Protein Is Required for Viral Replication, *Journal of Virology* **79**(10), 6207–6215.

EWING S. G., BYRD S. A., CHRISTENSEN J. B., TYLER R. E. and IMPERIALE M. J. (2007) Ternary Complex Formation on the Adenovirus Packaging Sequence by the IVa2 and L4 22-Kilodalton Proteins, *Journal of Virology* **81**(22), 12450–12457.

FARLEY D. C., BROWN J. L. and LEPPARD K. N. (2004) Activation of the Early-Late Switch in Adenovirus Type 5 Major Late Transcription Unit Expression by L4 Gene Products, *Journal of Virology* **78**(4), 1782–1791.

FERGUSON B., KRIPPL B., ANDRISANI O., JONES N., WESTPHAL H. and ROSENBERG M. (1985) E1A 13S and 12S mRNA Products Made in Escherichia coli Both Function as Nucleus-Localized Transcription Activators but Do Not Directly Bind DNA, *Molecular and Cellular Biology* **5**(10), 2653–2661.

FEUERBACH D., ETTELDORF S., EBENAU-JEHLE C., ABASTADO J. P., MADDEN D. and BURGERT H. G. (1994) Identification of amino acids within the MHC molecule important for the interaction with the adenovirus protein E3/19K, *The Journal of Immunology* **153**(4), 1626–1636.

FIELD J., NIKAWA J., BROEK D., MACDONALD B., RODGERS L., WILSON I. A., LERNER R. A. and WIGLER M. (1988) Purification of a RAS-responsive adenylyl cyclase complex from Saccharomyces cerevisiae by use of an epitope addition method, *Molecular and Cellular Biology* **8**(5), 2159–2165.

FLEISCHLI C., SIRENA D., LESAGE G., HAVENGA M. J., CATTANEO R., GREBER U. F. and HEMMI S. (2007) Species B adenovirus serotypes 3, 7, 11 and 35 share similar binding sites on the membrane cofactor protein CD46 receptor, *Journal of General Virology* **88**(11), 2925–2934.

FLEWETT T. H., BRYDEN A. S. and DAVIES H. (1975) Epidemic viral enteritis in a long-stay childrens's ward, *The Lancet* **1**(7897), 4–5.

FLOMM F. J., SOH T. K., SCHNEIDER C., BRITT H. M., THALASSINOS K., PFITZNER S., REIMER R., GRÜNEWALD K. and BOSSE J. B. (2021) Intermittent bulk release of human cytomegalovirus through multivesicular bodies, *bioRxiv* pp. 1–28.

FLORESCU D. F. and SCHAENMAN J. M. (2019) Adenovirus in solid organ transplant recipients : Guidelines from the American Society of Transplantation Infectious Diseases Community of Practice, *Clinical Transplantation* **33**, 1–8.

FORNEROD M., OHNO M., YOSHIDA M. and MATTAJ I. W. (1997) CRM1 is an export receptor for leucine-rich nuclear export signals, *Cell* **90**(6), 1051–1060.

Forrester N. A., Patel R. N., Speiseder T., Groitl P., Sedgwick G. G., Shimwell N. J., Seed R. I., Catnaigh P. O., McCabe C. J., Steward G. S., Dobner T., Grand R. J. A., Martin A. and Turnell A. S. (2012) Adenovirus E4orf3 Targets Transcriptional Intermediary Factor 1γ for Proteasome-Dependent Degradation during Infection, *Journal of Virology* **86**(6), 3167–3179.

Franqueville L., Henning P., Magnusson M., Vigne E., Schoehn G., Blair-Zajdel M. E., Habib N., Lindholm L., Blair G. E., Hong S. S. and Boulanger P. (2008) Protein crystals in adenovirus type 5-infected cells: Requirements for intranuclear crystallogenesis, structural and functional analysis, *PLoS One* **3**(8), e2894.

Frietze K. M., Campos S. K. and Kajon A. E. (2012) No evidence of a death-like function for species B1 human adenovirus type 3 E3-9K during A549 cell line infection, *BMC Research Notes* **5**(429), 1–9.

Fukuda M., Asano S., Nakamura T., Adachi M., Yoshida M., Yanagida M. and Nishida E. (1997) CRM1 is responsible for intracellular transport mediated by the nuclear export signal, *Nature* **390**(6657), 308–311.

Furcinitti P., van Oostrum J. and Burnett R. (1989) Adenovirus polypeptide IX revealed as capsid cement by difference images from electron microscopy and crystallography, *The EMBO Journal* **8**(12), 3563–3570.

Gaba A., Ayalew L., Makadiya N. and Tikoo S. (2017) Proteolytic Cleavage of Bovine Adenovirus 3-Encoded pVIII, *Journal of Virology* **91**(10), 1–18.

Garnett C. T., Talekar G., Mahr J. A., Huang W., Zhang Y., Ornelles D. A. and Gooding L. R. (2009) Latent Species C Adenoviruses in Human Tonsil Tissues, *Journal of Virology* **83**(6), 2417–2428.

Gastaldelli M., Imelli N., Boucke K., Amstutz B., Meier O. and Greber U. F. (2008) Infectious adenovirus type 2 transport through early but not late endosomes, *Traffic* **9**(12), 2265–2278.

Gautier R., Douguet D., Antonny B. and Drin G. (2008) HELIQUEST: A web server to screen sequences with specific α-helical properties, *Bioinformatics* **24**(18), 2101–2102.

Gavin P. J. and Katz B. Z. (2002) Intravenous Ribavirin Treatment for Severe Adenovirus Disease in Immunocompromised Children, *Pediatrics* **110**(1), 1–10.

Genoveso M. J., Hisaoka M., Komatsu T., Wodrich H., Nagata K. and Okuwaki M. (2019) Formation of adenovirus DNA replication compartments and viral DNA accumulation sites by host chromatin regulatory proteins including NPM1, *The FEBS Journal* **287**, 205–217.

Georgi F., Andriasyan V., Witte R., Murer L., Hemmi S., Yu L., Grove M., Meili N., Kuttler F., Yakimovich A., Turcatti G. and Greber U. F. (2020a) The FDA-Approved Drug Nelfinavir Inhibits Lytic Cell-Free but not Cell-Associated Nonlytic Transmission of Human Adenovirus, *Antimicrobial Agents and Chemotherapy* **64**(9), 1–23.

Georgi F., Kuttler F., Murer L., Andriasyan V., Witte R., Yakimovich A., Turcatti G. and Greber U. F. (2020b) A high-content image-based drug screen of clinical compounds against cell transmission of adenovirus, *Scientific Data* **7**(1), 1–12.

Ghosh M. K. and Harter M. L. (2003) A Viral Mechanism for Remodeling Chromatin Structure in G0 Cells, *Molecular Cell* **12**, 255–260.

GIARD D. J., AARONSON S. A., TODARO G. J., ARNSTEIN P., KERSEY J. H. and PARKS W. P. (1973) In vitro cultivation of human tumors: Establishment of cell lines derived from a series of solid tumors, *Journal of the National Cancer Institute* **51**(5), 1417–1423.

GIORDA K. M., RAGHAVA S., ZHANG M. W. and HEBERT D. N. (2013) The viroporin activity of the minor structural proteins VP2 and VP3 is required for SV40 propagation, *Journal of Biological Chemistry* **288**(4), 2510–2520.

GOODING L. R., SOFOLA I. O., TOLLEFSON A. E., DUERKSEN-HUGHES P. and WOLD W. S. M. (1990) The adenovirus E3-14.7K protein is a general inhibitor of tumor necrosis factor-mediated cytolysis, *Journal of Immunology* **145**(9), 3080–3086.

GOUTTENOIRE J., POLLÁN A., ABRAMI L., OECHSLIN N., MAURON J., MATTER M., OPPLIGER J., SZKOLNICKA D., DAO THI V. L., VAN DER GOOT F. G. and MORADPOUR D. (2018) Palmitoylation mediates membrane association of hepatitis E virus ORF3 protein and is required for infectious particle secretion, *PLoS Pathogens* **14**(12), 1–24.

GRÄBLE M. and HEARING P. (1990) Adenovirus type 5 packaging domain is composed of a repeated element that is functionally redundant, *Journal of Virology* **64**(5), 2047–2056.

GRAHAM F. L., SMILEY J., RUSSELL W. C. and NAIRN R. (1977) Characteristics of a human cell line transformed by DNA from human adenovirus type 5., *The Journal of General Virology* **36**(1), 59–74.

GREBER U. F., WEBSTER P., WEBER J. and HELENIUS A. (1996) The role of the adenovirus protease on virus entry into cells, *The EMBO Journal* **15**(8), 1766–1777.

GREBER U. F., WILLETTS M., WEBSTER P. and HELENIUS A. (1993) Stepwise dismantling of adenovirus 2 during entry into cells, *Cell* **75**(3), 477–486.

GREEN N. M., WRIGLEY N. G., RUSSELL W. C., MARTIN S. R. and MCLACHLAN A. D. (1983) Evidence for a repeating cross-beta sheet structure in the adenovirus fibre, *The EMBO Journal* **2**(8), 1357–1365.

GROS A. and GUEDAN S. (2010) Adenovirus Release from the Infected Cell as a Key Factor for Adenovirus Oncolysis, *The Open Gene Therapy Journal* **3**, 24–30.

GROTE P. and FERRANDO-MAY E. (2007) In vitro assay for the quantitation of apoptosis-induced alterations of nuclear envelope permeability, *Nature Protocols* **1**(6), 3034–3040.

GUIMET D. and HEARING P. (2013) The Adenovirus L4-22K Protein Has Distinct Functions in the Posttranscriptional Regulation of Gene Expression and Encapsidation of the Viral Genome, *Journal of Virology* **87**(13), 7688–7699.

GUPTA A., JHA S., ENGEL D. A., ORNELLES D. A. and DUTTA A. (2013) Tip60 Degradation by Adenovirus Relieves Transcriptional Repression of Viral Transcriptional Activator E1A, *Oncogene* **32**(42), 5017–5025.

GUPTA P., BILINSKA Z. T., SYLVIUS N., BOUDREAU E., VEINOT J. P., LABIB S., BOLONGO P. M., HAMZA A., JACKSON T., PLOSKI R., WALSKI M., GRZYBOWSKI J., WALCZAK E., RELIGA G., FIDZIANSKA A. and TESSON F. (2010) Genetic and ultrastructural studies in dilated cardiomyopathy patients: A large deletion in the lamin A/C gene is associated with cardiomyocyte nuclear envelope disruption, *Basic Research in Cardiology* **105**(3), 365–377.

GUPTA S., MANGEL W. F., MCGRATH W. J., PEREK J. L., LEE D. W., TAKAMOTO K. and CHANCE M. R. (2004) DNA binding provides a molecular strap activating the adenovirus proteinase, *Molecular and Cellular Proteomics* **3**(10), 950–959.

GUSTIN K. E. and IMPERIALE M. J. (1998) Encapsidation of Viral DNA Requires the Adenovirus L1 52/55-Kilodalton Protein, *Journal of Virology* **72**(10), 7860–7870.

GYOZO L. K., DAVISON A. J., PALYA V., HARRACH B. and BENKÖ M. (2012) Communication Genome sequence of a waterfowl aviadenovirus, goose adenovirus 4, *Journal of General Virology* **93**(8), 2457–2465.

HADV WORKING GROUP (2019) HAdV Working Group, http://hadvwg.gmu.edu (accessed 26.01.20).

HAGEN W. J., WAN W. and BRIGGS J. A. (2017) Implementation of a cryo-electron tomography tilt-scheme optimized for high resolution subtomogram averaging, *Journal of Structural Biology* **197**(2), 191–198.

HALBERT D. N., CUTT J. R. and SHENK T. (1985) Adenovirus Early Region 4 Encodes Functions Required for Efficient DNA Replication, Late Gene Expression, and Host Cell Shutoff, *Journal of Virology* **56**(1), 250–257.

HAN X., BUSHWELLER J. H., CAFISO D. S. and TAMM L. K. (2001) Membrane structure and fusion-triggering conformational change of the fusion domain from influenza hemagglutinin, *Nature Structural Biology* **8**(8), 715–720.

HANAHAN D. and MESELSON M. (1983) Plasmid screening at high colony density, *Methods in Enzymology* **100**, 333–342.

HARRACH B., BENKÖ M., BOTH G. W., BROWN M., DAVISON A. J., ECHAVARRIA M., HESS M., JONES M. S., KAJON A., LEHMKUHL H. D., MAUTNER V., MITTAL S. K. and WADELL G. (2012) Adenoviridae, in *Virus Taxonomy*, pp. 125–141, Elsevier, San Diego.

HARTLEY J. L., TEMPLE G. F. and BRASCH M. A. (2000) DNA Cloning Using In Vitro Site-Specific Recombination, *Genome Research* **10**(11), 1788–1795.

HASSON T. B., SOLOWAY P. D., ORNELLES D. A., DOERFLER W. and SHENK T. (1989) Adenovirus L1 52- and 55-kilodalton proteins are required for assembly of virions, *Journal of Virology* **63**(9), 3612–3621.

HAUSMANN J., ORTMANN D., WITT E., VEIT M. and SEIDEL W. (1998) Adenovirus death protein, a transmembrane protein encoded in the E3 region, is palmitoylated at the cytoplasmic tail, *Virology* **244**(2), 343–351.

HAWKINS L. K. and WOLD W. S. M. (1992) A 12,500 MW Protein Is Coded by Region E3 of Adenovirus, *Virology* **494**, 486–494.

HAYES B. W., TELLING G. C., MYAT M. M., WILLIAMS J. F. and FLINT S. J. (1990) The adenovirus L4 100-kilodalton protein is necessary for efficient translation of viral late mRNA species, *Journal of Virology* **64**(6), 2732–2742.

HAYLES M. F., STOKES D. J., PHIFER D. and FINDLAY K. C. (2007) A technique for improved focused ion beam milling of cryo-prepared life science specimens, *Journal of Microscopy* **226**(3), 263–269.

HEARING P., SAMULSKI R. J., WISHART W. L. and SHENK T. (1987) Identification of a repeated sequence element required for efficient encapsidation of the adenovirus type 5 chromosome, *Journal of Virology* **61**(8), 2555–2558.

HENRY C. J. and ATCHISON R. W. (1971) Paracrystal Formation in Cell Cultures Infected with Adenovirus Type 2, *Journal of Virology* **8**(6), 842–849.

HILGENDORF A., LINDBERG J., RUZSICS Z., HO S., ELSING A., LO M., ENGELMANN H. and BURGERT H.-G. (2003) Two Distinct Transport Motifs in the Adenovirus E3/10.4–14.5 Proteins Act in Concert to Down-modulate Apoptosis Receptors and the Epidermal Growth Factor Receptor, *The Journal of Biological Chemistry* **278**(51), 51872–51884.

HILLEMAN M. R. (1953) Epidemiology of Adenovirus Respiratory Infections in Military Recruit Populations, *Annals of the New York Academy of Sciences* **67**(8), 262–272.

HILLEMAN M. R. and WERNER J. H. (1954) Recovery of New Agent from Patients with Acute Respiratory Illness, *Experimental Biology and Medicine* **85**(1), 183–188.

HILLEMAN M. R., WERNER J. H., DASCOMB H. E. and BUTLER R. L. (1955) Epidemiologic investigations with respiratory disease virus RI-67, *American Journal of Public Health and the Nation's Health* **45**(2), 203–210.

HINDLEY C. E., LAWRENCE F. J. and MATTHEWS D. A. (2007) A role for transportin in the nuclear import of adenovirus core proteins and DNA, *Traffic* **8**(10), 1313–1322.

HO Q. Y., TAN C. S., THIEN S. Y., KEE T. and CHLEBICKI M. P. (2019) The use of intravesical cidofovir for the treatment of adenovirus-associated haemorrhagic cystitis in a kidney transplant recipient, *Clinical Kidney Journal* **12**(5), 745–747.

HOENIG E. M., MARGOLIS G. and KILHAM L. (1974) Experimental adenovirus infection of the mouse adrenal gland. I. Light microscopic observation, *American Journal of Pathology* **75**(2), 363–374.

HOGUE I. B., BOSSE J. B., HU J. R., THIBERGE S. Y. and ENQUIST L. W. (2014) Cellular Mechanisms of Alpha Herpesvirus Egress: Live Cell Fluorescence Microscopy of Pseudorabies Virus Exocytosis, *PLoS Pathogens* **10**(12).

HONG J.-Y., LEE H.-J., PIEDRA P. A., CHOI E.-H., PARK K.-H., KOH Y.-Y. and KIM W.-S. (2001) Lower Respiratory Tract Infections due to Adenovirus in Hospitalized Korean Children: Epidemiology, Clinical Features, and Prognosis, *Clinical Infectious Diseases* **32**, 1423–1429.

HORWITZ G. A., ZHANG K., MCBRIAN M. A., GRUNSTEIN M., KURDISTANI K. and BERK A. J. (2008) Adenovirus Small e1a Alters Global Patterns of Histone Modification, *Science* **321**(5892), 1084–1085.

HUANG F., BAI J. U. N., ZHANG J. and YANG D. (2019) Identification of potential diagnostic biomarkers for pneumonia caused by adenovirus infection in children by screening serum exosomal microRNAs, *Molecular Medicine Reports* **19**, 4306–4314.

HUANG W. and FLINT S. J. (2003) Unusual Properties of Adenovirus E2E Transcription by RNA Polymerase III, *Journal of Virology* **77**(7), 4015–4024.

HUEBNER R. J., ROWE W. P., WARD T. G., PARROTT R. H. and BELL J. A. (1954) Adenoidal-Pharyngeal-Conjunctival Agents, *New England Journal of Medicine* **251**(27), 1077–1086.

ISHIDA T. and KINOSHITA K. (2007) PrDOS: Prediction of disordered protein regions from amino acid sequence, *Nucleic Acids Research* **35**, 460–464.

ISHOV A. M. and MAUL G. G. (1996) The periphery of nuclear domain 10 (ND10) as site of DNA virus deposition, *Journal of Cell Biology* **134**(4), 815–826.

JAVIER R. T. (1994) Adenovirus Type 9 E4 Open Reading Frame 1 Encodes a Transforming Protein Required for the Production of Mammary Tumors in Rats, *Journal of Virology* **68**(6), 3917–3924.

JAWETZ E., KIMURA S. J., HANNA L., COLEMAN V. R., THYGESON P. and NICHOLAS A. (1955) Studies on the Etiology of Epidemic Keratoconjunctivitis, *American Journal of Ophthalmology* **40**(5), 200–211.

JIANG H., WHITE E. J., RIOS-VICIL C. I., XU J., GOMEZ-MANZANO C. and FUEYO J. (2011) Human Adenovirus Type 5 Induces Cell Lysis through Autophagy and Autophagy-Triggered Caspase Activity, *Journal of Virology* **85**(10), 4720–4729.

JONES M. S., HARRACH B., GANAC R. D., GOZUM M. M. A., CRUZ W. P., RIEDEL B., PAN C., DELWART E. L. and SCHNURR D. P. (2007) New Adenovirus Species Found in a Patient Presenting with Gastroenteritis, *Journal of Virology* **81**(11), 5978–5984.

KAJON A. E., LAMSON D. M., BAIR C. R., LU X., LANDRY M. L., MENEGUS M., ERDMAN D. D. and GEORGE K. S. (2018) Adenovirus Type 4 Respiratory Infections among Civilian Adults, Northeastern United States, 2011-2015, *Emerging Infectious Diseases* **24**(2), 2011–2015.

KALDOR S. W., KALISH V. J., DAVIES J. F., SHETTY B. V., FRITZ J. E., APPELT K., BURGESS J. A., CAMPANALE K. M., CHIRGADZE N. Y., CLAWSON D. K., DRESSMAN B. A., HATCH S. D., KHALIL D. A., KOSA M. B., LUBBEHUSEN P. P., MUESING M. A., PATICK A. K., REICH S. H., SU K. S. and TATLOCK J. H. (1997) Viracept (nelfinavir mesylate, AG1343): A potent, orally bioavailable inhibitor of HIV-1 protease, *Journal of Medicinal Chemistry* **40**(24), 3979–3985.

KAMPMANN B., CUBITT D., WALLS T., NAIK P., DEPALA M., SAMARASINGHE S., ROBSON D., HASSAN A., RAO K., GASPAR H., DAVIES G., JONES A., CALE C., GILMOUR K., REAL M. and FOO M. (2005) Improved outcome for children with disseminated adenoviral infection following allogeneic stem cell transplantation, *British Journal of Haematology* **130**, 595–603.

KANEKO H., ISHIKO H., OHGUCHI T., TAGAWA Y., AOKI K., SUZUTANI T. and OHNO S. (2009) Communication Nucleotide sequence variation in the hexon gene of human adenovirus type 8 and 37 strains from epidemic keratoconjunctivitis patients in Japan, *Journal of General Virology* **90**, 2260–2265.

KAREN K. A. and HEARING P. (2011) Adenovirus Core Protein VII Protects the Viral Genome from a DNA Damage Response at Early Times after Infection, *Journal of Virology* **85**(9), 4135–4142.

KHITTOO G. and WEBER J. (1977) Genetic analysis of adenovirus type 2, *Virology* **80**(1), 83–97.

KIM J.-S., HAN H. S., PARK S. H., CHUN Y. K., LEE H. J. and CHI J. G. (1997) Neonatal Adenoviral Pneumonia - Report of three Autopsy Cases, *Journal of Korean Medical Science* **12**, 146–150.

KIM S. J., KIM K., PARK S. B., HONG D. J. and JHUN B. W. (2015) Outcomes of Early Administration of Cidofovir in Non-Immunocompromised Patients with Severe Adenovirus Pneumonia, *Plos One* **10**(4), 1–13.

KINDSMULLER K., GROITL P., HARTL B., BLANCHETTE P., HAUBER J. and DOBNER T. (2007) Intranuclear targeting and nuclear export of the adenovirus E1B-55K protein are regulated by SUMO1 conjugation, *Proceedings of the National Academy of Sciences of the United States of America* **104**(16), 6684–6689.

KING A. and VAN DER VLIET P. (1994) A precursor terminal protein-trinucleotide intermediate during initiation of adenovirus DNA replication: regeneration of molecular ends in vitro by a jumping back mechanism, *The EMBO Journal* **13**(23), 5786–5792.

KJELLEN L. (1955) Studies on an unidentified group of cytopathic agents, *Archiv fur die gesamte Virusforschung* **6**(1), 45–59.

KLEINBERGER T. and SHENK T. (1993) Adenovirus E4orf4 protein binds to protein phosphatase 2A, and the complex down regulates E1A-enhanced junB transcription, *Journal of Virology* **67**(12), 7556–7560.

KOMATSU T., HARUKI H. and NAGATA K. (2011) Cellular and viral chromatin proteins are positive factors in the regulation of adenovirus gene expression, *Nucleic Acids Research* **39**(3), 889–901.

KOMATSU T., NAGATA K. and WODRICH H. (2016a) An Adenovirus DNA Replication Factor, but Not Incoming Genome Complexes, Targets PML Nuclear Bodies, *Journal of Virology* **90**(3), 1657–1667.

KOMATSU T., QUENTIN-FROIGNANT C., CARLON-ANDRES I., LAGADEC F. and RAYNE F. (2018) In Vivo Labelling of Adenovirus DNA Identifies Chromatin Anchoring and Biphasic Genome Replication, *Journal of Virology* **92**(18), 1–21.

KOMATSU T., ROBINSON D. R., HISAOKA M., UESHIMA S., OKUWAKI M., NAGATA K. and WODRICH H. (2016b) Tracking adenovirus genomes identifies morphologically distinct late DNA replication compartments, *Traffic* **17**(11), 1168–1180.

KOSTURKO L. D., SHARNICK S. V. and TIBBETTS C. (1982) Polar encapsidation of adenovirus DNA: cloning and DNA sequence of the left end of adenovirus type 3, *Journal of Virology* **43**(3), 1132–1137.

KOSULIN K., GEIGER E., VÉCSEI A., HUBER W. D., RAUCH M., BRENNER E., WRBA F., HAMMER K., INNERHOFER A., PÖTSCHGER U., LAWITSCHKA A., MATTHES-LEODOLTER S., FRITSCH G. and LION T. (2016) Persistence and reactivation of human adenoviruses in the gastrointestinal tract, *Clinical Microbiology and Infection* **22**(4), 381.e1–381.e8.

KOVÁCS E. R. and BENKÖ M. (2009) Confirmation of a novel siadenovirus species detected in raptors : Partial sequence and phylogenetic analysis, *Virus Research* **140**, 64–70.

KOVÁCS G. M., LAPATRA S. E., CLAUDE J., HALLUIN D. and BENK M. (2003) Phylogenetic analysis of the hexon and protease genes of a fish adenovirus isolated from white sturgeon (Acipenser transmontanus) supports the proposal for a new adenovirus genus, *Virus Research* **98**, 27–34.

KRÄTZER F., ROSORIUS O., HEGER P., HIRSCHMANN N., DOBNER T., HAUBER J. and STAUBER R. H. (2000) The adenovirus type 5 E1B-55K oncoprotein is a highly active shuttle protein and shuttling is independent of E4orf6 , p53 and Mdm2, *Oncogene* **19**, 850–857.

KREMER J. R., MASTRONARDE D. N. and MCINTOSH J. R. (1996) Computer Visualization of Three-Dimensional Image Data Using IMOD, *Journal of Szructural Biology* **116**(1), 71–76.

KRULL A., BUCHHOLZ T.-O. and JUG F. (2018) Noise2Void - Learning Denoising from Single Noisy Images, *Arxiv* pp. 1–9.

KUSCHNER R. A., RUSSELL K. L., ABUJA M., BAUER K. M., FAIX D. J., HAIT H., HENRICK J., JACOBS M., LISS A., LYNCH J. A., LIU Q., LYONS A. G., MALIK M., MOON J. E., STUBBS J., SUN W., TANG D., TOWLE A. C., WALSH D. S. and WILKERSON D. (2013) A phase 3, randomized, double-blind, placebo-controlled study of the safety and efficacy of the live, oral adenovirus type 4 and type 7 vaccine, in U.S. military recruits, *Vaccine* **31**(28), 2963–2971.

LAEMMLI U. K. (1970) Cleavage of Structural Proteins during the Assembly of the Head of Bacteriophage T4, *Nature* **227**, 680–685.

LAMMERDING J., STEWART C. L., LEE R. T., LAMMERDING J., SCHULZE P. C., TAKAHASHI T., KOZLOV S., SULLIVAN T., KAMM R. D., STEWART C. L. and LEE R. T. (2004) Lamin A/C deficiency causes defective nuclear mechanics and mechanotransduction, *The Journal of Clinical Investigation* **113**(3), 370–378.

LAN S., KAMEL W., PUNGA T. and AKUSJÄRVI G. (2017) The adenovirus L4-22K protein regulates transcription and RNA splicing via a sequence-specific single-stranded RNA binding, *Nucleic Acids Research* **45**(4), 1731–1742.

LE L. P., EVERTS M., DMITRIEW I. P., DAVYDOVA J. G., YAMAMOTO M. and CURIEL D. T. (2004) Fluorescently labeled adenovirus with pIX-EGFP for vector detection, *Molecular Imaging* **3**(2), 105–116.

LEE M. T., HUNG W. C., CHEN F. Y. and HUANG H. W. (2008) Mechanism and kinetics of pore formation in membranes by water-soluble amphipathic peptides, *Proceedings of the National Academy of Sciences of the United States of America* **105**(13), 5087–5092.

LEE T. W. R., LAWRENCE F. J., DAUKSAITE V., AKUSJÄRVI G., BLAIR G. E. and MATTHEWS D. A. (2004) Precursor of human adenovirus core polypeptide Mu targets the nucleolus and modulates the expression of E2 proteins, *Journal of General Virology* **85**(1), 185–196.

LEFKOWITZ E. J., DEMPSEY D. M., HENDRICKSON R. C., ORTON R. J., SIDDELL S. G. and SMITH D. B. (2018) Virus taxonomy: the database of the International Committee on Taxonomy of Viruses (ICTV), *Nucleic Acids Research* **46**, 708–717.

LENMAN A., LIACI A. M., LIU Y., ÅRDAHL C., RAJAN A., NILSSON E., BRADFORD W., KAESHAMMER L., JONES M. S., FRÄNGSMYR L., FEIZI T., STEHLE T. and ARNBERG N. (2015) Human Adenovirus 52 Uses Sialic Acid-containing Glycoproteins and the Coxsackie and Adenovirus Receptor for Binding to Target Cells, *PLoS Pathogens* **11**(2), 1–23.

LEUNG A. Y.-H., CHAN M., CHENG V. C.-C., YUEN K.-Y. and KWONG Y.-L. (2005) Quantification of Adenovirus in the Lower Respiratory Tract of Patients without Clinical Adenovirus-Related Respiratory Disease, *Clinical Infectious Diseases* **40**, 1541–1544.

LEWIS P. F., SCHMIDT M. A., LU X., ERDMAN D. D., CAMPBELL M., THOMAS A., CIESLAK P. R., GRENZ L. D., TSAKNARDIS L., GLEAVES C., KENDALL B. and GILBERT D. (2009) A Community-Based Outbreak of Severe Respiratory Illness Caused by Human Adenovirus Serotype 14, *Journal of Infectious Diseases* **199**(10), 1427–1434.

LI D., ZHOU J.-N., LI H., HE C.-Y., DAI Q.-S., LI X.-L., HE J.-F., HE H., LI M.-B., JIANG L. I.-L., CHEN Y.-Y. and XU W. (2019) An outbreak of epidemic keratoconjunctivitis caused by human adenovirus type 8 in primary school, southwest China, *BMC Infections Diseases* **19**(624), 1–10.

LI E., STUPACK D., BOKOCH G. M. and NEMEROW G. R. (1998a) Adenovirus Endocytosis Requires Actin Cytoskeleton Reorganization Mediated by Rho Family GTPases, *Journal of Virology* **72**(11), 8806–8812.

LI E., STUPACK D., KLEMKE R., CHERESH D. A. and NEMEROW G. R. (1998b) Adenovirus Endocytosis via αv Integrins Requires Phosphoinositide-3-OH Kinase, *Journal of Virology* **72**(3), 2055–2061.

LI Y., KANG J. and HORWITZ M. S. (1997) Interaction of an Adenovirus 14.7-Kilodalton Protein Inhibitor of Tumor Necrosis Factor Alpha Cytolysis with a New Member of the GTPase Superfamily of Signal Transducers, *Journal of Virology* **71**(2), 1576–1582.

LIAO Y., TAM J. P. and LIU D. X. (2006) Viroporin activity of SARS-CoV E protein, *Advances in Experimental Medicine and Biology* **581**, 199–202.

LIN M., YANG S., GONG Y., KUO C., CHIU C., CHEN C., HSIEH Y., KUO C., FANG C., TSAO K. and HUANG Y. (2017) Clinical and molecular features of adenovirus type 2, 3, and 7 infections in children in an outbreak in Taiwan, 2011, *Clinical Microbiology and Infection* **23**(2), 110–116.

LINDERT S., SILVESTRY M., MULLEN T.-M., NEMEROW G. R. and STEWART P. L. (2009) Cryo-Electron Microscopy Structure of an Adenovirus-Integrin Complex Indicates Conformational Changes in both Penton Base and Integrin, *Journal of Virology* **83**(22), 11491–11501.

LIU F. and GREEN M. R. (1994) Promoter targeting by adenovirus E1a through interaction with different cellular DNA-binding domains, *Nature* **368**(520-525).

LIU G.-Q., BABISS L. E., VOLKERT F. C., YOUNG C. S. H. and GINSBERG H. S. (1985) A Thermolabile Mutant of Adenovirus 5 Resulting from Substitution Mutation in the Protein VIII Gene, *Journal of Virology* **53**(3), 920–925.

LIU H., JIN L., KOH S. B. S., ATANASOV I., SCHEIN S., WU L. and ZHOU Z. H. (2010) Atomic structure of human adenovirus by cryoEM reveals interactions among protein networks, *Science* **329**(5995), 1038–1043.

LIU J., KLINE B. A., KENNY T. A., SMITH D. R., SOLOVEVA V., BEITZEL B., PANG S., LOCKETT S., HESS H. F., PALACIOS G., KUHN J. H., SUN M. G. and ZENG X. (2018) A novel sheet-like virus particle array is a hallmark of Zika virus infection article, *Emerging Microbes and Infections* **7**(1), 1–11.

LIU X. and MARMORSTEIN R. (2007) Structure of the retinoblastoma protein bound to adenovirus E1A reveals the molecular basis for viral oncoprotein inactivation of a tumor suppressor, *Genes & Development* **21**, 2711–2716.

LIU Y., SHEVCHENKO A., SHEVCHENKO A. and BERK A. J. (2005) Adenovirus Exploits the Cellular Aggresome Response To Accelerate Inactivation of the MRN Complex, *Journal of Virology* **79**(22), 14004–14016.

LIU Y., TRAN B. N., WANG F., OUNJAI P., WU J. and HEW C. L. (2016) Visualization of Assembly Intermediates and Budding Vacuoles of Singapore Grouper Iridovirus in Grouper Embryonic Cells, *Scientific Reports* **6**(18696), 1–12.

LIU Y. T., JIH J., DAI X., BI G. Q. and ZHOU Z. H. (2019) Cryo-EM structures of herpes simplex virus type 1 portal vertex and packaged genome, *Nature* **570**(7760), 257–261.

LIVNE A., SHTRICHMAN R. and KLEINBERGER T. (2001) Caspase Activation by Adenovirus E4orf4 Protein Is Cell Line Specific and Is Mediated by the Death Receptor Pathway, *Journal of Virology* **75**(2), 789–798.

LJUNGMAN P., RIBAUD P., EYRICH M., EINSELE H., BLEAKLEY M., MACHACZKA M., BIERINGS M., BOSI A., GRATECOS N. and CORDONNIER C. (2003) Cidofovir for adenovirus infections after allogeneic hematopoietic stem cell transplantation: a survey by the Infectious Diseases Working Party of the European Group for Blood and Marrow Transplantation, *Bone Marrow Transplantation* **31**, 481–486.

LU S. and CULLEN B. R. (2004) Adenovirus VA1 Noncoding RNA Can Inhibit Small Interfering RNA and MicroRNA Biogenesis, *Journal of Virology* **78**(23), 12868–12876.

LU Z.-Z., ZOU X.-H., LASTINGER K., WILLIAMS A., QU J.-G. and ESTES D. M. (2013) Enhanced growth of recombinant human Adenovirus type 41 (HAdV-41) carrying ADP gene, *Virus Research* **176**(1), 61–68.

LUFT J. H. (1961) Improvements in Epoxy Resin Embedding Methods, *The Journal of Biophysical and Biochemical Cytology* **9**, 409–414.

LUTZ P. and KEDINGER C. (1996) Properties of the adenovirus IVa2 gene product, an effector of late-phase-dependent activation of the major late promoter, *Journal of Virology* **70**(3), 1396–1405.

LUTZ P., PUVION-DUTILLEUL F., LUTZ Y. and KEDINGER C. (1996) Nucleoplasmic and nucleolar distribution of the adenovirus IVa2 gene product, *Journal of Virology* **70**(6), 3449–3460.

LUTZ P., ROSA-CALATRAVA M. and KEDINGER C. (1997) The product of the adenovirus intermediate gene IX is a transcriptional activator, *Journal of Virology* **71**(7), 5102–5109.

MA H.-C. and HEARING P. (2011) Adenovirus Structural Protein IIIa Is Involved in the Serotype Specificity of Viral DNA Packaging, *Journal of Virology* **85**(15), 7849–7855.

MA J., DUFFY M. R., DENG L., DAKIN R. S., UIL T., CUSTERS J., KELLY S. M., MCVEY J. H., NICKLIN S. A. and BAKER A. H. (2015) Manipulating Adenovirus Hexon Hypervariable Loops Dictates Immune Neutralisation and Coagulation Factor X-dependent Cell Interaction In Vitro and In Vivo, *PLoS Pathogens* **11**(2), 1–22.

MADISCH I., HOFMAYER S., MORITZ C., GRINTZALIS A., HAINMUELLER J., PRING-AKERBLOM P. and HEIM A. (2007) Phylogenetic analysis and structural predictions of human adenovirus penton proteins as a basis for tissue-specific adenovirus vector design, *Journal of Virology* **81**(15), 8270–8281.

MAIDORN M., OLICHON A., RIZZOLI S. O. and OPAZO F. (2019) Nanobodies reveal an extrasynaptic population of SNAP-25 and Syntaxin 1A in hippocampal neurons, *mAbs* **11**(2), 305–321.

MAIER O., GALAN D. L., WODRICH H. and WIETHOFF C. M. (2010) An N-terminal domain of adenovirus protein VI fragments membranes by inducing positive membrane curvature, *Virology* **402**(1), 11–19.

MAIER O., MARVIN S. A., WODRICH H., CAMPBELL E. M. and WIETHOFF C. M. (2012) Spatiotemporal Dynamics of Adenovirus Membrane Rupture and Endosomal Escape, *Journal of Virology* **86**(19), 10821–10828.

MAIZEL J. V. J., WHITE D. O. and SCHARFF M. D. (1968) The polypeptides of adenovirus. I. Evidence for multiple protein components in the virion and a comparison of types 2, 7A, and 12, *Virology* **36**(1), 115–125.

MANGEL W. F., BANIECKI M. L. and MCGRATH W. J. (2003) Specific interactions of the adenovirus proteinase with the viral DNA, an 11-amino-acid viral peptide, and the cellular protein actin, *Cellular and Molecular Life Sciences* **60**(11), 2347–2355.

MANGEL W. F., MCGRATH W. J., TOLEDO D. L. and ANDERSON C. W. (1993) Viral DNA and a viral peptide can act as cofactors of adenovirus virion proteinase activity, *Nature* **361**(6409), 274–275.

MANNERVIK M., FAN S., STROM A. C., HELIN K. and AKUSJARVI G. (1999) Adenovirus E4 open reading frame 4-induced dephosphorylation inhibits E1A activation of the E2 promoter and E2F-1-mediated transactivation independently of the retinoblastoma tumor suppressor protein, *Virology* **256**(2), 313–321.

MARAN A. and MATHEWS M. B. (1988) Characterization of the double-stranded RNA implicated in the inhibition of protein synthesis in cells infected with a mutant adenovirus defective for VA RNA, *Virology* **164**(1), 106–113.

MARANHÃO A. G., SOARES C. C., ALBUQUERQUE M. C. M. and SANTOS N. (2009) Molecular epidemiology of adenovirus conjuncitivits in Rio de Janeiro, Brazil, between 2004 and 2007, *Rev. Inst. Med. trop. S. Paulo* **51**(4), 227–229.

MARCELLUS R. C., LAVOIE J. N., BOIVIN D., SHORE G. C., KETNER G. and BRANTON P. E. (1998) The Early Region 4 orf4 Protein of Human Adenovirus Type 5 Induces p53-Independent Cell Death by Apoptosis, *Journal of Virology* **72**(9), 7144–7153.

MARTÍN C. S., GLASGOW J. N., BOROVJAGIN A., BEATTY M. S., KASHENTSEVA A., CURIEL D. T., MARABINI R. and DMITRIEV I. P. (2008) Localization of the N-terminus of minor coat protein IIIa in the adenovirus capsid, *Journal of Molecular Biology* **383**(4), 923–934.

MARTIN-FERNANDEZ M., LONGSHAW S. V., KIRBY I., SANTIS G., TOBIN M. J., CLARKE D. T. and JONES G. R. (2004) Adenovirus type-5 entry and disassembly followed in living cells by FRET, fluorescence anisotropy, and FLIM, *Biophysical Journal* **87**(2), 1316–1327.

MARTINEZ-CABALLERO S., DEJEAN L. M., KINNALLY M. S., JOON K., MANNELLA C. A. and KINNALLY K. W. (2009) Assembly of the Mitochondrial Apoptosis-induced Channel, MAC, *The Journal of Biological Chemistry* **284**(18), 12235–12245.

MASTRONARDE D. N. (2005) Automated electron microscope tomography using robust prediction of specimen movements, *Journal of Structural Biology* **152**(1), 36–51.

MATHEWS M. B. (1975) Genes for VA-RNA in Adenovirus 2, *Cell* **6**, 223–229.

MATTHEWS D. A. (2001) Adenovirus protein V induces redistribution of nucleolin and B23 from nucleolus to cytoplasm, *Journal of Virology* **75**(2), 1031–1038.

MATTHEWS D. A. and RUSSELL W. C. (1994) Adenovirus protein-protein interactions: Hexon and protein VI, *Journal of General Virology* **75**(12), 3365–3374.

MATTHEWS D. A. and RUSSELL W. C. (1995) Adenovirus protein-protein interactions : molecular parameters governing the binding of protein VI to hexon and the activation of the adenovirus 23K protease, *Journal of General Virology* **76**(1959), 1969.

MATTHEWS D. A. and RUSSELL W. C. (1998) Adenovirus core protein V is delivered by the invading virus to the nucleus of the infected cell and later in infection is associated with nucleoli, *Journal of General Virology* **79**(7), 1671–1675.

MCCUNE J. M., RABIN L. B., FEINBERG M. B., LIEBERMAN M., KOSEK J. C., REYES G. R. and WEISSMAN I. L. (1988) Endoproteolytic cleavage of gp160 is required for the activation of human immunodeficiency virus, *Cell* **53**(1), 55–67.

MCGRATH J. W., BANIECKI M. L., LI C., MCWHIRTER S. M., BROWN M. T., TOLEDO D. L. and MANGEL W. F. (2001) Human adenovirus proteinase: DNA binding and stimulation of proteinase activity by DNA, *Biochemistry* **40**(44), 13237–13245.

MEULENBROEK R. A., SARGENT K. L., LUNDE J., JASMIN B. J. and PARKS R. J. (2004) Use of adenovirus protein IX (pIX) to display large polypeptides on the virion - Generation of fluorescent virus through the incorporation of pIX-GFP, *Molecular Therapy* **9**(4), 617–624.

MILLER M. M., CORNISH T. E., CREEKMORE T. E., FOX K., LAEGREID W., MCKENNA J., VASQUEZ M. and WOODS L. W. (2017) Whole-genome sequences of Odocoileus hemionus deer adenovirus isolates from deer , moose and elk are highly conserved and support a new species in the genus Atadenovirus, *Journal of General Virology* **98**, 2320–2328.

MITSUDOMI T., STEINBERG S. M., NAU M. M., CARBONE D., D'AMICO D., BODNER S., OIE H. K., LINNOILA R. I., MULSHINE J. L. and MINNA J. D. (1992) p53 gene mutations in non-small-cell lung cancer cell lines and their correlation with the presence of ras mutations and clinical features, *Oncogene* **7**(1), 171–180.

MONAGHAN A., WEBSTER A. and HAY R. T. (1994) Adenovirus DNA binding protein: Helix destabilising properties, *Nucleic Acids Research* **22**(5), 742–748.

MORGAN C., GODMAN G. C., BREITENFELD P. M. and ROSE H. M. (1960) A correlative study by electron and light microscopy of the development of type 5 adenovirus, *The Journal of experimental medicine* **112**, 383–402.

MORRIS S. J., SCOTT G. E. and LEPPARD K. N. (2010) Adenovirus Late-Phase Infection Is Controlled by a Novel L4 Promoter, *Journal of Virology* **84**(14), 7096–7104.

MUL Y. and VAN DER VLIET P. (1992) Nuclear factor I enhances adenovirus DNA replication by increasing the stability of a preinitiation complex, *The EMBO Journal* **11**(2), 751–760.

MULLER S. and DOBNER T. (2008) The adenovirus E1B-55K oncoprotein induces SUMO modification of p53, *Cell Cycle* **7**(6), 754–758.

MÜLLER U., KLEINBERGER T. and SHENK T. (1992) Adenovirus E4orf4 protein reduces phosphorylation of c-Fos and E1A proteins while simultaneously reducing the level of AP-1, *Journal of Virology* **66**(10), 5867–5878.

MURALI V. K., ORNELLES D. A., GOODING L. R., WILMS H. T., HUANG W., TOLLEFSON A. E., WOLD W. S. M. and GARNETT-BENSON C. (2014) Adenovirus Death Protein (ADP) Is Required for Lytic Infection of Human Lymphocytes, *Journal of Virology* **88**(2), 903–912.

NAGATA K., GUGGENHEIMER R. A. and HURWITZ J. (1983) Specific binding of a cellular DNA replication protein to the origin of replication of adenovirus DNA, *Proceedings of the National Academy of Sciences* **80**(20), 6177–6181.

NAKANE S., IWAMOTO A. and MATSUDA Z. (2015) The V4 and V5 variable loops of HIV-1 envelope glycoprotein are tolerant to insertion of green fluorescent protein and are useful targets for labeling, *Journal of Biological Chemistry* **290**(24), 15279–15291.

NAKANO M. Y., BOUCKE K., SUOMALAINEN M., STIDWILL R. P. and GREBER U. F. (2000) The First Step of Adenovirus Type 2 Disassembly Occurs at the Cell Surface, Independently of Endocytosis and Escape to the Cytosol, *Journal of Virology* **74**(15), 7085–7095.

NARAYAN P. K. L. and KAJON A. E. (2020) Human mastadenovirus-B (HAdV-B)-specific E3-CR1β and E3-CR1γ glycoproteins interact with each other and localize at the plasma membrane of non-polarized airway epithelial cells, *Virology* **546**, 67–78.

NATCHIAR S. K., VENKATARAMAN S., MULLEN T.-M. and NEMEROW G. R. (2018) Revised crystal structure of human adenovirus reveals the limits on protein IX quasi-equivalence and on analyzing large macromolecular complexes, *Journal of Molecular Biology* **430**(21), 4132–4141.

NEBBIA G., CHAWLA A., SCHUTTEN M., ATKINSON C., RAZA M., JOHNSON M. and GERETTI A. M. (2005) Adenovirus viraemia and dissemination unresponsive to antiviral therapy in advanced HIV-1 infection, *AIDS* **19**(12), 1339–1340.

NILSSON E. C., STORM R. J., BAUER J., JOHANSSON S. M., LOOKENE A., ÅNGSTRÖM J., HEDENSTRÖM M., ERIKSSON T. L., FRÄCURRENCY SIGNNGSMYR L., RINALDI S., WILLISON H. J., DOMELLÖF F. P., STEHLE T. and ARNBERG N. (2011) The GD1a glycan is a cellular receptor for adenoviruses causing epidemic keratoconjunctivitis, *Nature Medicine* **17**(1), 105–109.

NORRBY E., BARTHA A., BOULANGER P., DREIZIN R. S., GINSBERG H. S., KALTER S. S., KAWAMURA H., ROWE W. P., RUSSELL W. C., SCHLESINGER W. and WIGAND R. (1976) Adenoviridae, *Intervirology* **7**(3), 117–125.

NUMAZAKI Y., KUMASAKA T., YANO N., YAMANAKA M., MIYAZAWA T., TAKAI S. and ISHIDA N. (1973) Further study on acute hemorrhagic cystitis due to adenovirus type 11, *The New England journal of medicine* **289**(7), 344–347.

OBERT S., O'CONNOR R. J., SCHMID S. and HEARING P. (1994) The adenovirus E4-6/7 protein transactivates the E2 promoter by inducing dimerization of a heteromeric E2F complex, *Molecular and Cellular Biology* **14**(2), 1333–1346.

O'CONNOR M. J., ZIMMERMANN H., NIELSEN S. and BERNARD H.-U. (1999) Characterization of an E1A-CBP Interaction Defines a Novel Transcriptional Adapter Motif (TRAM) in CBP/p300, *Journal of Virology* **73**(5), 3574–3581.

O'CONNOR R. J. and HEARING P. (2000) The E4-6/7 Protein Functionally Compensates for the Loss of E1A Expression in Adenovirus Infection, *Journal of Virology* **74**(13), 5819–5824.

ORAZIO N. I., NAEGER C. M., KARLSEDER J. and WEITZMAN M. D. (2011) The Adenovirus E1b55K / E4orf6 Complex Induces Degradation of the Bloom Helicase during Infection, *Journal of Virology* **85**(4), 1887–1892.

ORNELLES D. A. and SHENK T. (1991) Localization of the adenovirus early region 1B 55-kilodalton protein during lytic infection: association with nuclear viral inclusions requires the early region 4 34-kilodalton protein, *Journal of Virology* **65**(1), 424–9.

ORTEGA M. E. and CATALANO C. E. (2006) Bacteriophage lambda gpNu1 and Escherichia coli IHF proteins cooperatively bind and bend viral DNA: Implications for the assembly of a genome-packaging motor, *Biochemistry* **45**(16), 5180–5189.

OSTAPCHUK P., ALMOND M. and HEARING P. (2011) Characterization of Empty Adenovirus Particles Assembled in the Absence of a Functional Adenovirus IVa2 Protein, *Journal of Virology* **85**(11), 5524–5531.

OSTAPCHUK P. and HEARING P. (2008) Adenovirus IVa2 Protein Binds ATP, *Journal of Virology* **82**(20), 10290–10294.

OSTWALD W. (1900) Über die vermeintliche Isomerie des roten und gelben Quecksilberoxyds und die Oberflächenspannung fester Körper, *Zeitschrift für Physikalische Chemie* **34**(1), 495–503.

PANOU M. M., PRESCOTT E. L., HURDISS D. L., SWINSCOE G., HOLLINSHEAD M., CALLER L. G., MORGAN E. L., CARLISLE L., MÜLLER M., ANTONI M., KEALY D., RANSON N. A., CRUMP C. M. and MACDONALD A. (2018) Agnoprotein is an essential egress factor during BK Polyomavirus infection, *International Journal of Molecular Sciences* **19**(3), 1–16.

PARDO-MATEOS A. and YOUNG C. S. (2004) Adenovirus IVa2 protein plays an important role in transcription from the major late promoter in vivo, *Virology* **327**(1), 50–59.

PARK J. Y., KIM B.-J., LEE E. J., PARK K. S., PARK H. S., JUNG S. and KIM J. O. (2017) Clinical Features and Courses of Adenovirus Pneumonia in Healthy Young Adults during an Outbreak among Korean Military Personnel, *PLoS One* **12**(1), 1–14.

PARKER E. J., BOTTING C. H., WEBSTER A. and HAY R. T. (1998) Adenovirus DNA polymerase : domain organisation and interaction with preterminal protein, *Nucleic Acids Research* **26**(5), 1240–1247.

PARRY B. R., SUROVTSEV I. V., CABEEN M. T., O'HERN C. S., DUFRESNE E. R. and JACOBS-WAGNER C. (2014) The bacterial cytoplasm has glass-like properties and is fluidized by metabolic activity, *Cell* **156**(1), 183–194.

PEI J. and GRISHIN N. V. (2001) AL2CO: Calculation of positional conservation in a protein sequence alignment, *Bioinformatics* **17**(8), 700–712.

PELKA P., ABLACK J. N. G., TORCHIA J., TURNELL A. S., GRAND R. J. A. and MYMRYK J. S. (2009) Transcriptional control by adenovirus E1A conserved region 3 via p300/CBP, *Nucleic Acids Research* **37**(4), 1095–1106.

PENFOLD M. E. and MOCARSKI E. S. (1997) Formation of cytomegalovirus DNA replication compartments defined by localization of viral proteins and DNA synthesis, *Virology* **239**(1), 46–61.

PENNELLA M. A., LIU Y., WOO J. L., KIM C. A. and BERK A. J. (2010) Adenovirus E1B 55-Kilodalton Protein Is a p53-SUMO1 E3 Ligase That Represses p53 and Stimulates Its Nuclear Export through Interactions with Promyelocytic Leukemia Nuclear Bodies, *Journal of Virology* **84**(23), 12210–12225.

PEREZ D. and WHITE E. (1998) E1B 19K Inhibits Fas-mediated Apoptosis through FADD-dependent Sequestration of FLICE, *The Journal of Cell Biology* **141**(5), 1255–1266.

PEREZ-BERNA A. J., MANGEL W. F., MCGRATH W. J., GRAZIANO V., FLINT J. and SAN MARTIN C. (2014) Processing of the L1 52/55k Protein by the Adenovirus Protease: a New Substrate and New Insights into Virion Maturation, *Journal of Virology* **88**(3), 1513–1524.

PÉREZ-BERNÁ A. J., MARION S., CHICHÓN F. J., FERNÁNDEZ J. J., WINKLER D. C., CARRASCOSA J. L., STEVEN A. C., ŠIBER A. and SAN MARTÍN C. (2015) Distribution of DNA-condensing protein complexes in the adenovirus core, *Nucleic Acids Research* **43**(8), 4274–4283.

PEREZ-VARGAS J., VAUGHAN R. C., HOUSER C., HASTIE K. M., KAO C. C. and NEMEROW G. R. (2014) Isolation and Characterization of the DNA and Protein Binding Activities of Adenovirus Core Protein V, *Journal of Virology* **88**(16), 9287–9296.

PERSSON H., AKSAAS A. K., KVISSEL A. K., PUNGA T., ENGSTRÖM Å., SKÅLHEGG B. S. and AKUSJÄRVI G. (2012) Two cellular protein kinases, DNA-PK and pka, phosphorylate the adenoviral L4-33K protein and have opposite effects on L1 alternative RNA splicing, *PLoS One* **7**(2), 1–10.

PFITZNER S., HOFMANN-SIEBER H., BOSSE J. B., FRANKEN L. E., GRÜNEWALD K. and DOBNER T. (2020) Fluorescent protein tagging of adenoviral proteins pV and pIX reveals 'late virion accumulation compartment', *PLoS Pathogens* **16**(6), 1–25.

POMBO A., FERREIRA J., BRIDGE E. and CARMO-FONSECA M. (1994) Adenovirus replication and transcription sites are spatially separated in the nucleus of infected cells., *The EMBO Journal* **13**(21), 5075–5085.

POTTER R. N., CANTRELL J. A., MALLAK C. T. and GAYDOS J. C. (2012) Adenovirus-associated Deaths in US Military during Postvaccination Period, 1999-2010, *Emerging Infectious Diseases* **18**(3), 507–509.

PUNTENER D., ENGELKE M. F., RUZSICS Z., STRUNZE S., WILHELM C. and GREBER U. F. (2011) Stepwise Loss of Fluorescent Core Protein V from Human Adenovirus during Entry into Cells, *Journal of Virology* **85**(1), 481–496.

QUERIDO E., BLANCHETTE P., YAN Q., KAMURA T., MORRISON M., BOIVIN D., KAELIN W. G., CONAWAY R. C., CONAWAY J. W. and BRANTON P. E. (2001a) Degradation of p53 by adenovirus E4orf6 and E1B55K proteins occurs via a novel mechanism involving a Cullin-containing complex, *Genes & Development* **15**(23), 3104–3117.

QUERIDO E., MARCELLUS R. C., LAI A., CHARBONNEAU R., TEODORO J. G., KETNER G. and BRANTON P. E. (1997a) Regulation of p53 Levels by the E1B 55-Kilodalton Protein and E4orf6 in Adenovirus-Infected Cells, *Journal of Virology* **71**(5), 3788–3798.

QUERIDO E., MORISON M. R., CHU-PHAM DANG H., THIRLWELL S. W., BOIVIN D. and BRANTON P. E. (2001b) Identification of Three Functions of the Adenovirus E4orf6 Protein That Mediate p53 Degradation by the E4orf6-E1B55K Complex, *Journal of Virology* **75**(2), 699–709.

QUERIDO E., TEODORO J. G. and BRANTON P. E. (1997b) Accumulation of p53 Induced by the Adenovirus E1A Protein Requires Regions Involved in the Stimulation of DNA Synthesis, *Journal of Virology* **71**(5), 3526–3533.

RADKO S., JUNG R., OLANUBI O. and PELKA P. (2015) Effects of Adenovirus Type 5 E1A Isoforms on Viral Replication in Arrested Human Cells, *PLoS One* **10**(10), 1–18.

RAGHAVA S., GIORDA K. M., ROMANO F. B., HEUCK A. P. and HEBERT D. N. (2011) The SV40 late protein VP4 is a viroporin that forms pores to disrupt membranes for viral release, *PLoS Pathogens* **7**(6), e1002116.

RAJAN A., PERSSON B. D., FRÄNGSMYR L., OLOFSSON A., SANDBLAD L., HEINO J., TAKADA Y., MOULD A. P., SCHNAPP L. M., GALL J. and ARNBERG N. (2018) Enteric Species F Human Adenoviruses use Laminin-Binding Integrins as Co-Receptors for Infection of Ht-29 Cells, *Scientific Reports* **8**(1), 1–14.

RATHOD M., ROGERS P., VANGIPURAM S., MCALLISTER E. J. and DHURANDHAR N. (2009) Adipogenic Cascade can be Induced without Adipogenic Media by a Human Adenovirus, *Obesity* **17**(4), 657–664.

REDDY V. S., NATCHIAR S. K., STEWARD P. L. and NEMEROW G. R. (2010) Crystal structure of human adenovirus at 3.5 Å resolution, *Science* **329**(5995), 1071–1075.

REDDY V. S. and NEMEROW G. R. (2014) Structures and organization of adenovirus cement proteins provide insights into the role of capsid maturation in virus entry and infection, *Proceedings of the National Academy of Sciences* **111**(32), 11715–11720.

REICH N. C., SARNOW P., DUPREY E. and LEVINE A. J. (1983) Monoclonal Antibodies Which Recognize Native and Denatured Forms of the Adenovirus DNA-Binding Protein, *Virology* **128**(2), 480–484.

REKOSH D. M. K., RUSSEL W. C., BELLET A. J. D. and ROBINSON A. J. (1977) Identification of a Protein Linked to the Ends of Adenovirus DNA, *Cell* **11**, 293–295.

RIJNDERS A. W., VAN BERGEN B. G., VAN DER VLIET P. C. and SUSSENBACH J. S. (1983) Immunological characterization of the role of adenovirus terminal protein in viral DNA replication, *Virology* **131**(2), 287–295.

ROBERTS M. M., WHITE J. L., GRÜTTER M. G. and BURNETT R. M. (1986) Three-Dimensional Structure of the Adenovirus Major Coat Protein Hexon, *Science* **232**(4754), 1148–1151.

ROBIJNS J., MOLENBERGHS F., SIEPRATH T., CORNE T. D., VERSCHUUREN M. and DE VOS W. H. (2016) In silico synchronization reveals regulators of nuclear ruptures in lamin A/C deficient model cells, *Scientific Reports* **6**, 1–11.

ROCH N., SALAMEIRE D., GRESSIN R., MORAND P., PAVESE P., BRION J.-P., STAHL J.-P., ROCH N., SALAMEIRE D., GRESSIN R., MORAND P., EPAULARD O., PAVESE P., BRION J.-P., FATAL J.-P. S., EPAULARD O., PAVESE P., BRION J.-P. and STAHL J.-P. (2008) Fatal adenoviral and enteroviral infections and an Epstein-Barr virus positive large B-cell lymphoma after alemtuzumab treatment in a patient with refractory Sézary syndrome, *Scandinavian Journal of Infectious Diseases* **50**, 343–349.

RODRÍGUEZ E. and EVERITT E. (1996) Adenovirus uncoating and nuclear establishment are not affected by weak base amines., *Journal of Virology* **70**(6), 3470–3477.

RODRIGUEZ-ROCHA H., GOMEZ-GUTIERREZ J. G., GARCIA-GARCIA A., RAO X. M., CHEN L., MCMASTERS K. M. and ZHOU H. S. (2011) Adenoviruses induce autophagy to promote virus replication and oncolysis, *Virology* **416**(1-2), 9–15.

ROEHRIG S., TABBERT A. and FERRANDO-MAY E. (2003) In vitro measurement of nuclear permeability changes in apoptosis, *Analytical Biochemistry* **318**(2), 244–253.

ROELVINK P. W., LEE G. M., EINFLED D. A., KOVESDI I. and WICKHAM T. J. (1999) Identification of a Conserved Receptor-Binding Site on the Fiber Proteins of CAR-Recognizing Adenoviridae, *Science* **286**, 1568–1571.

ROELVINK P. W., LIZONOVA A., LEE J. G. M., LI Y., BERGELSON J. M., FINBERG R. W., BROUGH D. E., KOVESDI I. and WICKHAM T. J. (1998) The Coxsackievirus-Adenovirus Receptor Protein Can Function as a Cellular Attachment Protein for Adenovirus Serotypes from Subgroups A, C, D, E, and F, *Journal of Virology* **72**(10), 7909–7915.

RONAN B. A., AGRWAL N., CAREY E. J., DE PETRIS G., KUSNE S., SEVILLE M. T., BLAIR J. E. and VIKRAM H. R. (2014) Fulminant hepatitis due to human adenovirus, *Infection* **42**(1), 105–111.

ROSA-CALATRAVA M., GRAVE L., PUVION-DUTILLEUL F., CHATTON B. and KEDINGER C. (2001) Functional analysis of adenovirus protein IX identifies domains involved in capsid stability, transcriptional activity, and nuclear reorganization, *Journal of Virology* **75**(15), 7131–41.

ROSA-CALATRAVA M., PUVION-DUTILLEUL F., LUTZ P., DREYER D., DE THÉ H., CHATTON B. and KEDINGER C. (2003) Adenovirus protein IX sequesters host-cell promyelocytic leukaemia protein and contributes to efficient viral proliferation, *EMBO Reports* **4**(10), 969–975.

ROSEN L. (1960) A hemagglutination-inhibition technique for typing adenoviruses, *American Journal of Epidemiology* **71**(1), 120–128.

ROWE W. P., HOEBNER R. J., GILMORE L. K., PARROTT R. H. and WARD T. G. (1953) Isolation of a Cytopathogenic Agent from Human Adenoids Undergoing Spontaneous Degeneration in Tissue Culture, *Experimental Biology and Medicine* **84**(3), 570–573.

ROWE W. P., SEAL J. R., HUEBNER R. J., WHITESIDE J. E., WOOLREDGE R. L. and TURNER H. C. (1956) A Study of the Role of Adenoviruses in Acute Respiratory Infections in a Navy Recruit Population, *American Journal of Epidemiology* **64**(2), 211–219.

RUCHAUD S., KORFALI N., VILLA P, KOTTKE T. J., DINGWALL C., KAUFMANN S. H. and EARNSHAW W. C. (2002) Caspase-6 gene disruption reveals a requirement for lamin A cleavage in apoptotic chromatin condensation, *EMBO Journal* **21**(8), 1967–1977.

RUSSELL W. C. (2009) Adenoviruses: Update on structure and function, *Journal of General Virology* **90**(1), 1–20.

RUSSELL W. C., PATEL G., PRECIOUS B., SHARP I. and GARDNER P. S. (1981) Monoclonal antibodies against adenovirus type 5: Preparation and preliminary characterization, *Journal of General Virology* **56**(2), 393–408.

RUX J. J., KUSER P. R. and BURNETT R. M. (2003) Structural and Phylogenetic Analysis of Adenovirus Hexons by Use of High-Resolution X-Ray Crystallographic, Molecular Modeling, and Sequence-Based Methods, *Journal of Virology* **77**(17), 9553–9566.

SAIKI R. K., GELFAND D. H., STOFFEL S., SCHARF S. J., HIGUCHI R., HORN G. T., MULLIS K. B. and ERLICH H. A. (1988) Primer-Directed Enzymatic Amplification of DNA with a Thermostable DNA Polymerase, *Science* **239**(4839), 487–491.

SANCHEZ V., MAHR J. A., ORAZIO N. I. and SPECTOR D. H. (2007) Nuclear Export of the Human Cytomegalovirus Tegument Protein pp65 Requires Cyclin-Dependent Kinase Activity and the Crm1 Exporter, *Journal of Virology* **81**(21), 11730–11736.

SANGER F., NICKLEN S. and COULSON A. R. (1977) DNA sequencing with chain-terminating inhibitors, *Proceedings of the National Academy of Sciences* **74**(12), 5463–5467.

SAPHIRE A. C., GUAN T., SCHIRMER E. C., NEMEROW G. R. and GERACE L. (2000) Nuclear import of adenovirus DNA in vitro involves the nuclear protein import pathway and hsc70, *Journal of Biological Chemistry* **275**(6), 4298–4304.

SARNOW P., HEARING P., ANDERSON C. W., HALBERT D. N., SHENK T. and LEVINE A. J. (1984) Adenovirus early region 1B 58,000-dalton tumor antigen is physically associated with an early region 4 25,000-dalton protein in productively infected cells, *Journal of Virology* **49**(3), 692–700.

SAVÓN C., ACOSTA B., VALDÉS O., GOYENECHEA A., GONZALEZ G., PIÑÓN A., MÁS P., ROSARIO D., CAPÓ V., KOURÍ V., MARTÍNEZ P. A., MARCHENA J. J., GONZÁLEZ G., RODRIGUEZ H. and GUZMÁN M. G. (2008) A myocarditis outbreak with fatal cases associated with adenovirus subgenera C among children from Havana City in 2005, *Journal of Clinical Virology* **43**(2), 152–157.

SCARIA A., TOLLEFSON A. E., SAHA S. K. and WOLD W. S. M. (1992) The E3-11 . 6K Protein of Adenovirus Is an Asn-Glycosylated Integral That Localizes to the Nuclear Membrane Membrane Protein, *Virology* **753**, 743–753.

SCHAACK J., HO W. Y., FREIMUTH P. and SHENK T. (1990) Adenovirus terminal protein mediates both nuclear matrix association and efficient transcription of adenovirus DNA, *Genes and Development* **4**(7), 1197–1208.

SCHABERG K. B., KAMBHAM N., SIBLEY R. K. and HIGGINS J. P. T. (2017) Adenovirus Hepatitis: Clinicopathologic Analysis of 12 Consecutive Cases From a Single Institution, *The American Journal of Surgical Pathology* **41**(6), 810–819.

SCHALEY J., O'CONNOR R. J., TAYLOR L. J., BAR-SAGI D. and HEARING P. (2000) Induction of the Cellular E2F-1 Promoter by the Adenovirus E4-6/7 Protein, *Journal of Virology* **74**(5), 2084–2093.

SCHERER J. and VALLEE R. B. (2015) Conformational Changes in the Adenovirus Hexon Subunit Responsible for Regulating Cytoplasmic Dynein Recruitment, *Journal of Virology* **89**(2), 1013–1023.

SCHERER J., YI J. and VALLEE R. B. (2014) PKA-dependent dynein switching from lysosomes to adenovirus: A novel form of host-virus competition, *Journal of Cell Biology* **205**(2), 163–177.

SCHERES S. H. (2012) RELION: Implementation of a Bayesian approach to cryo-EM structure determination, *Journal of Structural Biology* **180**(3), 519–530.

SCHINDELIN J., ARGANDA-CARRERAS I., FRISE E., KAYNIG V., LONGAIR M., PIETZSCH T., PREIBISCH S., RUEDEN C., SAALFELD S., SCHMID B., TINEVEZ J.-Y., WHITE D. J., HARTENSTEIN V., ELICEIRI K., TOMANCAK P. and CARDONA A. (2012) Fiji: an open-source platform for biological-image analysis, *Nature Methods* **9**, 676.

SCHMID M., GONZALEZ R. A. and DOBNER T. (2012) CRM1-Dependent Transport Supports Cytoplasmic Accumulation of Adenoviral Early Transcripts, *Journal of Virology* **86**(4), 2282–2292.

SCHNELL U., DIJK F., SJOLLEMA K. A. and GIEPMANS B. N. G. (2012) Immunolabeling artifacts and the need for live-cell imaging, *Nature Methods* **9**(2), 152–158.

SCHREINER S., KINKLEY S., BÜRCK C., MUND A., WIMMER P., SCHUBERT T., GROITL P., WILL H. and DOBNER T. (2013) SPOC1-Mediated Antiviral Host Cell Response Is Antagonized Early in Human Adenovirus Type 5 Infection, *PLoS Pathogens* **9**(11), 1–16.

SCHREINER S., MARTINEZ R., GROITL P., RAYNE F., VAILLANT R., WIMMER P., BOSSIS G., STERNSDORF T., MARCINOWSKI L., RUZSICS Z., DOBNER T. and WODRICH H. (2012) Transcriptional Activation of the Adenoviral Genome Is Mediated by Capsid Protein VI, *PLoS Pathogens* **8**(2), 1–23.

SCHREINER S., WIMMER P., EVERETT R. D., BLANCHETTE P., GROITL P. and DOBNER T. (2010) Proteasome-Dependent Degradation of Daxx by the Viral E1B-55K Protein in Human Adenovirus-Infected Cells, *Journal of Virology* **84**(14), 7029–7038.

SEGALA M., SUN M., SHTENGEL G., VISWANATHAN S., BAIRD M., MACKLIN J., PATEL R., ALLEN J., HOWE E., PISZCZEK G., HESS H., DAVIDSON M., WANG Y. and LOOGER L. (2015) Fixation-resistant photoactivatable fluorescent proteins for correlative light and electron microscopy, *Nature Methods* **12**(3), 215–218.

SEIRADAKE E., LORTAT-JACOB H., BILLET O., KREMER E. J. and CUSACK S. (2006) Structural and Mutational Analysis of Human Ad37 and Canine Adenovirus 2 Fiber Heads in Complex with the D1 Domain of Coxsackie and Adenovirus Receptor *, *Journal of Biological Chemistry* **281**(44), 33704–33716.

SELIGMAN A. M., WASSERKRUG H. L. and HANKER J. S. (1966) A new staining method (OTO) for enhancing contrast of lipid-containing membranes and droplets in osmium tetroxide-fixed tissue with osmiophilic thiocarbohydrazide (TCH), *The Journal of cell biology* **30**(2), 424–432.

SELVARAJAN SIGAMANI S., ZHAO H., KAMAU Y. N., BAINES J. D. and TANG L. (2013) The Structure of the Herpes Simplex Virus DNA-Packaging Terminase pUL15 Nuclease Domain Suggests an Evolutionary Lineage among Eukaryotic and Prokaryotic Viruses, *Journal of Virology* **87**(12), 7140–7148.

SETH P., FITZGERALD D. J., WILLINGHAM M. C. and PASTAN I. (1984) Role of a low-pH environment in adenovirus enhancement of the toxicity of a Pseudomonas exotoxin-epidermal growth factor conjugate, *Journal of Virology* **51**(3), 650–655.

SETO D., CHODOSH J., BRISTER J. R. and JONES M. S. (2011) Using the Whole-Genome Sequence To Characterize and Name Human Adenoviruses, *Journal of Virology* **85**(11), 5701–5702.

SHANER N. C., CAMPBELL R. E., STEINBACH P. A., GIEPMANS B. N., PALMER A. E. and TSIEN R. Y. (2004) Improved monomeric red, orange and yellow fluorescent proteins derived from Discosoma sp. red fluorescent protein, *Nature Biotechnology* **22**(12), 1567–1572.

SHANG Q., WANG H., SONG Y., WEI L., LAVEBRATT C. and ZHANG F. (2014) Serological Data Analyses Show that Adenovirus 36 Infection Is Associated with Obesity: A Meta-Analysis Involving 5739 Subjects, *Obesity* **22**(3), 895–900.

SHAW A. R. and ZIFF E. B. (1980) Transcripts from the adenovirus-2 major late promoter yield a single early family of 3' coterminal mRNAs and five late families, *Cell* **22**(3), 905–916.

SHAYAKHMETOV D. M., EBERLY A. M., LI Z.-Y. and LIEBER A. (2005) Deletion of Penton RGD Motifs Affects the Efficiency of both the Internalization and the Endosome Escape of Viral Particles Containing Adenovirus Serotype 5 or 35 Fiber Knobs, *Journal of Virology* **79**(2), 1053–1061.

SHAYAKHMETOV D. M. and LIEBER A. (2000) Dependence of Adenovirus Infectivity on Length of the Fiber Shaft Domain, *Journal of Virology* **74**(22), 10274–10286.

SHENK T. and FLINT J. (1991) Transcriptional and Transforming Activities of the Adenovirus E1A Proteins, *Advances in Cancer Research* **57**, 47–85.

SHINDO K., KITAYAMA T., URA T., MATSUYA F., KUSABA Y., KANETAKE H. and SAITO Y. (1986) Acute hemorrhagic cystitis caused by adenovirus type 11 after renal transplantation, *Urologia internationalis* **41**(2), 152–155.

SHISLER J., YANG C. H. I., WALTER B., WARE C. F. and GOODING L. R. (1997) The Adenovirus E3-10.4K/14.5K Complex Mediates Loss of Cell Surface Fas (CD95) and Resistance to Fas-Induced Apoptosis, *Journal of Virology* **71**(11), 8299–8306.

SMITH C. D., CRAFT D. W., SHIROMOTO R. S. and YAN P. O. (1986) Alternative cell line for virus isolation, *Journal of Clinical Microbiology* **24**(2), 265–268.

SMITH J. G., SILVESTRY M., LINDERT S., LU W., NEMEROW G. R. and STEWART P. L. (2010) Insight into the mechanisms of adenovirus capsid disassembly from studies of defensin neutralization, *PLoS Pathogens* **6**(6).

SMITH K., GEHLE W. D. and TROUSDALE M. D. (1965) Architecture of the Adenovirus Capsid, *Journal of Bacteriology* **90**(1), 254–261.

SNIJDER J., REDDY V. S., MAY E. R., ROOS W. H., NEMEROW G. R. and WUITE G. J. L. (2013) Integrin and Defensin Modulate the Mechanical Properties of Adenovirus, *Journal of Virology* **87**(5), 2756–2766.

SÖDERLUND H., PETTERSSON U., VENNSTRÖM B., PHILIPSON L. and MATHEWS M. B. (1976) A new species of virus-coded low molecular weight RNA from cells infected with adenovirus type 2, *Cell* **7**(4), 585–593.

SOEUR M., WOUTERS A., DE SAINT-GEORGES A., CONTENT J. and DEPIERREUX M. (1991) Meningoencephalitis and meningitis due to an adenovirus type 5 in two immunocompetent adults, *Acta Neurologica Belgica* **91**(3), 141–150.

SONG C.-Z., LOEWENSTEIN P. M., TOTH K., TANG Q., NISHIKAWA A. and GREEN M. (1997) The Adenovirus E1A Repression Domain Disrupts the Interaction between the TATA Binding Protein and the TATA Box in a Manner Reversible by TFIIB, *Molecular and Cellular Biology* **17**(4), 2186–2193.

SORIA C., ESTERMANN F. E., ESPANTMAN K. C. and SHEA C. C. O. (2010) Heterochromatin silencing of p53 target genes by a small viral protein, *Nature* **466**(7310), 1076–1081.

SORIANO A. M., CRISOSTOMO L., MENDEZ M., GRAVES D., FROST J. R., OLANUBI O., SHYTE P. F., PATRICK H. and PELKA P. (2019) Adenovirus 5 E1A Interacts with E4orf3 To Regulate Viral Chromatin Organization, *Journal of Virology* **93**(10), 1–15.

SOURVINOS G., TAVALAI N., BERNDT A., SPANDIDOS D. A. and STAMMINGER T. (2007) Recruitment of Human Cytomegalovirus Immediate-Early 2 Protein onto Parental Viral Genomes in Association with ND10 in Live-Infected Cells, *Journal of Virology* **81**(18), 10123–10136.

STEENTOFT C., VAKHRUSHEV S. Y., JOSHI H. J., KONG Y., VESTER-CHRISTENSEN M. B., SCHJOLDAGER K. T., LAVRSEN K., DABELSTEEN S., PEDERSEN N. B., MARCOS-SILVA L., GUPTA R., PAUL BENNETT E., MANDEL U., BRUNAK S., WANDALL H. H., LEVERY S. B. and CLAUSEN H. (2013) Precision mapping of the human O-GalNAc glycoproteome through SimpleCell technology, *EMBO Journal* **32**(10), 1478–1488.

STEWART A. R., TOLLEFSON A. E., KRAJCSI P., YEI S.-P. and WOLD W. S. M. (1995) The Adenovirus E3 10.4K and 14.5K Proteins , Which Function To Prevent Cytolysis by Tumor Necrosis Factor and To Down-Regulate the Epidermal Growth Factor Receptor, Are Localized in the Plasma Membrane, *Journal of Virology* **69**(1), 172–181.

STEWART P. L., BURNETT R. M., CYRKLAFF M. and FULLERT S. D. (1991) Image Reconstruction Molecular Organization Reveals the Complex of Adenovirus, *Cell* **67**, 145–154.

STICHLING N., SUOMALAINEN M., FLATT J. W., SCHMID M., PACESA M., HEMMI S., JUNGRAITHMAYR W., MALER M. D., FREUDENBERG M. A., PLÜCKTHUN A., MAY T., KÖSTER M., FEJER G. and GREBER U. F. (2018) Lung macrophage scavenger receptor SR-A6 (MARCO) is an adenovirus type-specific virus entry receptor, *PLoS Pathogens* **14**(3), 1–33.

STRANG B. L., BOULANT S., CHANG L., KNIPE D. M., KIRCHHAUSEN T. and COEN D. M. (2012) Human Cytomegalovirus UL44 Concentrates at the Periphery of Replication Compartments, the Site of Viral DNA Synthesis, *Journal of Virology* **86**(4), 2089–2095.

STRAUSSBERG R., HAREL L., LEVY Y. and AMIR J. (2001) A Syndrome of Transient Encephalopathy Associated With Adenovirus Infection, *Pediatrics* **107**(5), 1–4.

STRUNZE S., ENGELKE M. F., WANG I. H., PUNTENER D., BOUCKE K., SCHLEICH S., WAY M., SCHOENENBERGER P., BURCKHARDT C. J. and GREBER U. F. (2011) Kinesin-1-mediated capsid disassembly and disruption of the nuclear pore complex promote virus infection, *Cell Host and Microbe* **10**(3), 210–223.

STRUNZE S., TROTMAN L. C., BOUCKE K. and GREBER U. F. (2005) Nuclear Targeting of Adenovirus Type 2 Requires CRM1-mediated Nuclear Export, *Molecular Biology of the Cell* **16**, 2999–3009.

STUBBE M., MAI J., PAULUS C., STUBBE H. C., BERSCHEMINSKI J., KARIMI M., HOFMANN S., WEBER E., HADIAN K., HAY R., GROITL P., NEVELS M., DOBNER T. and SCHREINER S. (2020) Viral DNA binding protein SUMOylation promotes PML nuclear body localization next to viral replication centers, *mBio* **11**(2), 1–21.

SUBACH F. V., PATTERSON G. H., RENZ M., LIPPINCOTT-SCHWARTZ J. and VERKHUSHA V. V. (2011) Bright monomeric photoactivatable red fluorescent protein for two-color super-resolution sptPALM of live cells, *Journal of the American Chemical Society* **132**(18), 6481–6491.

SUNDARARAJAN R., CUCONATI A., NELSON D. and WHITE E. (2001) Tumor Necrosis Factor-α Induces Bax-Bak Interaction and Apoptosis, Which Is Inhibited by Adenovirus E1B 19K, *The Journal of Biological Chemistry* **276**(48), 45120–45127.

SUNDARARAJAN R. and WHITE E. (2001) E1B 19K blocks Bax oligomerization and tumor necrosis factor alpha-mediated apoptosis., *Journal of Virology* **75**(16), 7506–7516.

SUOMALAINEN M., LUISONI S., BOUCKE K., BIANCHI S., ENGEL D. A. and GREBER U. F. (2013) A Direct and Versatile Assay Measuring Membrane Penetration of Adenovirus in Single Cells, *Journal of Virology* **87**(22), 12367–12379.

SUZUKI T., ORBA Y., OKADA Y., SUNDEN Y., KIMURA T., TANAKA S., NAGASHIMA K., HALL W. W. and SAWA H. (2010) The human polyoma JC virus agnoprotein acts as a viroporin, *PLoS Pathogens* **6**(3).

SWAMINATHAN S. and THIMMAPAYA B. (1995) Regulation of adenovirus E2 transcription unit, *Curr Top Microbiol Immunol* **199**(3), 177–194.

TAHERZADEH G., DEHZANGI A., GOLCHIN M., ZHOU Y. and CAMPBELL M. P. (2019) SPRINT-Gly: predicting N- and O-linked glycosylation sites of human and mouse proteins by using sequence and predicted structural properties, *Bioinformatics* **35**(20), 4140–4146.

TAMANOI F. and STILLMAN B. W. (1982) Function of adenovirus terminal protein in the initiation of DNA replication, *Proceedings of the National Academy of Sciences* **79**, 2221–2225.

TEODORO J. G. and BRANTON P. E. (1997) Regulation of p53-Dependent Apoptosis , Transcriptional Repression, and Cell Transformation by Phosphorylation of the 55-Kilodalton E1B Protein of Human Adenovirus Type 5, *Journal of Virology* **71**(5), 3620–3627.

TOLLEFSON A. E., RYERSE J. S., SCARIA A., HERMISTON T. W. and WOLD W. S. M. (1996a) The E3-11.6-kDa adenovirus death protein (ADP) is required for efficient cell death: Characterization of cells infected with adp mutants, *Virology* **220**(1), 152–162.

TOLLEFSON A. E., SCARIA A., HERMISTON T. W., RYERSE J. S., WOLD L. J. and WOLD W. S. M. (1996b) The adenovirus death protein (E3-11.6K) is required at very late stages of infection for efficient cell lysis and release of adenovirus from infected cells., *Journal of Virology* **70**(4), 2296–306.

TOLLEFSON A. E., SCARIA A., YING B. and WOLD W. S. M. (2003) Mutations within the ADP (E3-11.6K) protein alter processing and localization of ADP and the kinetics of cell lysis of adenovirus-infected cells, *J Virol* **77**(14), 7764–7778.

TOLLEFSON A. E., TOTH K., DORONIN K., KUPPUSWAMY M., DORONINA O. A., LICHTENSTEIN D. L., HERMISTON T. W., SMITH C. A. and WOLD W. S. M. (2001) Inhibition of TRAIL-Induced Apoptosis and Forced Internalization of TRAIL Receptor 1 by Adenovirus Proteins, *Journal of Virology* **75**(19), 8875–8887.

TOLLEFSON A. E., YING B., DORONIN K., SIDOR P. D. and WOLD W. S. M. (2007) Identification of a New Human Adenovirus Protein Encoded by a Novel Late l-Strand Transcription Unit, *Journal of Virology* **81**(23), 12918–12926.

TOTH K., DJEHA H., YING B., TOLLEFSON A. E., KUPPUSWAMY M., DORONIN K., KRAJCSI P., LIPINSKI K., WRIGHTON C. J. and WOLD W. S. (2004) An oncolytic adenovirus vector combining enhanced cell-to-cell spreading, mediated by the ADP cytolytic protein, with selective replication in cancer cells with deregulated wnt signaling, *Cancer Research* **64**(10), 3638–3644.

TOUSIMIS A. J. and HILLEMAN M. R. (1957) Electron Microscopy of Type Strain RI-67, *Virology* **4**, 499–508.

TREACY A., CARR M. J., DUNFORD L., PALACIOS G., CANNON G. A., GRADY A. O., MORAN J., HASSAN J., LOY A., CONNELL J., DEVANEY D., KELEHAN P. and HALL W. W. (2010) First Report of Sudden Death Due to Myocarditis Caused by Adenovirus Serotype 3, *Journal of Clinical Microbiology* **48**(2), 642–645.

TROTMAN L. C., MOSBERGER N., FORNEROD M., STIDWILL R. P. and GREBER U. F. (2001) Import of adenovirus DNA involves the nuclear pore complex receptor CAN/Nup214 and histone H1, *Nature Cell Biology* **3**(12), 1092–1100.

UGAI H., BOROVJAGIN A. V., LE L. P., WANG M. and CURIEL D. T. (2007) Thermostability/Infectivity Defect Caused by Deletion of the Core Protein V Gene in Human Adenovirus Type 5 Is Rescued by Thermo-selectable Mutations in the Core Protein X Precursor, *Journal of Molecular Biology* **366**(4), 1142–1160.

UGAI H., DOBBINS G. C., WANG M., LE L. P., MATTHEWS D. A. and CURIEL D. T. (2012) Adenoviral protein V promotes a process of viral assembly through nucleophosmin 1, *Virology* **432**(2), 283–295.

UGAI H., WANG M., LE L. P., MATTHEWS D. A., YAMAMOTO M. and CURIEL D. T. (2010) In Vitro Dynamic Visualization Analysis of Fluorescently Labeled Minor Capsid Protein IX and Core Protein V by Simultaneous Detection, *Journal of Molecular Biology* **395**(1), 55–78.

UHNOO I., WADELL G., SVENSSON L. and JOHANSSON M. E. (1984) Importance of Enteric Adenoviruses 40 and 41 in Acute Gastroenteritis in Infants and Young Children, *Journal of Clinical Microbiology* **20**(3), 365–372.

ULLMAN A. J., REICH N. C. and HEARING P. (2007) Adenovirus E4 ORF3 Protein Inhibits the Interferon-Mediated Antiviral Response, *Journal of Virology* **81**(9), 4744–4752.

UNITED NATIONS (2019) *Globally Harmonized System of Classification and Labelling of Chemicals (GHS)*, UN, New York.

VALENTINE R. C. and HOPPER R. K. (1957) Polyhedral Shape of Adenovirus, *Nature* **180**, 928.

VAN BREUKELEN B., KANELLOPOULOS P. N., TUCKER P. A. and VAN DER VLIET P. C. (2000) The formation of a flexible DNA-binding protein chain is required for efficient DNA unwinding and adenovirus DNA chain elongation, *Journal of Biological Chemistry* **275**(52), 40897–40903.

VAN OOSTRUM J. and BURNETT R. M. (1985) Molecular Composition of the Adenovirus Type 2 Virion, *Journal of Virology* **56**(2), 439–448.

VAN RAAIJ M. J., MITRAKI A., LAVIGNE G. and CUSACK S. (1999) A triple β-spiral in the adenovirus fibre shaft reveals a new structural motif for a fibrous protein, *Nature* **401**(6756), 935–938.

VASSAL-STERMANN E., MOTTET M., DUCOURNAU C., ISENI F., VRAGNIAU C., WANG H., ZUBIETA C., LIEBER A. and FENDER P. (2018) Mapping of Adenovirus of serotype 3 fibre interaction to desmoglein 2 revealed a novel 'non-classical' mechanism of viral receptor engagement, *Scientific Reports* **8**(1), 1–10.

VAYDA M. E., ROGERS A. E. and FLINT S. J. (1983) The structure of nucleoprotein cores released from adenovirions, *Nucleic Acids Research* **11**(2), 441–460.

VELLINGA J., VAN DEN WOLLENBERG D. J. M., VAN DER HEIJDT S., RABELINK M. J. W. E. and HOEBEN R. C. (2005) The Coiled-Coil Domain of the Adenovirus Type 5 Protein IX Is Dispensable for Capsid Incorporation and Thermostability, *Journal of Virology* **79**(5), 3206–3210.

VELTROP-DUITS L. A., VAN VREESWIJK T., HEEMSKERK B., THIJSSEN J. C., SEADY R. E., JOL-VAN DER ZIJDE E. M., CLAAS E. C., LANKESTER A. C., VAN TOL M. J. and SCHILHAM M. W. (2011) High titers of pre-existing adenovirus serotype-specific neutralizing antibodies in the host predict viral reactivation after allogeneic stem cell transplantation in children, *Clinical Infectious Diseases* **52**(12), 1405–1413.

VILASECA E., ISVORAN A., MADURGA S., PASTOR I., GARCÉS J. L. and MAS F. (2011) New insights into diffusion in 3D crowded media by Monte Carlo simulations: Effect of size, mobility and spatial distribution of obstacles, *Physical Chemistry Chemical Physics* **13**(16), 7396–7407.

VOLLMER B., PRAZÁK V., VASISHTAN D., JEFFERYS E. E., HERNANDEZ-DURAN A., VALLBRACHT M., KLUPP B. G., METTENLEITER T. C., BACKOVIC M., REY F. A., TOPF M. and GRÜNEWALD K. (2020) The prefusion structure of herpes simplex virus glycoprotein B, *Science Advances* **6**(39), 1–12.

WALKER P. J., SIDDELL S. G., LEFKOWITZ E. J., MUSHEGIAN A. R., DEMPSEY D. M., DUTILH B. E., HARRACH B., HARRISON R. L., HENDRICKSON R. C., JUNGLEN S., KNOWLES N. J., KROPINSKI A. M., KRUPOVIC M., KUHN J. H., NIBERT M., RUBINO L., SABANADZOVIC S., SIMMONDS P., VARSANI A., ZERBINI F. M. and DAVISON A. J. (2019) Changes to virus taxonomy and the International Code of Virus Classification and Nomenclature ratified by the International Committee on Taxonomy of Viruses (2019), *Archives of Virology* **164**(9), 2417–2429.

WALTON J. (1979) Lead aspartate, an en bloc contrast stain particularly useful for ultrastructural enzymology, *Journal of Histochemistry and Cytochemistry* **27**(10), 1337–1342.

WANG H., SUN L., SU L., RIZO J., LIU L., WANG L. F., WANG F. S. and WANG X. (2014) Mixed Lineage Kinase Domain-like Protein MLKL Causes Necrotic Membrane Disruption upon Phosphorylation by RIP3, *Molecular Cell* **54**(1), 133–146.

WANG I. H., BURCKHARDT C. J., YAKIMOVICH A., MORF M. K. and GREBER U. F. (2017) The nuclear export factor CRM1 controls juxta-nuclear microtubule-dependent virus transport, *Journal of Cell Science* **130**(13), 2185–2195.

WANG J., SAROV M., RIENTJES J., FU J., HOLLAK H., KRANZ H., XIE W., STEWART A. F. and ZHANG Y. (2006) An Improved Recombineering Approach by Adding RecA to λ Red Recombination, *Molecular Biotechnology* **32**, 43–53.

WANG K., HUANG S., KAPOOR-MUNSHI A. and NEMEROW G. (1998) Adenovirus Internalization and Infection Require Dynamin, *Journal of Virology* **72**(4), 3455–3458.

WATANABE K., TAKATSUKI H., SONODA M., TAMURA S., MURAKAMI N. and KOBAYASHI N. (2011) Anti-influenza viral effects of novel nuclear export inhibitors from Valerianae Radix and Alpinia galanga, *Drug Discoveries & Therapeutics* **5**(1), 26–31.

WEBER J. (1976) Genetic analysis of adenovirus type 2 III. Temperature sensitivity of processing viral proteins, *Journal of Virology* **17**(2), 462–471.

WEBER J. and STICH H. F. (1969) Electron Microscopy of Cells Infected with Adenovirus Type 2, *Journal of Virology* **3**(2), 198–204.

WEBSTER A., HAY R. T. and KEMP G. (1993) The adenovirus protease is activated by a virus-coded disulphide-linked peptide, *Cell* **72**(1), 97–104.

WEBSTER A., LEITH I. R. and HAY R. T. (1994) Activation of adenovirus-coded protease and processing of preterminal protein, *Journal of Virology* **68**(11), 7292–7300.

WEBSTER A., RUSSELL W. C. and KEMP G. D. (1989) Characterization of the adenovirus proteinase: Development and use of a specific peptide assay, *Journal of General Virology* **70**(12), 3215–3223.

WEIGERT M., BINKS A., DOWSON S., LEUNG E. Y., ATHINEOS D., YU X., MULLIN M., WALTON J. B., ORANGE C., ENNIS D., BLYTH K., TAIT S. W. and MCNEISH I. A. (2017) RIPK3 promotes adenovirus type 5 activity, *Cell Death and Disease* **8**(12).

WEINMANN R., RASKAS H. J. and ROEDER R. G. (1974) Role of DNA dependent RNA polymerases II and III in transcription of the adenovirus genome late in productive infection, *Proceedings of the National Academy of Sciences of the United States of America* **71**(9), 3426–3430.

WELLEHAN J. F. X., JOHNSON A. J., PESSIER A. P., JOHNSON C. M., GARNER M. M., CHILDRESS A. and JACOBSON E. R. (2004) Detection and Analysis of Six Lizard Adenoviruses by Consensus Primer PCR Provides Further Evidence of a Reptilian Origin for the Atadenoviruses, *Journal of Virology* **78**(23), 13366–13369.

WHITE E., SABBATINI P., DEBBAS M., WOLD W. S. M. and GOODING L. R. (1992) The 19-Kilodalton Adenovirus EBB Transforming Protein Inhibits Programmed Cell Death and Prevents Cytolysis by Tumor Necrosis Factor α, *Molecular and Cellular Biology* **12**(6), 2570–2580.

WHYTE P., BUCHKOVICH K. J., HOROWITZ J. M., FRIEND S. H., RAYBUCK M., WEINBERG R. A. and HARLOW E. (1988) Association between an oncogene and an anti-oncogene: the adenovirus E1A proteins bind to the retinoblastoma gene product, *Nature* **334**(6178), 124–129.

WICKHAM T. J., MATHIAS P., CHERESH D. A. and NEMEROW G. R. (1993) Integrins $\alpha v \beta 3$ and $\alpha v \beta 5$ promote adenovirus internalization but not virus attachment, *Cell* **73**(2), 309–319.

WIETHOFF C. M., WODRICH H., GERACE L. and NEMEROW G. R. (2005) Adenovirus Protein VI Mediates Membrane Disruption following Capsid Disassembly, *Journal of Virology* **79**(4), 1992–2000.

WIGAND R. and KÜMEL G. (1977) The kinetics of adenovirus infection and spread in cell cultures infected with low multiplicity, *Archives of Virology* **54**(3), 177–187.

WILLS E. J., RUSSEL W. C. and WILLIAMS J. F. (1973) Adenovirus-induced Crystals : studies with Temperature-sensitive Mutants, *Journal of General Virology* **20**, 407–412.

WIMMER P., SCHREINER S., EVERETT R. D., SIRMA H., GROITL P. and DOBNER T. (2010) SUMO modification of E1B-55K oncoprotein regulates isoform-specific binding to the tumour suppressor protein PML, *Oncogene* **1**, 5511–5522.

WINBERG G. and SHENK T. (1984) Dissection of overlapping functions within the adenovirus, *The EMBO Journal* **3**(8), 1907–1912.

WODRICH H., CASSANY A., D'ANGELO M. A., GUAN T., NEMEROW G. and GERACE L. (2006) Adenovirus Core Protein pVII Is Translocated into the Nucleus by Multiple Import Receptor Pathways, *Journal of Virology* **80**(19), 9608–9618.

WODRICH H., GUAN T., CINGOLANI G., SEGGERN D. V., NEMEROW G. and GERACE L. (2003) Switch from capsid protein import to adenovirus assembly by cleavage of nuclear transport signals, *The EMBO Journal* **22**(23), 6245–6255.

WOLFF G., LIMPENS R. W., ZHENG S., SNIJDER E. J., AGARD D. A., KOSTER A. J. and BÁRCENA M. (2019) Mind the gap: Micro-expansion joints drastically decrease the bending of FIB-milled cryo-lamellae, *Journal of Structural Biology* **208**(3), 1–4.

WU E., PACHE L., VON SEGGERN D. J., MULLEN T.-M., MIKYAS Y., STEWART P. L. and NEMEROW G. R. (2004) Flexibility of the Adenovirus Fiber Is Required for Efficient Receptor Interaction, *Journal of Virology* **78**(4), 2167–2167.

WU K., GUIMET D. and HEARING P. (2013) The Adenovirus L4-33K Protein Regulates both Late Gene Expression Patterns and Viral DNA Packaging, *Journal of Virology* **87**(12), 6739–6747.

WU K., OROZCO D. and HEARING P. (2012) The Adenovirus L4-22K Protein Is Multifunctional and Is an Integral Component of Crucial Aspects of Infection, *Journal of Virology* **86**(19), 10474–10483.

WU N., ZHANG H., DENG F., LI R., ZHANG W., CHEN X., WEN S., WANG N., ZHANG J., YIN L., LIAO Z., ZHANG Z., ZHANG Q., YAN Z., LIU W., WU D., YE J., DENG Y., YANG K., LUU H., HAYDON R. and HE T.-C. (2014) Overexpression of Ad5 precursor terminal protein accelerates recombinant adenovirus packaging and ampli fi cation in HEK-293 packaging cells, *Gene Therapy* **21**, 629–637.

WU P.-Q., ZENG S.-Q., YIN G.-Q., HUANG J.-J., XIE Z.-W., LU G. and JIANG W.-H. (2020) Clinical manifestations and risk factors of adenovirus respiratory infection in hospitalized children in Guangzhou, China during the 2011–2014 period, *Medicine* **99**(4), 1–6.

XI Q., CUESTA R. and SCHNEIDER R. J. (2004) Tethering of eIF4G to adenoviral mRNAs by viral 100k protein drives ribosome shunting, *Genes and Development* **18**(16), 1997–2009.

XI Q., CUESTA R. and SCHNEIDER R. J. (2005) Regulation of Translation by Ribosome Shunting through Phosphotyrosine-Dependent Coupling of Adenovirus Protein 100k to Viral mRNAs, *Journal of Virology* **79**(9), 5676–5683.

XIAO D. J., FEI L. I. A., QING L. I. R., SHUANG C., SONG Y. and YING Z. X. (2020) Letter to the Editor Epidemiological and Clinical Features of Rotavirus and Adenovirus Related Gastroenteritis in Beijing: A Retrospective Case-control Study in Pediatric, *Biomedical and Environmental Science* **33**(3), 196–200.

XIE Y., ZHENG Y., LI H., LUO X., HE Z., CAO S., SHI Y., ZHAO Q., XUE Y., ZUO Z. and REN J. (2016) GPS-Lipid: A robust tool for the prediction of multiple lipid modification sites, *Scientific Reports* **6**, 1–9.

YAKIMOVICH A., GUMPERT H., BURCKHARDT C. J., LUTSCHG V. A., JURGEIT A., SBALZARINI I. F., GREBER U. F., LÜTSCHG V. A., JURGEIT A., SBALZARINI I. F. and GREBER U. F. (2012) Cell-Free Transmission of Human Adenovirus by Passive Mass Transfer in Cell Culture Simulated in a Computer Model, *Journal of Virology* **86**(18), 10123–10137.

YAN J., DONG J., WU J., ZHU R., WANG Z., WANG B., WANG L., WANG Z., ZHANG H., WU H., YU B., KONG W. and YU X. (2016) Interaction between hexon and L4-100K determines virus rescue and growth of hexon-chimeric recombinant Ad5 vectors, *Scientific Reports* **6**, 1–13.

YING B., TOLLEFSON A. E. and WOLD W. S. M. (2010) Identification of a Previously Unrecognized Promoter That Drives Expression of the UXP Transcription Unit in the Human Adenovirus Type 5 Genome, *Journal of Virology* **84**(21), 11470–11478.

YING B. and WOLD W. S. (2003) Adenovirus ADP protein (E3-11.6K), which is required for efficient cell lysis and virus release, interacts with human MAD2B, *Virology* **313**(1), 224–234.

Yu X., Veesler D., Campbell M. G., Barry M. E., Asturias F. J., Barry M. A. and Reddy V. S. (2017) Cryo-EM structure of human adenovirus D26 reveals the conservation of structural organization among human adenoviruses, *Science Advances* **3**, 1–12.

Zając-Spychała O., Pieczonka A., Wachowiak J., Frączkiewicz J., Salamonowicz M., Kałwak K., Gorczyńska E., Kazanowska B., Wróbel G., Chybicka A., Czyżewski K., Dziedzic M., Wysocki M., Zalas-Więcek P., Szmydki-Baran A., Hutnik Ł., Matysiak M., Irga-Jaworska N., Bień E., Drożyńska E., Stolpa W., Sobol-Milejska G., Pierlejewski F., Młynarski W., Gryniewicz-Kwiatkowska O., Gietka A., Dembowska-Bagińska B., Semczuk K., Dzierżanowska-Fangrat K., Gamrot-Pyka Z., Woszczyk M., Urbanek-Dądela A., Karolczyk G., Płonowski M., Krawczuk-Rybak M., Zaucha-Prażmo A., Kowalczyk J., Goździk J. and Styczyński J. (2020) Adenovirus infection among pediatric patients with cancer and in pediatric recipients of hematopoietic stem cell: a multicenter nationwide study, *Journal of Medical Virology* **92**, 3187–3193.

Zhang H.-Y., Li Z.-M., Zhang G.-L., Diao T.-T., Cao C.-X. and Sun H.-Q. (2009) Respiratory viruses in hospitalized children with acute lower respiratory tract infections in harbin, China, *Japanese Journal of Infectious Diseases* **62**(6), 458–460.

Zhang W. and Arcos R. (2005) Interaction of the adenovirus major core protein precursor, pVII, with the viral DNA packaging machinery, *Virology* **334**(2), 194–202.

Zhang W. and Imperiale M. J. (2003) Requirement of the Adenovirus IVa2 Protein for Virus Assembly, *Journal of Virology* **77**(6), 3586–3594.

Zhang W., Low J. A., Christensen J. B. and Imperiale M. J. (2001) Role for the Adenovirus IVa2 Protein in Packaging of Viral DNA, *Journal of Virology* **75**(21), 10446–10454.

Zhang Y. and Schneider R. J. (1994) Adenovirus inhibition of cell translation facilitates release of virus particles and enhances degradation of the cytokeratin network, *Journal of Virology* **68**(4), 2544–2555.

Zhang Z., Greene B., Thuman-Commike P. A., Jakana J., Prevelige P. E., King J. and Chiu W. (2000) Visualization of the maturation transition in bacteriophage P22 by electron cryomicroscopy, *Journal of Molecular Biology* **297**(3), 615–626.

Zhao H., Chen M. and Pettersson U. (2014) A new look at adenovirus splicing, *Virology* **456-457**(1), 329–341.

Zhao H., Traganos F., Dobrucki J., Wlodkowic D. and Darzynkiewicz Z. (2009) Induction of DNA Damage Response by the Supravital Probes of Nucleic Acids, *Cytometry* **75**(6), 510–519.

Zheng S. Q., Palovcak E., Armache J.-P., Verba K. A., Cheng Y. and Agard D. A. (2017) MotionCor2 - anisotropic correction of beam-induced motion for improved cryo-electron microscopy, *Nature Methods* **14**(4), 331–332.

Zheng Y., Stamminger T. and Hearing P. (2016) E2F / Rb Family Proteins Mediate Interferon Induced Repression of Adenovirus Immediate Early Transcription to Promote Persistent Viral Infection, *PLoS Pathogens* **12**(1), 1–24.

Zhou Y., Pan Q., Wang X., Zhang L., Xiao F. and Guo L. (2018) The relationship between human adenovirus 36 and obesity in Chinese Han population, *Bioscience Reports* **38**, 1–7.

ZOU A., ATENCIO I., HUANG W. M., HORN M. and RAMACHANDRA M. (2004) Overexpression of adenovirus E3-11.6K protein induces cell killing by both caspase-dependent and caspase-independent mechanisms, *Virology* **326**(2), 240–249.

ZUBIETA C., SCHOEHN G., CHROBOCZEK J. and CUSACK S. (2005) The Structure of the Human Adenovirus 2 Penton, *Molecular Cell* **17**, 121–135.

Appendix

List of hazardous substances according to GHS classification

All hazardous compounds that were used in this work are listed below (Table 38) including their H-statements, P-statements and hazard pictograms (Figure 48).

Table 38: List of hazardous substances according to Globally Harmonized System of Classification and Labelling of Chemicals (GHS) classification including H-statements and P-statements and GHS hazard pictogram references.

Compound/Kit	H Statement	P Statement	Hazard pictogram
2-propanol	H225, H319, H336	P210, P233, P280, P305+P351+P338, P304+P340, P337+P313	02, 07
APS	H272, H302, H315, H317, H319, H334, H335	P210, P280, P301+P012+P030, P302+P352, P305+P351+P338	02, 07, 08
Ammonium chloride	H302, H319	P270, P305+P351+P338	07
Ampicillin sodium salt	H317, H334	P261, P280, P342+P311	08
β-mercaptoethanol	H227, H301 + H331, H310, H315, H317, H318, H361fd, H373, H410	P261, P273, P280, P302+P350, P305+P351+P338, P310, P501	05, 06, 08, 09
Boric acid	H360FD	P202, P281, P308+P313, P405, P501	08
bromophenol blue	H225, H319	P210, P241, P280, P303+P361+P353, P305+P351+P338, P501	02, 07
Caesium chloride	H361fd	P280, P308+P313	08
Calcium Chloride	319	280, P305+P351+P338, P337+P313	07
Chloramphenicol	H318, H351, H361	P201, P202, P280, P305+351+338, P308+313, P310	05, 08
Crystal Violet	H226, H319, H351, H411	P273, P281, P305+P351+P338	02, 07, 08, 09
DDSA	H315, H319, H335	P302+P352, P305+P351+P338	07
DMP-30	H302, H315, H319	P264, P270, P280, P301+P312, P302+P352, P305+P351+P338, P321, P330, P332+P313, P337+P313, P362, P501	07

Compound/Kit	H Statement	P Statement	Hazard pictogram
DTT	H302, H412	P264, P270, P273, P301+P312+P330, P501	07
Ethanol	H225, H319	P210, P233, P305+P351+P338	02, 07
Ethidium bromide solution	H331, H341	P261, P281, P311	06, 08
GA	H302, H314, H317, H330, H334, H335	P260, P280, P302+P352,P303+P361+P353, P304+P340, P305+P351+P338, P310, P342+P311, P403+P233	05, 06, 08
Glacial acetic acid	H226, H314, H318	P210, P280, P301+P330+P331, P303+P361+P353, P305+P351+P338, P310	02, 05
Glycid ether 100	H315, H319, H341, H361f	P280, P302+P352, P305+P351+P338, P308+P313, P337+P313, P501	07, 08
Hoechst 33342	302, 314, 335	261, 280, 05+351+338, 310	05, 07
Hydrochloric acid	H290, H314, H335	P280, P301 + P330 + P331, P305+P351+P338, P308 + P310	05, 07
Kanamycin A	H360	P201, P202, P280, P308+313	08
Lead nitrate	H302+H332, H360Df, H372, H410	P273, P281, P301+P312, P304+P340, P312, P405	07, 08, 09
Manganese chloride	H301, H318, H373	P260, P301+P310, P305+P351+P338, P321, P330, P501	05, 06, 08
Methanol	H225, H301+H311+H331, H370	P210, P270, P280	02, 06, 08
MNA	H302, H314, H315, H317, H318, H319, H331, H334, H335	P260, P261, P264, P270, P271, P272, P280, P285, P301+P312, P301+P330+P331, P302+P352, P303+P361+P353, P304+P340, P304+P341, P305+P351+P338, P310, P311, P312, P321, P330, P332+P313, P333+P313, P337+P313, P342+P311, P362, P363, P403+P233, P405, P501	05, 06, 07, 08
MOPS	H315, H319, H335	P261, P264, P271, P280, P302+352, P304+340, P305+351+338, P312, P321, P332+313, P337+313, P362, P403+233, P405, P501	07
Nonidet P-40	H315, H319	P264, P280, P302+352, P305+351+338, P332+313, P337+313, P362+364	07
Osmium tetroxide	H300+H310+H330, H314	P301+P330+P331, P302+P350, P304+P340, P305+P351+P338, P309+P311	05, 06
PEI	H302, H317, H319, H411	P273, P280, P305+P351+P338	07, 09

Compound/Kit	H Statement	P Statement	Hazard pictogram
PFA	H302, H312, H315, H317, H332, H335, H319, H341, H350	P201, P261, P264, P270, P280, P301+P310, P302+P352, P304+P340, P305+P351+P338, P308+P313	05, 07, 08
Penicillin-Streptomycin	H302, H317, H361	P280, P302 + P352, P308+P313	07, 08
PMSF	H301, H314	P280, P301+P310+P330, P303+P361+P353, P304+P340+P310, P305+P351+P338	05, 06
QIAPrep Spin Miniprep/Maxiprep kit	H225, H290, H315, H317, H319, H334, H336	P210, P261, P280, P284, P304+P340, P342+P311	02, 05, 07, 08
QIAquick Gel Extraction kit	H302, H318, H412	P280, P305+P351+P338+P310	05, 07
QIAquick PCR Purification kit	H225, H315, H319, H336	P210, P280	02, 07
30 % acrylamide/ bisacrylamide stock solution	H302, H315, H317, H319, H340, H350, H361f, H372	P201, P280, P302+P352, P308+P313	07, 08
Sodium deoxycholate	H302, H335	P261, P264, P270, P271, P301+P312, P304+P340, P312, P330, P403+P233, P405, P501	07
SDS	H228, H302+H332, H315, H318, H335, H412	P210, P261, P280, P302+P352, P305+P351+P338, P312	02, 05, 07
Sodium hydroxide	H290, H314	P233, P280, P303+P361+P353, P305+P351+P338, P310	05
Streptomycin	H302, H317, H361	P201, P202, P261, P264, P272, P280, P301+312, P302+352, P308+313, P330, P333+313, P362+364	07, 08
TEMED	H225, H302+H332, H314	P210, P280, P301+P330+P331, P303+P361+P353, P304+P340+P312, P305+P351+P338	02, 05, 07
Thiocarbohydrazide	H300, H311, H330	P260, P264, P270, P271, P280, P284, P301+P310, P302+P352, P304+P340, P310, P312, P320, P321, P322, P330, P361, P363, P403+P233, P405, P501	06
Triton X-100	H302, H315, H318, H410	P273, P280, P302+P352, P305+P351+P338, P313	05, 07, 09
Uranyl acetate	H300+H330, H373, H411	P260, P284, P301+P310, P320, P405, P501	06, 08, 09
Xylene cyanol	H315, H319, H335	P261, P305 + P351 + P338	07
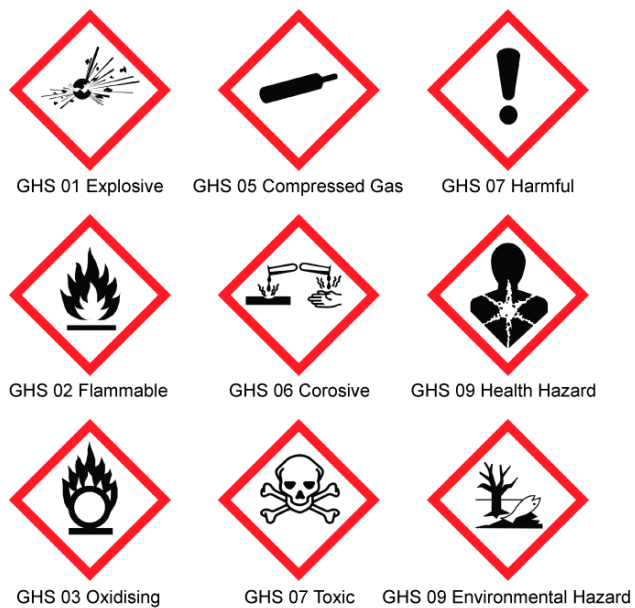
Figure 48: Overview of GHS hazard picograms The GHS hazard pictograms are labelled 01-09 as referred to in Table 38. Pictograms are shown as published by the United Nations (UNITED NATIONS, 2019)

.

Acknowledgements

First of all, I want to thank both my supervisors Prof. Kay Grünewald and Prof. Thomas Dobner for the opportunity to work in both their laboratories. This joint project was facilitated by the HPI strategic incentive programme. I believe this programme is extremely helpful and allowed me to gain valuable experience from both groups and combine their expertise in the field of virology.

In addition, I want to thank Prof. Grünewald for being part of the examination committee of my disputation and for writing the evaluation of this dissertation. My thanks also go to the other members of my examination committee, Prof. Wilson and Prof. Meier and to Prof. Brune for writing the second evaluation of this work.

I am incredibly grateful for the support and hugely helpful discussions with my lab supervisors Dr. Helga Hofmann-Sieber, Dr. Linda E. Franken and Dr. Jens B. Bosse. You have taught me so much about techniques in cell culture, light microscopy, electron cryo-microscopy and generally being a better scientist.

Thank you to all my lab members from both groups, you made my time at the HPI a highly memorable and enjoyable. Thank you Konstantin and Laura for all the fun kitchen talks, thank you Wingi and Linda for always lending an ear when I wanted to discuss data and for reading my dissertation. Thank you Carola and Rudi for the support in electron microscopy.

And lastly, I want to thank my parents. I know that without you I would not be anywhere near where I am now. I am very grateful for your everlasting support.

Declarations

„Hiermit versichere ich an Eides statt, die vorliegende Dissertation selbst verfasst und keine anderen als die angegebenen Hilfsmittel benutzt zu haben. Die eingereichte schriftliche Fassung entspricht er auf dem elektronischen Speichermedium. Ich versichere, dass diese Dissertation nicht in einem früheren Promotionsverfahren eingereicht wurde."

_____   _____

Datum   Unterschrift